Coupled Resonators for Ultraprecise Sensing Applications: Fabrication using State-of-the-art Laser Micromachining

By

Vinayak Pachkawade

Faculty of Applied Science

Department of Electrical Engineering and Computer Science

University of Liege

This dissertation is submitted for the degree of

Doctor of Philosophy

School of Engineering October 2019

I would like to dedicate this thesis to my loving child …*Grace*

Declaration

I, Vinayak Pachkawade, declare that except where specific reference is made to the work of others, the contents of this dissertation are original and have not been submitted in whole or in part for consideration for any other degree or qualification in this, or any other University. This dissertation contains less than 45,000 words including appendices, bibliography, footnotes, tables and equations and has less than 100 figures.

I further state that

- This work was done wholly or mainly while in candidature for a research degree at the University of Liege.
- A work in this thesis has attempted to the large extent to comply with the PhD research project that was drafted.
- A research presented in this thesis is the result of accumulative work that I have carried out on my own.
- A work done in this thesis complies the state-of-the-art in the field.
- All main resources and supports have been acknowledged.
- Parts of this work have been published in: 1) https://doi.org/10.1007/s00542-019-04549-2, and 2) [1].

Vinayak Pachkawade
October 2019

Acknowledgements

First, I expressed my sincere and deepest gratitude to the University of Liege for giving me an opportunity to do doctorate. It has been rewarding experience for me to do a PhD amidst thoughtful scientific community in the campus. This research was supported by University of Liege.

I thank my PhD advisor Prof. Dr. Michael Kraft. I learned from him not only about research but also many other things. As I move forward in my life, I adopt positives from him. I also would like to thank members of my thesis committee, Prof. Philippe Vanderbemden, Prof. Tristan Gilet, and Prof. Benoît Vanderheyden for their time, support and being my thesis committee members. Particularly, I thank Prof. Benoît Vanderheyden for his composed, reasonable perspective and support.

I also thank Prof. Guy Leduc, department chair, for his principle based approach and giving me an opportunity to continue my work at the University of Liege.

I extend my thanks to Dr. Serguei Stoukatch, for allowing me access to the Microsys clean room where, I could operate facilities such as optical microscope, wire bonding, etc. I also thanks other members of Microsys group, namely François Dupont, in supporting to arrange lab resources, Samuel Dricot for working with me in fabrication of prototype samples.

My thanks goes to one of the skilled technician of Montefiore institute, Mr. Thierry Legros, for continually helping me in circuit board assembly, support in arrangement of lab components at the earliest. I thank Pascal Harmeling for sharing his knowledge on board level electronics.

I acknowledge contribution from Delphine Cerica, then my lab mate and now a researcher in the department, with whom I used to discuss the research ideas. I also thank other lab mates for their cooperation during my work.

I show appreciation to many other people who directly/indirectly contributed in my work that I could reach to a stage of writing this dissertation.

I thank my family members, my wife for contributing in my well being, taking good care of my little daughter, Grace while I am at the office, working late hours often, and sometimes even during the weekends.

I thank my mother back in India who lent me her ears in difficult times, whenever I called her. She offered me an incredible sense and support.

Finally, I thank my graceful child Grace, whose delightful presence and charm contributed in supplying me energy and inspiration, to endure and accomplish my goal.

Vinayak Pachkawade

Abstract

This thesis documents a first time demonstration of electromechanical transducer and/or sensor fabricated using Direct Laser Writing (DLW). A low-cost prototype has been fabricated via a rapid and high-tech laser micro-milling technique to achieve a parallel kerf-width (capacitive gaps) of about 60 micrometers (*μm)* into a piece of aluminum and a stainless steel each of 1 and 2 millimeters (*mm*) thickness respectively, thus leading to a high-aspect ratio (> 33) structure. A device is demonstrated to facilitate actuation via electrostatic means and sense a capacitive change across its electrode. Experiments have been performed with a structure made of aluminum. Emphasis is on the fabrication and associated issues. A strategic fabrication and measurement of an average kerf-width of about 60 micrometres is reported, which is advantageous to develop our application. A detailed study of width variation using laser cut is also given. Based on the in-depth literature survey, it is postulated that achieving simultaneously a kerf-width as small as 60 μm with metal parts up to 2 mm thickness is unprecedented (either in the industry or in academia). This important aspect is one of the highlights of this research. Results comprising analytical modeling, fabrication, and electrical characterization are presented. An applicability of a device as a 2 degree-of-freedom (DoF) resonating mode-localization sensor that employs a weak electrostatic coupling is demonstrated to offer vibration amplitude based sensitivity to a relative change in the stiffness. This sensor is able to resolve a minimum stiffness perturbation (*normalized*), $\delta_{k_{\min}} = \frac{\Delta k}{K_{eff}}$ of the order of 7.98×10^{-4}. This magnitude is of the same order to that achievable in MEMS based coupled resonators. Based on our opening results, it is postulated that this navigating research opens up new possibilities to fabricate new devices and/or sensor based on alternative fabrication platform such as laser micromachining as reported here.

In parallel, a work in this thesis closely observes the state-of-the art for coupled resonators and thereby proposes realistic system level models in the context of our architecture fabricated using high-tech laser machining. Based on the representative system-level models developed in this thesis, theory estimate of maximum sensitivity to stiffness perturbation is found to be comparable to that achievable in MEMS for two degree of freedom (DoF) coupled resonating sensor. Developed models represents findings in open/closed loop implementation. A work on the most fundamental and crucial aspects such as sensitivity, resolution and noise floor of coupled resonators is reported.

Contents

List of Figures

List of Tables

Nomenclature

F	electrostatic forcing term
F_{noise_rms}	Noise forcing term (rms)
$F_{noise\_density}$	spectral density of a noise forcing term
F_{noise_avg}	mean square amplitude
x_{ji}	displacement amplitude of j^{th} resonator at i^{th} mode of frequency response
X_{ji}	noise displacement amplitude of j^{th} resonator at i^{th} mode of frequency response
X_{ji_avg}	mean square noise displacement amplitude of j^{th} resonator at i^{th} mode of frequency response
X_{ji_rms}	rms noise displacement amplitude of j^{th} resonator at i^{th} mode of frequency response
$imot_{ji}$	motional current amplitude of j^{th} resonator at i^{th} mode of frequency response
$imotX_{ji}$	fluctuation (due to noise) in the motional current amplitude of j^{th} resonator at i^{th} mode of frequency response
$\dot{x}$	velocity
M_{eff}	effective mass
K_{eff}	effective spring constant
c	damping coefficient
Δk	stiffness perturbation
δ_k	stiffness perturbation (normalized)
K_c	effective coupling spring constant
κ	coupling factor
d	capacitive gap
V	applied voltage
R_x	motional resistance
η	electromechnical transduction factor
ω_i	angular mode frequencies
Q	quality factor

df	bandwidth

Chapter 1

1 Introduction

In today's world, Microelectromechanical Systems (MEMS) based sensors have simplified our daily lives. There are quite a few MEMS based sensors in the smartphones, and many of them in every new car. In addition, there are many in drones, fitness modules, and automobiles. MEMS sensors are the building blocks of the connected world providing everyday objects with sensory awareness and connecting them with the internet [2].

MEMS are miniaturized mechanical features (springs, deformable membranes, vibrating structures, etc.) integrated with the electronic components. They are embedded into a single chip to sense, and report on the physical properties of their immediate or local environment. They are also used to perform some kind of controlled physical interaction or actuation. Some examples of MEMS-enabled functionality in everyday life are airbag arrangement in automobiles, motion and orientation detection in smartphones, blood pressure measurement, and the list goes on.

The physical transduction mechanisms underlying MEMS based devices can be capacitive, piezoelectric, piezoresistive, electromagnetic, optical etc. The most commonly used and successful types are based on electrostatic actuation and capacitive sensing; the reasons are the ease with which they can be batch fabricated using planer silicon fabrication technology (bulk and surface micromachining being the most common examples), low power consumption, good stability over temperature, etc.[3,4]

MEMS based solutions offer several advantages such as 1) monolithic integration of MEMS devices with electronics simplifies design cycles and speeds up time-to-market; 2) lower product cost for a given functionality; 3) MEMS based product reliability is considered to be good in rugged, real-world applications such as military, automotive and medical fields.

1.1 Motivation of research

Amongst variety of MEMS devices and/or sensors, MEMS resonators are also of key interest in the research and industrial community, particularly their placement as a sensing element in the simple or even a complex integrated system. MEMS resonators are micro-machined mechanical structures that vibrate at their natural resonant frequency when excited by an external force. This excitation force may arise from variety of sources such as electrostatic, piezoelectric, optical, mechanical vibration, or magnetic transduction. A single resonating structure can have several different mode shapes or resonant frequencies. Resonators generally employ flex (bending) mode or bulk acoustic (extension) mode of vibration for their operation. The frequency of the resonators is determined by both material properties and geometry of the resonators. A clamped-clamped beam, being a simple structure features a small mass and high stiffness, thus extending the frequency of operation. Silicon, which the structure is usually made of offers a high quality factor thus making these devices useful circuit elements in frequency reference applications [5]. Examples are the MEMS based oscillators in which resonators are inserted as a high-Q frequency reference tank, to determine the frequency and the stability of the oscillator, and an electronic circuit is interfaced to it to sustain the oscillation.

1.1.1 Principle of electromechanical transduction in micromachined resonators

In a typical microresonator application, the device/structure is forced into vibrations by converting an input electrical signal into a force and applying it to the device. Vibrations of the structure are then picked up and converted back to the electrical domain through various transduction techniques (for example: capacitive transduction). We may use the analogy between electrical and mechanical resonators to build an equivalent electrical circuit for a micromachined resonator. To represent a mechanical device with electrical elements, proper mapping of mechanical to electrical quantities can be done. A common set of mapping rules is provided in Table 1.1.

Table 1.1 Analogy between mechnical and electrical domains [6].

Mechanical domain	**Electrical domain**
Force, F	Voltage, V
Velocity, $\dot{x}$	Current, I
Displacement, x	Charge, q
Spring $1/k$	Capacitance, C
Mass, M	Inductance, L
Damping, ξ	Resistance, R

A resonant device can be modelled as a series Resistance-Inductance-Capacity (RLC) circuit. The transductions from the electrical to mechanical domain and vice versa can be modelled with transformers with proper winding ratios or controlled voltage or current sources. Other elements, especially parasitic and feedthrough capacitors may also be added to the equivalent circuit so that the model provides results similar to experimental measurements. Figure 1.1 illustrates an equivalent electrical model for a resonator with electrostatic input and output ports. The transformer at the input port converts an input voltage to a force, F_{in} and applies it to the mechanical system represented by the series RLC circuit. At the output, another transformer converts velocities of the mechanical structure back to an electrical current. In the model, η_{in} and η_{out} represent electromechanical coupling coefficients.

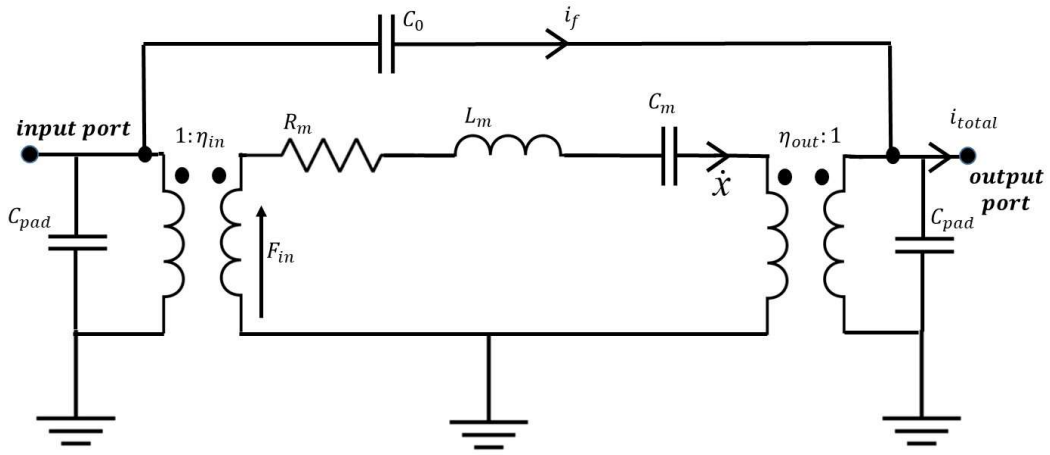

Figure 1.1 Electrical equivalent model for a MEMS resonator

Typical values of parasitic elements include as follows: C_{pad} is the shunt capacitor usually about 1 *pF* to 2 *pF*. C_0 is the nominal capacitor. A resonator model values are expressed as follows [7,8]: A nominal capacitor, C_0 is given as $C_o = \frac{\varepsilon A}{d}$. Other equivalent parameter values can be expressed as $L_m = \frac{m_{eff}}{\eta^2}, C_m = \frac{\eta^2}{k_{eff}}$ $R_m = \frac{\sqrt{KM}}{Q\eta^2} = \frac{\omega m_{eff}}{Q\eta^2}$ and $\eta = \frac{dc}{dx}V_{dc}; \frac{dc}{dx} = \frac{\varepsilon A}{d^2}$. L_m , C_m, R_m and η are equivalent inductance, capacitance, motional resistance and electromechanical coupling factor respectively. V_{dc} is the DC voltage used to polarize a micro capacitor. From the equivalent circuit, a series resonant frequency is given as $f_s = \frac{1}{2\pi\sqrt{L_m C_m}}$. A quality factor is expressed as $Q = \frac{\omega L_m}{R_m} = \frac{1}{\omega C_m R_m}$ and $\omega = 2\pi f$ is the angular frequency. The net admittance [9] between the input and the output port is given by

$$
\begin{aligned}
Y &= \frac{I}{v_{ac}} = \frac{i_f}{v_{ac}} + \frac{i_m}{v_{ac}} \\
&= j\omega C_o + \frac{j\omega C_m}{\left[1 - \left(\frac{\omega}{\omega_0}\right)^2\right] + \left[\frac{\left(\frac{j\omega}{\omega_0}\right)}{Q}\right]}
\end{aligned}
\tag{1.1}
$$

where, ω_0 is the resonant frequency of a resonator, Q is the quality factor and $j\omega C_0$ is the admittance of a capacitive parasitic. A denominator of the above equation determines the frequency response of a system.

1.1.2 Resonator in sensing applications

Resonant sensing is a promising method of detecting small linear parametric variations in the structural properties of micromechanical sensors. Typical examples of resonant sensing include strain sensing [10], angular motion detection [11], pressure sensing [12] and mass detection [13], etc. A key attribute of these entire sensors is that the output signal is the variation in the resonant frequency of a vibrating structure that is subjected to small perturbations in the structural parameters i.e. stiffness or mass. Additional features of this method of detection is simple mechanical design, quasi-digital nature of the signal (thus using simple frequency measurement system such as frequency counter), ultra-high resolution (up to 10^{-18} grams scale) [14], etc.. There are however also a drawback associated with resonant sensor employing only one resonator; sensors of these types are prone to environmental shifts such as pressure and/or temperature. Furthermore, these type of sensors, when used as a mass sensor are able to detect only one type of material at a time. Not to mention, long-term frequency stability [15] is also a limiting factor.

Since last decade, however, in the MEMS community, there has been a paradigm shift in the research referring to MEMS resonating sensors being developed for variety of sensing applications. Specifically, a widespread interest has aroused using *1-d* chain of a coupled

resonating proof masses, more familiarly refereed as multi degree-of-freedom (m-DoF) or ***weakly coupled resonator sensors*** [16,17]. These sensors attribute an ultra-high sensitivity [17,18] manifested via a novel transduction principle, i.e. sensing magnitude of vibrational energy exchange between the moving proof masses subject to a small disruption introduced into the system which alters either an effective mass, Δm or an effective mechanical stiffness, Δk of one of the proof mass element in a chain. In the following section, we explain a principle of transduction of coupled resonator sensor.

1.1.3 A new transduction principle: paradigm shift in resonant sensing applications

Due to the characteristic as mentioned above, ultimately, m-DoF coupled resonators have emerged as a new and promising sensing standard, which is attempting to revolutionize the sensing world. A sensor prototype as proposed in this thesis operates on the principle of mode-localization, a novel transduction paradigm in resonant sensing applications. As depicted by Figure 1.2 (a), it consists of two identical resonators coupled through a spring (either mechanical or electrostatic). Even a small disorder in the structural properties (stiffness or mass) of one of the coupled resonators inhibits the propagation of vibrations within the system leading to the confinement of vibration energy to small geometric regions. The extent of this vibration energy confinement depends not only on the magnitude of the periodicity breaking irregularity, but also on the strength of internal coupling between the resonators, resulting in large variations in the vibrational amplitudes (mode shape). Therefore, in contrast to the resonant sensors using only one resonators, this new class of sensor offers ultra high parametric sensitivity (up to three to four orders high in magnitude).

Other acknowledged characteristics of weakly-coupled resonating devices are linearity (attributed to high sensitivity [19], invulnerability against responding to ambient pressure and or temperature (i.e. common-mode rejection), [20]. These characteristics make these devices efficacious and hence being pursued over conventional method based on sensing the frequency variation of a single resonating device. In this context, **one of the primary motivation of this thesis is to investigate the most fundamental and central performance parameters of coupled resonators such as sensitivity, resolution, noise, etc as depicted in** Figure 1.2 (b**).**

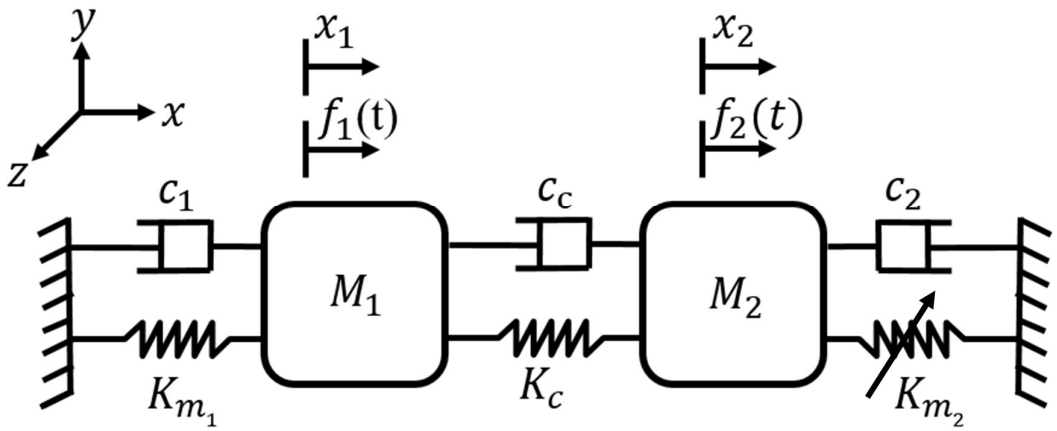

(a)

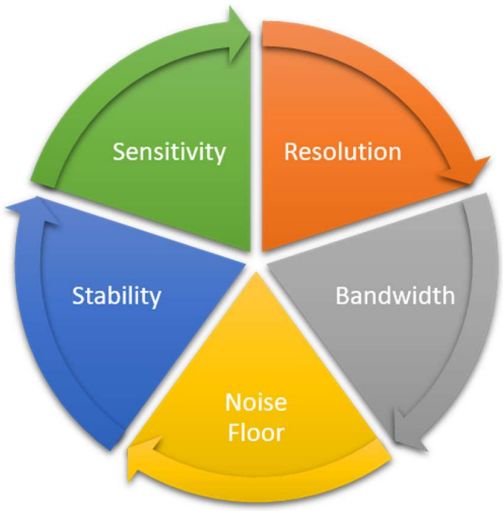

(b)

Figure 1.2 (a) A schematic representation of two identical mass-spring-damper system coupled by spring to illustrate transduction principle, (b) graphic showing key performance parameters pertaining to new class of resonant sensor based on mode-localization.

1.1.4 Potential applications for mode-localized sensors

Figure 1.3 shows a graphic to indicate potential sensing applications that can be developed with coupled resonators utilizing the concept of mode-localization. These applications are discussed as follows: (refer also Figure 1.2 (a))

A displacement sensor – During fabrication, a suspended proof mass can be realized and be placed adjacent to one of the resonator separated by a coupling gap. Transduction takes place when any displacement of this suspended proof mass modulates the coupling gap between proof mass and its adjacent resonator, thus altering the stiffness of that resonator causing system imbalance. [21].

A charge sensor (electrometer) - A separate input port can be used to apply different DC voltages to one of the resonator (across an electrostatic capacitive gap) implying the change in charge (δ_q) at this input port. This exerts an electrostatic force to the resonator thus altering the stiffness of the resonator causing system imbalance [22].

A force sensor- An electrostatic tensile force to one of the resonator can be applied, hence modulating the stiffness of that resonator. This electrostatic force can be generated by creating the voltage difference between the resonators and its neighbouring electrode separated by a coupling gap [23].

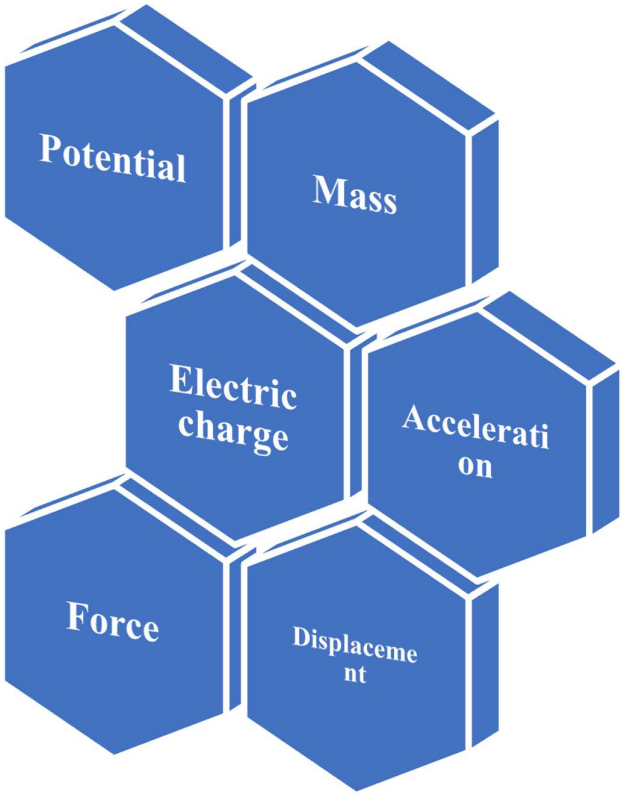

Figure 1.3 A graphic showing potential sensing applications that can be developed using coupled resonators.

An acceleration sensor- Given the same architecture of coupled resonators as in Figure 1.2 (a), when acceleration acts on the proof mass/es, single/differential electrostatic stiffness perturbation/s will be applied to the weakly coupled resonators, leading to mode localization, and thus, mode shape changes. Therefore, acceleration can be sensed by measuring the change in amplitude (or amplitude ratio) based readout as mentioned in section 1.1.3 above [24].

A mass sensor- A multi-DoF structure can be utilized to detect a change in the amplitude ratio output metric as a function of mass change (due to addition of mass [16] or removal of mass [25]) in a chain of 1-dimensional coupled resonating sensor architecture. Coupled resonators in mass sensing applications offer advantage of single measurement/device for multiple analytes.

Other applications may also be listed such as-electric field [26], tilt [27–29], etc. It is to be noted that all of these applications, excluding coupled resonators as a mass sensor, essentially implies the effective stiffness change of one or both (via differential perturbation) resonator/s. Therefore, all these sensors falls under the category of 'coupled resonators for stiffness change applications'.

1.1.5 Fabrication using the state-of-the-art laser micromachining

Electrostatic actuation and capacitive sensing are widely used principles in the micro-electro-mechanical system (MEMS) field. A variety of devices including gyroscopes, accelerometers, and resonators based on the principle of electrostatic actuation and capacitive sensing have been developed using existing silicon wafer lithography based processes [3,4]. One of the essential features of these devices is the requirement of forming micro-size gaps/trenches through the active device layer, thus forming parallel-plate capacitors.

Conventional MEMS fabrication processes, such as surface and bulk micromachining, offer the advantage of large area patterning to create batch-processed miniaturized devices with sub-micron level resolution [30,31]. These processes, however, require expensive clean-room facilities. A relatively high number of fabrication steps are involved starting with photo-mask preparation, followed by several cycles of lithography, deposition, selective etching and finally wafer dicing [32,33].

For the first time, we show that a laser micro-milling technique can be utilized to machine micro-size kerf-widths, (referred as a capacitive gap in MEMS) to perform electrostatic actuation and capacitive sensing. We demonstrate that laser micro machining could be used as a pathway towards developing a diverse range of structures and devices. Moreover, it is suggested as a hypothesis that, some other micro-milling techniques [34,35] , if capable to form a micro-size cuts through a device thickness (thus providing a reasonable aspect ratio) could also be used. The benefit of using laser micromachining is the possibility to utilize new materials to enhance device performance [36]. At present, most of the laser-assisted work was used for making micro-cuts, drilling holes, engraving or forming embroidery onto a piece of a material [36–39], creating channels for microfluidic applications [40–42], and realizing micro-optical devices using photoresist [43]. A laser machining was used to develop an *electro-mechanical based transducer* and it experimentally demonstrated the possibility to use direct laser writing (DLW) to fabricate electro-mechanical based actuators and sensors with high precision and resolution. This fabrication method as proposed here can be particularly useful when there is no cleanroom access and there is a requirement for quick prototyping with materials other than silicon. This can potentially also be extended for small or medium-scale series production.

Given the novel fabrication platform (laser micromachining) as proposed in this thesis, it is worth investigating the performance parameters pertaining to the coupled resonator sensors. These performance parameters are sensitivity (in both open and closed loop), resolution (lowest possible detection limit), effective noise floor, etc.

By doing so, objective is to explore whether and how our proposed design offers any performance benefit over the coupled resonator sensors realized using MEMS technology. **In this thesis, the possibility to fabricate such devices using state-of-the-art laser micro-machining/milling is also explored. Particularly, a goal is to fabricate a coupled resonator architecture and (as mentioned in the previous section above) evaluate its performance for stiffness sensing applications.**

1.2 Thesis organization

This thesis is organized as follows:

Chapter 2 provides a first principle of MEMS resonator. An in-depth, including most recent literature coverage relevant to ultra-sensitive coupled resonators in sensing application is provided.

Chapter 3 provides a theory of operation of mode-localized weakly coupled resonators. This background was used to design and fabricate (using laser micromachining) our macro-scale two degree-of-freedom (DoF) coupled resonators for stiffness sensing applications. We develop a theory model to estimate a device sensitivity. We also analyse performance of our design for various operating conditions. A model developed using COMSOL Multiphysics software is also given in this chapter.

Chapter 4 presents system level models for coupled resonators built using a SIMULINK. A simulation results for variety of operating conditions are provided. We derive and compare the theoretical and simulated results of device sensitivity. We estimate the theoretical noise floor of our design and, subsequently determine the minimum resolvable shifts in to the output. We therefore determine a resolution for our macro-scale two DoF coupled system. We compare results of our theoretical model and system-level simulation and report a good agreement between them.

Chapter 5 begins with overview of various potential micromachining high-tech methods. It presents a laser micromachining fabrication and assembly processes. Fabrication outcome at the University of Liege and with the outside manufacturing service is compared and discussed in detail. We demonstrate a micro-size capacitive gap fabrication into metal parts of up to 2 mm thickness, thus resulting a high aspect ratio structure. This is useful in terms of MEMS transduction in capacitive devices and fabricating such deep trenches using laser micromachining to develop a transducer and/or sensor is unprecedented.

Chapter 6 presents initial experiments and measurement results for the developed prototype.

Chapter 7 offers a platform for discussion and conclusion and future direction.

Appendix for the MATLAB script, circuit schematic, vacuum chamber used, etc. is presented at the end of this thesis.

Chapter 2

2 Literature Review

This chapter starts by reviewing the fundamentals of electromechanical transduction. A model for electrostatic actuation and capacitive sensing is given. Next, a theory for a resonator is formulated using a one degree of freedom mass-spring-damper model, transfer function analysis and electrical equivalent circuit model. Following this, an in-depth overview for ultra-precise weakly coupled resonators as sensors is presented.

2.1 Electrostatic actuation and capacitive sensing

Electrostatic actuation and capacitive sensing are widely used principles in the micro-electro-mechanical system (MEMS) field. A variety of devices including gyroscopes, accelerometers, and resonators based on the principle of electrostatic actuation and capacitive sensing have been developed using existing silicon wafer lithography based processes [3,4]. One of the essential features of these devices is the requirement of forming micro-size gaps/trenches through the active device layer, thus forming parallel-plate capacitors.

Figure 2.1 shows a schematic representation of an electrostatic actuation and capacitive sensing principle. It is one of the widely used principle amongst the devices for their operation. In resonator featuring electrostatic actuation and capacitive sensing, the electrical load and the mechanical restoring force govern the behaviour of a mechanical vibrating structure. The electrical load is composed of a DC polarization voltage, V_{dc} and an AC voltage v_{ac}. The DC component exerts an electrostatic force on the mechanical structure, thereby deflecting it to a new equilibrium position, while the AC component vibrates the structure around this equilibrium position.

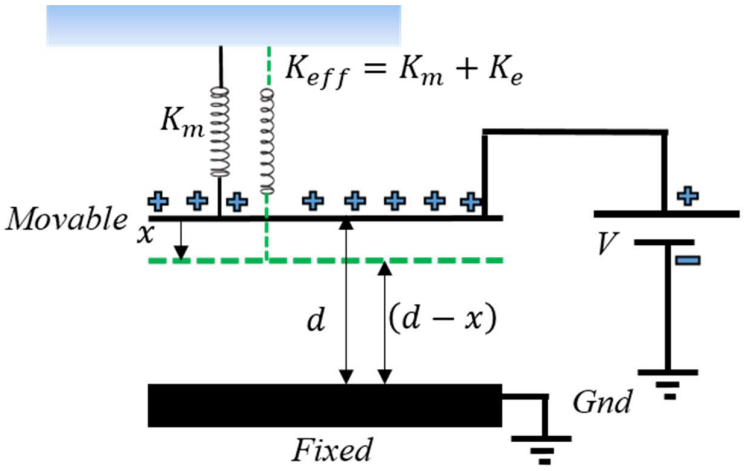

Figure 2.1 Electrostatic actuation and capacitive sensing in parallel plate actuator

The combined electrical load has an upper limit beyond which the mechanical restoring force can no longer resist its opposing force, thereby leading to the structural instability called as 'pull-in', and the hazardous voltage associated with it is called 'pull-in voltage'.

In a parallel plate actuator, a nominal capacitance is given as $C_0 = \frac{\varepsilon A}{d}$ where ε, A, and d are permittivity, nominal electrode area and nominal capacitive air gap used for electromechanical transduction. As shown in Figure 2.1, when the top movable plate moves by a distance x, a net capacitance is given by $C = \frac{\varepsilon A}{d-x}$. A total energy stored in the parallel-plate capacitor is given by $E = \frac{1}{2}CV^2$, where V is the potential applied across the capacitor plates. In case of a resonator, $V = V_{dc} + v_{ac}$. Therefore,

$$\begin{aligned} E &= \frac{1}{2}C\left(v_{ac} + V_{dc}\right)^2 \\ &= \frac{1}{2}C\left(v_{ac}^2 + V_{dc}^2 + 2v_{ac}V_{dc}\right) \end{aligned} \tag{2.1}$$

An associated net electrostatic force is therefore calculated as

$$\begin{aligned} F &= -\frac{\partial E}{\partial x} = -\frac{\partial}{\partial x}\left(\frac{1}{2}CV^2\right) \\ &= -\frac{1}{2}V^2\frac{\partial}{\partial x}\left(\frac{\varepsilon A}{d-x}\right) \\ &= \frac{1}{2}\frac{\varepsilon A}{\left(d-x\right)^2}V^2 \\ &= \frac{1}{2}\frac{\varepsilon A}{\left(d-x\right)^2}\left(v_{ac} + V_{dc}\right)^2 \\ &= \frac{1}{2}\frac{\varepsilon A}{\left(d-x\right)^2}\left(v_{ac}^2 + V_{dc}^2 + 2v_{ac}V_{dc}\right) \end{aligned} \tag{2.2}$$

Thus, we have components of this force at three frequencies: a force at DC, force at the excitation frequency f due to the term $2v_{ac}V_{dc}$ and force at twice the excitation frequency due to square term v_{ac}^2. A force F at the excitation frequency is given by

$$\begin{aligned} F &= \frac{1}{2}\frac{\varepsilon A}{\left(d-x\right)^2}\left(2v_{ac}V_{dc}\right) \\ &= \frac{\varepsilon A}{\left(d-x\right)^2}\left(v_{ac}V_{dc}\right) \end{aligned} \tag{2.3}$$

Assuming displacement of a proof mass , x is relatively very small in comparison to nominal air gap, d i.e., $x \ll d$, equation (2.3) takes the form as

$$\begin{aligned} F &= \frac{\varepsilon A}{d^2}\left(v_{ac}V_{dc}\right) \\ &= \eta V_{ac} \end{aligned} \tag{2.4}$$

A parameter, η is defined as the electrostatic transduction factor given by $\eta = \frac{\varepsilon A}{d^2}V_{dc} = \frac{\partial C}{\partial x}V_{dc} = \frac{C_0}{d}V_{dc}$. A term $\frac{\partial C}{\partial x}$ is called as a capacitive gradient. It is seen from above derivation that designing a large value of a nominal capacitance should benefit in enhancing a transduction factor, η.

2.2 Motional current

A charge voltage relationship in a capacitor is given by $Q=CV$. A current through the capacitor is given as

$$\begin{aligned} i &= \frac{\partial Q}{\partial t} = \frac{\partial CV}{\partial t} = C\frac{\partial V}{\partial t} + V\frac{\partial C}{\partial t} \\ &\approx C_0\frac{\partial V_{ac}}{\partial t} + V_{dc}\frac{\partial C}{\partial t} \end{aligned} \tag{2.5}$$

The second term in equation (2.5) is given as $V_{dc}\frac{\partial C}{\partial t} = V_{dc}\frac{\partial C}{\partial x}\frac{\partial x}{\partial t} \approx \eta\frac{\partial x}{\partial t}$. Equation (2.5) can therefore be written as

$$\begin{aligned} i &\approx C_0\frac{\partial V_{ac}}{\partial t} + \eta\frac{\partial x}{\partial t} \\ &= j\omega C_0 V_{ac} + \eta\frac{\partial x}{\partial t} \end{aligned} \tag{2.6}$$

The first term in the above equation is the ac or more commonly called feedthrough current and second term is called the motional current.

2.3 A mass-spring-damper system

Figure 2.2 shows a model for a typical one degree of freedom (DoF) mass-spring-damper system. An expression of a force can be written as $F_e = Ma = M\frac{\partial^2 x}{\partial t^2}$, where $a = \ddot{x} = \frac{\partial^2 x}{\partial t^2}$ is an acceleration, $v = \dot{x} = \frac{\partial x}{\partial t}$ is the velocity and x is the displacement from its equilibrium position. Summing the forces, one can write

$$\begin{aligned} \sum F &= F_e - F_C - F_S \\ &= M\frac{\partial^2 x}{\partial t^2} + C\frac{\partial x}{\partial t} + Kx \end{aligned} \tag{2.7}$$

Here, F_e is externally applied net electrostatic force, F_S is the restoring force of the spring, which often tries to balance a net externally applied force, and F_C is the force by the damper. For an undamped system, F_C=0.

For a static case (*i.e.,* x is *independent of time*), $F_S = Kx$. For a parallel-plate capacitive actuation, $F_{S_{eff}} = K_{eff}x$ where, $K_{eff} = K_m + K_e$ is effective spring constant, K_m is mechanical

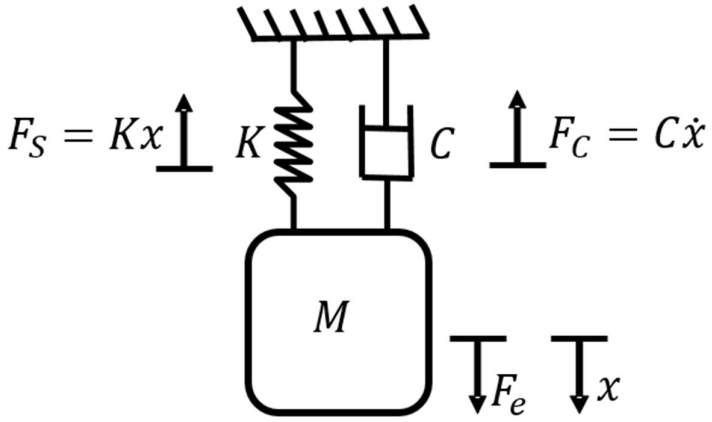

Figure 2.2 A mass-spring-damper system.

spring constant and K_e is electrical spring constant derived as (referring to equation (2.2))

$$\begin{aligned} K_e &= \frac{\partial F_e}{\partial x} = \frac{\varepsilon A}{(d-x)^2} V^2 \\ &= \varepsilon A V^2 \frac{\partial}{\partial x}\left(\frac{1}{(d-x)^2}\right) \\ &= -\frac{\varepsilon A}{(d-x)^3} V^2 \end{aligned} \tag{2.8}$$

Note that K_e has a negative effective value and therefore it causes a spring softening (decreasing the effective value) as illustrated in Figure 2.1. Assuming that displacement x of a proof mass M is relatively very small than that of original capacitive gap, d (i.e. $x << d$), K_e can be approximated as $K_e = -\frac{\varepsilon A}{d^3} V^2$ and ($V = v_{ac} + V_{dc}$) for resonator.

For a linear, dynamic case where x is a *time dependent*, an expression for an effective restoring force can be written as $F_{S_{eff}}(t) = K_{eff}x(t)$. An expression for K_{eff} can be derived as $K_{eff} = \frac{\partial F_{S_{eff}}}{\partial t} = \frac{\partial F_{S_{eff}}}{\partial x}\frac{\partial x}{\partial t}$.

2.4 Transfer function for one DoF system

From Figure 2.2, a governing equation of motion for a single Degree of Freedom (DoF) mass-spring-damper system can be given as [44]

$$M\ddot{x} + C\dot{x} + Kx = F \tag{2.9}$$

A transfer function can be derived as

$$\frac{X(s)}{F(\mathrm{s})} = \frac{1}{Ms^2 + Cs + K} = \frac{\frac{1}{M}}{s^2 + \frac{C}{M}s + \frac{K}{M}} \tag{2.10}$$

where, $\omega_n^2 = \frac{K}{M}$ is the undamped natural frequency, and,

$$\frac{C}{M} = 2\xi\omega_n = 2\xi\sqrt{\frac{K}{M}} \tag{2.11}$$

where, ξ is the amount of proportional damping, typically stated as percentage of critical damping, C_{cr} ($C_{cr} = 2\sqrt{KM}$ is the critical damping value). Equation (2.11) can also be written as $\frac{C}{M} = 2\frac{C}{C_{cr}}\sqrt{\frac{K}{M}} = \frac{2C}{2\sqrt{KM}}\sqrt{\frac{K}{M}}$. With this, equation (2.10) can further be written as:

$$\frac{X(s)}{F(\mathrm{s})} = \frac{\frac{1}{M}}{s^2 + 2\xi\omega_n s + \omega_n^2} \tag{2.12}$$

By using $s = j\omega$, we get,

$$\frac{X(j\omega)}{F(j\omega)} = \frac{\frac{1}{M}}{-\omega^2 + 2\xi\omega_n(j\omega) + \omega_n^2} = \frac{\left(\frac{1}{M\omega^2}\right)}{-1 + \frac{2\xi\omega_n(j\omega)}{\omega^2} + \frac{\omega_n^2}{\omega^2}} = \frac{\left(\frac{1}{M\omega^2}\right)}{\left[\left(\frac{\omega_n}{\omega}\right)^2 - 1\right] + j2\xi\left(\frac{\omega_n}{\omega}\right)} \tag{2.13}$$

Equation (2.13) shows how ratio $\frac{X(j\omega)}{F(j\omega)}$ varies as a function of frequency ω. This ratio being a complex number has properties at different values of the ratio $\left(\frac{\omega_n}{\omega}\right)$.

Case 1) at low frequencies, $\omega_n^2 >> \omega\omega_n >> \omega^2$

$$\frac{X(j\omega)}{F(j\omega)} = \frac{\frac{1}{M}}{\omega_n^2} = \frac{1}{K} \tag{2.14}$$

Magnitude and phase are expressed as $\left|\frac{X(j\omega)}{F(j\omega)}\right| = \frac{1}{K}; \angle\frac{X(j\omega)}{F(j\omega)} = 0$ (Phase is zero as the sign is positive)

Case 2) at high frequencies, $\omega^2 >> \omega\omega_n >> \omega_n^2$

$$\frac{X(j\omega)}{F(j\omega)} = \frac{-1}{M\omega^2} \tag{2.15}$$

Magnitude and phase are expressed as $\left|\frac{X(j\omega)}{F(j\omega)}\right| = \frac{1}{M\omega^2}$ and $\angle\frac{X(j\omega)}{F(j\omega)} = -180^0$ respectively. (Phase is -180^0 as the sign is negative)

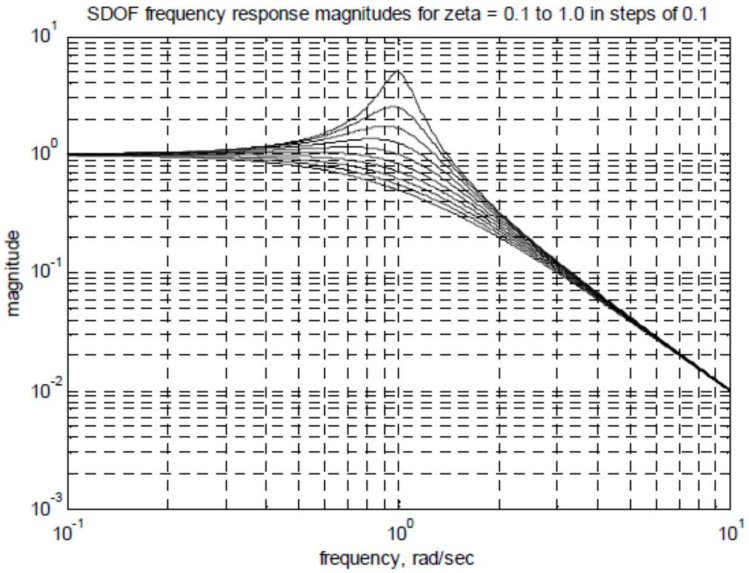

Figure 2.3 Magnitude-frequency response of a single DoF mass spring damper system [44]

Case 3) at Resonance, $\omega = \omega_n$

$$\frac{X(j\omega)}{F(j\omega)} = \frac{\frac{1}{M}}{2\xi j\omega_n^2} = \frac{-\frac{j}{K}}{2\xi} \tag{2.16}$$

Magnitude and phase are expressed as $\left|\frac{X(j\omega)}{F(j\omega)}\right| = \frac{1}{2\xi K}$ and $\angle\frac{X(j\omega)}{F(j\omega)} = -90^0$ respectively. At resonance phase angle is -90^0.

For $\xi < 1$, system is underdamped. This means energy dissipation is sufficiently small so that free-vibration response of the system is oscillatory. This is the case with most MEMS resonators. The free-vibration response of an underdamped one degree of freedom (DoF) system takes the form as

$$x(t) = e^{-\xi\omega_0 t}\left(A\cos\omega_d t + B\sin\omega_d t\right) \tag{2.17}$$

Where, A and B are constants that depend on the initial values of $x(0)$ and $\dot{x}(0)$ that set the system into free vibration and ω_d is the damped natural frequency given as $\omega_d = \omega_0\sqrt{1-\xi^2}$. For a damping ratio, $\xi < 0.2$ $\omega_d \approx \omega_0 = \sqrt{\frac{K}{M}}$ where ω_0 is the undamped natural frequency as stated earlier. Since $\xi = \frac{C}{2\sqrt{KM}}$, a quality factor for a resonator is given as $Q = \frac{1}{2\xi} = \frac{\sqrt{KM}}{C}$. Figure 2.3 shows a magnitude-frequency response of a system.

2.5 Coupled resonators

Using an array of resonators for frequency and timing application has been quite well known in the MEMS field. An array of mechanically coupled structures have been proposed for increasing the transmission gain of the signal [45], for oscillator application [7], etc.. In [46], two microscale clamped-clamped beams were mechanically coupled by a soft flexural-mode mechanical spring and demonstrated its usage for filtering application. A study [47] presents coupling techniques for implementation of high order narrow-bandwidth bandpass filters from micromechanical resonators using electrical coupling elements. Active and passive coupling elements were used in this work to implement high order resonant systems from individual MEMS resonators. The concept of passive coupling of resonators used capacitors as the coupling elements for filter synthesis. Active coupling of resonators used transistor-based amplifying circuits. In a more recent study [48], A CMOS-MEMS fabrication platform was used to implement a mechanically coupled array of free-free beams resonators and filter application was demonstrated [43].

2.6 Coupled resonators in sensing applications

Since last decade, in the MEMS community, there has been a paradigm shift in the research referring to MEMS resonating sensors being developed for variety of sensing applications. Specifically, a widespread interest has aroused using *1-d* chain of a coupled resonating proof masses, more familiarly refereed as ***weakly coupled resonator sensors*** [16,17]. These sensors attribute an ultra-high sensitivity [17,18] manifested via novel transduction principle, i.e. sensing magnitude of vibrational energy exchange between the moving proof masses subject to a small disruption introduced into the system which alters either an effective mass, Δm or an effective mechanical stiffness, Δk of one of the proof mass element in a chain. In coupled resonating sensor devices, a coupling between the proof masses is constituted either electrostatically or mechanically. Such sensors are also characterized by a veering point or loci which is described as a reference point from where eigenvalues and/or eigenvectors of this coupled system abruptly change and move away from each other (eigenvalues do not cross one another but eigenvectors do) subject to a small disorder injected into the system. This change

in eigenvalues and/or eigenvectors is larger and linear to some extent as the magnitude of an applied disorder is further increased. Veering point thus is also used to describe the amount of spacial energy re-distribution amongst the vibrating proof masses in a chain when there is a disorder present into the otherwise originally balanced system. If this reference veering point/loci is at the centre, it is regarded as an inherent symmetric system. Ideally, this condition should occur when Δk or Δm is zero, i.e. without the introduction of any disruption into the system. However, owing to the manufacturing tolerances, ideal symmetric system does not exist into the practice and individual devices coupled together as a whole system exhibit mismatch in the geometric features [49]. Unequal energy distribution is also a result of choice of driving scheme used for operation and it has recently been shown in [50] that in-phase mode, simultaneous driving of both the proof masses resulted in symmetric veering point for the eigenvalues of the system. However, the veering loci of eigenvectors was observed to be shifted away from the symmetry. In such situation, by introducing an external disruption into the system, equal energy distribution between vibrating

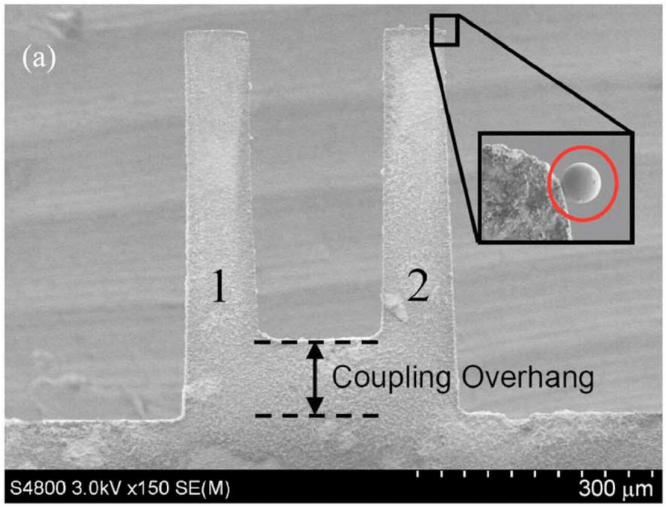

Figure 2.4 Ultrasensitive mass sensor using a mode localization in coupled microcantilevers [16]

proof masses was achieved and the point/loci at which this happened was refereed as revived veering point of the system. This act could be viewed similar to a calibration scheme for any sensor wherein a sensible measurement can be done and therefore accuracy in the measured physical quantity can be assured. Away form this veering point, magnitude of energy exchange between proof masses resonating in a particular mode was measured and thereby device sensitivity and linear measurement range could be determined. Potential applications of coupled resonator sensors are classified as mass detection and identification [51], force sensor, electrometer (electrical charge measurement), displacement sensor, and acceleration sensor, to name a few.

Spletzer et al., [16] proposed for the first time that a vibration mode localization can be used for sensing purpose. This is shown in Figure 2.4. Two mechanically coupled cantilevers were used that experimentally demonstrated about two orders of higher in magnitude relative changes into the eigenstates (5% to 7%) than relative changes in frequencies (0.01%).

Following this, a study in which an array of four microbeam sensors (cantilevers) were used for the detection and identification of multiple analytes [52]. It is shown in Figure 2.5 below. A single output signal was measured optically from the shuttle mass, using a laser vibrometer, to determine the resonance frequencies M_1–M_4, which correspond to the localized microbeam modes of the coupled system.

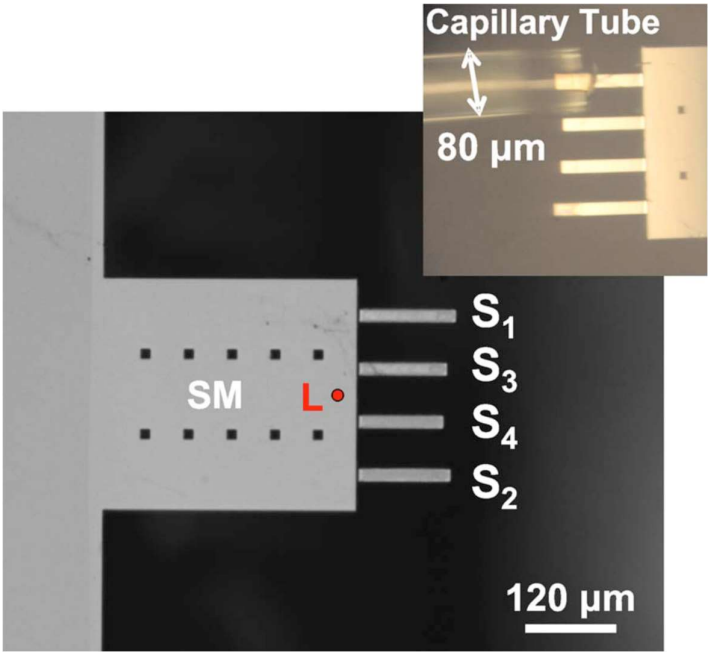

Figure 2.5 A microbeam sensors utilizing mode-localization to detect and identify the analyte [52]

In the work reported by Thiruvenkatanathan *et al*,[17], authors used two different types of MEMS structures namely free-free beam and double-ended tuning fork as shown in Figure 2.6. An electrical coupling as opposed to the mechanical coupling was used and about two orders of high sensitivity to eigenstate shifts was demonstrated. In the same study, an effect of initial mechanical asymmetry was also investigated. Amplitude change instead of a frequency change as a sensor output was proposed. A maximum percentage change in eigenstates and resonant frequency shift of about 8.9% and 0.019% respectively were reported. Same group also showed a mode-localized MEMS electrometer [22] with the double-ended tuning fork resonator topology and also a mode-localized displacement sensor [21]. Reported shifts in eigenstates

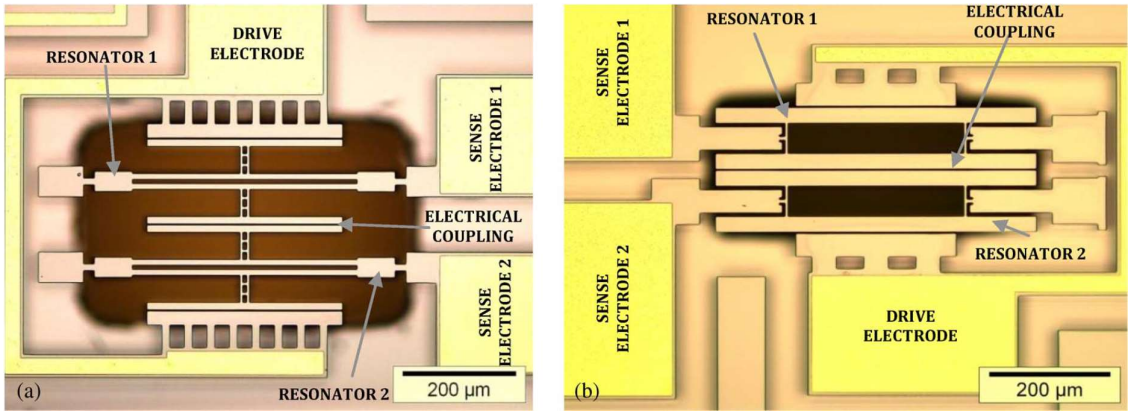

(a) (b)

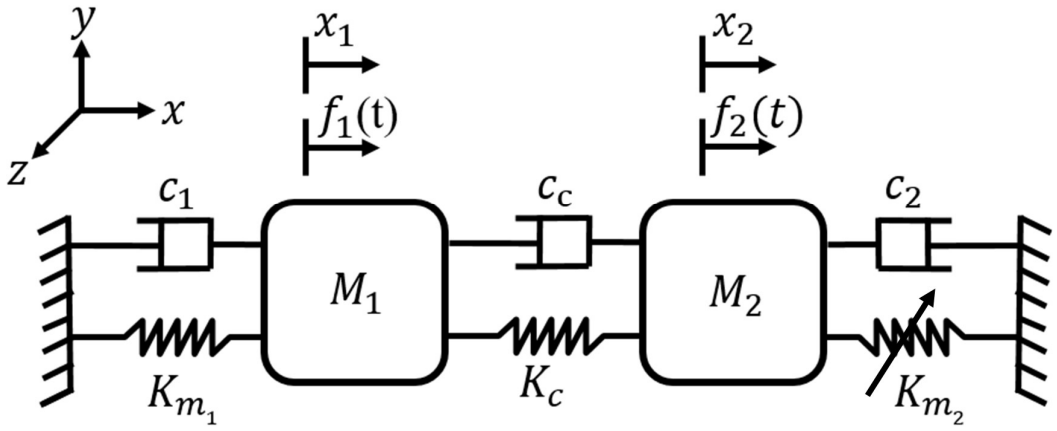

(c)

Figure 2.6 Electrically coupled weakly coupled resonators with enhanced sensitivity (a) A fabricated double-ended tuning fork and (b) two free-free beam resonators and (c) a representative two DoF coupled resonator model [17]

were about three orders of magnitude higher than resonant frequency variations. Equal but of opposite polarity DC voltage difference was applied on the two resonators, which are coupled by an electrostatic spring. Note that $K_{m1} = K_{m2} = K_m$, $k_{e1} = k_{e2} = k_e$, $k_{eff} = k_m - k_e$, this put the system under initial symmetry and at the same time established a coupling spring, K_c between the two resonators. Later, the DC voltage on one of the resonators was varied thereby altering the effective stiffness of that particular resonator (electrostatic spring-softening effect) to introduce a disorder, $\Delta k = k_{eff1} - k_{eff2}$. (In initially established symmetry of the system $k_{eff1} \approx k_{eff2}$, $\Delta k = 0$). The approximation sign denotes an initial asymmetry due to fabrication tolerances). By decreasing the DC voltage on one of the resonator also alters a coupling spring, K_c and it was called as a way to tune the mode shape sensitivity of the system under test.

This action as mentioned above also decreased the effective value of K_c, making it weaker. For $|\Delta k| \ll |K_c|$ sensitivity to mode shape changes, i.e. shifts in eigenstates were reliably measured. In short, with such biasing schemes as reported in this research, K_c is also changing (thus

parametric sensitivity) for a given stiffness imbalance between the resonators which, in real systems is undesirable as usually K_c has to be fixed to reliably measure the impact of Δk, as an external disturbances into the system.

It was proposed that mode shape sensitivity could be enhanced either by increasing the magnitude of externally added perturbation and/or by simply altering (decreasing) the coupling spring, K_c between the two resonators. It is also noteworthy that by decreasing K_c could increase the mode shape sensitivity of the system under investigation but it remains 'insensitive to the variations in the resonant signal frequency shifts. In other words, frequency sensitivity to the varying coupling strength is ideally zero.

Zhao *et al.*, [18,23,53] demonstrated a highest possible amplitude ratio based sensitivity of amplitude ratio to stiffness perturbation (about 13558) with the coupled resonators employing an array of three adjacent resonators. A prototype fabricated by this research group is shown in Figure 2.7. Same group also reported a force sensor [23] with a sensitivity of about 4.9×10^6/N. A concept of bias

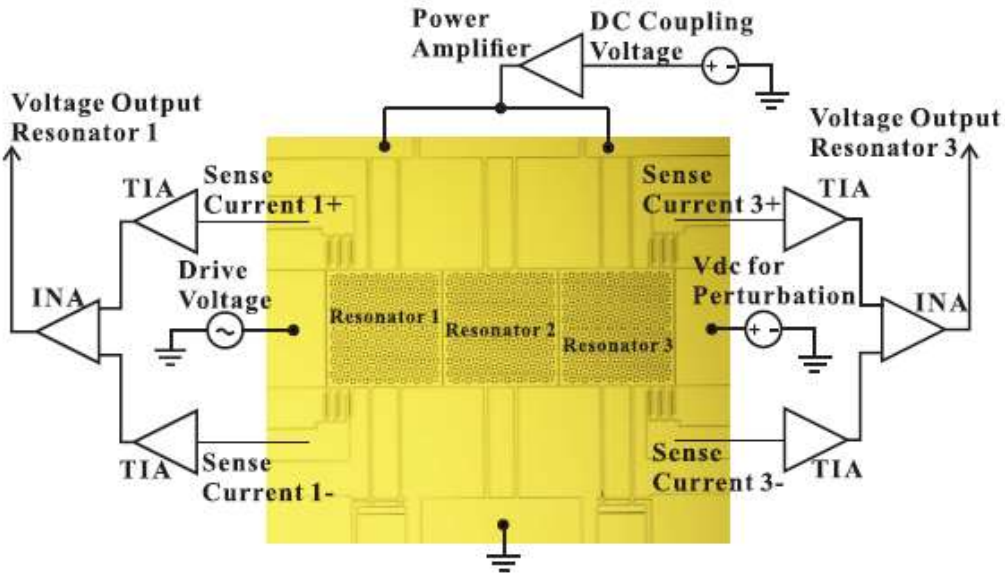

Figure 2.7 A coupled resonator sensor employing an array of three resonators [18]

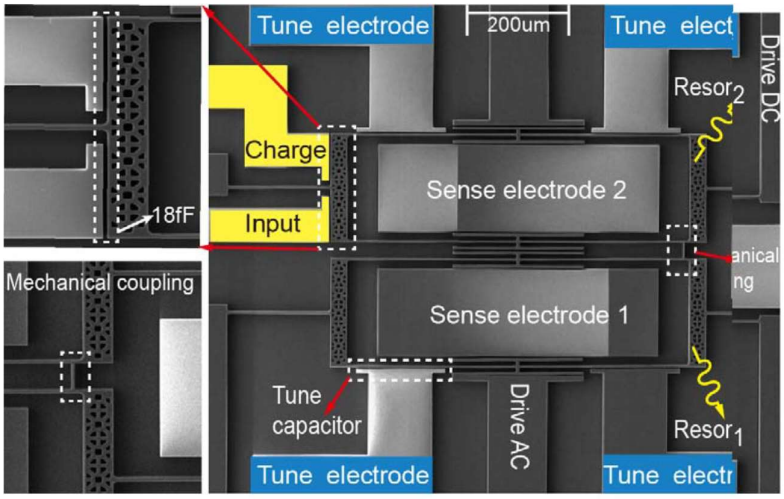

Figure 2.8 A mode-localized MEMS electrometer based on two mechanically coupled resonators [54]

stiffness perturbation was introduced in this work to avoid mode-overlap. A sensor was designed in a way that mechanical spring of the middle resonator was designed to be not equal to the mechanical spring of other two resonators. It was identified that the third resonator in the middle of a two identical resonators reduces the energy propagation due to its absorption of energy, thus increases the energy attenuation along the chain. Amplitude ratio based output was proposed for the first time highlighting the benefit of common mode rejection. In this work, two different approaches for detection were investigated, perturbing the stiffness in the form of either an axial electrostatic force or change in electrostatic spring. Using the same prototype an electric potential sensor was also reported in [26].

Reportedly, a high amplitude ratio based sensitivity to input charge (about 2151) MEMS based electrometer [54] as shown in Figure 2.8 was also demonstrated that used two mechanically coupled resonators to show a mode-localization effect. In this work, it was shown that when charges are applied to the external electrode, the stiffness of specific resonator is perturbed, owing to the mode-localization. A reported minimum charge that this electrometer could resolve was approximately 1.29 *fC* for amplitude ratio based output. An electrometer using a 3 DoF weakly coupled resonators as sensing element was proposed in [55]. In this work, an input charge causes stiffness perturbation to one resonator and leads to a drastic change of the mode shape owing to the mode localization phenomenon

A research on comparative study of different output metric has been given in [53]. In this study, different outputs have been compared based on sensitivity, nonlinearity, etc. for a sensor based on three weakly and electrically coupled resonators. Another study [56] showed that algebraic summation of eigenstates as a sensor output are effective to extend the linearity of a two weakly coupled resonators. There is a study [57] reporting on influence of the feedthrough capacitance on the performance of a weakly coupled resonators. It was shown that undesired signal output from the feedthrough, if not reduced, could have a negative effect on matching the resonant frequencies of a two resonators at the two vibration modes for a two-coupled resonator. This can lead to the measurement errors in the output metric.

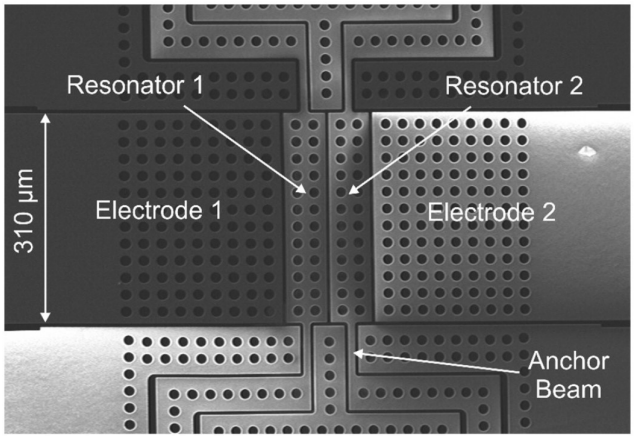

Figure 2.9 A mass sensor using two DoF coupled resonators [25]

A mode-localized mass sensor using two electrically coupled resonators has been demonstrated in [25]. A structure was fabricated using a silicon-on-insulator (SOI) process as shown in Figure 2.9. In this work , a mass has been removed as opposed to mass addition process shown in [16]. An amplitude ratio based sensitivity has been reported which is 5.4 times the sensitivity based on conventional resonant frequency shift output. A highest reported mass sensitivity is about 34,361 for an electrical coupling spring of -8.88 N/m. Same group also investigated the developed prototype performance for stiffness imbalance between two electrically coupled resonators [49]. A highest reported amplitude ratio sensitivity in this work was 3257 for a anchor beam length of 55 µm.

Few studies have characterized the sensor at atmospheric pressure. A sensor based on three electrically coupled resonators with sensitivity to stiffness change was reported with a quality factor, Q as low as 5 in [58]. With the same prototype, an amplitude ratio based mass sensitivity of 17.29 with a quality factor of about 8 was reported in [1,59].

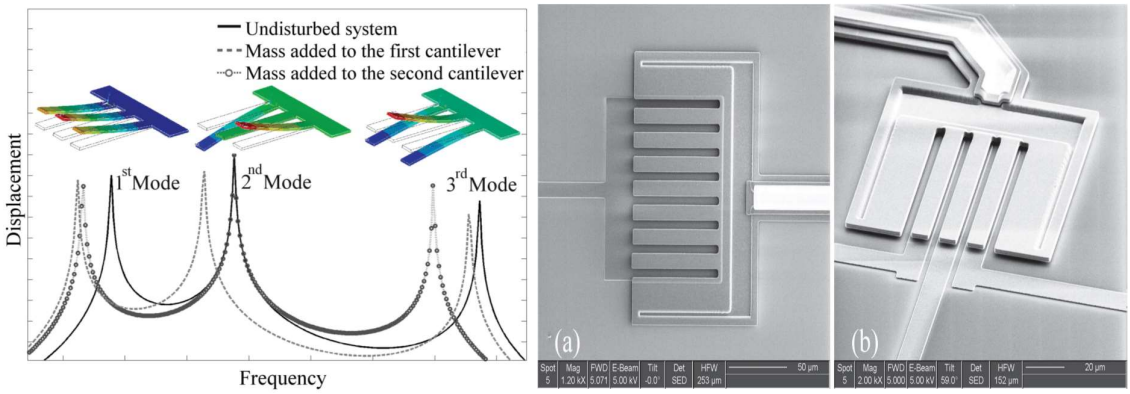

(a) (b)

Figure 2.10 A cantilever based mass sensor (a) simulated frequency response and (b) fabricated prototype [60]

A study [60] reported the characterization of disturbances in coupled micro-resonators, in which set of cantilevers were used to detect a mass change. A fabricated prototype and

simulated results are shown in Figure 2.10. From the frequency response, a relative change in eigenvalues (resonant frequencies) were recorded to identify which resonator was perturbed and by what amount. An advantage of this method was that an output signal from only any one of the resonator provides an information about parameters of the other resonators in a chain through a system matrix. A micro-size structure with a three cantilevers coupled mechanically were used in [61]. A mass perturbation approximately 10 *pg* was applied and changes into the output amplitudes were shown.

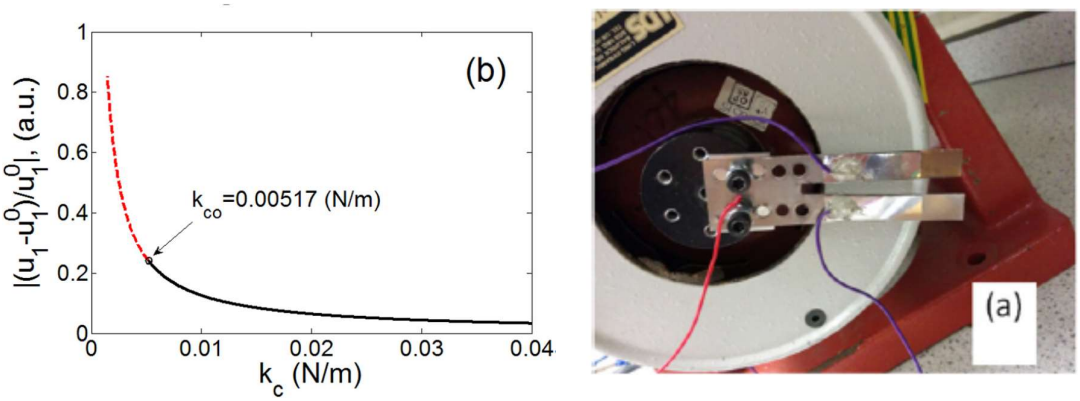

(a) (b)

Figure 2.11 In search of optimal mode localization in a mechanically coupled resonators (a) graph showing coupling spring optimization and (b) implemented prototype in a mechanical workshop [62]

For the resonators that are electrically coupled, it was suggested that a spring coupling the individual resonators should be designed as low as possible to enhance the parametric sensitivity. However, a study[62] proposed that there instead exists an optimal coupling for the coupled mechanical structures at which the mode-localization phenomenon reaches a maximum. Figure 2.11 shows calculated ratio of the change in the eigenvector to the coupling spring factor. A macro-scale two-cantilever structure fabricated in a mechanical workshop was mounted on an excitation equipment. An amplitude ratio output was extracted from the vibrational output signal. It is seen that maximum amplitude ratio is achieved for an optimized value of coupling factor between the two cantilevers (and not necessarily a lowest value of a coupling factor).

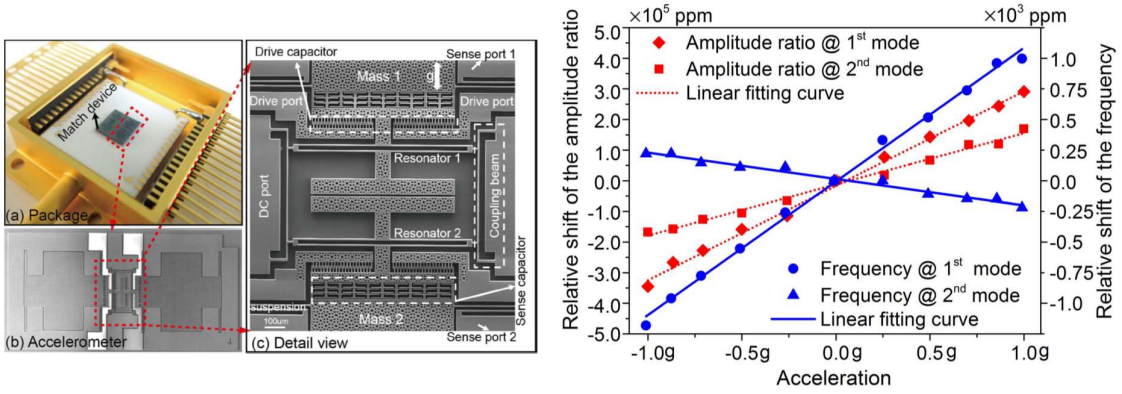

(a) (b)

Figure 2.12 An accelerometer based on mode-localization (a) a prototype image and (b) output of an sensor as a function of acceleration [24]

A research on weakly coupled resonators also has demonstrated an accelerometer that uses a mode-localization phenomenon [24]. An amplitude ratio shifts (about 300 times higher) than the frequency shifts are reported for a prototype fabricated as shown in Figure 2.12. A nonlinearity of about 3.5% and about 1.6 % was observed for an amplitude based and a frequency based output respectively. An accelerometer using 3 weakly coupled resonators was demonstrated in [63,64]. Following this, an accelerometer using 4 weakly coupled resonators was demonstrated in [65]. In [66], an accelerometer using 2 weakly coupled resonators was investigated. An amplitude ratio output was proposed for enhanced sensitivity and resolution.

A RLC circuit based approach was used in [67,68] to form two weakly coupled resonators and measure changes into the capacitance. This research was done in the context of capacitance sensors. A sensitivity of about 300 times higher was shown in capacitance measurement for coupled resonators as compared to the method based on frequency shift output in [68]. Figure 2.13 shows a circuit representation of two weakly coupled resonators and theory model results.

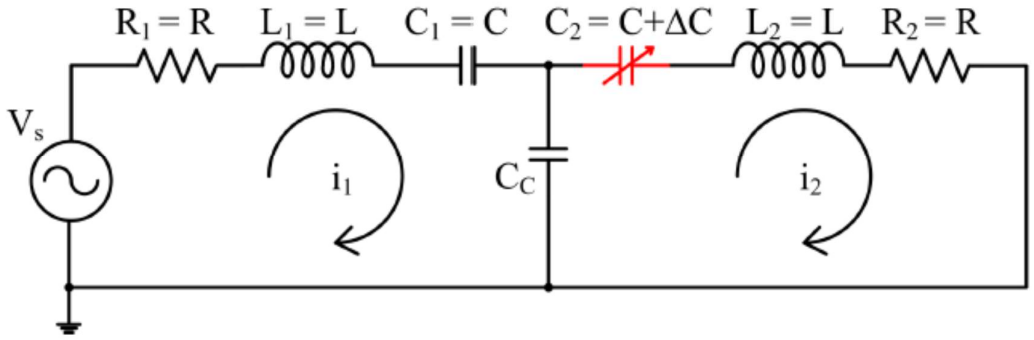

(a)

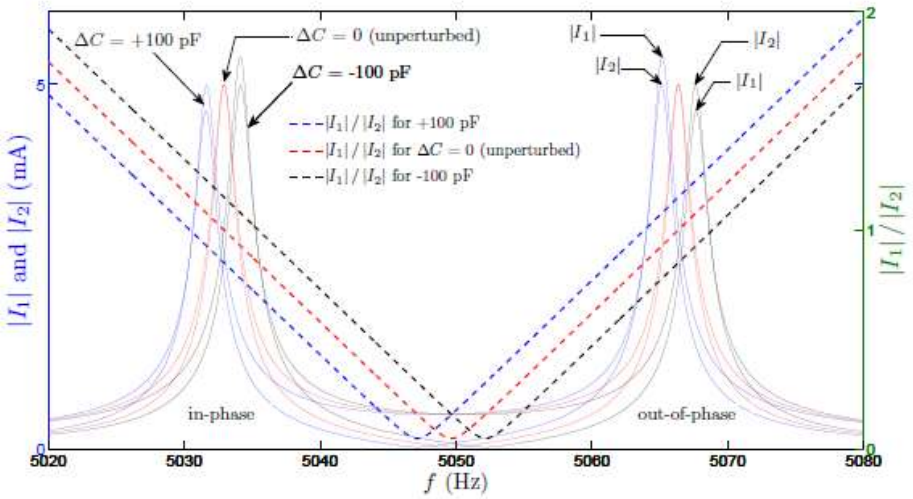

(b)

Figure 2.13 (a) A circuit network of two RLC components, representing two series resonant tanks. A capacitor C_c is the coupling capacitor, coefficient of coupling is set by the ratio C/C_c. (b) frequency response of the system for three values of perturbation [67,68]

The role of asymmetry in the design of devices and its influence on sensitivity was investigated in [69,70]. It was shown that asymmetry in devices can lead to even higher sensitivities than reported in the literature. A design using combs were used to allow large vibration amplitudes of resonators thereby increasing the signal to noise ratio.

A mode localization based resonant MEMS tilt sensor with a linear measurement range of 360^0 was reported in [28]. The input tilt angle caused changes of the mode shape of both accelerometers that were used in this work. An amplitude ratio based sensitivity of about 169 times higher than frequency shift was reported with nonlinearity of 4.5%.

A research on the linear sensing range for mode localized sensor was done in [56]. Algebraic summation of eigenstates (normalised eigenvectors) was proposed as a novel output metric to extend the linear sensing range of mode-localized sensors. In [71], it was proposed that if the resonators were driven simultaneously, a linear sensing range across the veering point can be extended if amplitude difference, rather than ratio is chosen as an output metric. Figure 2.14 shows simulation and measurement for the amplitude difference readout.

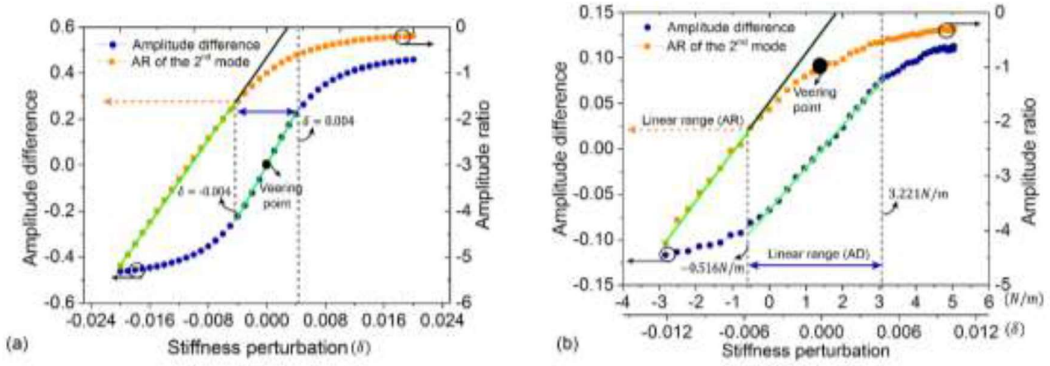

(a) (b)

Figure 2.14 The simulated (a) and measured (b) amplitude difference (AD) amplitude ratio (AR) of the 2nd mode under the Out-Driven scheme [71]

A study utilized two DoF coupled resonators to theoretically estimate a ultimate detection limit (resolution) [72]. A prototype was electrically characterised and shifts into the eigenstates (normalized amplitudes) were deduced from the measured response. A theory estimate for the various intrinsic and extrinsic noise sources (namely mechanical-thermal noise, momentum-exchange noise, and noise fluctuations arising from sensor's interface circuit such as electronic preamplifier) was calculated. It was concluded that, an electronic interface circuit has a major contribution and it acts as a dominant factor in resolving the minimum possible shifts into the output of a sensor. Figure 2.15 shows measured shifts for three samples that were used in this research. Resolving the lowest possible shifts into the mode amplitude was also attributed to the coupling factor, κ, with the claim that lower κ leads to the higher resolution. It was claimed that the ultimate detection limits as derived in this work might surpass that of resonant sensors based on frequency shift output.

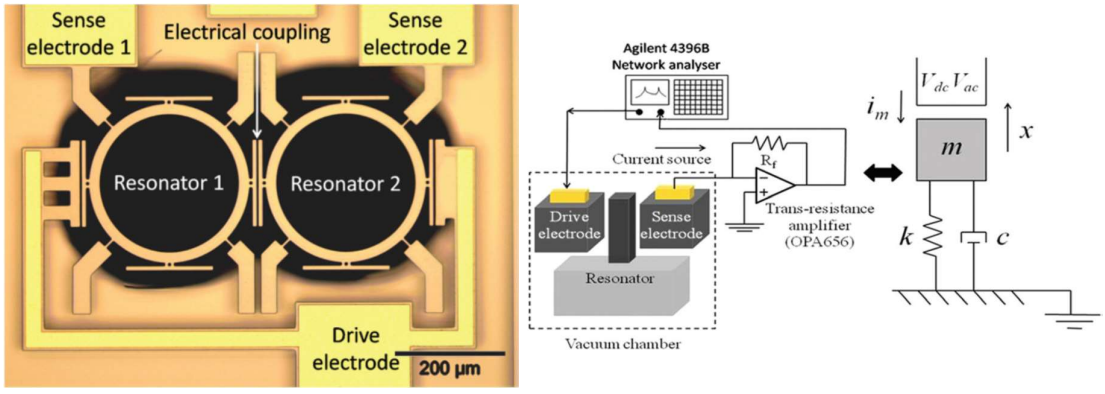

(a) (b)

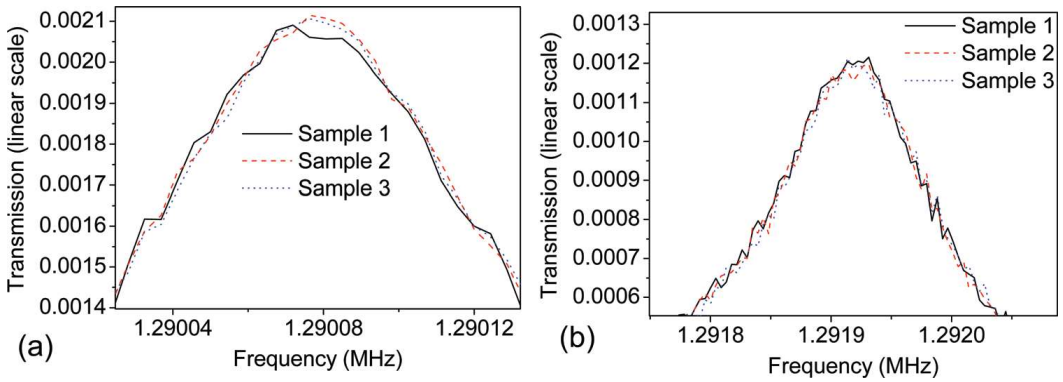

(c)

Figure 2.15 Limits to mode-localisation in a weakly coupled resonators (a) fabricated prototype (b) measurement setup in open loop and (c) measured response [72]

In the work reported by Tao *et al*, inverse eigenvalue analysis was performed for an array of five square plate coupled resonators [73,74]. In this method, two sets of eigenvalues (before and after perturbation) were obtained, by which system matrix for the coupled resonators was extracted. With this method, it was claimed that a coupling ratio and a spring constant and sensitivity could be characterised. In [75], a technique to couple an electrical resonator to an array of MEMS resonators was introduced. Two sets of eigenvalues were measured by connecting/disconnecting the electrical resonator.

Mode-localized sensors are also noticeable for common mode rejection properties as reported in [20,76]. As reported in [76], amplitude ratio based output showed maximum error of 2.74 % for a pressure range of 2.6 to 20 Pa. In [77], immunity to temperature fluctuations (between 35°C and 60°C) in weakly coupled MEMS resonators was reported.

A work on characterizing the nonlinearity of coupled resonators as a sensor has been reported by few research groups. In [78], it was postulated that loci veering of amplitude ratio over a range of stiffness perturbations generate nonlinearities, thus limiting the linear sensing. It was proposed that algebraic summation of amplitude ratio of two vibration modes can extend the linear sensing range (thus minimizing the nonlinearity error) of the mode-localized sensors. An electrical test and characterization of a prototype was done using two and three coupled resonators.

A research work in [79,80], proposed to operate a weakly coupled resonators beyond the threshold (commonly known as a bifurcation point in MEMS resonators) of a linear operating region. A sensitivity and a noise floor were characterized in the nonlinear region to benefit in resolving the lowest possible shifts into the output metric. In [80], sensor was operated in closed loop configuration. In [81], two weakly coupled resonators, biased in a strong nonlinear region of operation showed improved resolution in the output metric (amplitude and frequency). An amplitude and frequency stability was characterised for a coupled resonators operating at various bifurcation points. A prototype was characterised in a closed loop mode.

In [82], an improved output response of a weakly coupled resonators was shown by operating the device at the specific operating point. A working region for the device was selected where mechanical nonlinearity of the resonators and the electrical nonlinearity of the electrostatic coupling cancelled. It therefore enhanced the output current amplitudes by 4 times, while preserving the trend of amplitude variations as a function of stiffness perturbations.

A research on the noise floor optimization in weakly coupled resonators was done in [83]. A mode-localized sensor was proposed to be operated in an optimal operating region to benefit in resolving the lowest possible shifts in the output metric (amplitude ratio in this work). Two parameters, coupling strength and stiffness mismatch were attributed to the maximum possible resolution.

A research reported in [84], provided a theoretical study and simulations to conclude that resolution of a weakly coupled sensor is independent of the coupling factor. This research claimed to show contradiction with the findings in [72], where, it was postulated that lower coupling factor leads to improved resolution, and ultimate resolution (i.e. measurement limit imposed by noise processes in the system) is linearly proportional to the coupling factor.

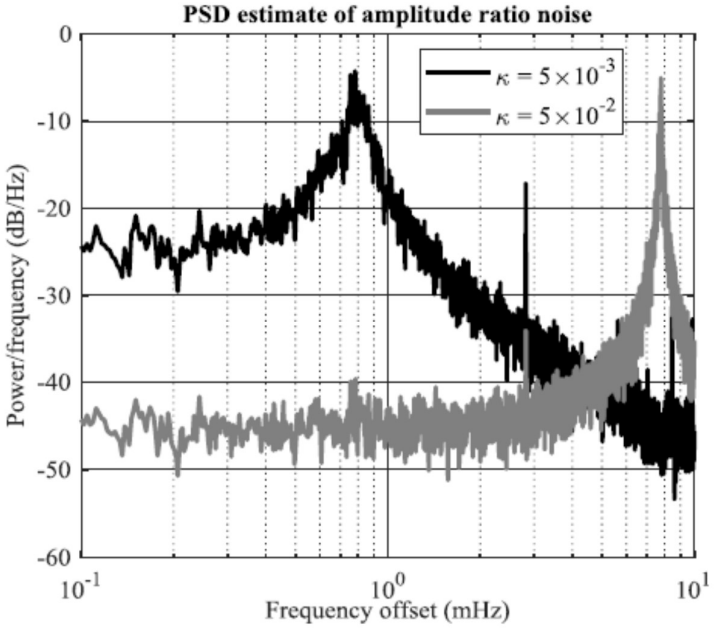

Figure 2.16 Simulated spectrum of amplitude ratio fluctuations when the system is subject to independent white noise perturbations. Simulation parameters are F=1, ω=1, Q=1000, ε=0 [84,85]

A work in [84] was extended and a prototype developed in [85] was characterised in both open and closed loop. An investigation on influence of a mechanical-thermal noise on the ultimate resolution of a sensor was carried out. Figure 2.16 shows a simulated power spectral density estimate of amplitude ratio noise. It was reported that for amplitude ratio based measurements of mode-localised sensors; a resolution is independent of coupling strength. It was concluded that lowering the coupling factor leads to enhancement in sensitivity for an amplitude ratio

based output. However, at the same time, it also increases an influences of an additive noise processes (e.g. thermo-mechanical noise of a sensor) and thus it compensates the gain in sensitivity (due to lower coupling strength) and thus impedes an improved resolution.

A resolution of a mode-localised sensor was compared with resolution of a single resonator that provides frequency shift output. It was concluded that mode-localised sensor (in open and closed loop case with all output metric in [84,85]) still do not break the ultimate limit set by the measurement of an oscillation frequency of a single resonator. No experimental verification was provided to justify the claims, however.

A circuit based simulations for self-oscillation of mode localized sensors was reported in [86]. In [87,88], results with experiments were reported. Figure 2.17 shows a prototype and measurements reported in [88]. A linear amplitude ratio based sensitivity about 391 was reported. A real time monitoring of mode localization effect and frequency shift was presented in this work.

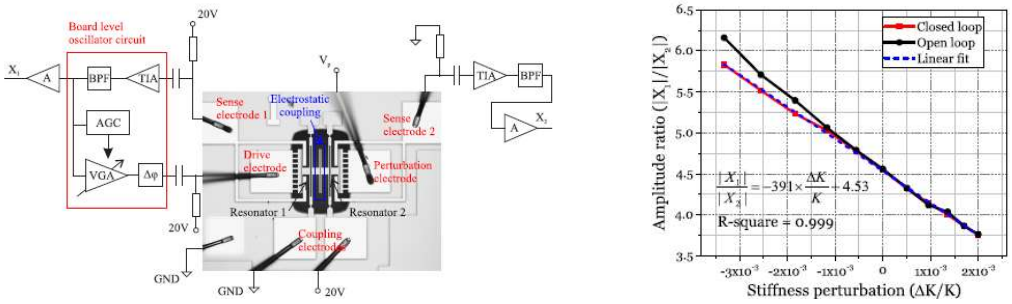

(a) (b)

Figure 2.17 (a) Oscillator schematics including the optical micro-graph of the prototype mode-localized resonant sensor and (b) amplitude ratios variations for varying the normalized stiffness perturbations [88]

A recent research on the long-term stability of output metric (amplitude ratio shift and frequency shift) was carried out in [15,89]. It was shown that for long-term, amplitude ratio is more stable and preferable in order to resolve the stiffness perturbations and for a short-term frequency shift output can be utilized to resolve changes in the stiffness perturbations. A measurement over a long integration time was done for a prototype arranged in the open loop and closed-loop configuration.

A noise analysis performed in this work emphasized the dominance of external electronics in setting the noise floor. This research work can be seen as an optimization of a work done in [72]. A noise floor for an amplitude ratio based output was determined to be about $4.4\times10^{-3}/Hz^{0.5}$. In [89], An amplitude ratio sensitivity to stiffness perturbations of 5250 was determined for the device operating in the linear region. Amplitude and frequency stability of a mode-localized sensor were characterized in a closed loop setup.

In [90], a prototype was characterised for varying power levels of a AC drive signal and its impact on the amplitude ratio was investigated. It was found that in/near the veering zone, amplitude ratio exhibits minimum variations against changes in the input AC drive signal. This

effect was seen as a pathway to high-resolution long term measurements in mode localized sensing.

In all of the electrically or mechanically coupled resonators referred so far, a sensor performance was determined either by an amplitude based and/or frequency based output. A work carried out in [91–93], an output metric based on phase change was proposed. A "mutually injection-locked oscillators" (MILOs) based on two synchronized oscillators were discussed. This work was shown to operate on the principle of differential resonant sensing. Here, the phase difference between the resonators serves as an output metric to mismatch in stiffness or mass, thus providing a differential measurement of a physical quantity of interest. Due to the similarity of a working principle, this study of MILO was called to be analogous with the mode-localized sensors.

Summary

In this chapter, basics of a MEMS resonator are reviewed. A principle of electrostatic actuation and capacitive sensing is presented. An in-depth literature converge in the context of a coupled resonators, with emphasis on its applications in sensing is provided. This literature review was used as a foundation stone in modelling and designing our coupled resonators for fabrication using the state-of-the-art micromachining using laser.

Chapter 3

3 Theory and Design

In this chapter, an analytical part and the formation of a theory of our design is presented. First, a design procedure for the millimetre (mm) scale electromechanical transducer is described. Following this, two such MEMS resonating elements were electrically coupled to form a two degree of freedom (DoF) coupled resonators. A theoretical model for two degrees of freedom (DoF) and three DoF coupled resonators is prepared based on the governing set of equations of motion. Design equations were used to determine various performance parameters such as mode frequencies, mode amplitude ratio, sensitivity, etc.

3.1 Device geometry and design parameters

This section covers a design and a model for a macro-scale device that uses electrostatics to form capacitive resonating sensor. This principle of electrostatic actuation and capacitive sensing was applied to design and model a weakly coupled two DoF resonating sensor device. For this study, we can refer a micro-design that is presented in [18,23,58,59] and present few modifications into our scaled-up macro-design presented in this chapter. Geometric features of our design are scaled-up. And, a critical analysis is done on the basis of the magnitude of net electrostatic forces that are produced, the material used for fabrication, electro-mechanical transduction factor, coupling ratio for coupled sensor application, motion sensing output signal, etc. In the micro-device presented in [18,23], we calculated that nominal overlap area for actuation and therefore the net actuation force (for a given gap of 4.5 μm and a DC voltage of 60 V) is about $7.92\times10^{-9}\ m^2$ and $1.3198\times10^{-5}\ N$ respectively. Therefore, the initial effort was taken to produce the net excitation/drive force in our macro-device to be of a similar order of magnitude.

Figure 3.1(a) shows a representative graphic view of a two DoF electrostatically coupled resonating sensor prototype depicting all geometric features. In this design, a lowest possible kerf-width (capacitive air gap) of about 60 μm has been fabricated by laser micromachining. A detail on fabrication is reported in the following chapters of this thesis. Usually in a micro-device, often a gap, d realized photo lithographically for electrostatic transduction is in the range of few μm [30]. Fundamentally, this would pose a severe restriction onto realizing a movable capacitor and/or relevant devices with an arbitrarily large gap, which, in our case, is 60 μm. In essence, the net electrostatic force for actuation would be low (assuming (a) displacement of a proof mass, $x<<d$ and (b) other parameters such as geometric features and applied voltages of a design are of similar scale as in micro-design). This situation therefore virtually rules out a possibility to electrostatically actuate and thus sense any motion using a device with larger gaps. To circumvent this issue while attesting the benefits of using laser micro machining to manufacture such device, geometric features of this design were scaled-up, making it a millimetre (mm) scale-device. By doing so, it is possible not only to produce a net excitation/drive force of about same order of magnitude as in conventionally fabricated micro-devices but also a motion out of such device can reliably be sensed capacitively. A

design parameters are given in Table 3.1 for a refereed micro-size [18,23] and this scaled-up movable plate capacitor. Figure 3.1 (b) depicts a 3D view of a design to relate with the parameters given in Table 3.1.

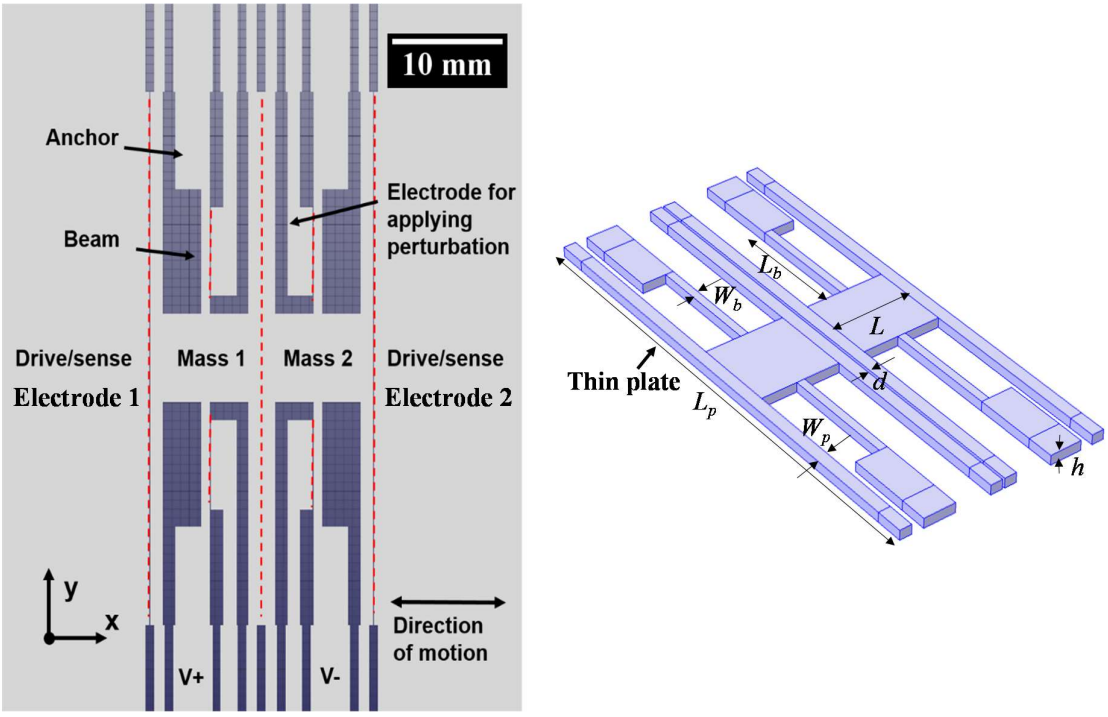

(a) (b)

Figure 3.1 (a) A perspective view schematic of a two DoF weakly coupled resonators highlighting the entire necessary feature. Red dotted lines indicate parallel kerf-widths to be machined through entire device thickness for capacitive transduction. The shaded area in dark blue indicates material to be ablated during machining. As shown, the DC voltages V+ and V− to be applied not only to polarize the individual micro-machined gap capacitors but also couple them through this electric potential difference. (b) 3D view of the design.

Table 3.1:Design parameters for a developed prototype

Parameters	**Reference[18]**	**Scale-up factor**	**This design**
Thin plate length, L_p *(μm)*	NA	NA	60000
Thin plate width, W_p *(μm)*	NA	NA	1500
Proof mass side length, L*(μm)*	360	27.77	10000
Kerf-width (gap), d*(μm)*	4.5	13.30	60
Device thickness, h*(μm)*	30	33.33	1000
		66.66	2000
Suspension Beam design			
Beam length, L_b*(μm)*	350	40	14000
Beam width, W_b*(μm)*	5	200	1000

Materials used			
	Silicon	Aluminum	Stainless steel
Young's modulus of elasticity, *E (Pa)*	170×10^9	70×10^9	200×10^9
Density, *(kg/m³)*	2330	2700	7850

3.1.1 A MEMS electromechanical transducer design

Based on the design parameters as given in the Table 3.1, an effective value of a proof mass was calculated to be 5.5×10^{-4} *g*. As shown in Figure 3.1, a nominal overlap area for capacitive transduction is determined to be 6×10^{-5} m^2. This is also the transduction area at electrode 1/electrode 2 (Note that electrode 1/electrode 2 is also depicted as drive/sense electrodes in Figure 3.1 (a)) as well as area coupling the two masses. Using the same dimensional values given in Table 3.1, a model in COMSOL Multiphysics software [94] was built (A COMSOL model and simulations are presented in Chapter 4). An eigenfrequency analysis was performed in COMSOL and a resonator frequency (2483 *Hz*) and a mode shape of a single resonator was determined. A COMSOL simulated eigenfrequency value was used and a value of effective stiffness was extracted as

$$\begin{aligned} K &= M\times(2\pi f)^2 \\ &= 5.5\times10^{-4}\times(2\times3.1415\times2483.2)^2 \\ &= 1.34\times10^5\, N/m \end{aligned} \tag{3.1}$$

A nominal capacitance value for this design is calculated as follows:

$$\begin{aligned} C_0 &= \frac{\varepsilon A}{d} = \frac{8.854\times10^{-12}\times6\times10^{-5}}{60\times10^{-6}} \\ &= 8.854\times10^{-12}\, F \end{aligned} \tag{3.2}$$

Note that this is the nominal capacitance at the electrode 1/electrode 2 as well as the capacitance coupling the two masses. For a device thickness, h=2 *mm*, $C_0 = 1.77\times10^{-11}$ *F*. Assuming a DC voltage V_{dc}=200 *V* is applied for the polarization, a net electrostatic force at DC, can be calculated as

$$\begin{aligned} F_{DC} &= \frac{1}{2}\frac{\varepsilon A}{(d-x)^2}\left(V_{dc}^2\right) \\ &\approx \frac{1}{2}\frac{\varepsilon A}{(d)^2}\left(V_{dc}^2\right)\left[\because x << d\right] \\ &\approx \frac{1}{2}\left(\frac{8.854\times10^{-12}\times6\times10^{-5}}{\left(60\times10^{-6}\right)^2}\right)\left(200^2\right) \\ &\approx 3\times10^{-3}\, N \end{aligned} \tag{3.3}$$

With the introduction of a DC voltage, an effective stiffness of the transducer becomes $k_{eff}=k+k_e$, where,

$$\begin{aligned} k_e &\approx \frac{-\varepsilon A}{(d-x)^3}\left(\Delta v^2\right) \\ &\approx \frac{-\varepsilon A}{(d)^3}\left(\Delta v^2\right)\left[\because x << d\right] \\ &\approx -\left(\frac{8.854\times10^{-12}\times6\times10^{-5}}{\left(60\times10^{-6}\right)^3}\right)(200-0)^2 \\ &\approx \text{ -98.377 N/m} \end{aligned} \tag{3.4}$$

Therefore, an effective value of a spring constant is calculated as $k_{eff}=k+k_e=1.34\times10^5+(\text{-}98.377)=1.339\times10^5\,N/m$.

A displacement of a proof mass, x for this applied force for a given spring constant is calculated as $x=\frac{F_{DC}}{k_{eff}}=\frac{3\times10^{-3}}{1.339\times10^5}\approx22.02\times10^{-9}m$. This value of x is 0.036% of the nominal capacitive air gap, d, which is 60 μm in our design.

Assuming an AC signal of 5 V in magnitude at the resonant frequency is applied along with a DC voltage, V_{dc}. Therefore, a net electrostatic force is given as $F_e=\frac{1}{2}\frac{\varepsilon A}{(d-x)^2}\left(v_{ac}^2+V_{dc}^2+2v_{ac}V_{dc}\right)$ (refer equation (2.2)). A net electrostatic force at the excitation frequency is given as

$$\begin{aligned} F_e &= \frac{1}{2}\frac{\varepsilon A}{(d-x)^2}\left(2v_{ac}V_{dc}\right) \\ &\approx \frac{\varepsilon A}{(d)^2}\left(v_{ac}V_{dc}\right)\left[\because x << d\right] \\ &\approx \left(\frac{8.854\times10^{-12}\times6\times10^{-5}}{\left(60\times10^{-6}\right)^2}\right)(5\times200) \\ &\approx 147\times10^{-6}\,N \end{aligned} \tag{3.5}$$

A displacement of a proof mass, x for this applied force for a given spring constant and quality factor Q=2000 is calculated as $x=\frac{QF_e}{k_{eff}}=\frac{2000\times147\times10^{-6}}{1.339\times10^5}\approx2.592\times10^{-6}m$. This value of x is 4.32% of the nominal capacitive air gap, d, which is 60 μm in our design. It is to be noted that in micro device [18,23] a DC voltage of 50 V was applied to bias the device and to also form an electrical coupling between the proof masses. This exerted an attractive net actuation force

of magnitude 4.33 $\times 10^{-6}$ *N* that caused about 90 *nm* displacement of a proof mass which is 2 % of the effective air gap (4.5 μm) that forms this movable capacitor.

For a designed geometry and selected material, natural resonant frequency of the single resonator (i.e. without coupling) was theoretically calculated as 2.483×10^3 *Hz*. Figure 3.2 shows the plot for resonant frequency, *f* as a function of r, (r is ratio of suspension beam width W_b to the beam length L_b). Computations are shown for two values of device thickness i.e. *h=1 mm and h=2 mm*. In order to keep about the same order of magnitude of resonant frequency as in [18,23], we scaled-up an effective mechanical spring constant of the suspension beams attached to the relatively large proof mass (5.13×10^{-4} g).

For this design, beam width W_b = 1 *mm* and a beam length L_b =14 *mm* is chosen as shown in Figure 3.1(b). Smaller ratio leads to a design that is more compliant towards direction of motion. However, it also pushes the design towards sub-*kHz* resonant frequency for a given size of a proof mass, which is 0.51 *mg* in this design. As shown in Figure 3.1 (a), only two suspension springs were attached to each of the proof mass. This was done to not only to enhance the displacement amplitude for an applied actuation/drive force but also to further aid in reduction of otherwise inevitably higher motional resistance (owing to the gap of 60 μm).

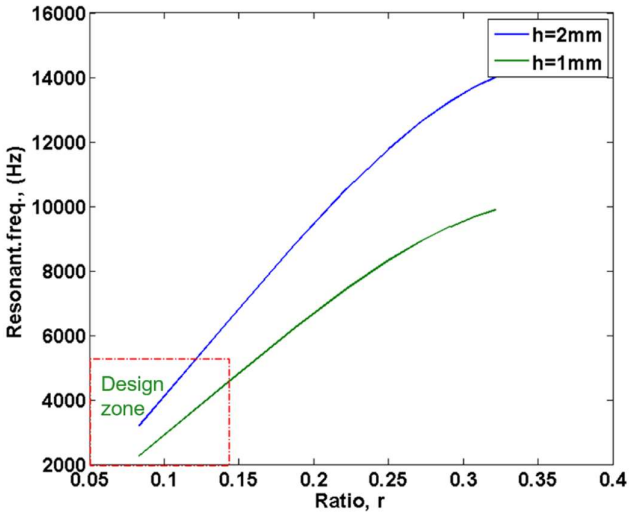

Figure 3.2 resonant frequency variation as a function of ratio, r.

Through our COMSOL simulation as reported in section 3.4, we found that in order to make the system compliant in the direction of motion, flexible beams formed with a smaller width and longer length (referring to Figure 3.1 and Table 3.1) are of advantage in addition to using a softer material such as aluminium. Lower effective value of a spring constant also means lowering the restriction on the net actuation force (lower applied voltages) to attain same order of a displacement of a proof mass for a fixed gap and area. Also, through our analytical study, (referring to the expression of motional resistance in section 3.1.2 and Table 3.2 below) we found that to facilitate sensing, the smaller value of an effective mechanical spring constant is beneficial to keep motional resistance below 10 $M\Omega$ for quality factor Q = 2000.

Two thin plates of 60 *mm* length and 1.5 *mm* width are attached to the proof mass in an aid to enhance an actuation and sensing out of the device. A device that was finally fabricated (more on the device fabrication is given in chapter on fabrication) is supported by only two springs to further enhance the sensitivity for an applied force. Two such devices electrostatically coupled will form coupled resonating sensor. Coupling strength between two proof masses is determined by the plate overlap area and potential difference between them for a designed capacitive gap. An overlap area for transduction and capacitance of perturbation electrode are calculated as follows: length of a perturbation electrode were designed to be 2 *mm* therefore making the overlap area to be about $2\times10^{-6}\ m^2$. A resultant capacitance for the same is $C_{per} = 2.951\times10^{-13}\ F$.

3.1.2 A motional resistance estimation in our design

In electrostatically transduced resonators, motional resistance, R_x is directly proportional to the 4^{th} power of a capacitive air gap. It is expressed as $R_x = \dfrac{d^4\sqrt{k_{eff}M}}{V_{dc}^2\varepsilon^2A^2Q}$ [95,96]. A calculated value of R_x is about 8 $M\Omega$ in a refereed micro-sensor design [18]. If the dimensional features were kept same as in micro-design, value of R_x would be orders of magnitude high owing to the gap of 60 μm of this design. Therefore, it was necessary to scale-up a nominal overlap area for sensing side of this macro capacitor in order to measure an output signal and changes into it subject to externally applied disturbances in various sensing applications. As a result, a structure as shown in Figure 3.1 employs thin plates of 1.5 *mm* wide attached to the either side of proof mass and nominal area of this sensing/actuation macro-capacitor was increased eventually taking it to the level of $5\times10^{-5}\ m^2$. To keep the geometric symmetry for a two DoF weakly coupled resonant sensor, similar scaling up of nominal area (via attachment of thin plate) was done at the driving side of the macro-capacitor. During the design phase, it was supposed that there is virtually no control over other parameters such as relative permittivity, ε, DC voltage, V^+=200 *V* used in the computations to polarize this macro-capacitor and also to establish a electrical spring between the proof masses for coupled resonating sensor, and an assumed value of quality factor, Q = 2000.

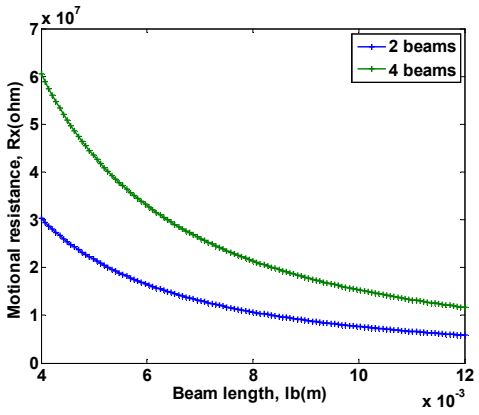

(a)

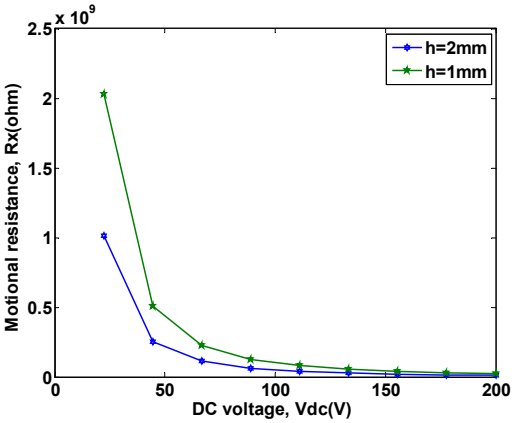

(b)

Figure 3.3 A variation in a resonator motional resistance for a) a varying beam width, W_b and b) a varying DC voltage, V_{dc}.

All these factors influence a motional resistance in a positive way (i.e. decrease it to the magnitude similar to micro-sensor discussed earlier). To further scale-down down the motional resistance, suspension springs (as described earlier in section 3.1.1) attached to the proof mass were designed to be more compliant in the direction of motion (making them 14 *mm* longer, 1 *mm* wider and hence softer, refer Figure 3.1). This design optimization eventually matched the value of motional resistance to be same order of magnitude as that in micro-sensor design that was refereed [18,23]. Figure 3.3 shows how motional resistance would scale down as a function of geometric variations and/or a DC voltage used for polarization in this design.

Table 3.2 shows calculations based upon theory and COMSOL model developed (COMSOL simulations are presented in chapter 4) for this macro-capacitor design for two different device thickness, *h*.

Table 3.2: Detailed calculation for the device. (*h* represents device thickness)

Design of a MEMS transducer for weakly coupled resonators			
Calculations	**Micro-design** [18,23,59]	**Macro-design**	
		h=1 *mm*	*h*=2 *mm*
Nominal capacitance of a parallel plate @ driving/sensing ports, $C_0(F)$	1.56×10^{-14}/ 1.82×10^{-14}*	8.854×10^{-12}/8.854×10^{-12}	1.77×10^{-11}/1.77×10^{-11}
Natural frequency of a single resonator, theory/FEM $f(Hz)$	≈13700	2483	
Effective overlap area @drive/sense electrodes, $A(m^2)$	7.92×10^{-9}/1.54×10^{-9}	6×10^{-5}/6×10^{-5}	1.2×10^{-4}/1.2×10^{-4}
Effective mass, $m(g)$	6.64×10^{-9}	5.5×10^{-4}	1.1×10^{-3}
Effective spring constant, K_m (N/m)	55.73	1.34×10^{5}	2.681×10^{5}
Magnitude of applied AC voltage, (V)	10×10^{-3}	5	
Applied potential difference for a electrostatic actuation, V_{dc} (V)	50	200	
Net DC force @electrode 1, F_{DC} (N)	4.918×10^{-6}	3×10^{-3}	5.9×10^{-3}
Resulting displacement of a proof mass, (F_{DC} / K_m), $x(m)$	$\approx91\times10^{-9}$	$\approx22\times10^{-9}$	
Net change in capacitance, ΔC (F)	3.65×10^{-16}	3.25×10^{-15}	6.5×10^{-15}
Capacitive gradient at drive/sense electrode, (F/m)	4.09×10^{-9}	1.59×10^{-7}	3.18×10^{-7}
Net AC force @ resonance, $F_e(N)$	1.96×10^{-9}	1.47×10^{-4}	2.95×10^{-4}
Resulting displacement of a proof mass, (F_e / K_m), $x(m)$	$\approx183\times10^{-9}$**	$\approx2.592\times10^{-6}$	
Transduction factor at drive/sense electrode, η	1.96×10^{-7}	5.9×10^{-5}	
Motional resistance, R_x (Ω)	8×10^{6}**	4.93×10^{6}	2.46×10^{6}
Quality factor, Q	5000	2000	
Design of a weakly , electrostatically coupled resonator			
Negative electrical coupling spring, K_c (N/m)***	-1.9238	-393.511	-787.022

Natural frequencies of coupled system, in-phase/out-of-phase, *f (Hz)*	13752/13750	2482/2474

** Design employed 3 sets of a gap varying interdigitated fingers plus differential sense configuration*
*** For a quality factor Q=2000*
****For an applied DC voltage of 50 V*

3.1.3 Choice of material from a design perspective

Aluminium was selected as material for manufacturing as it is relatively soft (young's modulus, E=70 *GPa*) and has a relatively lower density ρ = 2700 kg/m^3 as compared to other commonly found metals such as steel, copper, brass, etc. Although usage of all these other mentioned materials for device making may also be advantageous as these material generally are incompatible to be used with the typical micro (MEMS) fabrication processes [33]. Aforementioned property of aluminium makes it more compliant towards flexural bending in such scaled-up geometry. Moreover, it is relatively less expensive than other common metals available. From manufacturing perspective, it was necessary to make the design free from heat-induced effects and structural cracks (residual stress) that may cause a device geometry to bend if the feature sizes in the pattern being machined are very thin i.e. below sub-*mm* size. Preferring aluminium for this application also offered a convenience towards further lowering the resistance to motion (relatively lower material density, and modulus of elasticity contribute in lowering the effective mass and effective mechanical stiffness respectively).

3.2 A coupled resonator design (scaled-up architecture)

We can refer back Figure 3.1 that shows a schematic diagram for the two electrically coupled resonating elements. In regard with the two coupled resonators design, a DC voltage, V^+=200V is applied to the proof mass M_1 and electrode 1 is held at ground potential. Also, a DC voltage of equal magnitude but opposite polarity, V^-=-200 V is applied to the proof mass M_2 and electrode 2 is initially held at ground potential.

$$
\begin{aligned}
k_{e1} &\approx \frac{-\varepsilon A}{(d-x)^3}(\Delta v)^2 \\
&\approx \frac{-\varepsilon A}{(d)^3}(\Delta v)^2 \left[\because x << d\right] \\
&\approx \frac{-\varepsilon A}{(d)^3}(V^+ - 0)^2 \\
&\approx -\left(\frac{8.854\times10^{-12}\times6\times10^{-5}}{(60\times10^{-6})^3}\right)(200-0)^2 \\
&\approx \text{ -98.377 N/m}
\end{aligned}
\tag{3.6}
$$

$$
\begin{aligned}
k_{e2} &\approx \frac{-\varepsilon A}{(d-x)^3}(\Delta v)^2 \\
&\approx \frac{-\varepsilon A}{(d)^3}(\Delta v)^2 \left[\because x << d\right] \\
&\approx \frac{-\varepsilon A}{(d)^3}\left(0 - V^-\right)^2 \\
&\approx -\left(\frac{8.854\times10^{-12}\times6\times10^{-5}}{\left(60\times10^{-6}\right)^3}\right)\left(0-(-200)\right)^2 \\
&\approx \text{ -98.377 N/m}
\end{aligned}
\tag{3.7}
$$

With the introduction of a DC voltages into the system, a mechanical spring K_{m1} and K_{m2} of both the proof masses become softer (commonly referred as spring softening effect in the literature) and effective value of a mechanical springs of both the proof masses can be written as $k_{eff1}=k_{m1}+k_{e1}$, $k_{eff2}=k_{m2}+k_{e2}$. A value of electrical stiffness, k_{e1} and k_{e2} can be calculated as given in equations (3.6) and (3.7) respectively: Here, note that electrical spring has a negative effective value and $k_{e1}=k_{e2}$ and therefore, $k_{eff1}=k_{eff2}$. It is to be noted that electrode 2 being held at ground potential sets an operating/bias point of this design.

As proof mass M_1 is held at V^+ and proof mass M_2 is held at V^-, a potential difference is established between the two that sets the coupling spring constant, K_c in a two DoF weakly coupled resonators. A value of a coupling spring constant is calculated as

$$
\begin{aligned}
K_c &\approx \frac{-\varepsilon A}{(d-x)^3}(\Delta v)^2 \\
&\approx \frac{-\varepsilon A}{(d)^3}(\Delta v)^2 \left[\because x << d\right] \\
&\approx \frac{-\varepsilon A}{(d)^3}\left(V^+ - V^-\right)^2 \\
&\approx -\left(\frac{8.854\times10^{-12}\times6\times10^{-5}}{\left(60\times10^{-6}\right)^3}\right)\left(200-(-200)\right)^2 \\
&\approx \text{ -393.511} N/m
\end{aligned}
\tag{3.8}
$$

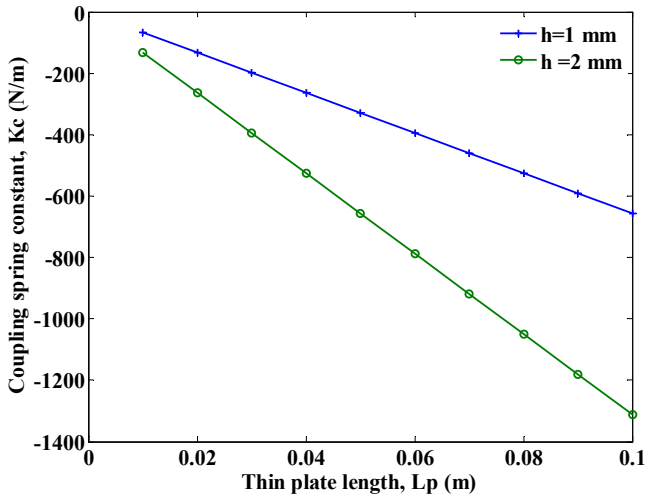

Figure 3.4 Variation of coupling spring constant, K_c as a function of thin plate length that is attached to either side of each of the proof mass in a coupled resonating sensor. With higher device thickness, h, it is beneficial to create a larger electrostatic force between the gap coupling two proof masses.

This value of K_c is for device thickness h=1 *mm*. Higher device thickness yields higher negative effective value as provided in Table 3.2. A negative effective value of K_c determines the parametric sensitivity (by lowering K_c) but it also may result in mode merging [17,18,97]. A corresponding coupling factor for the calculated value of K_c is calculated as

$$\kappa = \left|\frac{K_c}{k_{eff}}\right| = \left|\frac{-393.511}{1.339\times10^{5}}\right| = 0.0029 \text{ (dimensionless)}$$

Figure 3.4 shows a variation in a coupling spring constant with parameters as indicated.

In this macro-device, a coupling voltage of ±200 *V* is used and an effective value of coupling spring is computed to be -393.51 *N/m* (negative sign indicates the electrostatic coupling being established). As discussed in 3.1.1, two thin plates are added to the either side of the proof masses and thus the effective overlap area is increased to enhance a coupling between two masses. This increases an electrostatic force between the two proof masses for the given gap and applied voltages.

The lower value of coupling spring constant, K_c is useful in enhancing the mode amplitude based sensitivity of the device for an applied perturbation into the system. However, it also makes it difficult to selectively identify and lock to the in-phase or out-of-phase mode of interest as in such situation two resonating mode frequency signals are likely to merge. In this scenario, a higher quality factor is desirable as it assures lower -3 *dB* bandwidth of the individual mode and therefore there is relaxation on the mode frequency difference. This difference is required to be at least twice the value of -3 *dB* bandwidth of a particular mode to restrict two modes being merged [18,54,98].

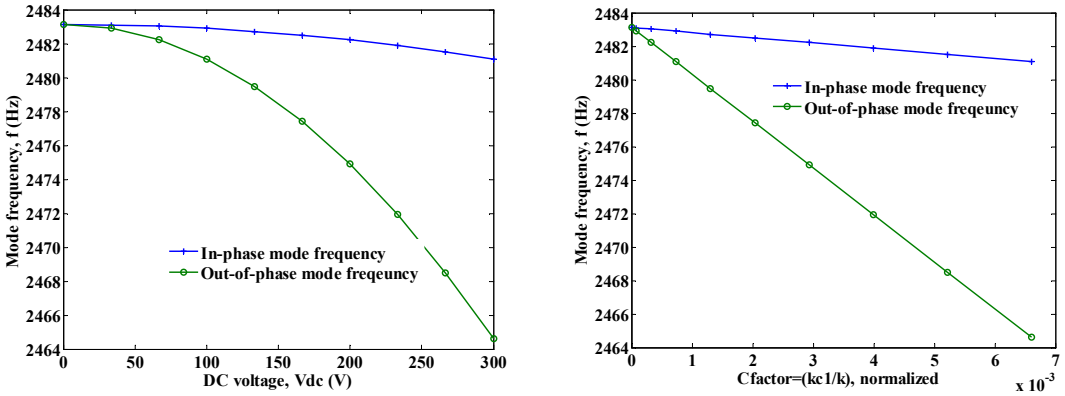

(a) (b)

Figure 3.5 Resonant mode frequencies of a device as a function of a) a varying DC voltage used in the system and b) a normalized coupling factor. Out-of-phase mode frequency always precedes in-phase mode frequency due to negative effective value of a coupling stiffness between the two proof masses. As seen, a specific value of coupling factor helps attain a adequate mode-frequency difference.

Theoretical resonant mode-frequencies when system is balanced (Δk=0) is calculated as

$$\omega_{r1}=\sqrt{\frac{k_{eff}}{M}}=\sqrt{\frac{1.339\times10^{5}}{5.508\times10^{-4}}}=1.559\times10^{4}\,rad/\sec$$
$$\therefore f_{ip\_0}=\frac{\omega_{r1}}{2\pi}=\frac{1.559\times10^{4}}{2\pi}\approx 2482Hz \tag{3.9}$$

$$\omega_{r2}=\sqrt{\frac{k_{eff}+2k_{c}}{M}}=\sqrt{\frac{1.339\times10^{5}+2(-393.511)}{5.508\times10^{-4}}}=\ 1.555\times10^{4}\,rad/\sec$$
$$\therefore f_{op\_0}=\frac{\omega_{r2}}{2\pi}=\frac{1.555\times10^{4}}{2\pi}\approx 2474Hz \tag{3.10}$$

A corresponding frequency difference is calculated as

$$f_{diff}=\left|f_{ip\_0}-f_{op\_0}\right|=\left|2482-2474\right|\approx 7.3Hz \tag{3.11}$$

Figure 3.5 (a) shows variations into the mode frequencies as a function of a DC voltage and Figure 3.5 (b) depicts a variation in resonant mode frequencies as a function of a normalized coupling factor, κ. Figure 3.6 shows a graph of mode-frequency difference as a function of a coupling factor in weakly coupled resonators.

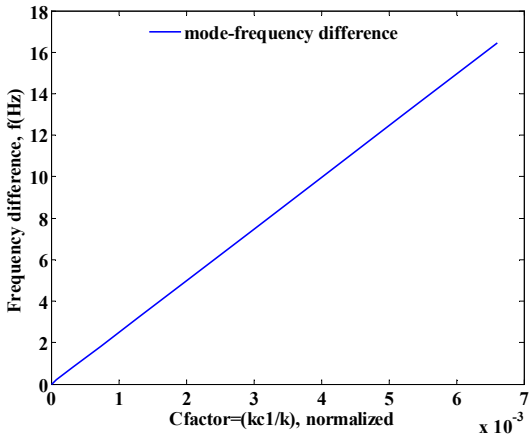

Figure 3.6 Mode-frequency difference as a function of coupling factor in weakly coupled resonators.

3.2.1 Design of a perturbation electrode

To apply an electrostatic force/perturbation, it is preferred to place electrodes in the locations as shown in Figure 3.1(a). A DC voltage, V_{per} can be applied to the external electrode reserved to apply perturbations. This voltage, V_{per} along with a DC bias voltage, V_{dc} present on to the body of the device creates an electrical spring directly proportional to the voltage difference between these two. A stiffness perturbations in this case can be calculated as $\Delta k = \frac{-\varepsilon A}{d^3}(\Delta v)^2$, where Δv refers a potential difference applied between the proof mass and the reserved electrode as shown in Figure 3.1(a). This action exerts an electrostatic force to modulate a stiffness of the resonator. This force is in the direction of motion of the beams and vibrating proof masses unlike that of [23] where electrostatic force is applied transverse to the direction of motion (*i.e.* along with the length of a beam). In our design, it is expected that, due to moderately designed stiffness (1.247×10^5 *N/m*) in the direction of motion, a relatively larger force could be exerted into the factory-made kerf-width (gap) between suspension beams and adjacent electrodes. It is expected that it would manifest adequate sensitivity and/or resolution while avoiding nonlinearity and device instability owing to the larger gap of 60 μm in our device. It is anticipated that for applying perturbations, placing electrodes in the direction transverse to the motion indicates relatively higher effective (>>1.247×10^5 *N/m*) stiffness of the beams that would likely deteriorate the mode amplitude based sensitivity and/or resolution of this coupled resonating sensor system. With this analysis, we can determine that, such macro-size sensor could be useful in measurement of relatively larger forces in applications where its micro-sensor counterpart may prove to be vulnerable. In the prototype that was fabricated, a DC voltage, V_{per} was applied to electrode 2 (refer Figure 3.1(a)) to apply stiffness perturbations. This was done to increase the transduction area by one order of magnitude (6×10^{-5} m^2) as compared to the earlier case where a DC voltage can be applied to the reserved electrode of 2 *mm* long as shown in Figure 3.1(a). Stiffness perturbations in this present case can be calculated as $\Delta k = \frac{-\varepsilon A}{d^3}(\Delta v)^2$, where Δv refers a potential difference applied between the electrode 2 and proof mass 2 as shown in Figure 3.1. A corresponding normalised stiffness perturbations can be calculated as $\delta_k = \Delta k / k_{eff}$.

3.3 Theoretical transfer function of our design

Here, we derive a transfer function of our design as follows:

3.3.1 A two DoF coupled mass-spring-damper system

We can refer back to Figure 2.6 (c) that shows a lumped parameter model of a two DoF mass-spring-damper system in the context of coupled resonators.

It shows proof masses, M_i with individual mechanical spring constant, K_{m_i} and damping coefficients, c_i (i=1, 2). Two proof masses are coupled through another spring, K_c as shown. A normalized displacement of the proof mass, X_{m_i} in response to the applied force, f is expressed as $X_{m_i} = \frac{x_i}{X_{0_i}}$; ($i$=1, 2) where, X_{0_i} is the position of the proof mass at static equilibrium condition. Following assumptions hold true for a symmetric device- $M_1 = M_2 = M$, $K_{m_1} = K_{m_2} = K_m$ and $c_1 = c_2 = c$. Force vectors f_1 and f_2 acting on the proof masses are the harmonic excitation (drive) forces that cause displacements, x_1 and x_2, assumed to occur at one frequency. A set of governing motion of equation are given as follows:

When system experiences imbalance into the initial symmetry *i.e.* $\Delta k \neq 0$, governing equation of motion for the two-coupled proof masses as shown in Figure 2.6 (c) is given as follows:

$$M\ddot{x}_1 + (c + c_c)\dot{x}_1 + (K_m + K_c)x_1 - c\dot{x}_2 - K_c x_2 = f_1(t) \tag{3.12}$$

$$M\ddot{x}_2 + (c + c_c)\dot{x}_2 + (K_m + K_c + \Delta k)x_2 - c\dot{x}_1 - K_c x_1 = f_2(t) \tag{3.13}$$

By operating the device under vacuum, we can mitigate the impact of (a) damping force of individual proof mass and (b) damping force that occurs between two proof masses, hence we can assume $c_1 = c_2 = c_c = 0$. Therefore, equations (3.12) and (3.13) are modified as below:

$$M\ddot{x}_1 + (K_m + K_c)x_1 - K_c x_2 = f_1(t) \tag{3.14}$$

$$M\ddot{x}_2 + (K_m + K_c + \Delta k)x_2 - K_c x_1 = f_2(t) \tag{3.15}$$

By applying a Laplace transformation to equations (3.14) and (3.15), we can obtain the following:

$$H_{11}(s)X_1(s) - H_{12}(s)X_2(s) = f_1(s) \tag{3.16}$$

$$H_{22}(s)X_2(s) - H_{21}(s)X_1(s) = f_2(s) \tag{3.17}$$

where,

$$H_{11}(s) = s^2 M + \left(K_m + K_c\right) \tag{3.18}$$

$$H_{12}(s) = H_{21}(s) = K_c \tag{3.19}$$

$$H_{22}(s) = s^2 M + \left(K_m + K_c + \Delta k\right) \tag{3.20}$$

In equation (3.17), we set $f_2(s) = 0$, and derive an expression for $X_1(s)$ and $X_2(s)$ to use these values back in equation (3.16) to obtain an output transfer function, as follows:

$$H_1(s) = \frac{X_1(s)}{f_1(s)} = \frac{H_{22}(s)}{H_{11}(s)H_{22}(s) - H_{12}(s)H_{21}(s)} \tag{3.21}$$

$$H_2(s) = \frac{X_2(s)}{f_1(s)} = \frac{H_{21}(s)}{H_{11}(s)H_{22}(s) - H_{12}(s)H_{21}(s)} \tag{3.22}$$

Similar procedure can be applied to obtain an expression for $H_3(s) = \frac{X_1(s)}{f_2(s)}$ and $H_4(s) = \frac{X_2(s)}{f_2(s)}$. Using the values of $H_{11}(s), H_{12}(s)$ $H_{21}(s)$ and $H_{22}(s)$ derived earlier in equation (3.18) through (3.20), we can obtain

$$H_1(s) = \frac{X_1(s)}{f_1(s)} = \frac{s^2 M + (K_\alpha + \Delta k)}{s^4 M^2 + s^2 M(2K_\alpha + \Delta k) + K_\alpha^2 + K_\alpha \Delta k - K_c^2} \tag{3.23}$$

$$H_2(s) = \frac{X_2(s)}{f_1(s)} = \frac{K_c}{s^4 M^2 + s^2 M(2K_\alpha + \Delta k) + K_\alpha^2 + K_\alpha \Delta k - K_c^2} \tag{3.24}$$

respectively, where, $K_\alpha = (K_m + K_c)$. Using $s = j\omega$, equations (3.23) and (3.24) can be modified to attain

$$H_1(j\omega) = \frac{X_1(j\omega)}{f_1(j\omega)} = \frac{-\omega^2 M + (K_\alpha + \Delta k)}{\omega^4 M^2 - \omega^2 M(2K_\alpha + \Delta k) + K_\alpha^2 + K_\alpha \Delta k - K_c^2} \tag{3.25}$$

$$H_2(j\omega) = \frac{X_2(j\omega)}{f_1(j\omega)} = \frac{K_c}{\omega^4 M^2 - \omega^2 M(2K_\alpha + \Delta k) + K_\alpha^2 + K_\alpha \Delta k - K_c^2} \tag{3.26}$$

A denominator of equations (3.25) and (3.26) is given by

$$\omega^4 M^2 - \omega^2 M(2K_\alpha + \Delta k) + K_\gamma = 0 \tag{3.27}$$

where, $K_\gamma = K_\alpha^2 + K_\alpha \Delta k - K_c^2$. Equation (3.27) is called as characteristic equation of this two DoF coupled system. Roots of equation (3.27) provide poles and zeros (resonance and anti-resonance frequencies respectively).

$$\omega_{ip}^2 \approx \frac{M(2K_\alpha + \Delta k) + \sqrt{4M^2(K_c^2 - K_\gamma) + M^2 + \Delta k^2}}{2M^2} \tag{3.28}$$

$$\omega_{op}^2 \approx \frac{M(2K_\alpha + \Delta k) - \sqrt{4M^2(K_c^2 - K_\gamma) + M^2 + \Delta k^2}}{2M^2} \tag{3.29}$$

where, ω_{ip}^2 and ω_{op}^2 are in-phase and out-of-phase natural mode frequencies of the device. With Δk = 0, equations (3.28) and (3.29) take the form $\omega_{ip}^2 = \frac{K}{M}$ and $\omega_{op}^2 = \frac{K + 2K_c}{M}$. Dividing equation (3.25) by equation (3.26), we obtain a ratio of amplitudes

$$\frac{H_1(j\omega)}{H_2(j\omega)} = \frac{-\omega^2 M + (K_\alpha + \Delta k)}{K_c} \tag{3.30}$$

We can refer equations (3.28) and (3.29) to obtain simplified expressions for the pole frequencies given as

$\omega_{ip}^2 \approx \frac{\Delta k + K_\alpha + \sqrt{K_\alpha^2 - K_\gamma}}{M}$; $\omega_{op}^2 \approx \frac{\Delta k + K_\alpha - \sqrt{K_\alpha^2 - K_\gamma}}{M}$. Substituting these values in place of ω in equation (3.30), we can obtain the expression for mode amplitude ratio as a function of stiffness perturbation, Δk as follows:

$$\frac{H_1(j\omega_{ip})}{H_2(j\omega_{ip})} = \frac{-\sqrt{K_\alpha^2 - K_\gamma}}{K_c}; \frac{H_1(j\omega_{op})}{H_2(j\omega_{op})} = \frac{\sqrt{K_\alpha^2 - K_\gamma}}{K_c} \tag{3.31}$$

With $\Delta k = 0$, equation (3.31) takes the form as

$$\frac{H_1(j\omega_{ip})}{H_2(j\omega_{ip})} = 1; \frac{H_1(j\omega_{op})}{H_2(j\omega_{op})} = -1 \tag{3.32}$$

thus representing initial balanced condition of a two coupled resonating devices.

3.3.2 A three DoF coupled mass-spring-damper system

Figure 3.7 shows a lumped parameter model of a three DoF mass-spring-damper system in the context of coupled resonators.

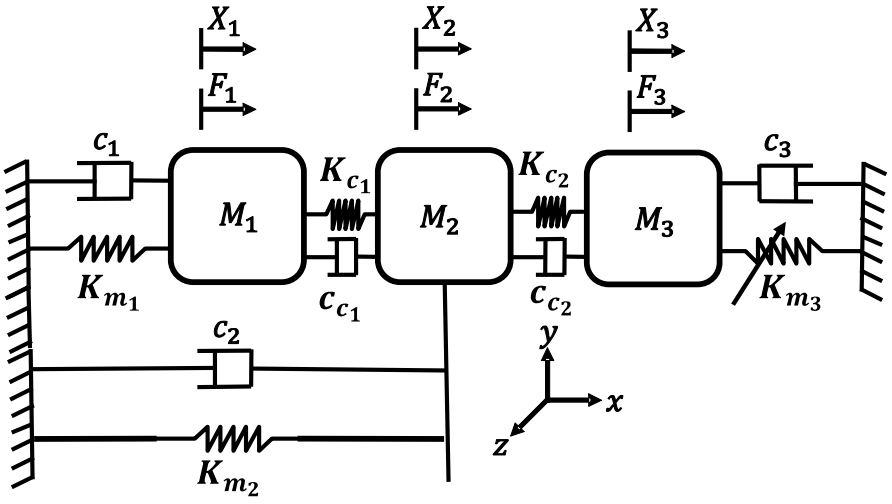

Figure 3.7 A lumped parameter model for a three DoF coupled resonators

It shows proof masses, M_i with individual mechanical spring constant, K_i and damping coefficients, c_i (i=1, 2, 3). Proof masses M_1 and M_2 are coupled through another spring, K_{c1} and proof masses M_2 and M_3 are coupled through another spring, K_{c2} as shown. A normalized displacement of the proof mass, X_{m_i} in response to the applied force, f is expressed as $X_{m_i} = \frac{x_i}{X_{0_i}}$; ($i$=1, 2, 3) where, X_{0_i} is the position of the proof mass at static equilibrium condition. Following assumptions hold true for a symmetric device: $M_1 = M_2 = M_3 = M$, $Km_1 = Km_2 = Km_3 = Km$, $c_1 = c_2 = c_3 = c$. Force vectors f_1, f_2 and f_3 acting on the proof masses are the harmonic excitation (drive) forces that cause displacements, x_1, x_2 and x_3, assumed to occur at one frequency. We assume that $Kc_1 = Kc_2 = Kc$, $c_{c_1} = c_{c_2} = c_c$. A set of governing motion of equation are given as follows:

When system experiences imbalance into the initial symmetry i.e. $\Delta k \neq 0$, governing equation of motion for the three-coupled proof masses as shown in Figure 3.7 is given as follows:

$$M\ddot{x}_1 + (c + c_c)\dot{x}_1 + (K_m + K_c)x_1 - c\dot{x}_2 - K_c x_2 = f_1(t) \tag{3.33}$$

$$M\ddot{x}_2 + (c + c_c)\dot{x}_2 + (K_m + 2K_c)x_2 - c\dot{x}_1 - K_c x_1 - K_c x_3 = f_2(t) \tag{3.34}$$

$$M\ddot{x}_3 + (c + c_c)\dot{x}_3 + (K_c + K_m + \Delta k)x_3 - c\dot{x}_2 - K_c x_2 = f_3(t) \tag{3.35}$$

By operating the device under vacuum, we can mitigate the impact of (a) damping force of individual proof mass and (b) damping force that occurs between proof masses, hence we can assume $c_1 = c_2 = c_3 = c_{c_1} = c_{c_2} = 0$. Therefore, equations (3.33) through (3.35) are modified as below:

$$M\ddot{x}_1 + (K_m + K_c)x_1 - K_c x_2 = f_1(t) \tag{3.36}$$

$$M\ddot{x}_2 + (K_m + 2K_c)x_2 - K_c x_1 - K_c x_3 = f_2(t) \tag{3.37}$$

$$M\ddot{x}_3 + (K_c + K_m + \Delta k)x_3 - K_c x_2 = f_3(t) \tag{3.38}$$

By applying a Laplace transform identities, an expression for the output transfer function can be derived similar to as derived in section 3.3.1 for two DoF mass-spring-damper system. More on a model based on three coupled resonators can be found in [7,37].

3.4 COMSOL design (A finite element model)

In this section we analyzed a mode shape and resonant frequencies of our design using COMSOL Multiphysics [94] Figure 3.8 shows a COMSOL mode shape simulation for a designed geometry of a weakly coupled resonator. A small mechanical beam placed between the two resonating elements emulates an electrostatic coupling, as this is difficult to include in the COMSOL model. The two simulated mode frequencies are 2483.9 *Hz* and 2490.9 *Hz* for mode 1 (in-phase) and mode 2 (out-of-phase), respectively. Due to negative effective value of a coupling spring, K_c however, mode 2 (out-of-phase) precedes mode 1 at 2476 *Hz* as our theory calculations suggest.

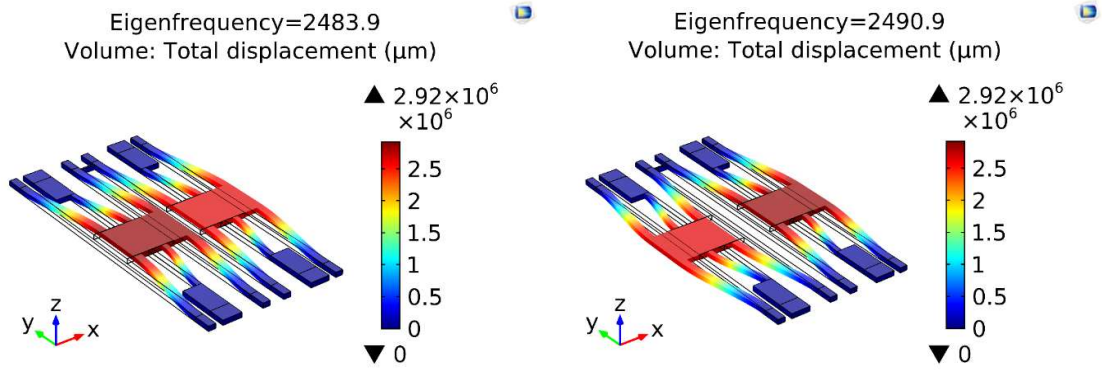

(a) (b)

Figure 3.8 A COMSOL mode shape simulation for a structure**,** (a) mode 1 (in-phase mode) and (b) mode 2 (out-of-phase mode). These two distinct modes are separated by a distance of approximately 7 *Hz*. An individual resonating element is coupled to its neighbour by a mechanical beam thus emulating an electrical coupling spring in the actual fabricated prototype

3.5 Performance parameters

For a 2-DoF weakly coupled resonator sensor, relative changes for amplitude ratio, eigenstate and resonant frequency are expressed as $\left(\frac{x1}{x2}\right)_{ji} = \left|\frac{r_n - r_0}{r_0}\right| \approx \left|\frac{\Delta k}{2K_c}\right|$, $(x)_{ji} = \frac{|a_n - a_0|}{|a_0|} \approx \left|\frac{\Delta k}{4K_c}\right|$ and $(f_i) = \frac{|f_n - f_0|}{|f_0|} \approx \left|\frac{\Delta k}{2K_{eff}}\right|$, respectively for j^{th} resonator (j=1, 2) at i^{th} mode of the frequency

response. (i=1, 2) [17,21,22,49,98]. An effective stiffness of the electrostatic coupling spring between the two resonators is $K_c = -(\Delta v^2)\frac{\varepsilon_0 A}{g^3}$, where Δv refers the potential difference applied between the two masses. Sensitivity expressions for all the relevant output metric can be expressed as:

$S_{R_i} = \frac{\partial\left(\frac{r_n - r_0}{r_0}\right)}{\partial(\delta_k)}, S_{a_{ji}} = \frac{\partial\left(\frac{a_n - a_0}{a_0}\right)}{\partial(\delta_k)}, S_{f_i} = \frac{\partial\left(\frac{f_n - f_0}{f_0}\right)}{\partial(\delta_k)}$, where, S_{R_i}, $S_{a_{ji}}$ and S_{f_i} denote the *theoretical maximum sensitivity* for amplitude ratio, amplitude and frequency for j^{th} resonator (j=1, 2) at i^{th} mode of the frequency response (i=1, 2), respectively. Based on our design values, we found $S_{R_i} > S_{a_i} \gg S_{f_i}$.

Table 3.3 shows calculated values of the design and performance parameters for two DoF weakly coupled resonators.

As can be seen from Table 3.3, an intrinsic higher value of mechanical spring constant of a device contributes to further enhancing sensitivity to vibrational mode amplitude variations for a given coupling spring constant whereas sensitivity to resonant frequency variation is lowered. In our device, mechanical spring constant is designed to be in the order of 1.247×10^5 *N/m*. While higher mechanical spring constant of the design yield an enhanced mode amplitude sensitivity to external quantity to be measured, one has to be careful in the design that lower value of mechanical spring is desirable not only for an electrostatic actuation but also to reliably sense the motion of a device. Hence, there is a trade-off between value of effective mechanical spring constant and attaining mode amplitude based sensitivity of the device. As one of the operating case, in the simulation (refer to following chapter 4 on simulations), we excited both the proof

Table 3.3 Calculations for performance parameters (*h* represents device thickness)

Parameters	**Theoretical estimate**	
	h=1 mm	*h=2 mm*
Amplitude ratio sensitivity, $S_{R_i} \approx \left\|\frac{K_{eff}}{2K_c}\right\|$	135*	
Amplitude sensitivity, $S_{a_i} \approx \left\|\frac{K_{eff}}{4K_c}\right\|$	23.73*	
Frequency sensitivity, S_{f_i}	0.284*	
Coupling ratio, κ (*normalized*)	-0.0032	
Effective coupling stiffness, K_c (*N/m*)	-393.51	-787.02
Effective mass, *m* (*g*)	5.13×10^{-4}	1×10^{-3}
Effective mechanical stiffness, K_{eff} (*N/m*)	1.247×10^5	2.495×10^5

Natural frequencies of a coupled system, mode 1/mode 2, f_i (*Hz*) (*i=1,2*) (when $\delta_k = 0$)	2483/2476

* Calculation for a finite value of a quality factor $Q \approx 2547$.

masses in the out-of-phase mode. We found that it was difficult to resolve in simulation very small variations (0.0001 *Hz* in theory) into the resonant mode frequency subject to applied perturbations, Δk. It is only after a larger Δk is applied, we could see a slight variation (0.005 *Hz*) in the frequency output of a system. While, this could be a disadvantage towards a sensor using single resonator. However, designing the inherently larger mechanical stiffness of coupled resonating sensor benefit in conveniently resolving variations into the mode amplitudes subject to even relatively smaller values of stiffness perturbations, Δk. Sensitivity to mode amplitude variations is found to be orders of magnitude higher to sensitivity to frequency variations (refer chapter on simulations and experiments).

3.5.1 Mode frequencies as a function of a perturbation

For a two DoF coupled resonator sensor, a characteristic equation given in equation (3.27) in section 3.3.1 can be referred. By putting ω^2=r, and setting Δk=0, equation (3.27) takes the form as follows

$$r^2M^2 - 2MK_\alpha r + K_\alpha^2 - K_c^2 = 0 \tag{3.39}$$

Two roots of this characteristic equation are the natural eigenfrequenies and can be derived as follows

$$\begin{aligned} r_{1,2} &= \frac{2MK_\alpha \pm \sqrt{4M^2K_\alpha^2 - 4M^2\left(K_\alpha^2 - K_c^2\right)}}{2M^2} \\ &= \frac{2MK_\alpha \pm \sqrt{4M^2\left[K_\alpha^2 - \left(K_\alpha^2 - K_c^2\right)\right]}}{2M^2} \\ &= \frac{2MK_\alpha \pm 2M\left[K_\alpha - \left(K_\alpha - K_c\right)\right]}{2M^2} \end{aligned} \tag{3.40}$$

Therefore, we may write

$$\begin{aligned} r_1 = \omega_{ip}^2 &= \frac{2MK_\alpha + 2M\left[-K_c\right]}{2M^2} \\ &= \frac{K}{M}\left(\because K_\alpha = K + K_c\right) \end{aligned} \tag{3.41}$$

$$\begin{aligned} r_1 = \omega_{op}^2 &= \frac{2MK_\alpha - 2M\left[-K_c\right]}{2M^2} \\ &= \frac{K + 2K_c}{M}\left(\because K_\alpha = K + K_c\right) \end{aligned} \tag{3.42}$$

Equation (3.41) is called the first mode (in-phase) and equation (3.42) is called the second mode (out-of-phase). Note that due to negative effective value of K_c, mode 2 precedes mode 1 in the frequency response.

Figure 3.9 shows how eigenvalues veer away as a function of stiffness perturbation for varying values of coupling spring, K_c. A veering zone narrows for a smallest value of a coupling spring. Figure 3.10 depicts variations in the mode frequencies as a function of applied stiffness perturbations. It also shows how mode frequency difference can be attained for a specific value of stiffness perturbation. This is particularly useful when there is a mode merging either due to lack of adequate quality factor and/or coupled resonator sensor is designed with a significant weaker coupling spring for the sake of increasing the parametric sensitivity. It has also been shown that a separate bias voltage can be applied which may cause an adequate mode-separation in the frequency response [18,23]. Figure 3.11 shows how amplitude ratio output for both the modes varies as a function of applied perturbations into the stiffness.

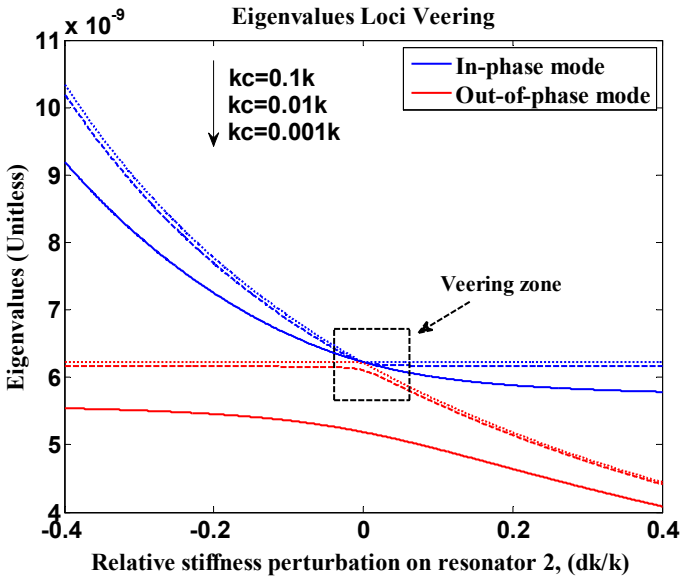

Figure 3.9 Eigenvalue loci veering

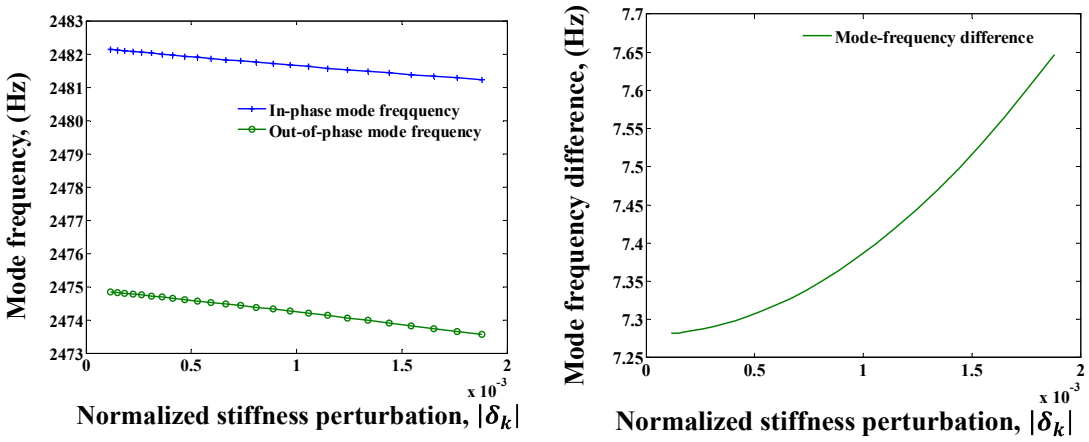

(a) (b)

Figure 3.10 (a) Mode-frequency variations as a function of stiffness perturbations. (b) Mode-frequency difference as a function of stiffness perturbations

Figure 3.12 shows variations in the different form of an output for coupled resonators. It is to be noted that these plots are presented for a condition where it is assumed that no damping

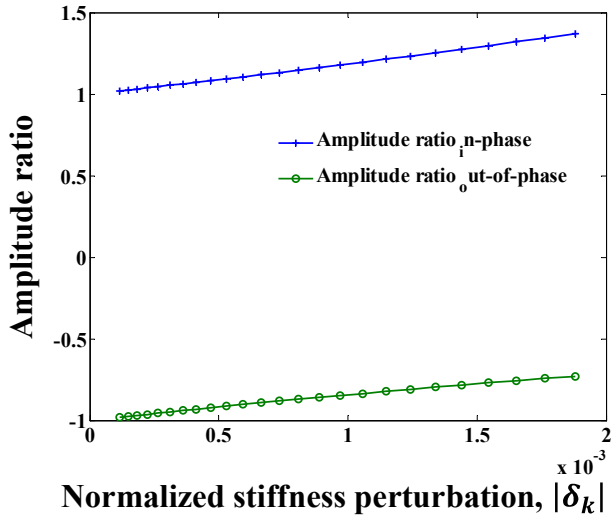

Figure 3.11 Variation in the amplitude ratio output as a function of stiffness perturbations

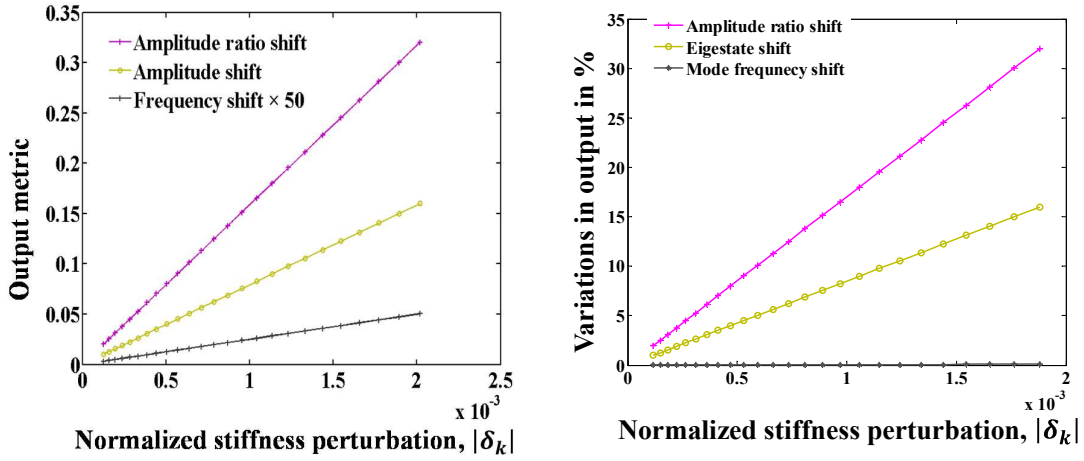

(a) (b)

Figure 3.12 Comparative output performance as a function of stiffness perturbations (a) absolute values (b) in percentage. A comparative performance for all the outputs for damping coefficient (in *Ns/m*) $c = 0 (Q \to \infty); \Delta k \neq 0$

source exist into the system. Therefore, the shifts into the different outputs are likely to deteriorate for a finite value of a quality factor, Q as a case in the practical system. In addition, it can be noted that amplitude ratio based shifts are higher than any other output shifts. Using an amplitude ratio based shifts are advantageous due to the common mode rejection capability. More on this is reported into the following chapter 4 on simulation where, we have presented models for a finite value of Q.

3.5.2 Structural damping in coupled resonators

In weakly coupled resonators, damping plays an important role. In our theoretical model, we investigate the impact of a damping on the behaviour of coupled resonators and its output response as a sensor.

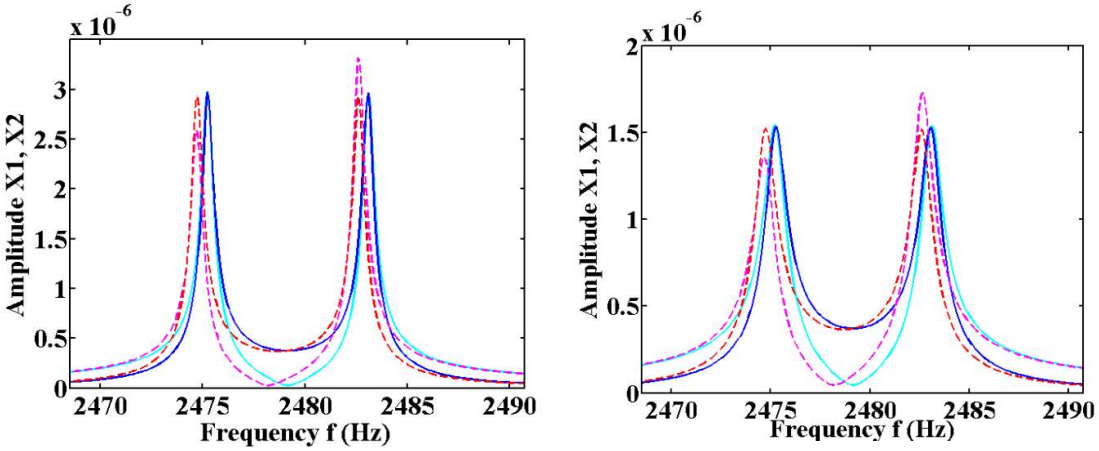

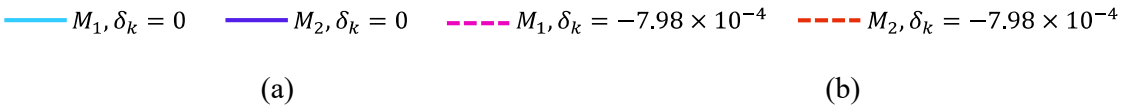

Figure 3.13 Output response of our weakly coupled resonators under practical operating conditions with (a) damping coefficient, *c* set to 0.0016 *Ns/m* (Q ≈ 5000) and (b) for damping coefficient, *c* set to 0.0031 *Ns/m* (Q ≈ 2547). M_1 and M_2 denote proof mass 1 and 2 respectively, while δ_k is applied stiffness perturbations (normalized)

Figure 3.13 shows an output response of the two weakly coupled resonators as a function of damping and a stiffness perturbation. (a) Damping coefficient, *c* set to 0.0016 *Ns/m* ($Q \approx 5000$) and (b) damping coefficient, *c* set to 0.0031 *Ns/m* ($Q \approx 2547$). Note that these same values of damping coefficients are used in the Simulink model we have developed, and is presented in the following chapter 4 on simulation.

In the frequency response, in order to avoid a mode-overlap [54], following condition is to be satisfied: $|f_1 - f_2| \geq 2 \times f_{BW_{3dB}}$ where, $|f_1 - f_2|$ is the minimum frequency difference and $f_{BW_{3dB}}$ is the maximum 3_{dB} bandwidth of i^{th} mode (i=1, 2). In our design, to resolve a mode frequency difference, $f_{BW_{3dB}} \leq 3.546$ Hz is required. In other words, for this design, we estimate that minimum required quality factor, $Q_{i\min} \geq 698$ $\left(Q_{i\min} = \frac{f_i}{f_{BW_{3dB}\max}} \right)$ would be required if two distinct modes are to be observed. Figure 3.14 illustrates the theoretical model behaviour for a two DoF weakly coupled resonators with damping coefficient *c* >0.0114 *Ns/m* ($Q < 698$) also depicting mode-overlap. As seen in the Figure 3.14, with decrease in damping (increase in quality factor), two distinct modes can effectively be resolved. Other studies have demonstrated an operation of a coupled resonating sensors operating even at atmospheric pressure [70], with the measured quality factor as low as 5 [58,59]. In summary, for our design we establish this condition of operation as follows: $Q \geq Q_{i\_mismatch} > Q_{imin}$. Here, $Q_{i\_mismatch}$ (≈ 2547) is the quality factor at which we make sure j^{th} (j = 1, 2) resonator vibrates at the same frequency at the i^{th} (i = 1, 2) mode of the frequency response. Q_{imin} is the minimum quality factor to make sure two modes can effectively be resolved in the frequency response for a fixed coupling factor.

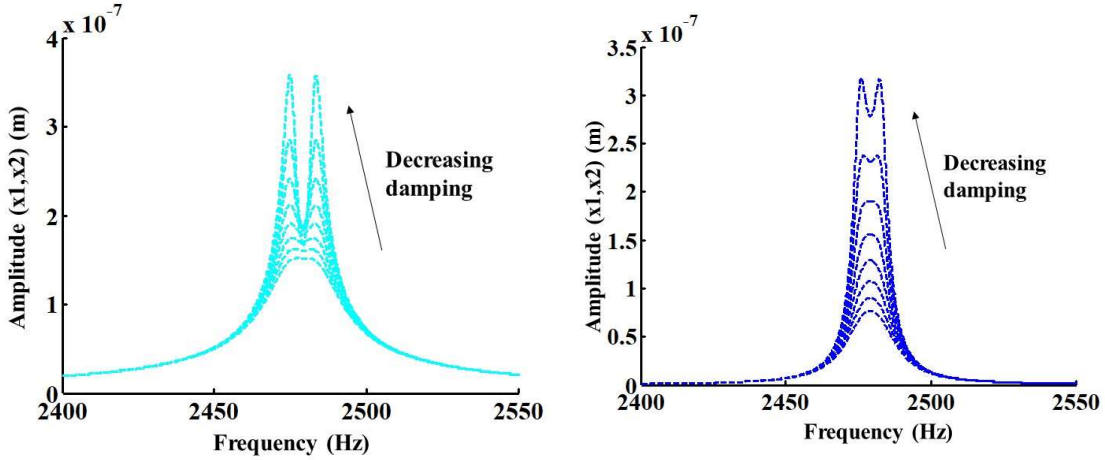

(a) (b)

Figure 3.14 Theory model for our two DoF weakly coupled resonating sensor illustrating an impact of a damping for (a) resonator 1 and (b) resonator 2. With higher damping (lower quality factor), two distinct modes overlap.

3.6 Dynamic response of our design

In this section, we propose a theory to analyze a dynamic response of our design for two coupled resonators. We refer back Figure 3.1 (a) for this analysis. With the applied bias voltages as shown in Figure 3.1 (a), we recall that a net change in capacitance per unit displacement is $\frac{\partial C}{\partial x} = \frac{\varepsilon A}{(d-x)^2} \approx \frac{\varepsilon A}{d^2} (\because x \ll d)$, K_m is the mechanical stiffness of the resonator and K_e is the resulting electrical spring stiffness due to the applied DC voltage for polarization and it is given as $K_e \approx -\frac{\varepsilon_0 A}{g^3}(V_{dc}^2)$. An effective spring stiffness is given as $K_{eff} = K_m + K_e$. For a static case, i.e. an effective stiffness perturbation, Δk is not a function of time and can be calculated as

$$\begin{aligned} \Delta k &\approx -\frac{\varepsilon_0 A}{g^3} V^2 \\ &\approx -\frac{\varepsilon_0 A}{g^3}(V_{dc} - V_p)^2 \end{aligned} \tag{3.43}$$

where, V_p is the DC voltage applied on electrode 2 (refer Figure 3.1 (a)) to alter the stiffness of the resonator 2. When $V_p = V_{dc}$, $\Delta k = 0$. We can apply a dynamic or time-varying perturbation (sinusoidal signal) on electrode 2 to time-modulate the stiffness of a resonator 2. Note that a net electrostatic force in this case remains the same given as $F_e \approx \frac{\varepsilon A}{g^3}(V_{ac} + V_{dc})^2$. Here, Δk is now a function of time and we can write $\Delta k(t) \approx -\frac{\varepsilon_0 A}{g^3}(V^2)$,

where V is a potential difference between a DC polarization voltage V_{dc} (applied on proof mass M_2) and an externally applied time-varying signal applied on electrode 2. We can write this time-varying signal as $V_{per}\sin\omega_{per}t$ (V_p is the amplitude of an applied time-varying signal and ω_p is the angular frequency (rad/sec) of this signal). Here, we note that $\omega_p \ll \omega_d$, where ω_p is the angular frequency (in rad/sec) of externally applied time-varying signal as a perturbation and ω_d is the angular frequency (in rad/sec) of applied net time-varying electrostatic driving force.

To simplify, we can write

$$\begin{aligned}\Delta k(t) &\approx -\frac{\varepsilon_0 A}{g^3}V^2 \\ &\approx -\frac{\varepsilon_0 A}{g^3}(V_{dc}-V_p\sin\omega_p t)^2 \\ &\approx -\frac{\varepsilon_0 A}{g^3}(V_{dc}^2+V_p^2\sin^2\omega_p t-2V_{dc}V_p\sin\omega_p t)\end{aligned} \tag{3.44}$$

We note from (3.44) that Δk we have components of this stiffness perturbation at three frequencies: a Δk at DC, Δk at the ω_p due to the term $2V_{dc}V_p\sin\omega_p t$ and Δk at twice ω_p due to square term $V_p^2\sin^2\omega_p t$. A Δk at the ω_p can be written as

$$\Delta k(t) \approx \frac{\varepsilon_0 A}{g^3}(2V_{dc}V_p\sin\omega_p t) \tag{3.45}$$

From (3.45), we note that $\Delta k\ (t)$ is a function of amplitude V_p of applied low frequency signal and its frequency, ω_p.

Therefore, with K_m being the mechanical stiffness of the resonator 2 and $\Delta k(t)$ being the electrical spring stiffness, effective stiffness can be evaluated as follows:

$$\begin{aligned}K_{eff}(t) &= K_m + K_e + \Delta k(t) \\ &= K_m - \frac{\varepsilon_0 A}{g^3}V_{dc}^2 - \frac{\varepsilon_0 A}{g^3}(V_{dc}^2+V_p^2\sin^2\omega_p t-2V_{dc}V_p\sin\omega_p t) \\ &= K_m - \frac{\varepsilon_0 A}{g^3}\left[V_{dc}^2+(V_{dc}^2+V_p^2\sin^2\omega_p t-2V_{dc}V_p\sin\omega_p t)\right] \\ &= K_m - \frac{\varepsilon_0 A}{g^3}(2V_{dc}^2+V_p^2\sin^2\omega_p t-2V_{dc}V_p\sin\omega_p t)\end{aligned} \tag{3.46}$$

K_{eff} @ ω_p is

$$K_{eff}(t) = K_m + \frac{\varepsilon_0 A}{g^3}(2V_{dc}V_p\sin\omega_p t) \tag{3.47}$$

Equation (3.47) infers how spring constant is time modulated by an applied sine wave of magnitude Vp and frequency ω_p. At the same time, effective spring force as a function of

time is given as $F_s(t) = K_{eff}(t)x(t)$. With this derived expressions we can analyze a dynamic response of our macro-scale coupled resonator system.

Summary

In this chapter, we presented a systematic design approach of our macro-scale two weakly, electrically coupled resonators for stiffness sensing applications. A state-of-the-art in our case is fabricating coupled resonators using laser micromachining. Details of fabrication is discussed in chapter 5. We found a trade-off amongst design/performance parameters such as spring constant (sensitivity), resonant frequencies, motional current and device size. An optimized design solution was then proposed based on this trade-off. We derived a theoretical transfer function model for our two coupled resonator system to monitor mode-frequencies and amplitude ratio as function of stiffness perturbations. For our scaled-up structure, we determined the maximum theoretical device sensitivity. Amplitude ratio based sensitivity is 135, which is comparable to that attained using a MEMS two DoF coupled resonators. We also have introduced a theory to analyse the coupled resonator's response to the low frequency signal applied to time modulate a stiffness of one of the resonators.

Chapter 4

4 System level models and simulation

In this chapter, we propose and develop system level models using SIMULINK, to analyse our multi-domain dynamical systems consisting two scaled-up coupled resonators. Our proposed models are for variety of operating conditions, such as finite quality factor, varying coupled electrostatic spring strength, operation with in-phase and out-of-phase mode, open loop and closed loop operation. We determined the sensitivity of our proposed design (in both open/closed loop circuit) for stiffness sensing application Moreover, we also have theoretically estimated the impact of fundamental noise processes into our system that govern the ultimate resolution of the device for various sensing applications.

4.1 A Simulink model

Figure 4.1 depicts a system level model for our two weakly and electrically coupled mass-spring-damper system.

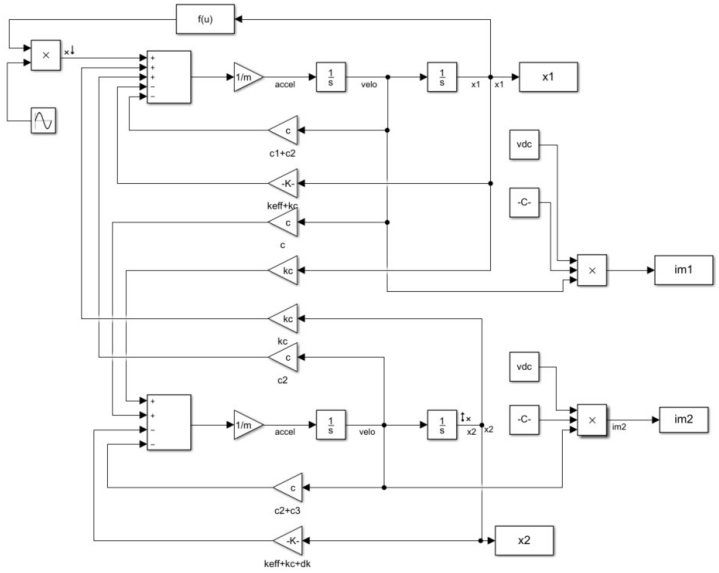

Figure 4.1 A system level model (using SIMULINK) for a two coupled resonators to evaluate its performance as a sensor

Table 4.1 shows parameters for a model under investigation. A values of the parameters used in this model are obtained through calculation as given in Table 3.1 and Table 3.2 in chapter 3.

During simulation, we operate the coupled system in the linear mode, (*i.e.* $x_{ji} << d$). Here, x_{ji} is the vibrational displacement amplitudes of j^{th} resonator (j = 1, 2) at the i^{th} (i = 1, 2) mode of

frequency response, and, d is the nominal capacitive air gap. A steady-state time response for a coupled resonator is then analysed for applied stiffness perturbations, δ_k.

As such, we have built two system level Simulink models. One is the open loop (being discussed here) and other is the closed-loop (discussed in section 4.10). In both these models, a coupling spring constant, K_c = -393.51 *N/m* (or a coupling factor, $\kappa = 3.2\times10^{-3}$ (dimensionless)) is established with proper DC polarization voltages. A disorder into the system, Δk is separately

Table 4.1 A system-level model parameters

System parameters	Value	Unit	Description
m	5.5×10^{-4}	g	Proof mass of each resonating element
$k_{eff1}=k_{eff2}=k_{eff}$	1.339×10^{5}	N/m	Mechanical spring constant of proof mass 1 and 2
K_c	-393.5	N/m	Electrostatic spring between the two resonators
κ	0.0032	*(unitless)*	Effective coupling factor
c_{max}	0.0031	Ns/m	Damping coefficient limit for our coupled resonators design. ($Q \approx 2547$)
v_{ac}	5	V	AC drive voltage provided by the signal generator in open/closed-loop configuration
$\lvert V_{dc}\rvert$	200	V	DC voltage used to polarize a macro-size capacitors and to also establish a coupling between the resonators
ε	8.854×10^{-12}	$f\cdot m^{-1}$	Permittivity of free space
gap	60	μm	Capacitive air gap of transduction
Parameters for a closed-loop configuration (using Phase-locked-loop, (PLL)) for our design			
F_{vco} $(\omega_r/(2\times\pi))$	*2482/2474*	Hz	Quiescent/free running frequency of voltage-controlled oscillator (VCO) in PLL*
K_{vco}	1	Hz/v	Input sensitivity of a VCO
v_{ac}	5	V	AC drive voltage provided by VCO of phase-locked loop (PLL) system for auto-tracking output metric

* *In-phase/out-of-phase*

introduced to alter the effective stiffness (thus causing stiffness imbalance in the system) of one of the resonator (resonator 2 in our case). A stiffness perturbation, Δk in our design is chosen such that $|\Delta k| < |K_c| < |K_{eff}|$. We recall from the previous chapter 3 that the initial resonant frequencies ($\Delta k = 0$ *N/m*) of the weakly coupled system using pair of two resonators (2 DoF) are given as follows [17,99]:

$\omega_1 = \sqrt{\frac{k}{m}}$ and $\omega_2 = \sqrt{\frac{k+2k_c}{m}}$, where, ω_1 is the in-phase mode frequency and ω_2 is the out-of-phase mode frequency. As noted from the above equations, out-of-phase mode occurs first (as verified and shown in section 4.3) due to the negative effective value of a spring coupling the two resonators. It is to be noted that for our design, the value of a spring constant coupling the two masses *i.e.* K_c is much smaller (referring Table 4.1) than the individual effective spring constant, k_{eff} of any of the two resonators.

4.2 Operating conditions in our design

In this section, we present a frequency and time characterization of our design. In the frequency domain, we applied the Fourier transform to obtain power spectrum of our time-domain output signals. We simulate the model shown in Figure 4.1 and obtain graphs for various operating conditions as explained below:

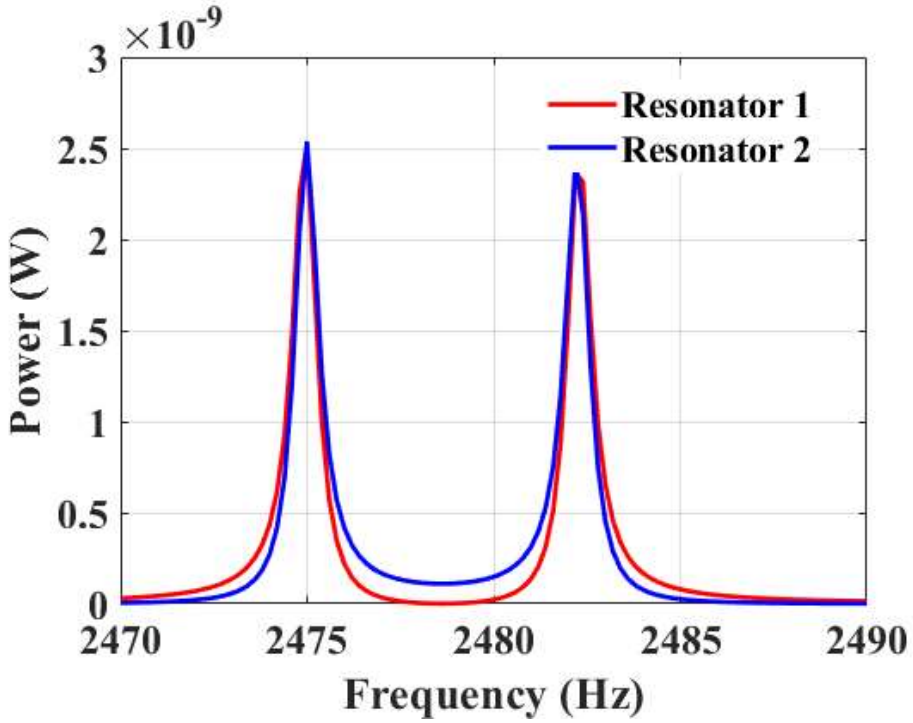

Figure 4.2 Simulated power spectrum of our design across the frequency range of interest. Two resonant peaks are seen to be separated by about 7 *Hz*. Operating conditions are $c = 0$ *Ns/m*, ($Q \rightarrow \infty$), $\Delta k = 0$, $\kappa = -0.0032$, unit force, F=1 *N* exerted on proof mass M_1

Figure 4.2 shows a simulated spectrum of our design across a range of frequencies of interest. As we predicted in theory in chapter 3, two resonant modes are seen to be separated by ≈ 7 *Hz* for a fixed value of a coupling spring, K_c established between the two resonators, (when $\Delta k = 0$ *N/m*). Simulation conditions are as reported in section 4 below:

4.2.1 Case I

$c = 0$ *Ns/m*, ($Q \rightarrow \infty$), $\Delta k = 0$, $\kappa = -0.0032$, net electrostatic driving force applied to proof mass M_1.

Figure 4.3 shows time-plot of a net excitation force that is applied onto one of the resonators in our design. A magnitude of this force is kept constant during all the operating condition. A value of this force is set as per $F_e \approx \frac{\varepsilon A}{d^2} V^2$ as given in Table 3.2 in Chapter 3. We applied the same magnitude of this force (as shown in Figure 4.3) during all the operating conditions in time characterization of our model.

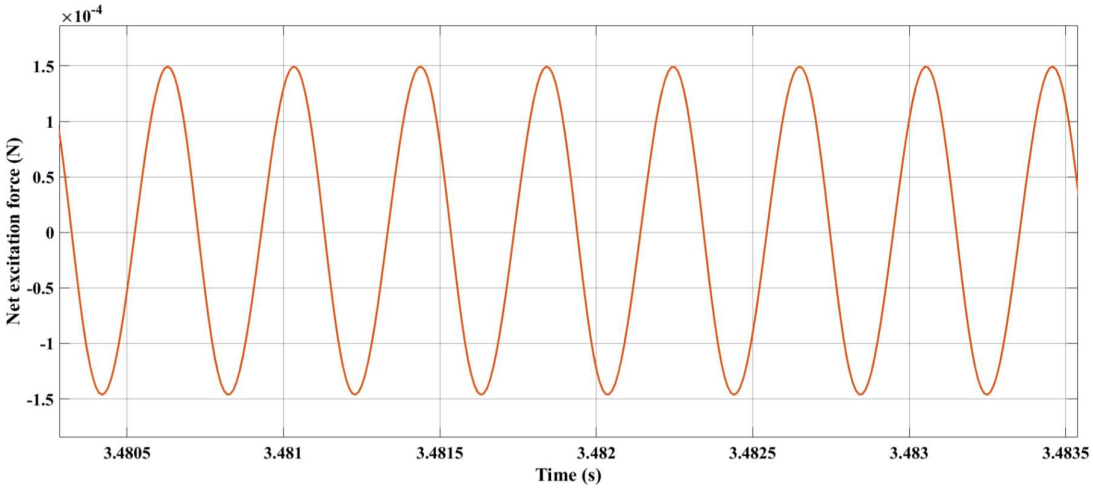

Figure 4.3 Steady-state time-response for a net applied electrostatic force at the *out-of-phase* excitation frequency, ω_{op}, 2474 *Hz*. A maximum value of this force is simulated to be ≈ 149 μN. (peak-to-peak is 295 μN)

Figure 4.4 shows a time plot for an out-of-phase and in-phase mode displacement outputs of our two electrically coupled resonators. A maximum value of the displacement can be given as x_{ji} for the j^{th} (j =1, 2) resonator at the i^{th} (i = 1, 2) mode of frequency response. Therefore, we can write the simulated values as follows: $x_{11} = 1.788\ \mu m$, $x_{21} = 1.756\ \mu m$, $x_{12} = 1.74\ \mu m$ and $x_{22} = 1.756\ \mu m$. Here, for the case when $c = 0$ *Ns/m* ($Q \rightarrow \infty$), we note that $x_{11} \approx x_{21}$, and $x_{12} \approx x_{22}$. We also note that displacement amplitude of j^{th} resonator at the i^{th} mode of response are

approximately equal, i.e. $x_{j1} = x_{j2}$ (j = 1, 2). We have also verified such behaviour of two coupled resonators shown in Figure 4.2.

Figure 4.5 shows a corresponding time plots for a motional currents when the system is excited at the out-of-phase and in-phase mode frequency. A maximum value of the motional current can be given as $i_{mot_{ji}}$ for the j^{th} (j =1, 2) resonator at the i^{th} (i = 1, 2) mode of frequency. Therefore, we can write the simulated values as follows: $i_{mot11} = 820\ nA$, $i_{mot\ 21} = 800\ nA$, $i_{mot\ 12} = 800\ nA$ and $i_{mot\ 22} = 806\ nA$. Here, for the case when $c = 0\ Ns/m$ ($Q \rightarrow \infty$), we note that $i_{mot11} \approx$

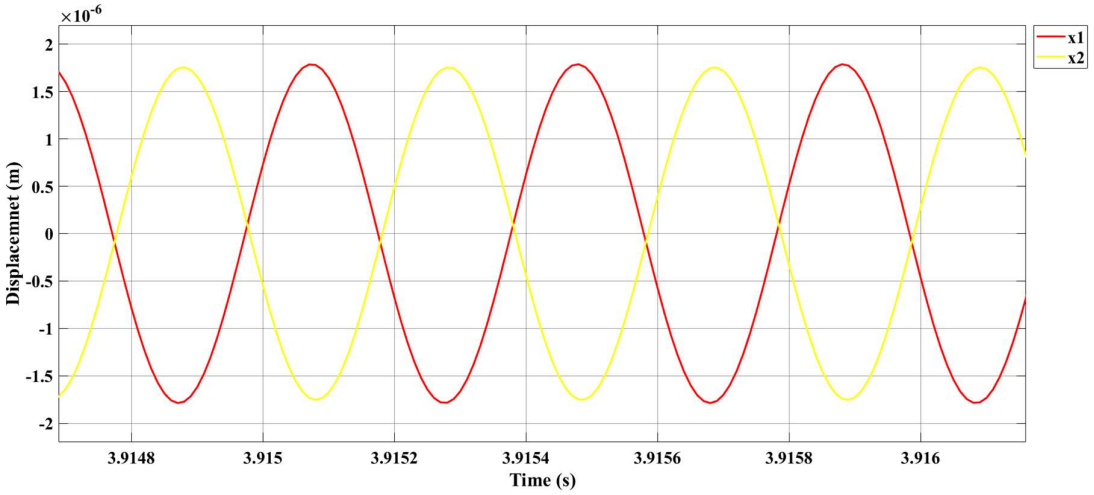

(a)

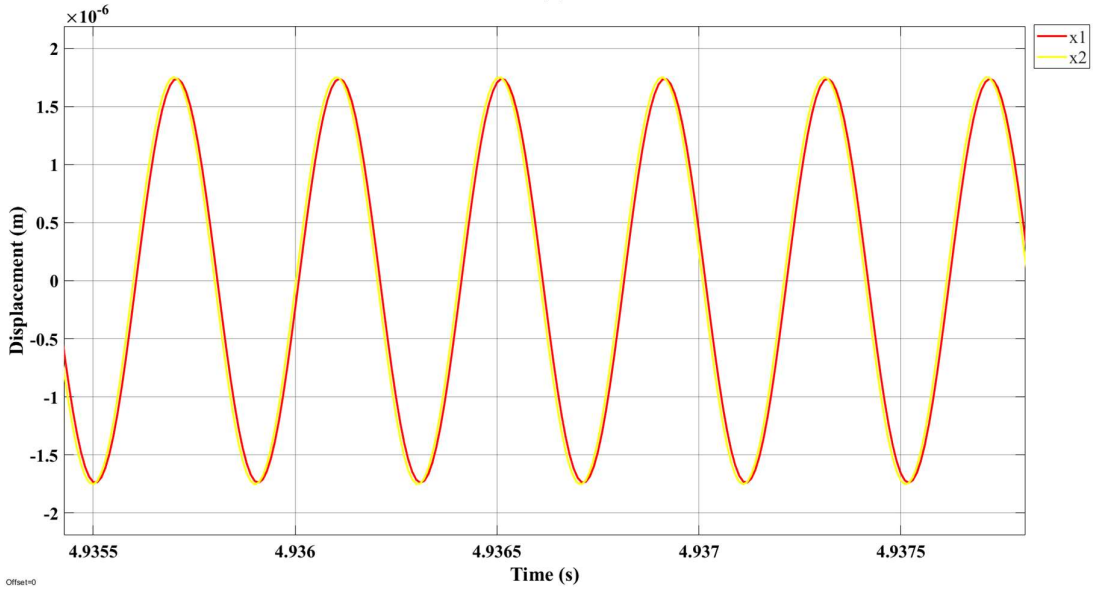

(b)

Figure 4.4 Steady-state time-response for displacement x_1 and x_2 from mass M_1 and M_2 respectively, (a) at the out-of-phase excitation frequency, ω_{op}, 2474 *Hz*. (b) at the in-phase excitation frequency, ω_{ip}, 2482 *Hz*.

i_{mot21}, and $i_{mot12} \approx i_{mot22}$. We also note that motional current of j^{th} resonator at the i^{th} mode of response are of same order of magnitude, i.e. $i_{motj1} = i_{motj2}$ (j = 1, 2).

Figure 4.6 shows a time plot demonstrating a **mode-localization effect** for the output displacement amplitudes x_{ji} for the j^{th} (j =1, 2) resonator at the i^{th} (i = 1, 2) mode of frequency response. A maximum stiffness perturbation that we applied is Δk_{max} = -251.8 *N/m*, or δ_{kmax} = -0.0019 (*normalized*). Note that excitation frequency is a function of Δk. It was assumed that it is an undamped system *i.e.* damping coefficient, c = 0 *Ns/m, (Q→∞).* As can be noticed from Figure 4.6, there is an amplitude change of a j^{th} resonator at the i^{th} mode of response.

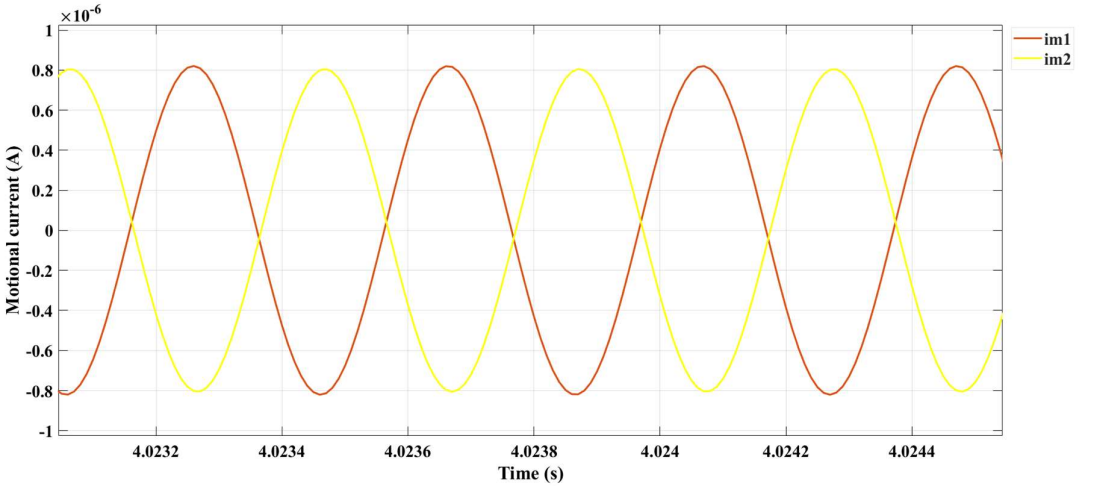

(a)

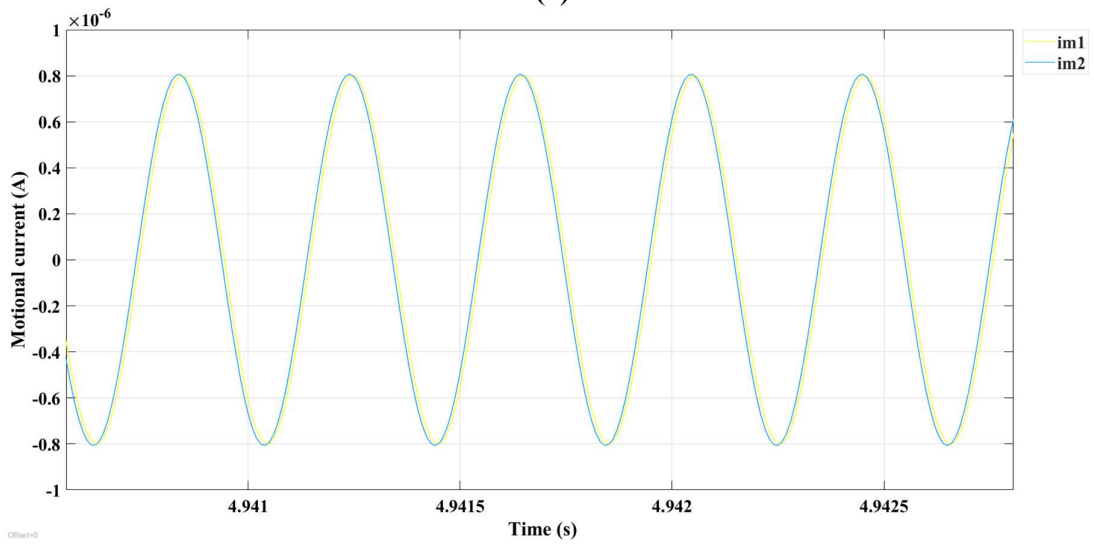

(b)

Figure 4.5 Steady-state time-response for motional current *im1* and *im2* from mass *M1* and *M2* respectively, (a) at the *out-of-phase* excitation frequency, ω_{op}, 2474 *Hz* (b) at the *in-phase* excitation frequency, ω_{op}, 2482 *Hz*.

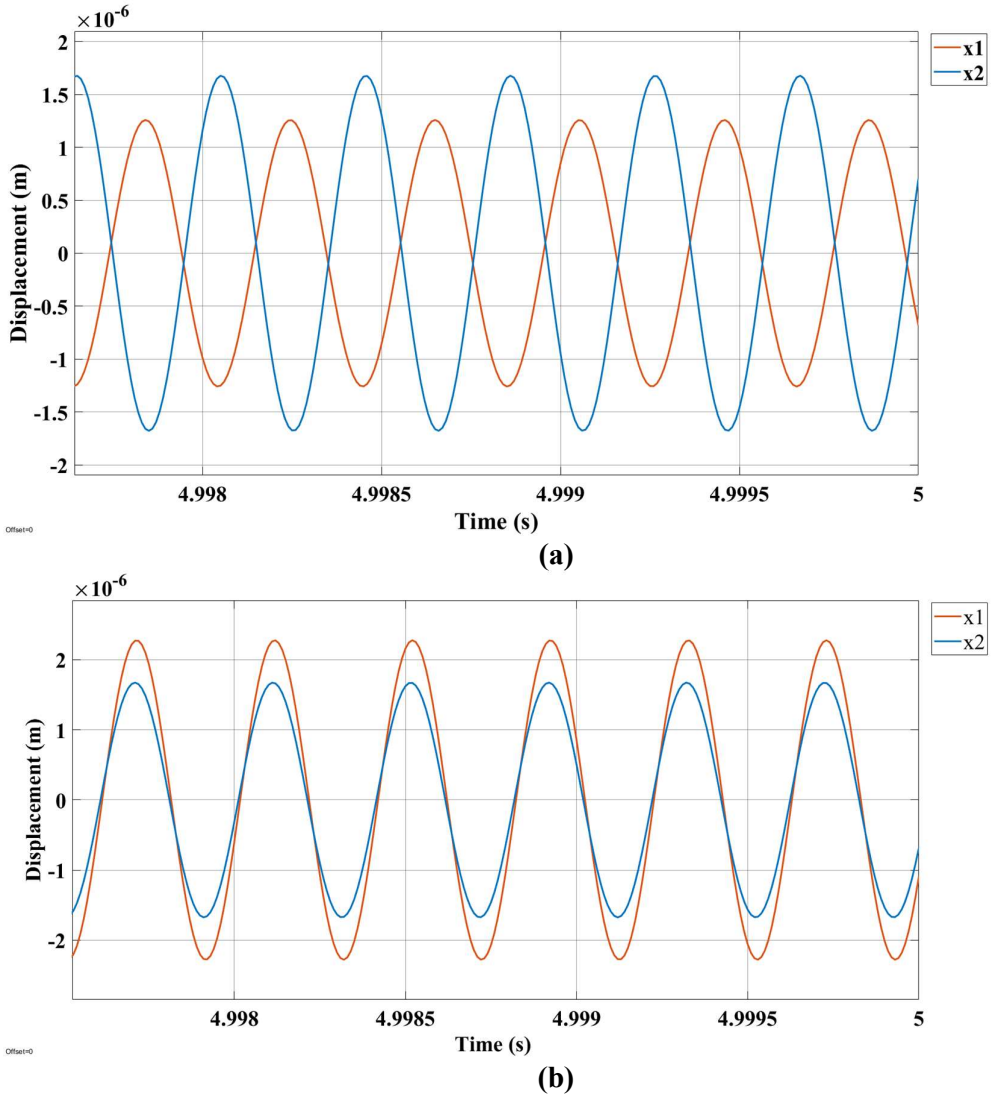

Figure 4.6 A mode-localization effect in our macro-scale coupled resonators (a) out-of-phase and (b) in-phase mode. x_1 and x_2 are amplitude of displacement for resonator 1 and 2 respectively.

Following this analysis, we applied a range of stiffness perturbations to modulate the effective stiffness of resonator 2 in our model. We then recorded the relative shifts in to the amplitude ratio, and mode frequencies as shown in Figure 4.7. From this graph, a maximum amplitude ratio sensitivity to stiffness perturbation is about 159 when our system is driven in out-of-phase mode.

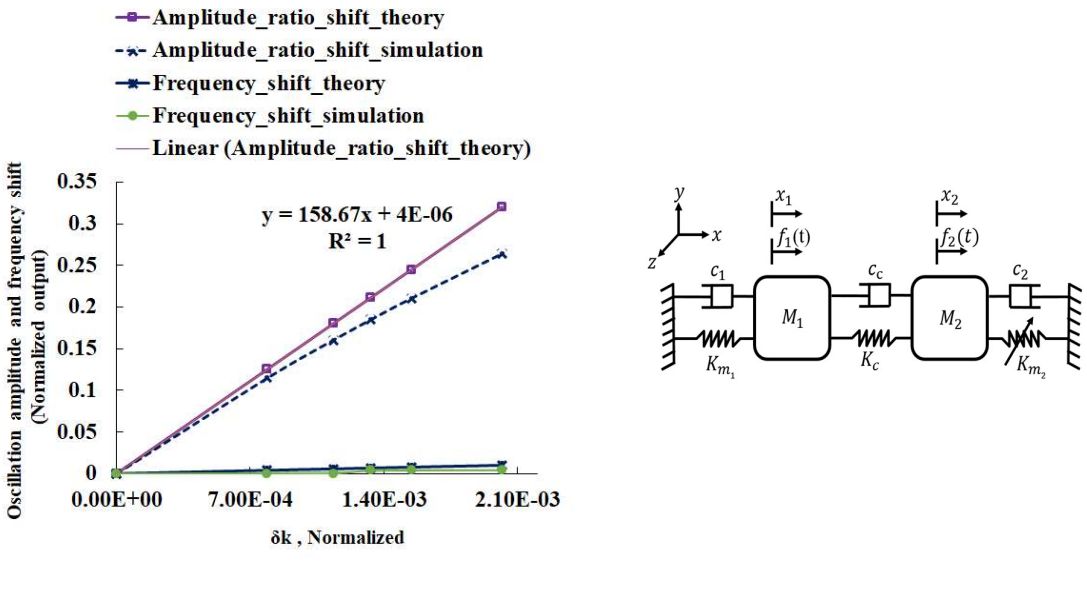

(a) (b)

Figure 4.7 (a) Output metric for our design of two DoF coupled resonators for the following operating condition: damping coefficient, $c = 0$ *Ns/m*; A proof mass M_1 is driven at out-of-phase frequency, ω_{op} which is a function of Δk, (b) representative equivalent model

In the lumped element model as shown in Figure 4.7 (b), we can set $c_1 = c_2 = c_c = 0$, however, in a practical resonant system, there exist several other forces, which may damp the oscillating behaviour of a system [100]. Therefore, we model our coupled oscillatory system for real operating condition and include a realistic, net value of a damping coefficient into our Simulink model. We therefore propose the following operating conditions given as case II in section 4.2.2 below.

4.2.2 Case II

$c = 0.0031$ *Ns/m*, (Q ≈ 2547), $\Delta k = 0$, $\kappa = -0.0032$, excitation force applied to mass M_1.

For the prototype designed in this work, a finite value of a quality factor, $Q \approx 2547$ is required (refer the condition $Q \geq Q_{i\_mismatch} > Q_{imin}$ we established in section 3.5.2 in chapter 3).

Figure 4.8 (a) and (c) shows a time plot for an out-of-phase and in-phase mode displacement outputs of a two electrically coupled resonators. A maximum value of the displacement can be given as x_{ji} for the j^{th} (j =1, 2) resonator at the i^{th} (i = 1, 2) mode of frequency. Therefore, we can write the simulated values as follows: $x_{11} = 0.419$ μm, $x_{21} = 0.394$ μm, $x_{12} = 0.836$ μm and $x_{22} = 0.804$ μm. Here, for the case when $c = 0.0031$ *Ns/m* ($Q \approx 2547$), we note that $x_{11} \neq x_{21}$, and $x_{12} \neq x_{22}$. We also note that displacement amplitude of j^{th} resonator at mode 1 is not equal to the displacement amplitude of j^{th} resonator at mode 2, *i.e.* $x_{j1} \neq x_{j2}$ (j = 1, 2). This is the observation for a *finite value of a quality factor* in our macro-scale two coupled resonators.

Figure 4.8 (b) and (d) shows a corresponding time plots for a motional currents when the system is excited at the out-of-phase and in-phase mode frequency, respectively. A maximum value of the motional current can be given as $i_{mot_{ji}}$ for the j^{th} (j =1, 2) resonator at the i^{th} (i = 1, 2) mode of frequency. Therefore, we can write the simulated values as follows: i_{mot11} = 195 nA, $i_{mot\ 21}$ = 183 nA, $i_{mot\ 12}$ = 384 nA and $i_{mot\ 22}$ = 370 nA. Here, for the case when c = 0.0031

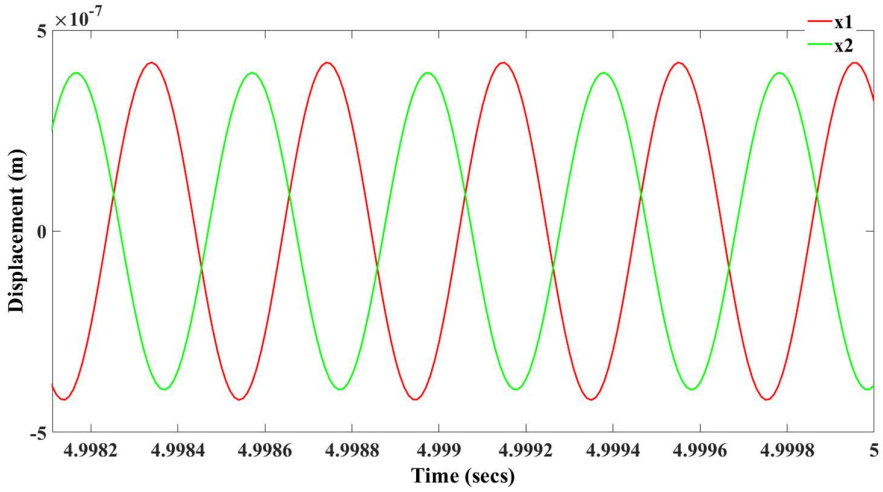

(a)

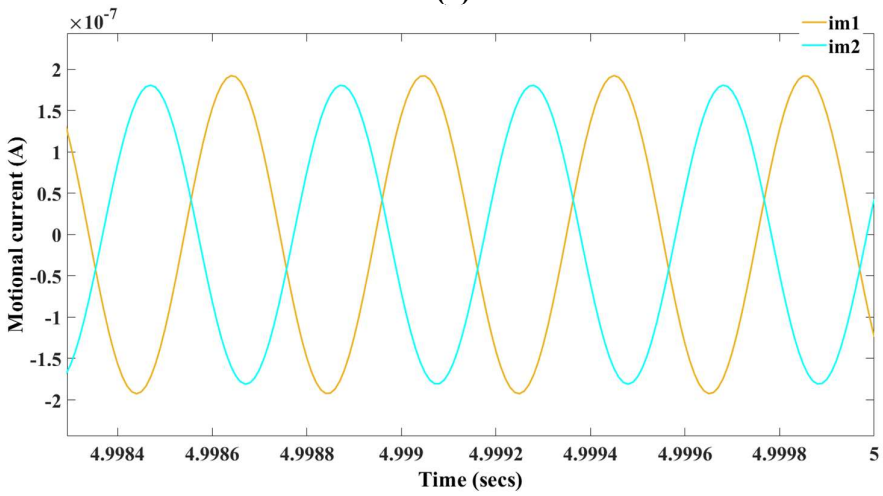

(b)

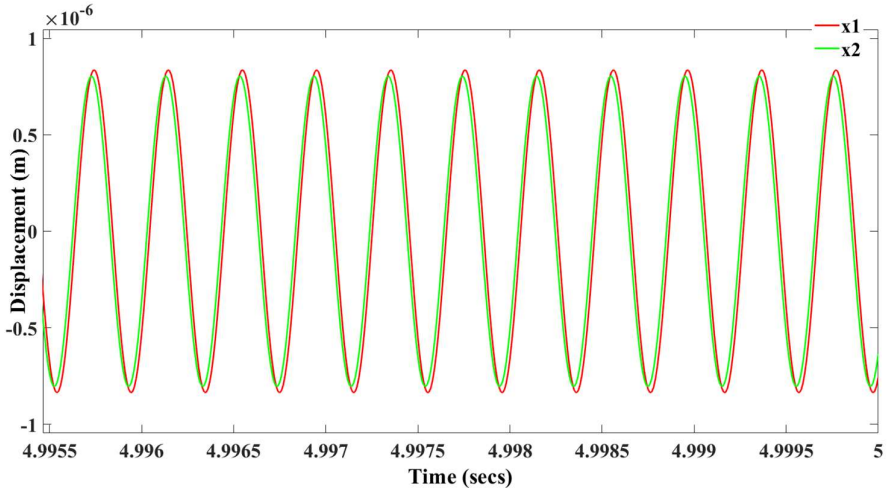

(c)

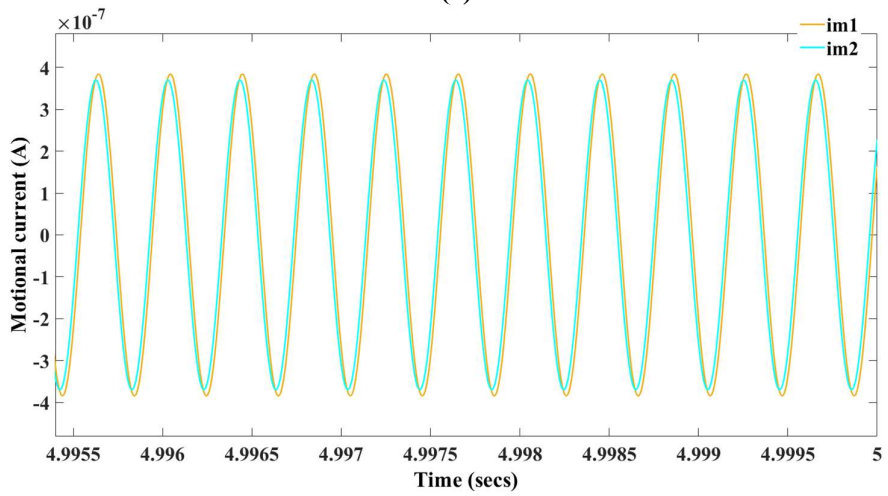

(d)

Figure 4.8 Steady-state time-response (a) and (b) at the out-of-phase excitation frequency, ω_{op}, 2474 *Hz*, (c) and (d) at the in-phase excitation frequency, ω_{ip}, 2482 *Hz*. x_1 and x_2 are displacements, *im1* and *im2* are motional current from mass M_1 and M_2 respectively.

Ns/m ($Q \approx 2547$), we note that $i_{mot11} \neq i_{mot21}$, and $i_{mot12} \neq i_{mot22}$. We also note that motional current amplitude of j^{th} resonator at mode 1 is not exactly equal to the motional current amplitude of j^{th} resonator at mode 2, *i.e.* $i_{motj1} \neq i_{motj2}$ (j = 1, 2).

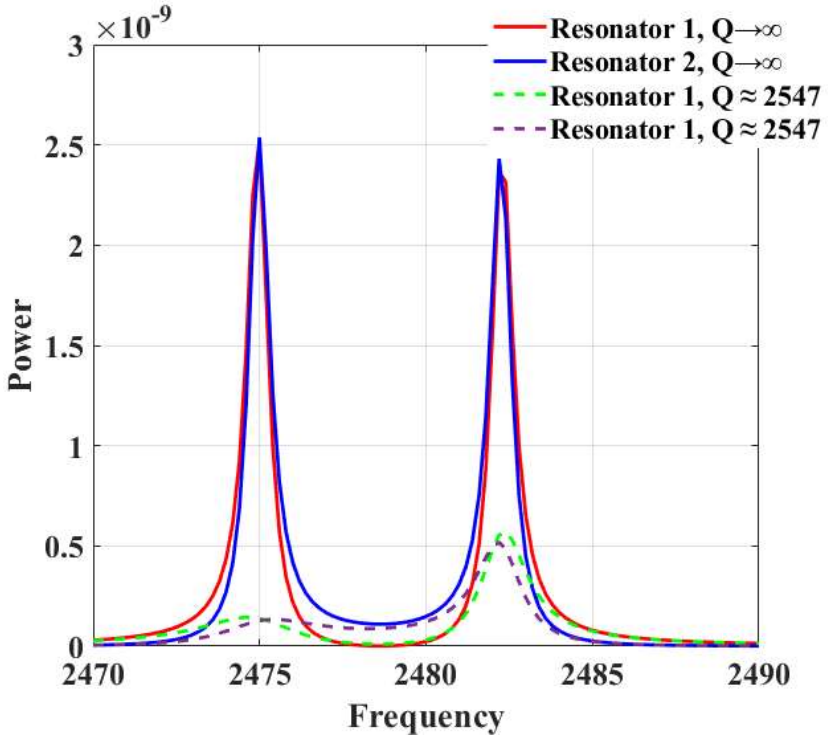

Figure 4.9 Simulated power spectrum of our design across the frequency range of interest for finite value of a quality factor. Two resonant peaks are seen to be separated by about 7 *Hz*.

Figure 4.9 shows a plotted graph of the power spectrum of our design for the two operating conditions: 1) $c = 0$ *Ns/m*, ($Q \rightarrow \infty$), $\Delta k = 0$, $\kappa = -0.0032$, electrostatic driving force, $F = 1$ *N* applied to proof mass M_1. 2) $c = 0.0031$ *Ns/m*, ($Q \approx 2547$), $\Delta k = 0$, $\kappa = -0.0032$, excitation force, $F = 1$ *N* applied to mass M_1. As seen in Figure 4.9, for a finite value of Q, output signal level of the j^{th} resonator at the i^{th} mode drops. Moreover, amplitude of the j^{th} resonator at mode 1 is smaller than amplitude of the j^{th} resonator at mode 2. Outputs are the motional current signals.

Figure 4.10 shows a time plot demonstrating a **mode-localization effect** for the displacement amplitudes x_{ji} for the j^{th} (j =1, 2) resonator at the i^{th} (i = 1, 2) mode of frequency response. A maximum stiffness perturbation that is applied is. $\Delta k_{max} = -251.8$ *N/m*, or $\delta_{kmax} = -0.0019$ (*normalized*). Note that excitation frequency is a function of Δk. A response is obtained for a damping coefficient, $c = 0.0031$ *Ns/m, (*$Q \approx 2547$*).*

A maximum value of the displacements in this case are x_{ji} for the j^{th} (j =1, 2) resonator at the i^{th} (i = 1, 2) mode of frequency. Therefore, we can write the simulated values as follows: $x_{11} = 310$ *nm*, $x_{21} = 380$ *nm*, $x_{12} = 1.04$ μm and $x_{22} = 0.75$ μm. A maximum value of the motional current can be given as $i_{mot_{ji}}$ for the j^{th} (j =1, 2) resonator at the i^{th} (i = 1, 2) mode of frequency. Therefore, we can write the simulated values as follows: $i_{mot11} = 142$ *nA*, $i_{mot\ 21} = 174$ *nA*, $i_{mot\ 12} = 480$ *nA* and $i_{mot\ 22} = 345$ *nA*.

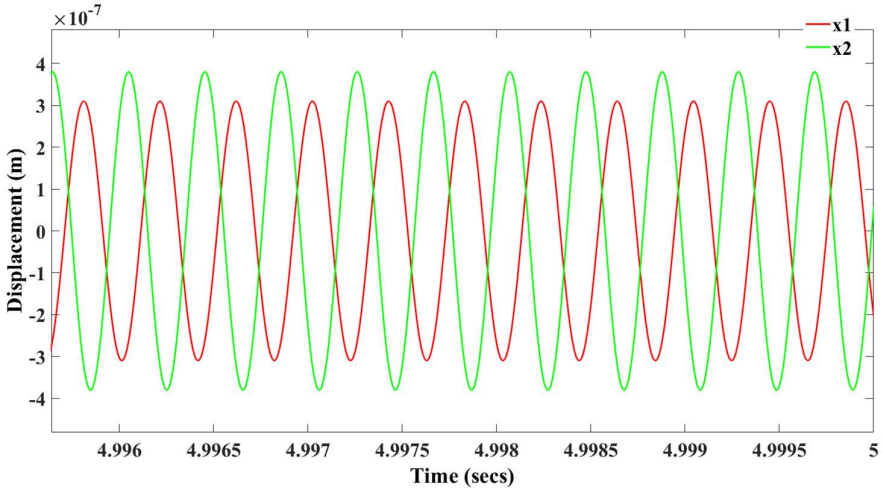
×10^-7
x1
x2
Displacement (m)
4
3
2
1
0
-1
-2
-3
-4
4.996
4.9965
4.997
4.9975
4.998
4.9985
4.999
4.9995
5
Time (secs)

(a)

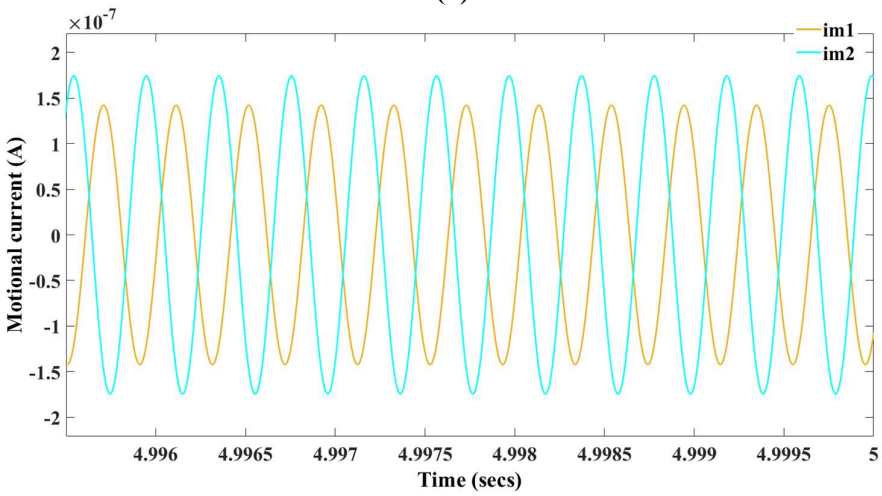
×10^-7
im1
im2
Motional current (A)
2
1.5
1
0.5
0
-0.5
-1
-1.5
-2
4.996
4.9965
4.997
4.9975
4.998
4.9985
4.999
4.9995
5
Time (secs)

(b)

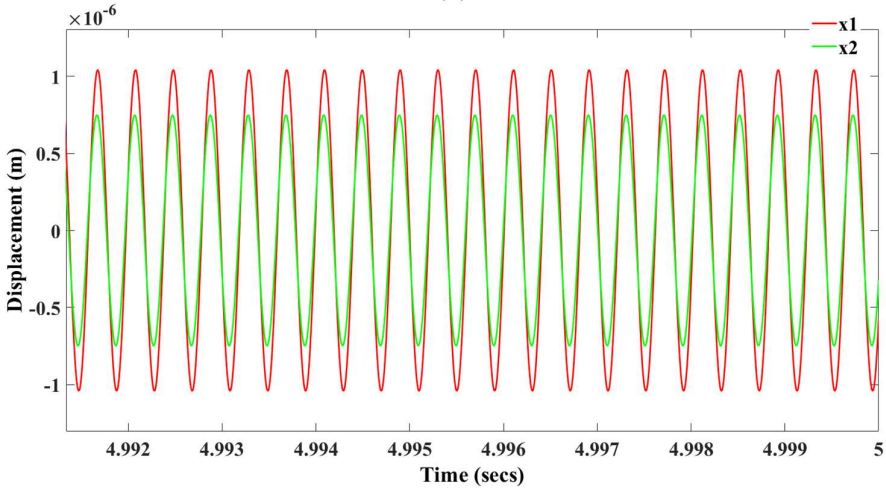
×10^-6
x1
x2
Displacement (m)
1
0.5
0
-0.5
-1
4.992
4.993
4.994
4.995
4.996
4.997
4.998
4.999
5
Time (secs)

(c)

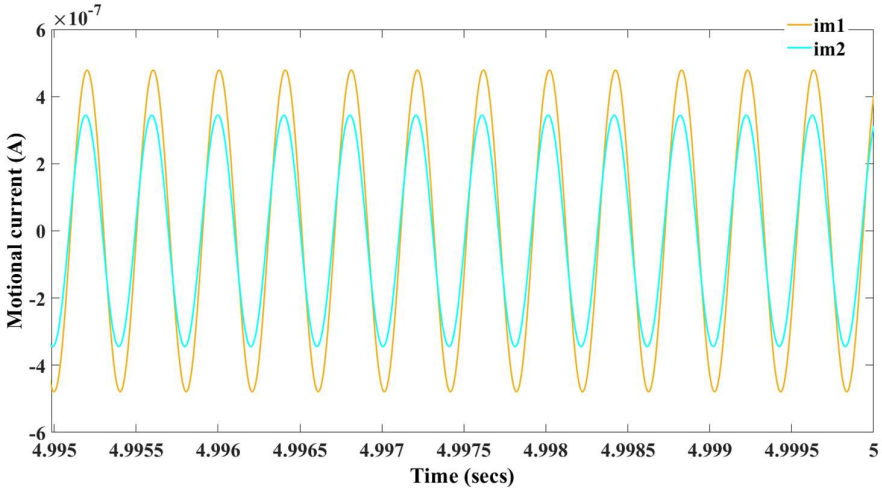

(d)

Figure 4.10 A mode-localization effect in coupled resonators (a) and (b) out-of-phase and (c) and (d) in-phase mode. x_1 , x_2 are amplitudes of displacement and *im1*, *im2* are motional currents for resonator 1 and 2 respectively, c = 0.0031 *Ns/m*, ($Q \approx 2547$), κ = -0.0032

Following the analysis in section 4.2.2 above, we applied a range of stiffness perturbations to modulate the effective stiffness of resonator 2 in our model. We then recorded the relative shifts (for $Q \approx 2547$) in to the amplitude ratio, mode amplitude and mode frequencies as shown in Figure 4.11. A maximum sensitivity of amplitude ratio shift to stiffness perturbation of about **134.54** is obtained. A maximum sensitivity of amplitude shift to stiffness perturbation of about **23.73** is obtained. A maximum sensitivity of frequency shift to stiffness perturbation of about **0.284** is obtained.

A maximum sensitivity value of 134.54 (for amplitude ratio output for a finite quality factor of 2547) may be compared with that calculated maximum theoretical sensitivity of 158 (for amplitude ratio output when $Q \rightarrow \infty$). Note that one such reason of variation in the quality factor is the ambient pressure drifts. Therefore, this design confirms a robustness (to a certain extent) of our design against varying effective value of a quality factor.

For our macro-scale design, a sensitivity of amplitude ratio output to stiffness perturbations is comparable to that achievable with MEMS structures of two coupled resonators reported in [17,21,22,98].

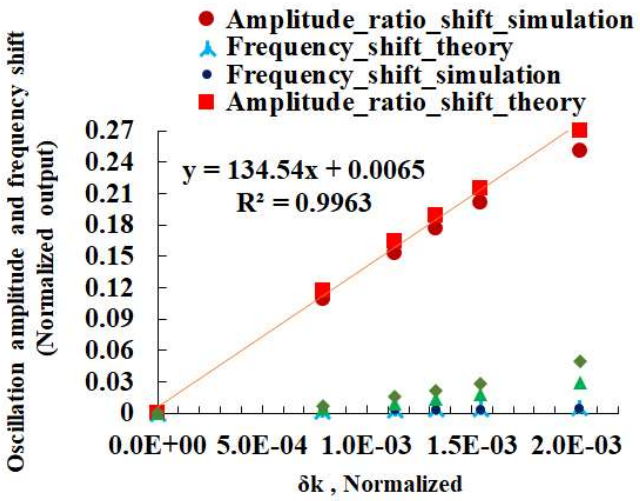

Figure 4.11 A comparative performance for all the outputs for $c = 0.0031$ *Ns/m* ($Q \approx 2547$); $\Delta k \neq 0$, $\kappa = -0.0032$. A representation for a frequency shift output is shown 10× times scaled up to illustrate a comparison among other outputs. A reasonable match was observed between the simulation and theory. Magnitude of δ_k used in theory and/or simulations are same as used during the experiments. A proof mass M_1 is driven at out-of-phase frequency, ω_{op} which is a function of Δk

We applied the net excitation force on the proof mass M_1 first at the *out-of-phase mode* frequency and recorded corresponding variations in the amplitude ratio based output to the applied stiffness perturbation. A maximum simulated sensitivity in this case is about 135 (refer Figure 4.11). Later, we applied the net excitation force on the proof mass M_1 at the *in-phase mode* frequency and recorded corresponding variations in the amplitude ratio based output to the applied stiffness perturbation. A maximum simulated sensitivity in this case is about 177 and a graph showing it is presented in Figure 4.12. Therefore, we found that amplitude ratio based sensitivity to the applied stiffness perturbation is larger for the in-phase mode than its out-of-phase mode counterpart for a given operating conditions as presented in section 4.2.2 above. Owing to the higher output signal level (referring Figure 4.9), in-phase mode offers higher sensitivity to applied disorder in our design.

Note that the maximum theoretical amplitude ratio based sensitivity to the stiffness perturbation in our macro-design was determined from the expression, $S_{\hat{R}} \approx \left|\frac{K_{eff}}{2K_c}\right|$ given in [49] and it is calculated to be about 170 in our design. We however observe that 1) this expression of effective sensitivity has no dependence on the quality factor as we demonstrate through our simulation model, 2) for a finite value of a quality factor effective values of sensitivity differ as we have shown. Therefore, a more realistic expression to determine the sensitivity needs to be derived.

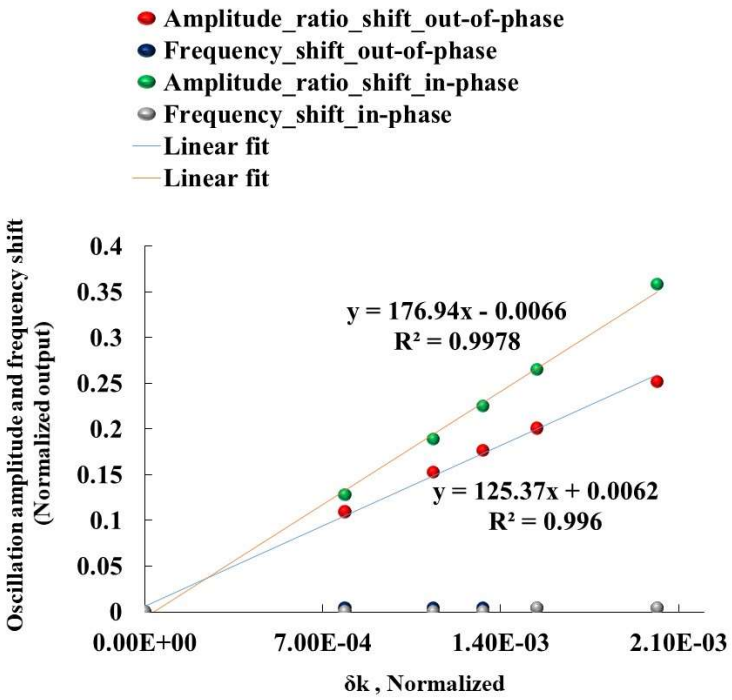

Figure 4.12 A comparative performance for the amplitude ratio based output metric, for c = 0.0031 *Ns/m* ($Q \approx 2547$); $\Delta k \neq 0$, κ = -0.0032. A representation for a frequency shift output is shown 10× times scaled up to illustrate a comparison among other outputs. A proof mass M_1 is driven at out-of-phase frequency, ω_{op} first and then at the in-phase mode frequency, ω_{ip} (mode frequenies being a function of Δk)

4.3 Frequency response of our design

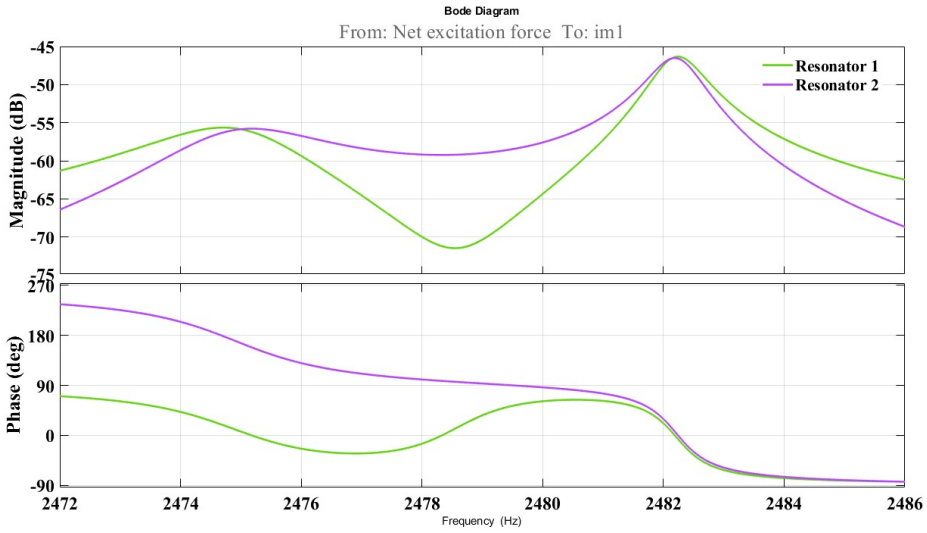

Figure 4.13 A simulated frequency response of our design

Figure 4.13 represents a frequency response obtained through the transfer function of our design we have derived in section 3.3.1 of chapter 3. Operating conditions are those reported in section 4.2.2 above. As seen, for a finite value of a quality factor, mode 1 (out-of-phase) signal drops to relatively lower level than its mode 2 (in-phase) signal. Both modes are seen to be separated by about 7 Hz. A phase difference of about 180^0 at mode 1, and phase difference of about 0^0 at mode 2 confirm the functionality of our scaled-up weakly, electrically coupled 2 DoF resonators.

4.4 Impact of Q, K_c and δ_k in our design

In this section, we attempt to carry a spectral analysis of our system for variety of operating conditions such as impact of structural damping (alternatively say Q), varying strength of electrostatic coupling, K_c and applied stiffness perturbation, δ_k. We thereby propose a generalized design method for this scaled-up geometry fabricated using laser machining.

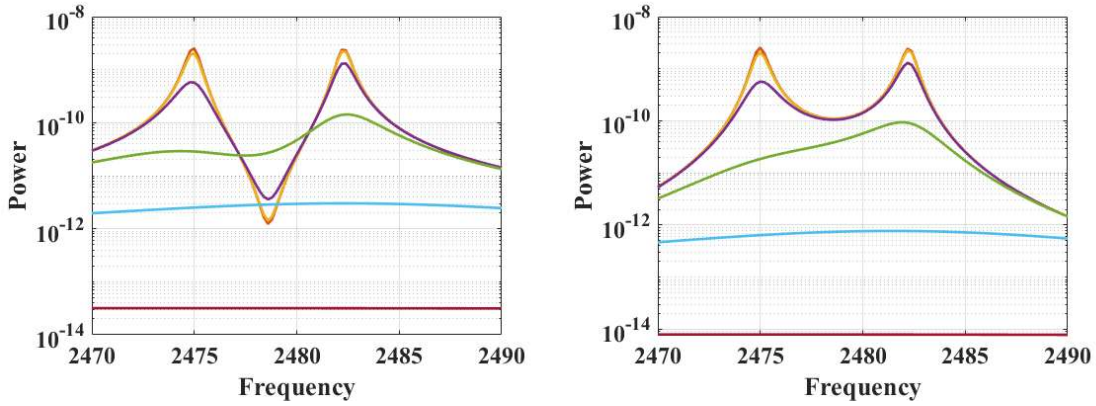

Figure 4.14 Simulated output response showing impact of structural damping (a) resonator 1 and (b) resonator 2, operating conditions are F= 1N, Q varying from infinity to about 8, K_c = -393.51 N/m, δ_k = 0, Y-axis is log scale

From Figure 4.14, we can infer that with increase in the structural damping, that may stem from various damping sources including an atmospheric pressure, an output response (motional current output) of both the resonators start to diminish. This is the case for a fixed value of a coupling factor K_c = -393.51 N/m in our design. Damping coefficient in our model was set as a variable to have following effective values: 0, 1×10^{-6}, 1×10^{-4}, 1×10^{-3}, 1×10^{-2}, 1×10^{-1}, 1, all in Ns/m. These values correspond to effective quality factor, Q as follows: ∞, 8.84×10^6, 8.84×10^4 8.84×10^3, 859, 85, 8.5 respectively. For a quality factor of about 859 (referring light green curve in Figure 4.14), we observe i^{th} mode (i = 1, 2) of the j^{th} resonator (j = 1, 2) starts to show up and two modes can distinctly be resolved. This validates the theoretical condition we derived in 3.5.2 in chapter 3.

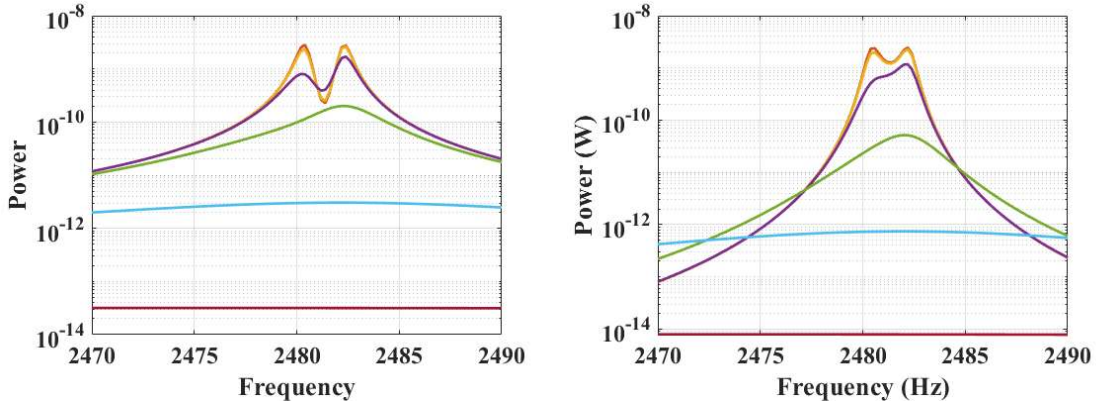

Figure 4.15 Simulated output response showing impact of structural damping (a) resonator 1 and (b) resonator 2, operating conditions are F= 1N, Q varying from infinity to about 8, K_c = -100 N/m, δ_k = 0, Y-axis is log scale

From Figure 4.15 we observe that with relatively lower value of a coupling factor, K_c = -100 N/m, two modes appear as combined one (referring light green curve in Figure 4.15) for the same value of a quality factor of about 859. In other words, a higher quality factor is needed to resolve two distinct modes if the coupling spring becomes smaller. Figure 4.16 presents this comparative analysis.

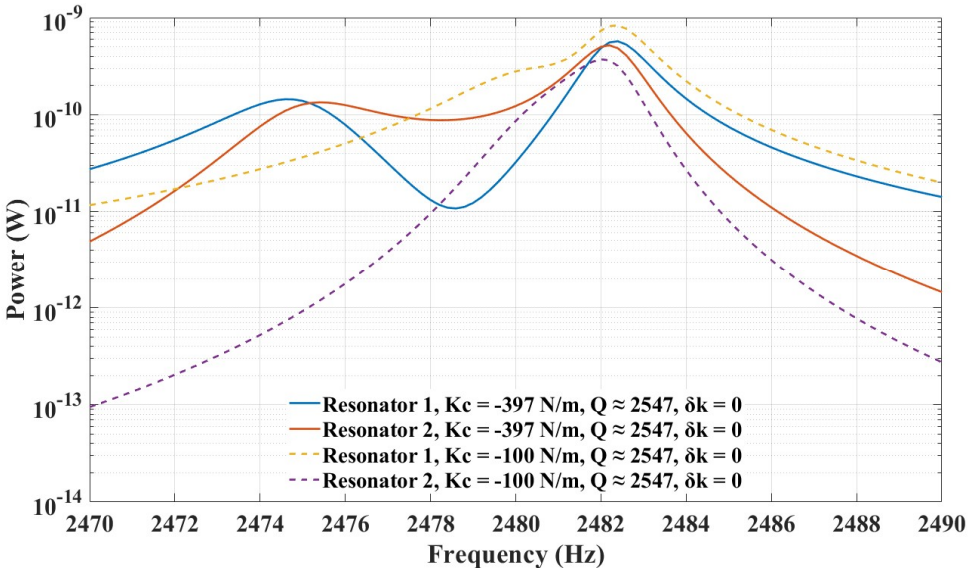

Figure 4.16 Simulated output response (a) resonator 1 and (b) resonator 2, operating conditions are F= 1N, Q is about 2547, varying K_c, δ_k = 0, Y-axis is log scale.

From Figure 4.16, we can observe that for the given set of operating conditions, with a Q of 2547, K_c = -397 N/m, two distinct modes for both the resonators can effectively be resolved.

Figure 4.17 presents a plot showing an effect of applied stiffness perturbations on the output response of either resonators at the two distinct modes.

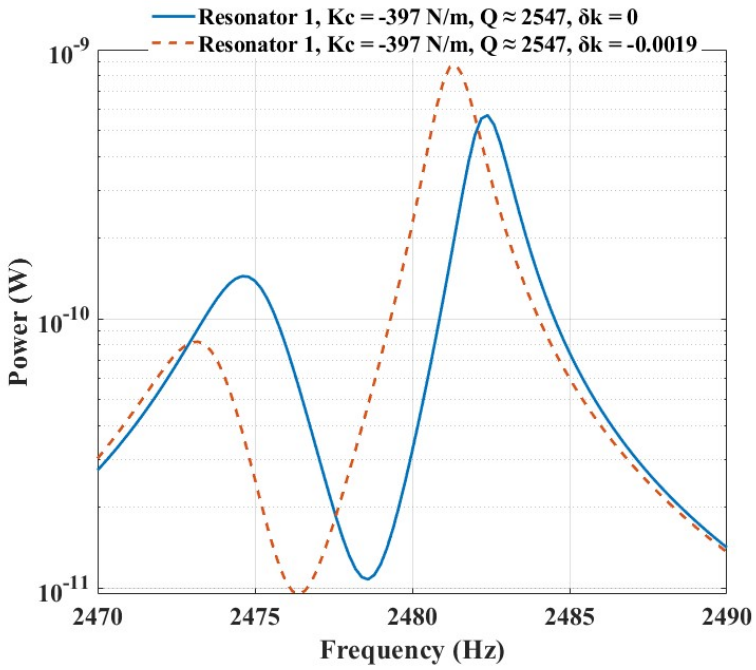

(a)

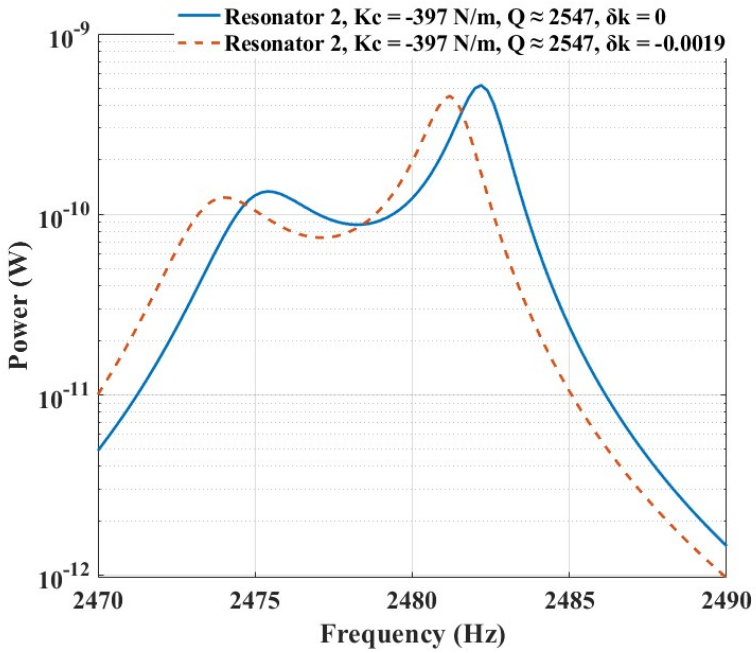

(b)

Figure 4.17 Operating conditions are F= 1N, Q is about 2547, K_c = -393.51 N/m, $\delta_k \neq 0$, Y-axis is log scale

Note that observed power levels in our spectral analysis should be scaled by the factor 1/149 μN for the accurate estimation of the signal power levels of our design.

4.5 Noise analysis in our design

In this section, we attempt to model an impact of a noise into our macro-size two weakly coupled resonator system. Through mathematical analysis and simulations obtained through our Simulink model, we attempt to quantify an effective noise floor in our design. Following this, we therefore propose a finest possible resolution for our device.

4.5.1 Noise in a mechanical sensing system

In a typical MEMS resonator system, electronic circuits (typically a current to voltage converter, also called transimpedance amplifier) is used for readout and processing of the electrical signal (output motional current from a resonator) provided by the sensing element. A total noise level of the system is therefore due to the combined effect of the mechanical–thermal noise in the mechanical domain, the electrical noise of the (resistive) mechanical sensing element [100] and the input referred noise of the readout circuits [15,84,85,100]. An input referred noise is obtained by dividing the estimated output referred noise by the circuit gain.

In a typical MEMS system, noise from a readout circuit dominates the noise performance [6]. However, the details of the mechanical–thermal noise should also be considered relevant, and a noise source (mechanical or electronic) that determines the detection limit of the sensor should be analysed.

4.5.2 Noise floor in a mode-localized sensor

In order to understand the impact of a system noise on the performance of a coupled resonator as a mode-localised sensor, we added a noise source (with calculated equivalent noise power as given in the following sections) into our model and analysed the response for the ultimate detection limit, *i.e.* resolution of our sensor. We used fixed design value of a coupling factor and a finite value of a net damping force (*i.e*. effective value of a quality factor).

4.5.3 Thermo-mechanical noise in our design

In this section, we attempt to model and quantify a magnitude of a thermal-mechanical noise in our design. Small moving parts in MEMS are especially susceptible to mechanical noise resulting from molecular agitation.[100]. In ultra-low level signal detection, mechanical-thermal noise plays an important role in setting up the effective noise floor of a sensor system, and, thus a minimum detection limit. In the context of a coupled resonators as a sensor, it has been concluded in [84,85] that it is a thermal-mechanical noise that governs the ultimate detection limit of a coupled resonating sensor. We model a mechanical-thermal noise source in our macro-scale 2 DoF weakly coupled resonators and quantify its impact on the resolution

(i.e. lowest possible detectable physical quantity) with the two output metric (amplitude ratio and amplitude) of our device.

In our design, we state that X_{ji} is the amplitude variations for a j^{th} resonator (j =1, 2) at the i^{th} mode of a frequency response (i =1, 2) due to the noise induced into the system. Therefore, we get an expression of the following output metric (considering a system involving an intrinsic (mechanical) and extrinsic (electronic) noise sources). Therefore, we derive a minimum resolvable amplitude ratio shift as $\left(\frac{X_1}{X_2}\right)_{\min_{ji}} = \left|\frac{R_n - R_0}{R_0}\right|_{\min_{ji}}$ and a minimum resolvable amplitude shift is $(X)_{\min_{ji}} = \left|\frac{A_n - A_0}{A_0}\right|_{\min_{ji}}$. Therefore, we investigated (through our Simulink model) a power spectral density (PSD) of an amplitude noise of j^{th} resonator (j = 1, 2) at the i^{th} mode of the frequency response (i = 1, 2). We modelled an effect of a mechanical noise by adding a force term into the governing set of equations of motion (for 2 DoF) as follows

$$M\ddot{X}_1 + (c + c_c)\dot{X}_1 + (K_m + K_c)X_1 - c\dot{X}_2 - K_c X_2 = F_{noise\_rms} \tag{4.1}$$

$$M\ddot{X}_1 + (c + c_c)\dot{X}_1 + (K_m + K_c)X_1 - c\dot{X}_2 - K_c X_2 = F_{noise\_rms} \tag{4.2}$$

A spectral density of a noise forcing term is given as $F_{noise\_density} = \sqrt{4\ k_B T\ c}\ N/\sqrt{Hz}$ [100,101]. Here, k_B is the Boltzmann constant (≈ 1.380×10^{-23} *Joule/Kelvin*), T is the temperature (300 *Kelvin*) and c is the damping coefficient (c = 0.0031 *Ns/m* in our case). As observed, the spectral density of a mechanical noise force depends on temperature and the magnitude of mechanical damping. We calculated the power spectral density (PSD) of *mechanical noise force generator* as below.

$$\begin{aligned} \left(F_{noise\_\text{density}}\right)^2 &= 4\ k_B T\ c \\ &= 4\times1.380\times10^{-23}\times300\times0.0031 \\ &= 5.136\times10^{-23}\ N^2/Hz \end{aligned} \tag{4.3}$$

Assuming a measurement bandwidth of 10 *Hz*, an average (mean square) value of a mechanical thermal noise force generator will be

$$
\begin{aligned}
F_{noise\_avg} &= \int_0^{10} \left(\sqrt{4\, k_B T\, c} \right)^2 df \\
&= \int_0^{10} \left(\sqrt{4\times 1.380\times 10^{-23}\times 300\times 0.0031}\, \frac{N}{\sqrt{Hz}} \right)^2 df \\
&= \int_0^{10} \left(7.166\times 10^{-12} \right)^2 \frac{N^2}{Hz}\, df \\
&= 5.13\times 10^{-23}\, \frac{N^2}{Hz} \times 10 Hz \\
&= 5.136\times 10^{-22}\, N^2
\end{aligned}
\tag{4.4}
$$

An effective *rms* amplitude of this mechanical noise forcing term then is

$$
\begin{aligned}
F_{noise\_\mathrm{rms}} &= \sqrt{F_{noise\_avg}} \\
&= \sqrt{5.136\times 10^{-22}\, N^2} \\
&= 2.26\times 10^{-11}\, N
\end{aligned}
\tag{4.5}
$$

A noise forcing term with the calculated average value, $F_{noise\_avg} = 5.136 \times 10^{-22}\ N^2$ was added as an excitation force in to the Simulink model.

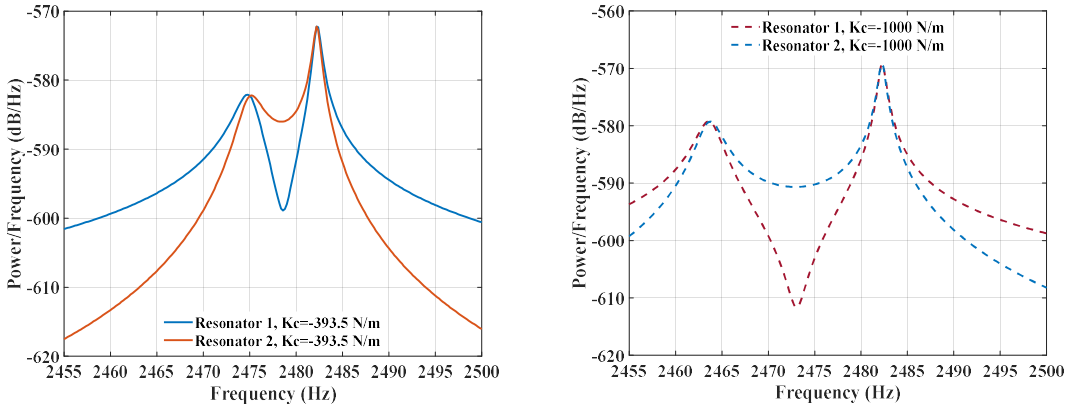

(a) (b)

Figure 4.18 Simulated power spectrum density (PSD) of an displacement noise of resonator 1 and 2 subject to mechanical-thermal noise forcing term on resonator 1. (a) K_c = -393.5 *N/m* and (b) K_c = -1000 *N/m*. Simulation conditions are those reported in section 4.2.2, case 2.

A noise PSD (in *dB/Hz*) for displacements x_1 and x_2 was plotted as shown in Figure 4.18. Simulations were run for the varying strength of a coupling between two resonators in our design with the conditions as given in 4.2.2. A resultant displacement noise PSD (due to noise forcing term) is -582.2 *dB/Hz* (at mode 1) and -572.2 *dB/Hz* (at mode 2) (referring Figure 4.18 (a)) which correspond to an equivalent magnitude $|X_j|$ of 7.76×10^{-30} m^2/Hz (at mode 1) and 2.45×10^{-29} m^2/Hz (at mode 2) respectively. Assuming a measurement bandwidth of 10 *Hz*, an average (mean square) value of a mechanical thermal noise of j^{th} resonator at the i^{th} mode (j, i

= 1, 2) will be $X_{ji\_avg} = |X_{ji}| \times df$. As observed from Figure 4.18, noise magnitude is lower for mode 1; therefore, we compute a best-case estimate for average noise power for this mode given as

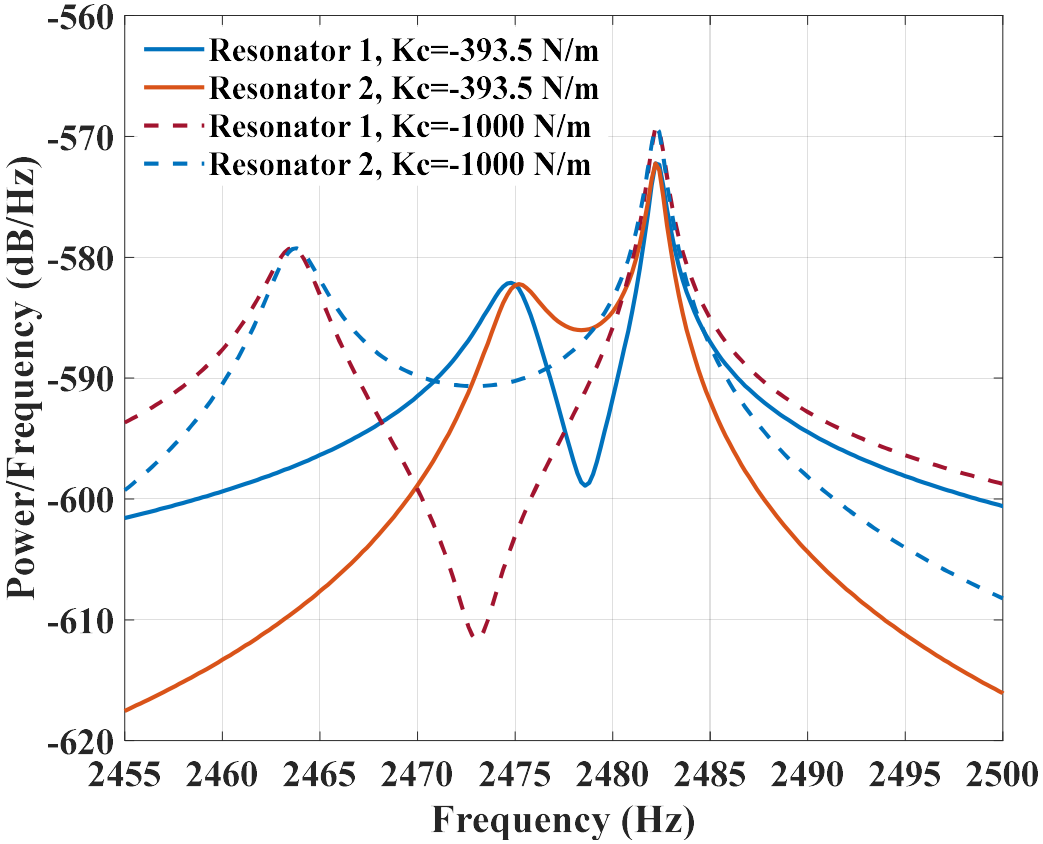

Figure 4.19 Simulated power spectrum density (PSD) of an displacement amplitude noise in resonator 1 and 2 for varying coupling strength, K_c.

$$X_{j1\_avg} == 7.762\times10^{-30}\,\frac{m^2}{Hz}\times10Hz \approx 7.762\times10^{-29}\,m^2 \tag{4.6}$$

An effective *rms* value of a mechanical-thermal noise, X_{ji_rms} in our design then is (for mode 1)

$$X_{j1\_rms} = \sqrt{X_{j1\_avg}} = \sqrt{7.762\times10^{-29}\,m^2} \approx 8.81\times10^{-15}\,m \tag{4.7}$$

Note that during the analysis, we hold on to the condition $Q \geq Q_{\,i\_mismatch} > Q_{imin}$, as set out in section 3.5.2 in chapter 3 to ensure that modes in our design can effectively be resolved during the analysis.

Figure 4.19 explains the comparative PSD plot of mechanical thermal noise of our design for two coupling stiffness, K_c = -393.5 *N/m* and K_c = -1000 *N/m*. From Figure 4.19, we can infer that with lower coupling strength, mechanical-thermal noise amplitude of our design decreases (≈ -3 *dB* gain in displacement noise amplitude for either mode with K_c = -393.5 *N/m*).

In [72], for a reported MEMS 2 DoF architecture, it was postulated that lower coupling factor leads to improved resolution, and ultimate resolution (i.e. measurement limit imposed by noise processes in the system) is linearly proportional to the coupling factor. Our calculations supplemented by the simulations (Figure 4.19) confirms this for our scaled-up 2 DoF structure. However, a research reported in [84], has provided a theoretical study and simulations to conclude that ultimate resolution of a weakly coupled sensor is independent of the coupling factor. This research shows contradiction with the findings in [72] and the results reported in this section of thesis.

A theoretical estimation of effective noise current for our device (due to intrinsic mechanical-thermal noise) is $i_{motX_{ji}} = \eta\omega_i X_{ji}$, where η, ω_i, and X_{ji} are transduction factor, angular frequency and the maximum displacement amplitude of the j^{th} resonator (j=1,2) at the i^{th} mode of the frequency response (i=1,2), respectively [53,72]. By determining the X_{ji}, (refer equation 4.7) we quantified the effective mechanical-thermal noise current (i.e. corresponding variations in the motional currents, $i_{motX_{ji}}$ due to noise forcing term). Since, a thermal noise amplitude of the mode 1 is relatively lower (referring Figure 4.18), we do the computation for the best case as below.

$$\begin{aligned} i_{motX_{j1}} &= \eta\omega_1 X_{j1} \\ &= 2.95\times10^{-5}\times2474\times8.81\times10^{-15} \\ &\approx 4.29\times10^{-15}\, A_{rms} \end{aligned} \tag{4.8}$$

Equation 4.8 signifies the lower limit of detecting the change in the quantity to be measured (Δk in our case). Furthermore, a higher quality factor can further improve this detection limit.

In our design, we conclude that any variation in the modal amplitudes is resolvable only so long as the simulated/measured individual *rms* amplitude shifts, x_{ji} ($i_{mot_{ji}}$) is greater than the *rms* amplitude fluctuations, X_{ji} ($i_{motX_{ji}}$) induced by noise in the system, *i.e* SNR ≥ 1 (referring to equation 4.8).

4.6 Modelling the impact of electronic noise in our design

Figure 4.20 (a) represents the schematic representation of transimpedance amplifier that may be realized using OPA 381 [102] integrated circuit (IC) as an interface circuit to our coupled resonator design. Two such ICs may be deployed for motional current pick-up into each output channel of the coupled resonator output. Figure 4.20 (b) is the equivalent noise model for the interface circuit used as transimpedance amplifier. We estimated noise contributions from each of these sources by superposition and nodal analysis.

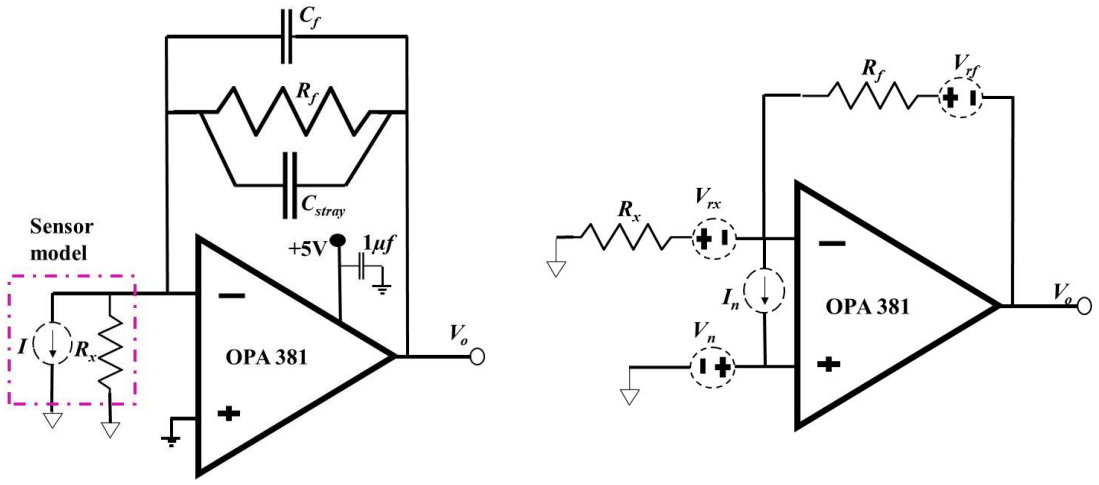

(a) (b)

Figure 4.20 (a) OPA 381 interface with our sensor design (b) equivalent noise circuit to evaluate circuit dominant noise.

An expected variation in the current arising from the intrinsic and extrinsic noise sources were theoretically evaluated as explained in Table 4.2. The impact of thermomechanical noise on the theoretically calculated motional current is evaluated by first estimating the displacement due to thermal noise (refer section 4.5.3) and then calculating its corresponding current variation as detailed in Table 4.2.

Table 4.2 Noise calculations

Sr. No.	Noise sources	Effective noise current (A_{rms})	Expression used
1	Mechanical thermal-noise	$4.9\times10^{-15*}$	$i_{X_{ji}} = \eta\omega_i X_{ji}$
2	Feedback resistance	4.06×10^{-13}	$\sqrt{\frac{4k_B T \times B}{R_f}}$
3	Input voltage noise of a pre-amplifier	4.34×10^{-13}	$\sqrt{v_n^2\left(1+\frac{R_x}{R_f}\right)^2 / R_x^2} \times \sqrt{B} \times 1.57$
4	Input current noise of a pre-amplifier	9.92×10^{-14}	$\sqrt{i_n^2} \times \sqrt{B} \times 1.57$

* *best-case calculation for the out-of-phase mode as it shows the lower noise amplitude*

** *factor 1.57 is the roll-off rate of a filter (1-pole)* [103].

Note that an amplifier (OPA 381) [102] we choose in our analysis has an input current noise density ≈ 20 $fA/Hz^{0.5}$, and an input voltage noise density ≈ 70 $nV/Hz^{0.5}$. We converted this spectral density of input current noise and input voltage noise-assuming measurement bandwidth B =10 *Hz,* as follows:

I_{noise} *(rms)* = spectral density of current input noise (in $A/\ Hz^{0.5}$) × $\sqrt{B}$ × 1.57

$$I_{noise_{rms}} = 20\times10^{-15}\frac{A}{\sqrt{Hz}}\times\sqrt{10}\sqrt{Hz}\times1.57 \approx 9.92\times10^{-14}\,A_{rms} \tag{4.9}$$

V_{noise} *(rms)* = spectral density of voltage input noise (in $V/\ Hz^{0.5}$) × $\sqrt{B}$ × 1.57

$$V_{noise_{rms}} = 70\times10^{-9}\frac{V}{\sqrt{Hz}}\times\sqrt{10}\sqrt{Hz}\times1.57 \approx 4.34\times10^{-13}\,A_{rms} \tag{4.10}$$

We can evaluate the impact of noise on the motional current output $i_{mot_{ji}}$ of j^{th} resonator (j=1, 2) at the i^{th} mode of a response (i=1, 2) in the presence of an applied ac signal v_{ac} (refer Figure 4.1). This ac voltage signal together with the DC voltage, V_{dc} exerts a net electrostatic actuation force at the resonant frequency.

An impact of a feedthrough capacitance [57] may further be added into our model. This may adversely influence the maximum shifts (thus sensitivity) and lowest possible resolvable shifts, (thus resolution) in the output metric for a given quality factor, Q into our two DoF coupled resonant system.

In order to evaluate the impact of the electronic preamplifier (OPA 381) noise on the minimum shifts into the output metric (and thus quantify measurand $\delta_{k_{\min}}$ in our case), we re-expressed all noise components as equivalent currents and evaluated the effect of noise on the simulated motional current.

We can use a simple circuit analysis of operational amplifier to be used a transimpedance amplifier to calculate total input referred current noise [104,105]. Evaluating the preamplifier noise when modelling the j^{th} resonator as a current source results in [72]

$$i_j^{noise} = \sqrt{\left(i_j^{noise}\right)^2} = \sqrt{\left[i_n^2 + v_n^2\left(1+\frac{R_x}{R_f}\right)^2 / R_x^2 + \frac{4k_BT}{R_f}\right]} \tag{4.11}$$

where, i_j^{noise} (*rms*) is the noise current from the j^{th} resonator at the i^{th} mode of response. R_x is the motional resistance (4 $M\Omega$ for a $Q \approx 2547$ with other parameters being constant, refer section 3.1.2 in chapter 3 for the expression of a motional resistance), R_f is the effective value of a feedback resistor used in the circuit (1 $M\Omega$) in our case. k_B is the Boltzmann constant ($\approx 1.380\times10^{-23}$ *Joule/Kelvin*) and T is the temperature (300 *Kelvin*). Terms i_n and v_n represent the input current noise and input voltage noise of the trans-resistance amplifier (OPA 381) considered for the analysis (refer equation 4.9 and 4.10). Term *df* is the integration bandwidth of 10 Hz. Given that resonator has a bandpass filtering characteristics, frequency range of 10 *Hz* around the resonator's mode frequencies, f_ip and f_op) has been taken for computations for optimum noise estimation. Larger integration bandwidth will account for higher noise levels.

Therefore, solving equation 4.11, we can get an effective theoretical noise floor (due to electronic readout) of our design ≈ 1.56 ×10^{-13} A_{rms}. (Equivalent to -256 *dB*. Equation 4.11 can be compared to equation 4.8 to see that though mechanical-thermal noise sets the ultimate noise floor of our design, it is an electronic noise that dominates the overall performance (electronics noise exceeds mechanical noise by two orders of magnitude). A total noise (mechanical resonator + electronics) in our system is then estimated by vector sum of the uncorrelated noise sources i.e. $I_t^2 = I_1^2 + I_2^2$, where, I_1 is effective mechanical noise current and I_2 is effective electronic readout noise current. From equation 4.8 and equation 4.11, I_t is calculated to be ≈ 1.56 ×10^{-13} A_{rms}. An effective electronic noise current spectral density (in a 10 Hz bandwidth) is $1.56\times10^{-13}\frac{A_{rms}}{\sqrt{10Hz}} \approx 4.933\times10^{-14} A/\sqrt{Hz}$. An equivalent noise power spectral density is $\approx 2.43\times10^{-27} A^2/Hz$ (-532 *dB/Hz*).

We recall from section 4.2.2, maximum theoretical displacement amplitudes, $|x_{ji}|$ (as derived from the Simulink) are $x_{j1} \approx 0.419\ \mu m$ (mode 1) and $x_{j2} \approx 0.836\ \mu m$ (mode 2). Corresponding theoretical motional current amplitudes, $i_{mot_{ji}}$ are $i_{mot_{j1}} \approx \eta\times 2\pi f_{\_op}\times x_{j1} \approx 192nA$ (mode 1) and $i_{mot_{j2}} \approx \eta\times 2\pi f_{\_ip}\times x_{j2} \approx 384nA$. We observed that calculated values for motional current amplitudes are in agreement with the simulated values. Furthermore, with additional amplification factor (R_f = 1 *M*Ω, a feedback resistor in preamplifier OPA 381), we get a total output voltage, $V_{out_{ji}}$ of $V_{out_{j1}} = i_{mot_{j1}}\times R_f \approx 0.192V_{\max} = 0.135V_{rms}$ (mode 1) and $V_{out_{j2}} = i_{mot_{j2}}\times R_f \approx 0.384V_{\max} = 0.271V_{rms}$ (mode 2). A calculated input-referred electronic noise current is ≈ 1.56×10^{-13} A_{rms} (mode 1). Therefore, output referred noise voltage, V_{ji}^{noise} is 1.56× 10^{-13}× R_f ≈ 156 ×10^{-9} V_{rms}.

4.6.1 Noise analysis in SPICE

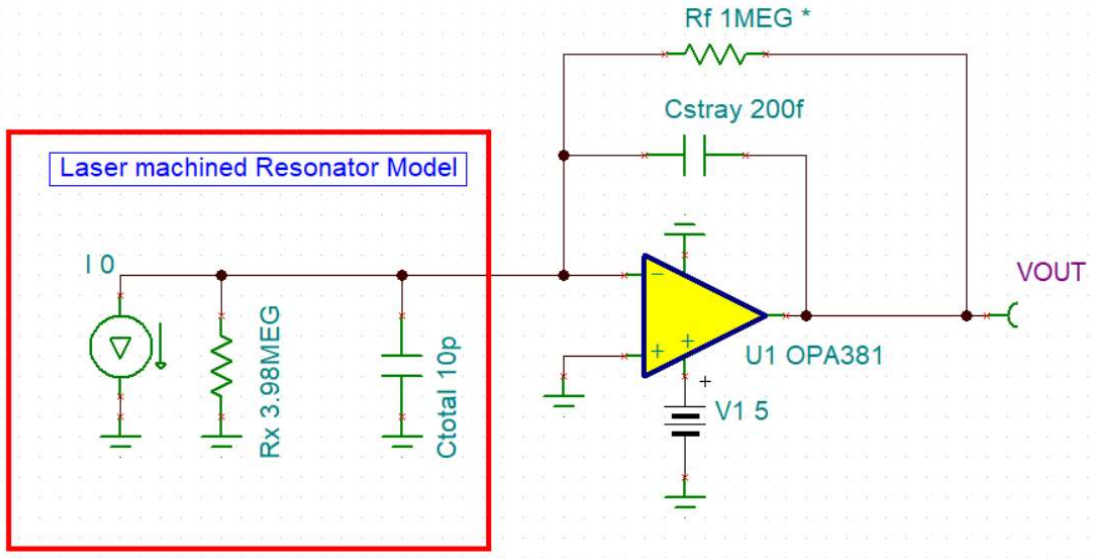

(a)

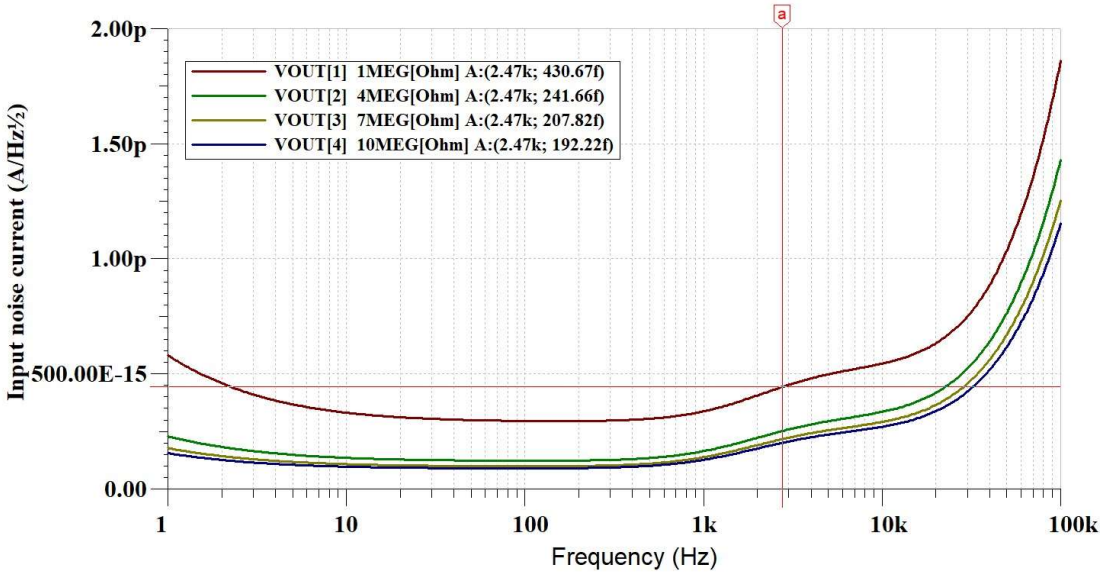
a
2.00p
1.50p
1.00p
500.00E-15
0.00
Input noise current (A/Hz½)
VOUT[1] 1MEG[Ohm] A:(2.47k; 430.67f)
VOUT[2] 4MEG[Ohm] A:(2.47k; 241.66f)
VOUT[3] 7MEG[Ohm] A:(2.47k; 207.82f)
VOUT[4] 10MEG[Ohm] A:(2.47k; 192.22f)
1
10
100
1k
10k
100k
Frequency (Hz)

(b)

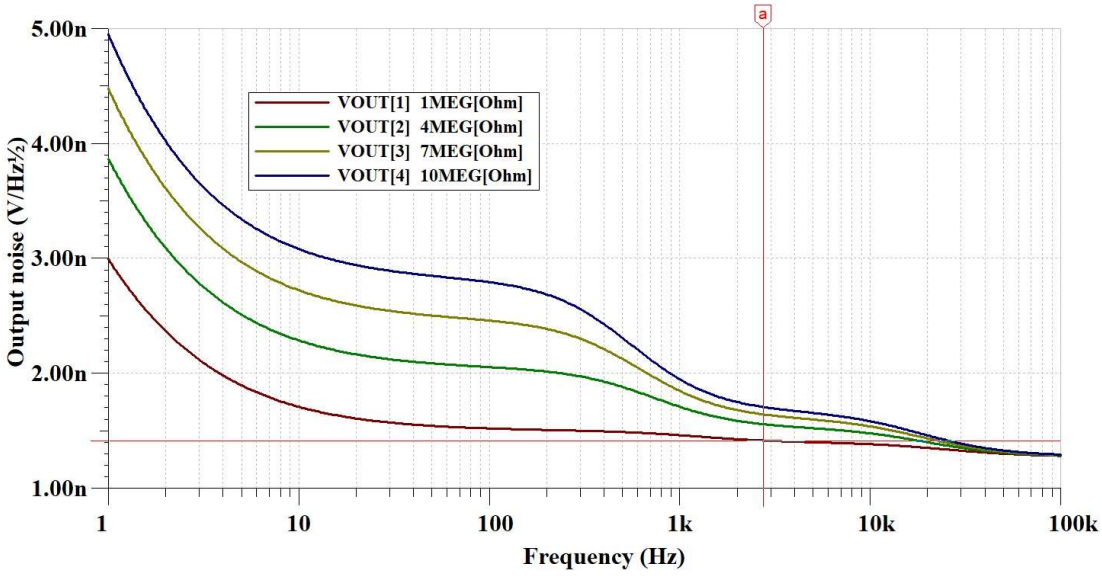
a
5.00n
4.00n
3.00n
2.00n
1.00n
Output noise (V/Hz½)
VOUT[1] 1MEG[Ohm]
VOUT[2] 4MEG[Ohm]
VOUT[3] 7MEG[Ohm]
VOUT[4] 10MEG[Ohm]
1
10
100
1k
10k
100k
Frequency (Hz)

(c)

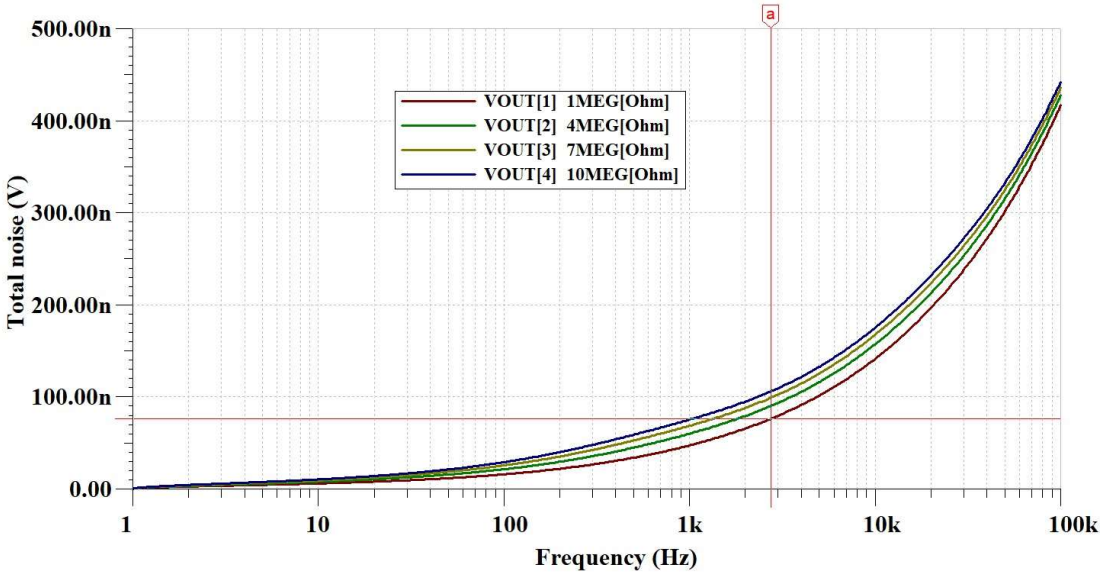

(d)

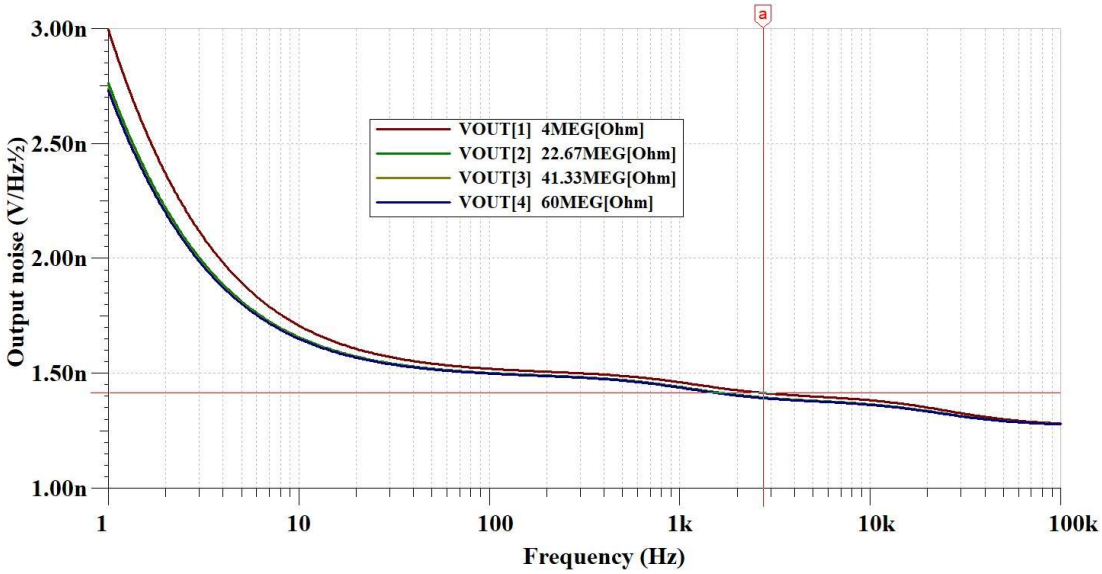

(e)

Figure 4.21 (a) OPA 381 interface with our sensor design (b) equivalent input noise current for varying feedback gain, (c) output noise voltage for varying feedback gain, (d) total integrated output noise in rms for varying feedback gain, and (e) output noise density for varying R_x and fixed R_f of 1Meg.

Figure 4.21 (a) shows schematic of OPA381: Precision, Low Power, 18 MHz Transimpedance Amplifier we used in circuit simulator program for the noise analysis. As seen each resonator in the coupled array of a mode-localized sensor were modelled as an equivalent current source for the purpose of noise analysis. A design operates with a single 5V DC supply. *Ctotal* represents the total input capacitance consisting of the resonator's parasitic capacitance ($C_p \approx$ 6.5pF) plus the parasitic common-mode and differential-mode input capacitance (2.5pF + 1pF

for the OPA381) at the input node of the amplifier. C_f as shown in Figure 4.20 (a) is optional to prevent gain peaking. R_x and R_f are equivalent motional resistance (in either output channel of coupled resonator) and feedback resistor of amplifier respectively.

Figure 4.21 (b) shows spectral density of input noise current (in $A/Hz^{0.5}$) for varying feedback gain, R_f in the circuit. As given in Table 4.3, a good agreement was found between theory and simulation done using a circuit simulator. Figure 4.21 (c) shows output voltage noise (in $V/Hz^{0.5}$) of the circuit for varying feedback gain, R_f in the circuit. Output voltage noise will be less for using lower feedback gain in the circuit. Figure 4.21 (d) shows total output noise voltage (*rms*) in the circuit. Figure 4.21 (e) attempts to evaluate output voltage noise density for varying range of structural damping loss, modelled by varying motional resistance, *Rx*. *Rx* is varying from 3.98 *M*Ω ($Q \approx 2547$) to 60 MΩ ($Q \approx 400$). It is seen that output voltage noise remains relatively insensitive to the varying quality factor in the resonators. Table 4.3 shows a comparative noise analysis of our system. A reasonable match is obtained between theory and simulation.

Table 4.3 Comparative noise analysis of our design

Comparative noise analysis			
Sr. No.		Theory	SPICE simulation (refer graphs)
1	Input noise current density ($A/\sqrt{Hz}$)	4.933×10^{-14}	44×10^{-14}
3	Output noise voltage density ($V/\sqrt{Hz}$)	4.93×10^{-8}	1.49×10^{-9}
4	Total* voltage noise (V_{rms})	156×10^{-9}	228×10^{-9}
* Integrated over a 10 *Hz* measurement bandwidth from the simulated graph ** Note that noise bandwidth and measurement bandwidth are two different terms			

4.6.2 Resolving the lowest possible shifts (i.e. resolution) in our design

The minimum resolvable shift in the voltage amplitudes of our two DoF mode-localized sensor were derived using the following equation [72]:

$$\approx \frac{V_{ji}^{noise}}{V_{out_{ji}}} \tag{4.12}$$

where, V_{ji}^{noise} represents the output refereed noise voltage of the j^{th} coupled resonator at the i^{th} mode. $V_{out_{ji}}$ represents the noiseless deterministic output voltages (determined from the theoretical expression given as $V_{out_{ji}} = i_{mot_{ji}} \times R_f$, where, $i_{mot_j i} = \eta\omega_i x_{ji}$). Therefore, for the j^{th} resonator lowest possible resolvable mode amplitude shift, $\frac{V_{j1}^{noise}}{V_{out_{j1}}}$ for mode 1 is

$\approx \frac{156\times10^{-9}}{0.135} \approx 1.15\times10^{-6}$ (dimensionless), and $\frac{V_{j2}^{noise}}{V_{out_{j2}}}$ for mode 2 as $\approx \frac{156\times10^{-9}}{0.271} \approx 5.756\times10^{-7}$ (dimensionless). Similarly, minimum resolvable shift in the amplitude ratio readout, A_{ri} (i = 1, 2) is $\sqrt{\left(\frac{V_{11}^{noise}}{V_{out_{11}}}\right)^2+\left(\frac{V_{21}^{noise}}{V_{out_{21}}}\right)^2} \approx 1.481\times10^{-6}$ (dimensionless) for mode 1 and $\sqrt{\left(\frac{V_{12}^{noise}}{V_{out_{12}}}\right)^2+\left(\frac{V_{22}^{noise}}{V_{out_{22}}}\right)^2} \approx 3.89\times10^{-7}$ (dimensionless) for mode 2. Here, V_{ji}^{noise} and $V_{out_{ji}}$ are the corresponding noise and output voltages of the j^{th}-coupled resonators at their associated i^{th} mode of the frequency response. Since *rms* amplitudes of output voltage (essentially a motional current) at the mode 1 for j^{th} resonator is relatively closer (*worst-case* signal-to-noise (*S/N*) ratio) to the *rms* noise amplitude, it gives us possibility to determine the *worst-case* lowest possible shift (thus resolution) of our design (thus resolution). The effective resolution (theoretical) of our design for amplitude ratio based readout is $\approx 3.89\times10^{-7}$ which may also be compared to the theoretically calculated resolution ($\approx 6\times10^{-3}$) in MEMS coupled resonator design in [72].

4.7 Influence of coupling strength on the effective noise floor

In this section, we show how electrostatic spring strength coupling the two resonators influence the effective noise floor. Therefore, we attempt to set a generalised guideline in design of coupled resonators for sensing applications. For the analysis, we considered the coupling factor, κ that separates two modes by about 7 *Hz* and a quality factor, Q of about 2547.

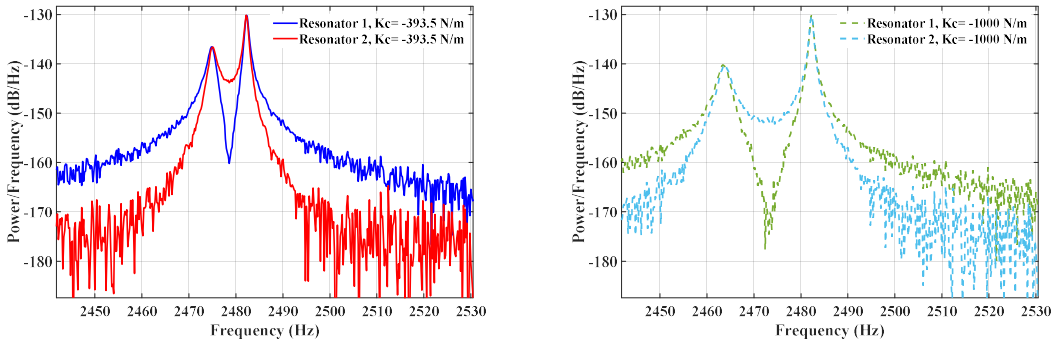

Figure 4.22 Simulated power spectrum density (PSD) of the motional current output signal in a two weakly macro-scale coupled resonator for the following operating condition, Q = 2547, κ = -0032, δ_k = 0, F =1 N

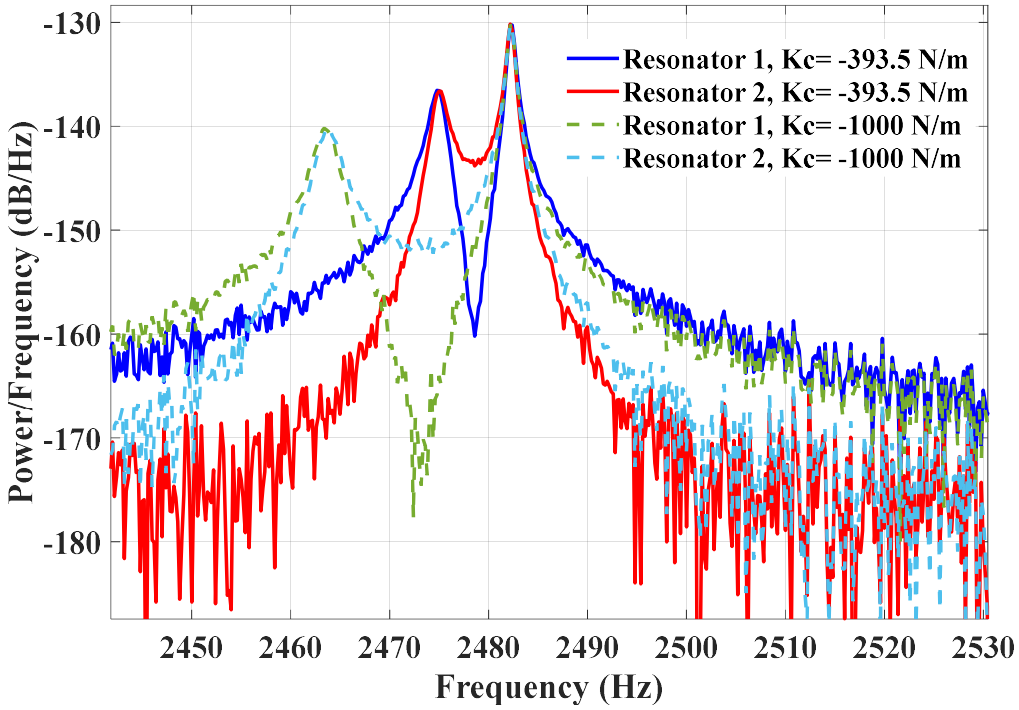

Figure 4.23 Simulated power spectrum density (PSD) of the motional current output signal for varying coupling strength, K_c. electrostatic drive forcing term set to unity

Figure 4.22 shows a simulated spectrum of both the resonators for an electrostatic forcing term. As observed, with the given set of operating conditions, motional current output signal from resonator 2 offers relatively lower noise floor as compared to resonator 1 and is *independent of the coupling strength* (refer Figure 4.22 (a) and (b)). In addition, it is beneficial to utilize output of j^{th} resonator at mode 2 as it offers a higher amplitude and thus maximum shifts (sensitivity).

From Figure 4.23, we can infer that smaller coupling strength in our design leads to reduced noise floor (about -12 *dB* gain in noise floor) for the resonating output of the j^{th} resonator (j = 1, 2).

4.8 Equivalent circuit Models in SPICE

We also perform analysis of our two coupled mass-spring-damper physical system by drawing the electrical equivalent circuit and use a software circuit-analysis program to determine the response. Since the mechanical dampers translate to electrical resistors and the Johnson noise of resistors is well known, we can estimate an effective mechanical-thermal noise into our system. Figure 4.24 illustrates a simplistic equivalent circuit representation for our two coupled resonators. Equivalent parameter values for electrical components such as R_m, L_m and C_m are computed using the formula as presented in chapter 1, section 1.1.1 above. A shunt coupling capacitor, *Cc* here represents an equivalent electrostatic coupling we used in the mechanical design. C_{per} models the applied stiffness perturbations. Voltage sources, *V1* and *V2* represent equivalent applied forces *F1* and *F2* respectively.

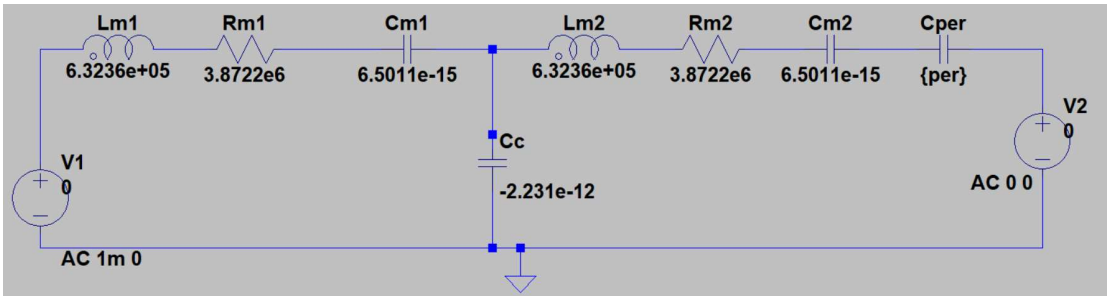

(a)

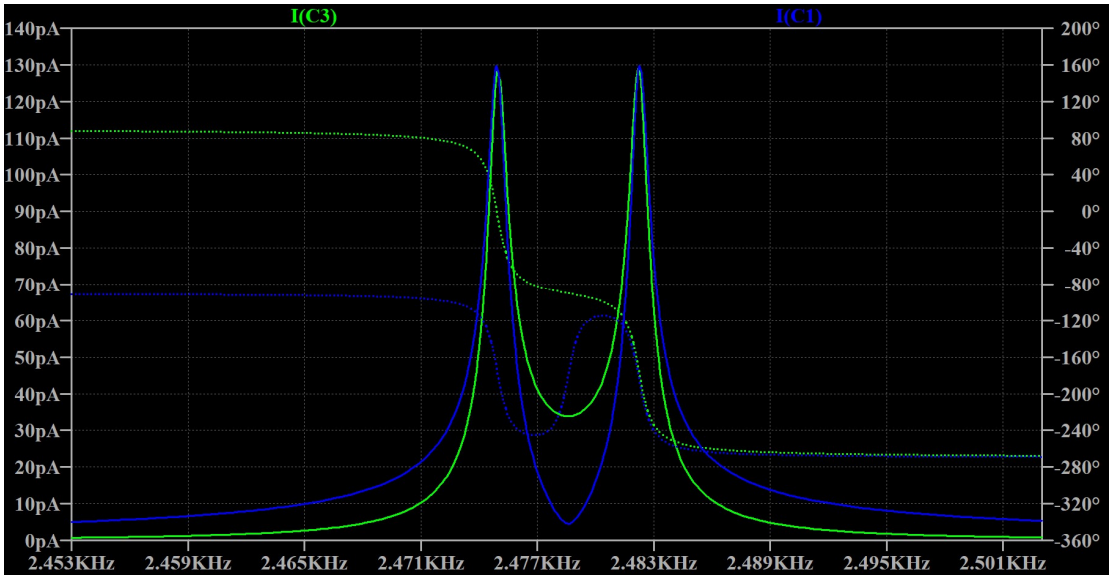

b)

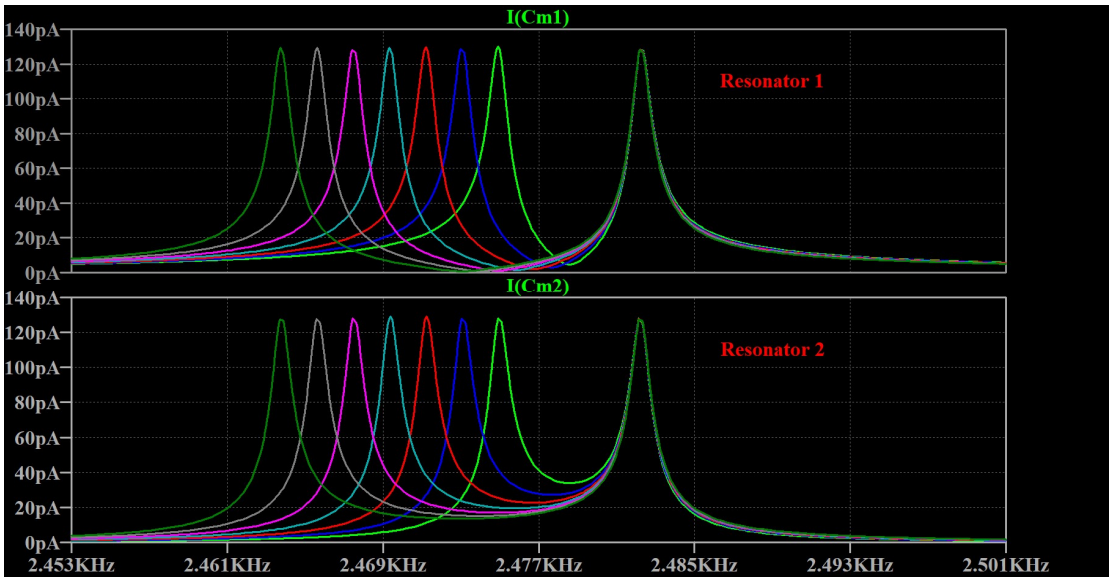

(c)

Figure 4.24 A SPICE analysis: (a) Equaivalent circuit model for our design, (b) Simulated graph of the motional current output signal for fixed coupling strength, K_c, left side of the

graph is magnitude and right side of the graph is phase, (c) frequency response as a function of varying (negatively increasing) coupling strength, K_c varying from -393.51 *N/m* to -1000 *N/m*.

Values of all the electrical components are as depicted in Figure 4.24 (a). Quality factor is taken to be about 2547 as derived in the condition in case II of section 4.2.2 above. This value of the quality factor provides a motional resistance of about 3.87 *MΩ* keeping all other parameters constant in equation of motional resistance as given in section 3.1.2 above. For the operation, *V2* is set to 0V and only *V1* is in action thus representing the condition of driving the resonator 1 with force *F1*. Due to the coupled action (owing to coupling spring constant), both resonators start resonating at the mode frequencies as captured in the frequency response shown in Figure 4.24 (b). Note that SPICE also verifies the working principle of our design as already explained in section 4.3 above. Figure 4.24 (c) shows simulated plots of the frequency response of both the resonators for varying coupling strength between them. Coupling capacitor is varied in the range of Cc = -2.2135×10^{-12} F, Cc = -2.4135×10^{-12} F, Cc = -2.6135×10^{-12} F, Cc = -2.8135×10^{-12} F (value negatively increasing and thus increasing the strength of electrostatic coupling).

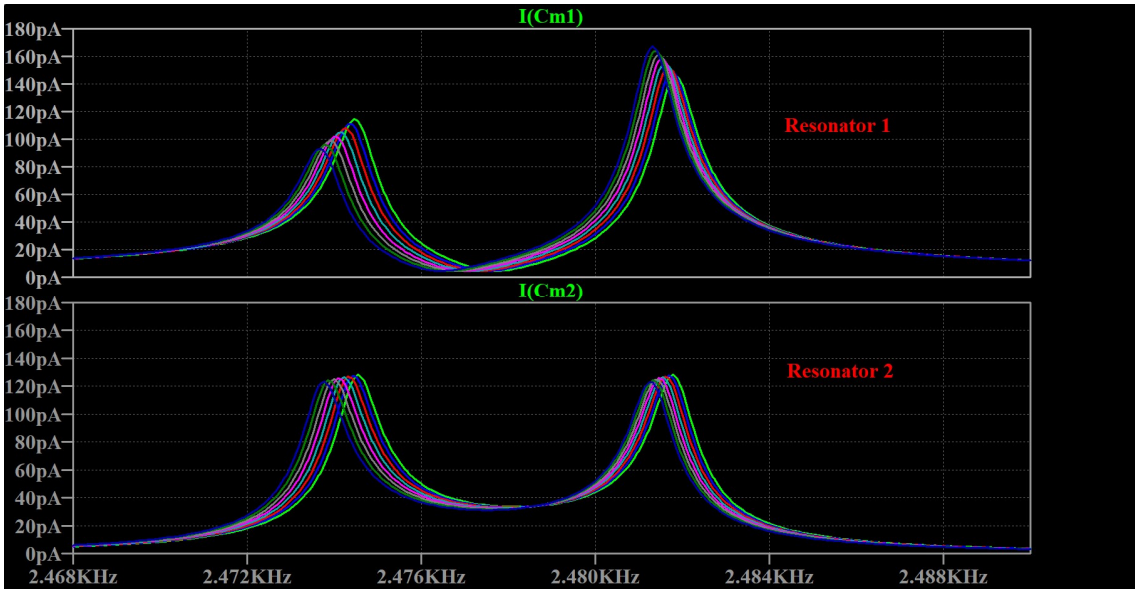

Figure 4.25 An effect of applied perturbations into the coupled resonator model for c = 0.0031 *Ns/m*, (Q ≈ 2547), $\Delta k \neq 0$, κ = -0.0032. Applied negative stiffness perturbations vary from -98.37 *N/m* to -238.37 *N/m*.

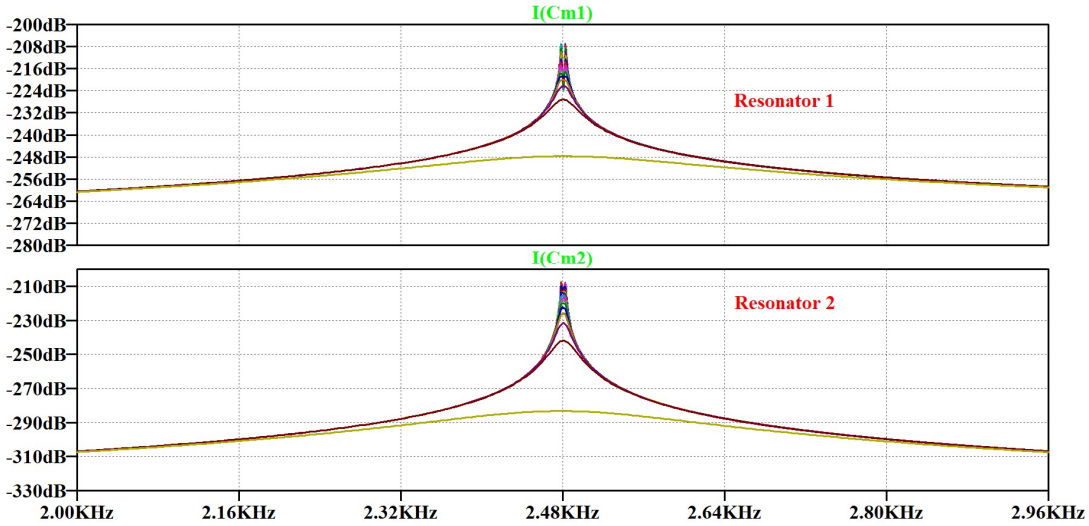

Figure 4.26 An effect of varying structural damping showing eventually modes being merged. Effective quality factor varies from 2600 to 10.

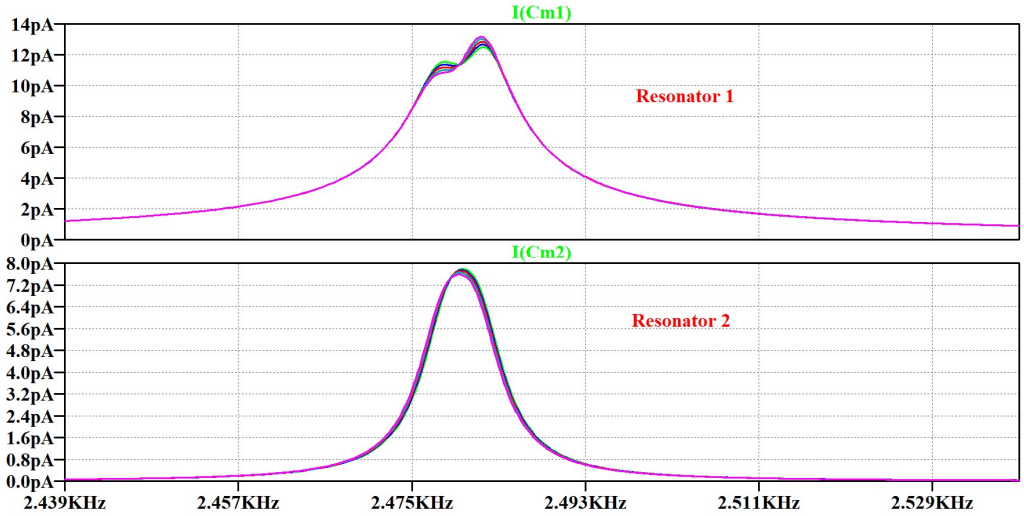

Figure 4.27 Simulated output response of the resonators for varying perturbations. Perturbation applied range from: Cper = -6.324e-12 F to Cper = -2.480e-12 F. Perturbation range from -51.62 N/m to -132.16 N/m. An extracted value of the quality factor, Q from the model is about 410.

Figure 4.25 shows an effect of applied stiffness perturbations into the coupled resonator electrical model. Applied equivalent negative stiffness perturbations is shown in Table 4.4.

Table 4.4 Calculation for applied stiffness perturbations

Sr. No.	C_{per} (F)	Δk (N/m)
1	-8.85×10^{-12}	-98.37
2	-6.14×10^{-12}	-141.66

3	-5.23×10^{-12}	-166.25
4	-4.51×10^{-12}	-192.82
5	-3.45×10^{-12}	-251.84

Figure 4.26 shows an effect of an effect of varying effective structural damping showing eventually modes being merged. Effective quality factor varies from 2600 to 10. Figure 4.27 shows simulated output response of the resonators for varying perturbations. Perturbation applied range from: C_{per} = -6.324e-12 *F* to C_{per} = -2.480e-12 *F*. Perturbation range from -51.62 *N/m* to -132.16 *N/m*. An extracted value of the quality factor, *Q* from the model is about 410.

4.9 Amplitude stability of output signals

Figure 4.28 shows a model built using Simulink incorporating an effective noise power that stem from the electronics. A noise source is added into the readout path of both the resonators. An equivalent noise power used in our model here represents theoretically estimated effective *rms* noise current (refer Table 4.2) with all the accountable noise sources in each of the readout path (resonator + electronics). Model parameters set are same as given in Table 4.1 and simulations are run for the operating conditions as follows: c = 0.0031 *Ns/m* (Q = 2547), δ_k = 0 (*normalized*), proof mass M_1 driven by net electrostatic force at the resonant mode frequency, ω_i (i = 1,2). As explained in section 4.6 above, a motion current output from each of the resonator is converted to amplified voltages (by factor R_f = 1$M\Omega$), $vout_j$ (j = 1, 2).

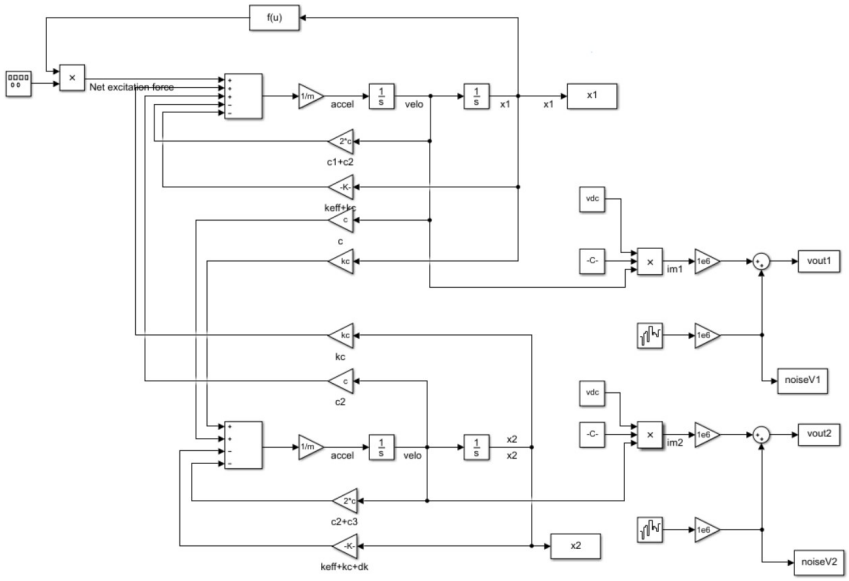

Figure 4.28 A model for the noise analysis in a coupled resonators

Figure 4.29 shows a simulated effective noise floor in one of the output readout path (resonator 1 in our case). An effective value of noise current is ≈ 0.7 × 10^{-13} A_{rms} that is a reasonable match with what we estimated in theory (≈ 1.56 ×10^{-13} A_{rms}) of our design. (refer Table 4.5)

Table 4.5: Noise estimation in macro-scale coupled resonator design

Noise floor estimate for our design		
Sr. No.	Theory calculation	Simulation
Noise current (A_{rms})*	1.56×10^{-13}	$\approx 0.7 \times 10^{-13}$

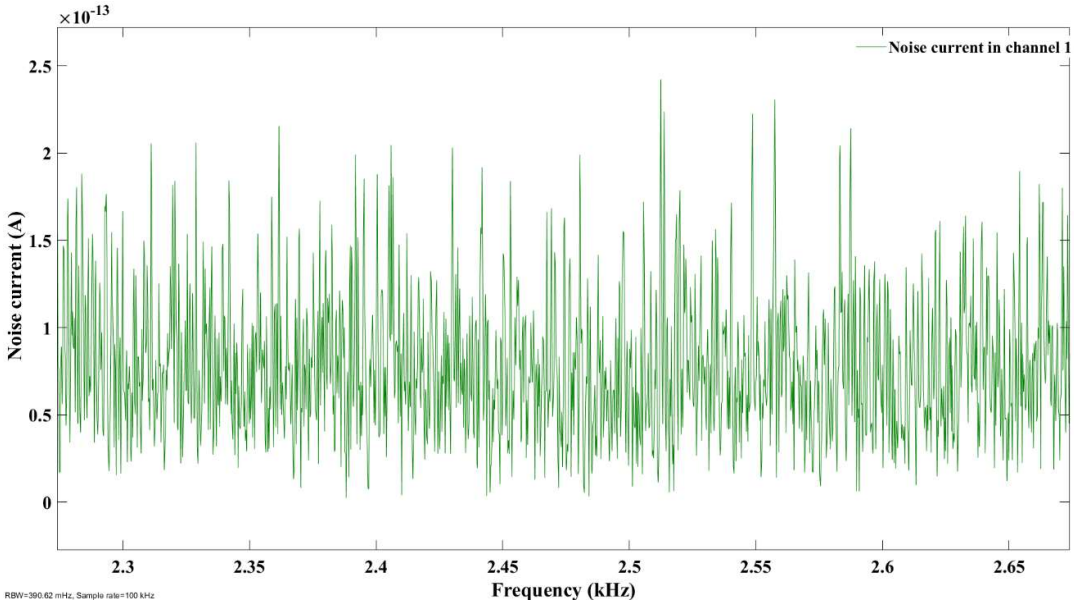

Figure 4.29 Simulated effective noise floor in either of the output channel. A simulated value of effective noise current is $\approx 0.7 \times 10^{-13}$ A_{rms} (equivalent to -263 *dB* for reference load of 1 Ω)

Figure 4.30 shows steady-state time plots of output signals (motional current outputs) in our design with increased noise levels in the system ($\approx$ 100 pA_{rms}). Output signals for both the modes are shown. We therefore computed the relative shifts into the amplitudes of im_1 and im_2 at the in-phase mode for range of applied perturbations into the stiffness. We subsequently determined the sensitivity in the presence of a noise for a given set of operating conditions as given in case II of section 4.2.2. As observed from Figure 4.30, in-phase mode provides relatively higher amplitudes of motional current output signals (for a given $Q \approx 2547$). This resulted in higher amplitude ratio based sensitivity (for the in-phase mode) to the applied stiffness perturbations. Moreover, in-phase mode showed better amplitude stability as compared to its out-of-phase mode counterpart. Therefore, it is recommended to choose to lock to the in-phase mode of this device for variety of sensing applications.

Figure 4.31 captures a mode-localization effect at the in-phase mode frequency, in the presence of a noise into the system for applied stiffness perturbation, $\delta_k = -0.0019$ (normalized). As stated earlier, amplitudes of motional currents, im_1 and im_2 at the in-phase mode frequency are higher and thus relatively stable as compared to its out-of-phase mode counterpart. Therefore, we can infer that with increasing noise floor in the system, while the amplitudes and hence the relative shifts are difficult to resolve in either resonators at the out-of-phase mode, an in-phase mode can be utilised in this situation to determine sensitivity and/or resolution for a given operating conditions.

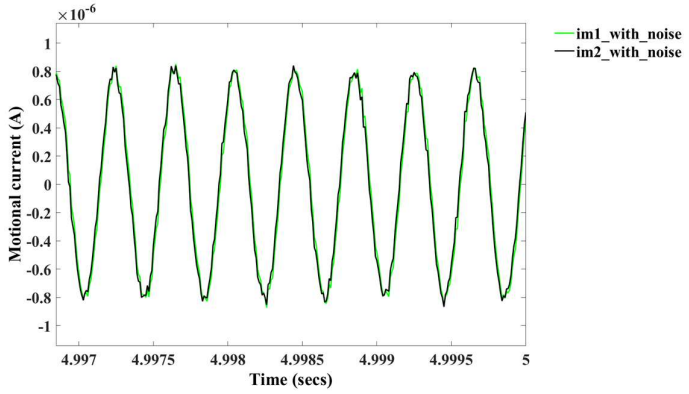

(a)

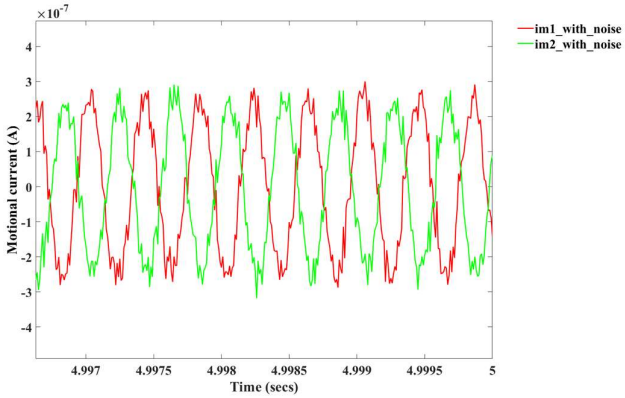

(b)

Figure 4.30 Simulated time-plots of a motional currents im_1 and im_2 at (a) in-phase mode frequency, (b) out-of-phase mode frequency. Operating conditions are $\delta_k = 0$ and (Q =2547). Added noise level is ≈ 100 pA_{rms}

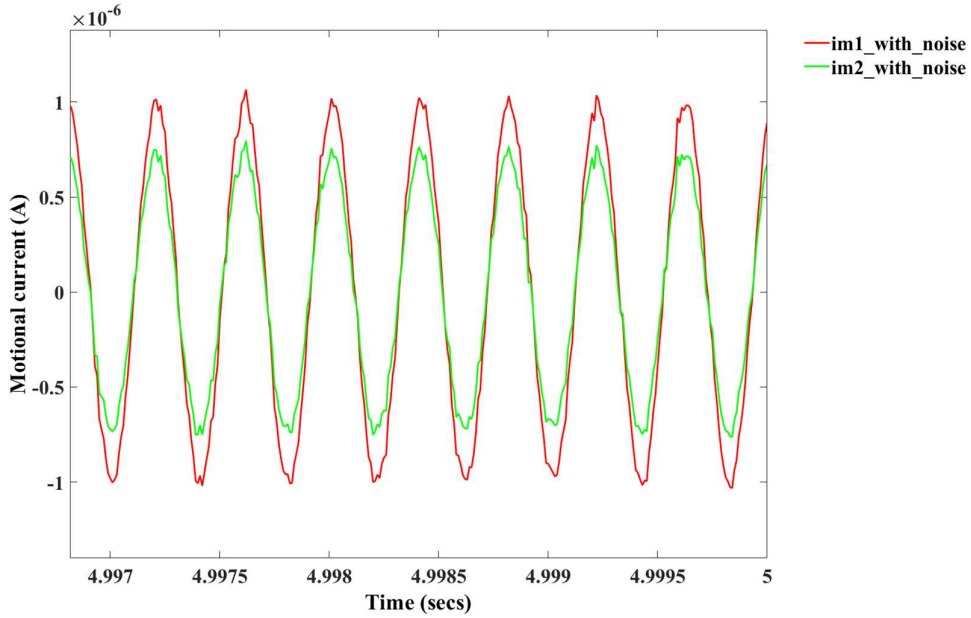

Figure 4.31 Mode-localization at the in-phase mode frequency, in the presence of a noise into the system. δ_k= -0.0019 (normalized) Q=2547 approximately. In-phase mode chosen because it showed better amplitude stability as compared to its out-of-phase mode counterpart

4.9.1 Spectral analysis

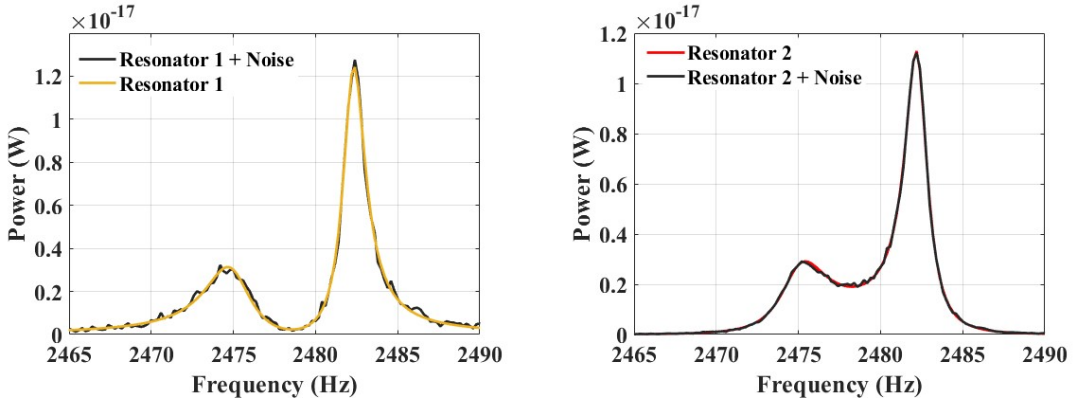

(a) (b)

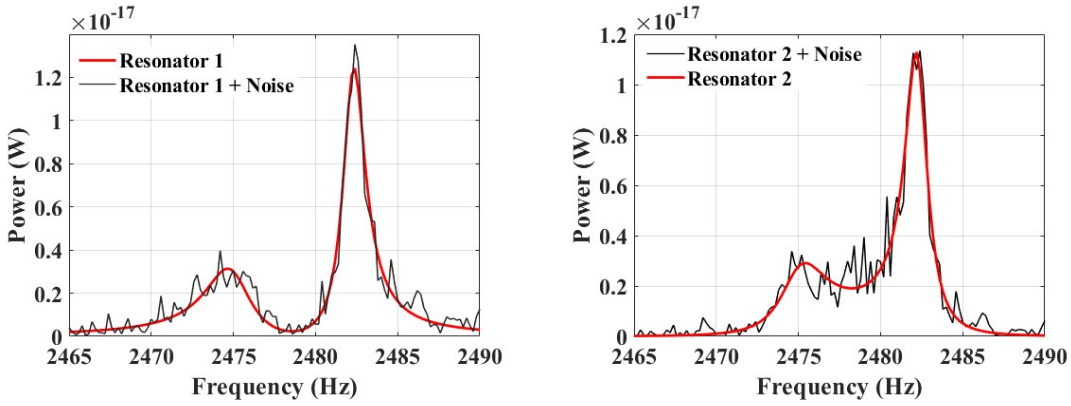

(c) (d)

Figure 4.32 Simulated power spectrum of our design across the frequency range of interest. (a) and (b) with less noise current, (c) and (d) with increased noise current, operating conditions is given in case II in section 4.2.2.

Figure 4.32 illustrates a power spectrum of our design for the motional current outputs for the condition $c = 0.0031$ *Ns/m*, ($Q \approx 2547$), $\Delta k = 0$, $\kappa = -0.0032$, excitation force $F \approx 149$ μN applied to mass M_1. Signal power levels at the resonant frequencies are determined with and without noise added to the system. A value of an effective noise power used in the Simulink block is $\approx 1\times10^{-26}$ W and $\approx 1\times10^{-24}$ W for two cases respectively as shown in Figure 4.32. Figure 4.33 represents the similar representation as in Figure 4.32 except that Y-axis scale is logarithmic.

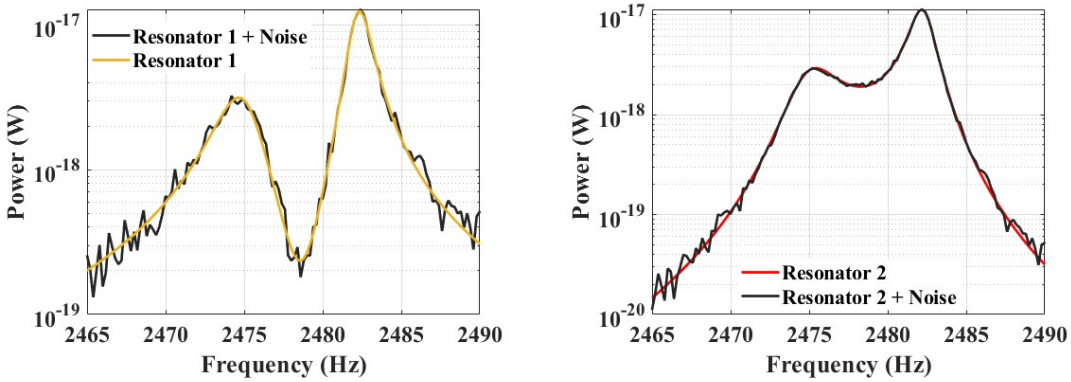

(a) (b)

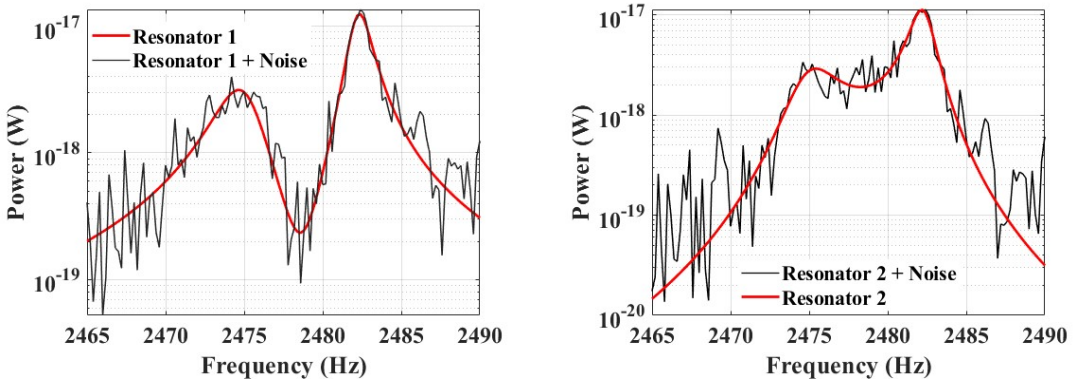

(c) (d)

Figure 4.33 Simulated power spectrum of our design across the frequency range of interest. (a) and (b) with less noise current, (c) and (d) with increased noise current, operating conditions is given in case II in section 4.2.2. Y-axis is log-scale.

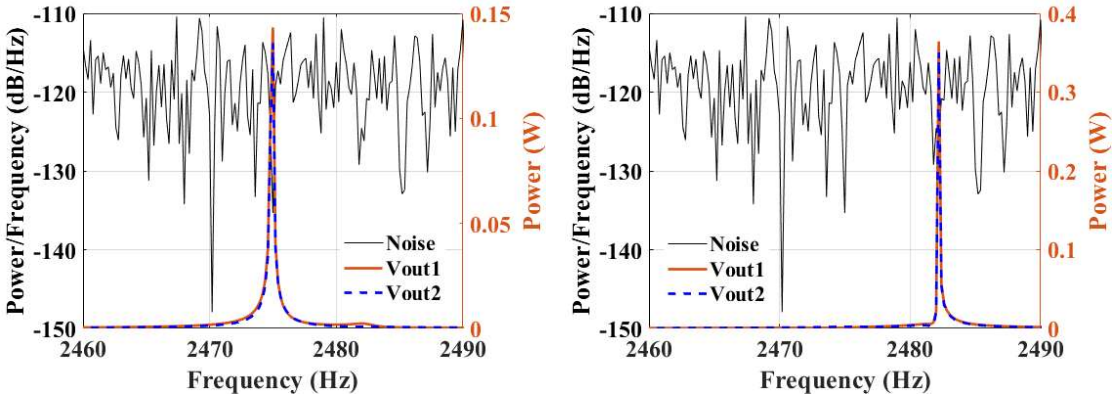

(a) (b)

Figure 4.34 Simulated PSD and power spectrum plot: For an effective output referred noise (left y-axis) and signal power output (right y-axis) for (a) mode 1 and (b) mode 2 in our two scaled-up weakly coupled 2 DoF architecture

Figure 4.34 presents PSD curves (left Y-axis) of an effective output referred noise power and power output signal for j^{th} resonator at the mode 1 and mode 2 of the frequency response, respectively. We used MATLAB to estimate the signal's total average power by "integrating" under its PSD curve. A calculated average power for noise is $\approx 1\times 10^{-7}$ W (equivalent to effective output referred noise voltage of 3.16×10^{-4} Volts). Note that, actual estimated noise floor (both in theory and simulation) is $\approx 1\times 10^{-13}$ Amp (1×10^{-26} W), which, post amplification (by factor 1 $M\Omega$), provides a output referred noise voltage $\approx 1\times 10^{-7}$ Volts (1×10^{-14} W). A

calculated average signal power is ≈ 0.2 Volts (0.07 W) for resonator 1 and 0.254 Volts (0.064 W). All our calculations are for a reference load of 1Ω.

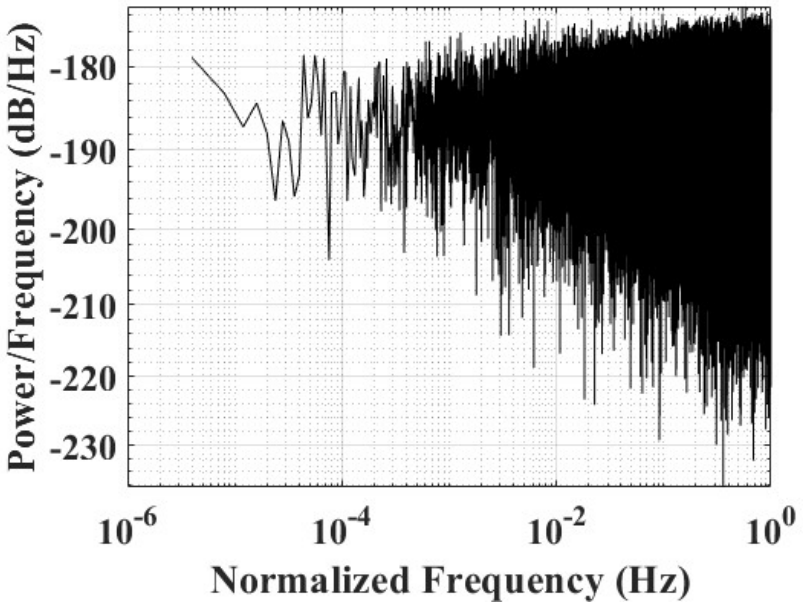

Figure 4.35 Amplitude noise PSD in our design

Figure 4.35 shows a PSD plot of an effective output referred noise plotted against a normalized frequency. This corresponds to the estimated amplitude noise in either channel of the resonator output.

4.10 Closed-loop arrangement

Figure 4.36 depicts a system-level model we developed for our design in a closed loop configuration. A simple phase-locked-loop (PLL) circuit was utilized to model the effect of resonant mode-frequency tracking in our system. For better locking to the corresponding modes, we amplified the motional current outputs by factor 1×10^6. Motional current output from the resonator 1 was used as a reference signal to the phase-detector block of the PLL.

In the closed-loop arrangement, we made sure that a net electrostatic force (time varying) that is exerted on the proof mass M_1 is of the same order in magnitude as in the case with the open-loop (refer Figure 4.3). We then applied the range of stiffness perturbations in to our model and simulated the time-plots of the motional currents of the j^{th} resonators at the *in-phase mode* of the frequency response. As explained in the previous section 4.9 above, an in-phase mode was chosen for the simulation at ($Q \approx 2547$) as it offers higher signal level and thus higher shifts against applied stimulus perturbations (sensitivity) and/or resolution in our design. We then recorded the steady-state motional current amplitudes of the j^{th} resonator as a function of applied stiffness perturbations (mode-localization effect in our macro-scale two weakly coupled resonators).

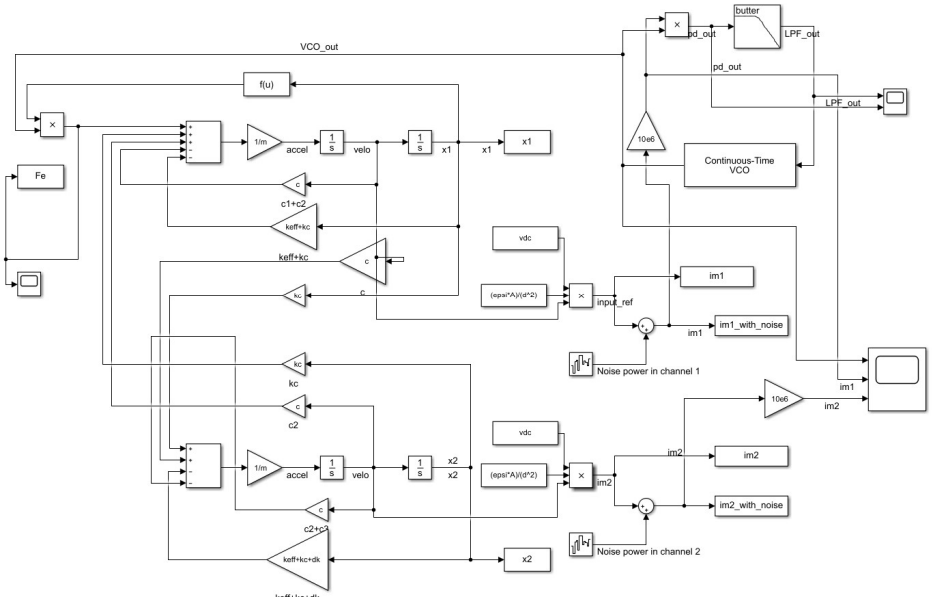

Figure 4.36 Simulink model for a closed loop arrangement

4.10.1 Design of a PLL

A phase-locked loop (PLL) in our design consist of phase-detector, low pass filter and a voltage controlled oscillator (VCO). A (VCO) output frequency is given as

$$F = (K_{vco} \times V_{ctrl}) + F_{out} \tag{4.13}$$

where, K_{vco} is the voltage sensitivity of the VCO (*Hz/V*), V_{ctrl} is the control voltage, and, F_{out} is the free-running frequency of the VCO [106].

In our design, applied stiffness perturbation range (Δk_{min} = -98.3 *N/m* to Δk_{max} = -251.8 *N/m*). For this range, we computed maximum theoretical variation in the mode-frequencies to be 1.3 *Hz* and 1 *Hz* for the out-of-phase mode and the in-phase mode, respectively. In both the modes, lowest possible frequency shift is 0.1 *Hz*. This requires the VCO sensitivity to be about 1 *Hz* for frequency tracking in our design. We calculated parameter K_{vco} from the above expression and determined its value to be 1 *Hz* and found (through simulation) that VCO frequency is scaled appropriately subject to applied perturbations in the system.

Table 4.6 below provides simulated mode-frequency shifts for both open and closed-loop case.

Table 4.6 A frequency tracking table for the comparative purpose.

Sr. No.	Parameters		Frequency of output signal *im1*/*im2* (*Hz*)		
	Δk (*N/m*)	δ_k (normalized)	Open-loop	Closed-loop	VCO output frequency in closed-loop (*Hz*)
1	0	0	2482	2484	2484
2	-98.3	7.88×10^{-4}	2482	2484	2484
3	-141.6	1.134×10^{-3}	2482	2483	2483
4	-166.6	1.331×10^{-3}	2482	2483	2483

5	-192.8	1.544×10^{-3}	2481	2483	2483
6	-251.8	2.017×10^{-3}	2481	2483	2483
*In-phase mode was chosen as it offered higher output signal level					

Operating condition are ($Q \approx 2547$); $\Delta k \neq 0$. A proof mass M_1 is driven at in-phase frequency, ω_{ip} that is a function of Δk, in both the circuit configuration. An in-phase mode was chosen for the operation since motional current amplitudes of both the resonators were found to be oscillating with higher amplitudes at this mode relative to the oscillation amplitudes at the out-of-phase mode). This resulted in higher amplitude ratio based sensitivity to stiffness perturbation for in-phase mode as compared to the out-of-phase mode.

Note that maximum amplitude ratio based theoretical sensitivity $\left|\frac{\Delta k}{2k_{eff}}\right|$ as derived in [49] can be determined for our design and it is about 170 for amplitude ratio based output.

Figure 4.37 shows a comparative performance for amplitude ratio based outputs in open and closed loop. Sensitivity in closed-loop configuration is seen to be enhanced due to closed-loop operation. A plot shown in Figure 4.37 shows a similar trend as demonstrated in [15], where, a sensitivity of amplitude ratio to the stiffness perturbation is seen higher in closed loop as opposed to in open loop. A good agreement was found between open loop and closed loop simulated graphs. From the graph, linearity for stiffness sensing applications also seems to be improved in closed loop arrangement.

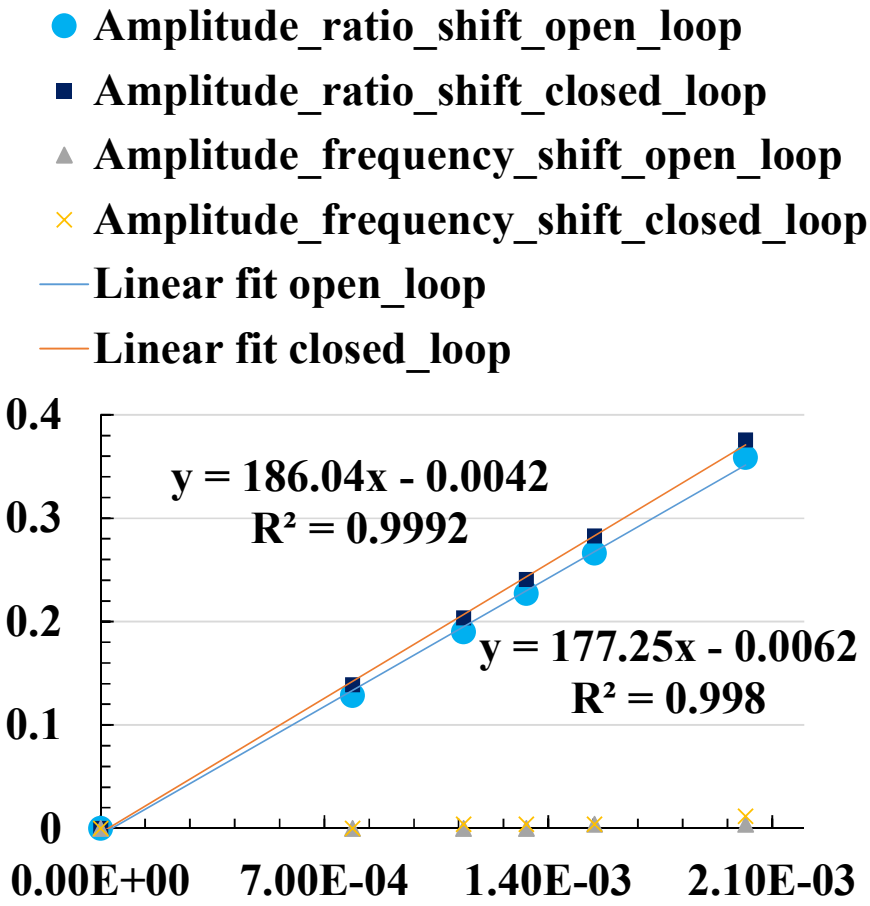

Figure 4.37 A comparative performance of our design in closed-loop and open loop circuit arrangement. Graphs obtained from the simulation of a model of our macro-scale coupled resonators.

Summary

In this chapter, we developed system-level models for our macro-scale coupled resonators for stiffness sensing applications. A model was simulated for variety of operating conditions such as quality factor, coupling coefficient between resonators, etc. An in-phase mode of a design exhibited higher amplitude ratio based sensitivity (about 187). This sensitivity is comparable to that achieved with 2 DoF MEMS coupled resonator architecture. We developed models to determine an impact of intrinsic and extrinsic noise sources in our design. We theoretically derived a noise floor of our design and found a good agreement of our calculations with the simulations. With the derived noise floor of our design, we also theoretically calculated minimum resolvable shifts (1.21×10^{-7}) in the output metric and thus resolution ($\approx 4.8 \times 10^{-3}$) of our macro-scale design. These values are also comparable to that achieved with MEMS coupled resonators. A closed-loop configuration of our design showed enhanced amplitude ratio based sensitivity and linearity to the applied stiffness perturbations as compared to when operated in open loop for the associated in-phase mode of operation.

Chapter 5

5 Fabrication

In this chapter, we explore the possibilities to fabricate our design prototype using state-of-the-art nonconventional micromachining technology. In general, we utilized fabrication platform at the University of Liege and from the manufacturing service provided by Synova, Inc. We then compared the fabrication outcome from both these places. We then carried out test and electrical characterization of our developed prototype and initial measurements are presented.

5.1 Overview of fabrication techniques

Here, various emerging and nonconventional yet high-tech fabrication methods and their overview is presented. These methods are particularly useful in creating various devices/structures particularly with range of new materials, which can otherwise be a challenge to process in a typical clean room used for micromachining. Potentials and demerits are studied and best machining method to develop our application is justified through technical reasoning.

5.1.1 Wire-electro-discharge machining (EDM)

In electro-discharge machining (EDM) category, micro-wire EDM process also appears to offer a smallest electrode wire diameter up to 20 μm [35]. A stainless steel with 100 μm thickness, a kerf-width of 30.8 μm (thus aspect ratio defined as the quotient of workpiece thickness to kerf-width of about 3) was shown in [107]. Usage of wire-EDM technique was shown for slicing silicon into wafers [108] with a kerf width of > 140 μm. A hexagonal microelectrode arrays (with tungsten carbide as a workpiece) with side length of 40 μm (with aspect ratio of 17.5) was also reported in [109]. In industry [110], a service is available to machine kerf-width of > 100 μm into variety of materials with larger thickness, thus leading to very high aspect ratio. We studied that while wire-EDM offers a potential to fabricate a high standing structure, it however falls short in capabilities to machine a below 100 μm capacitive gap (kerf-width) as thickness of a metal workpiece increases (for e.g. > 1 mm). This limitation poses a challenge to perform electrostatic transduction on to device under our consideration. In addition, EDM is associated with slow ablation process, time-consuming preparation, and expensive consumables (e.g. EDM wire) [111].

5.1.2 Additive manufacturing (3D printing)

In the area of additive manufacturing, we reviewed the printing methods in the context of fabricating a planer structures. A metal-insulator-metal capacitors was fabricated on a flexible structure using inkjet printing method [112]. A millimetre scale parts were made using 3-D inkjet printing [113]. A 3D printed coils/inductors were demonstrated in [114,115]. In [115], a coils, helical springs on a silicon substrate, a butterfly 3D structure on a plastic structure were printed. A capacitive touch sensor fabricated using aerosol jet based additive printing method was shown in [116]. A capacitive humidity sensor [117,118] was also reported by inkjet print method. A micro-scale interdigitated capacitive humidity sensor on paper substrate [119] was shown. An air-gap MEMS switches on plastic lamination for RF power transmission was

demonstrated in [120]. Using printing method, microelectromechanical relay [121], a strain gauge [122], relay switch [123] was also reported.

An additive manufacturing such as 3D printing [124] seemed promising technology in realizing our prototype. However this method, usually involves deposition of a conducting ink (for e.g. silver nanoparticles) supplied by annealing process as a following or combined step for printing the structures (for e.g. metallic) on a substrate (e.g. plastic). Printing methods also has issues such as lateral resolution, structural thickness control [125]. Moreover, in our observation, there is no encouraging literature available on printing a moving planer structure (based on electromechnical transduction) with sufficiently high aspect ratio. ***This is central idea of our work presented in this thesis.***

5.1.3 Laser micromachining

Laser micro-machining is a widely-used manufacturing process, wherein a laser beam is focused to melt and vaporize unwanted materials from the workpiece [126]. Conventional dry laser micro-machining is an efficient manufacturing process because of its high lateral resolution, low heat input, and high flexibility [38]. The benefit of laser micromachining is the possibility to utilize new materials to enhance device performance [36]. Creating micro-cuts/trenches using a laser is a function of laser machining parameters such as speed, power, focus, etc. We found that laser machining has been used for making micro-cuts, drilling holes, engraving or forming embroidery onto a piece of a material [35–39,126]. Laser machining has also been used in creating channels for microfluidic applications [40–42], and realizing micro-optical devices using photoresist [43]. A lowest possible kerf-width, $> 200\ \mu m$, (with steel as a workpiece) was reported in [127]. A narrow kerf width ($< 0.4\ mm$) in [128], $\approx 200\ \mu m$ in [129], $\approx 103\ \mu m$ in [130] and, $> 300\ \mu m$ in [131] was demonstrated. Fibre metallic laminates up to 10 *mm* thickness were cut using abrasive waterjet process resulting in a kerf-width of $\approx 500\ \mu m$ [132]. A laser cutting of aluminium, titanium, and steel using a water jet guided laser was demonstrated in [133] resulting in kerf-width between 100-120 μm, thus giving high aspect ratio of 12.5 in steel, 39.2 in titanium, and 66.7 in aluminium. An aspect ratio of 5.7 with a kerf width of 35 μm post cutting 200 μm stainless steel was shown in [134].

For the reasons explained in 5.1.1 and 5.1.2 above, neither wire-EDM, nor printing method is preferable to fabricate a micro-gap capacitive transducer featuring electrostatic actuation and capacitive sensing in the same device. As a industrial solution[111,135,136], we eventually resolved to use direct laser writing (DLW), a state-of-the-art laser technology that simultaneously offered us a required relatively lower micro-gap ($\approx 60\ \mu m$) into the thick (up to 2 *mm*) piece of metals (aluminium and stainless steel). This leads to high standing parallel capacitive walls in our fabricated prototype, to favour an electrostatic actuation and capacitive sensing in resonators.

Using a state-of-the-art laser technology provided by Synova Inc. [136] we developed our *first-generation* device prototype of an electrostatically coupled two DoF resonating sensor. This laser technology offered us numerous advantages such as high-aspect-ratio (> 33) with a reasonable mechanical precision, parallel kerf walls (i.e. no V-shape), unlike in [137,138], relatively smooth cutting surfaces, etc. [136]. A prototyping fabrication method as proposed here can be particularly useful when there is no cleanroom access and there is a requirement

for quick prototyping with materials other than silicon. This can potentially also be extended for small or medium-scale series production.

To our knowledge, this is the first time that direct laser writing (DLW) is used to manufacture a capacitive resonating device/sensor.

5.2 Fabrication at the University of Liege

First, we report on the fabrication activity that was carried out in the clean room of Microsys laboratory at the University of Liege. An outcome of this activity is also reported in this chapter.

It was envisaged that fabricating a micrometer size capacitive gaps for electrostatic transduction could be a challenging with the fabrication method other than traditional silicon micromachining. Therefore, we researched other alternative microfabrication methods as explained in sections 5.1.1 through 5.1.3 above.

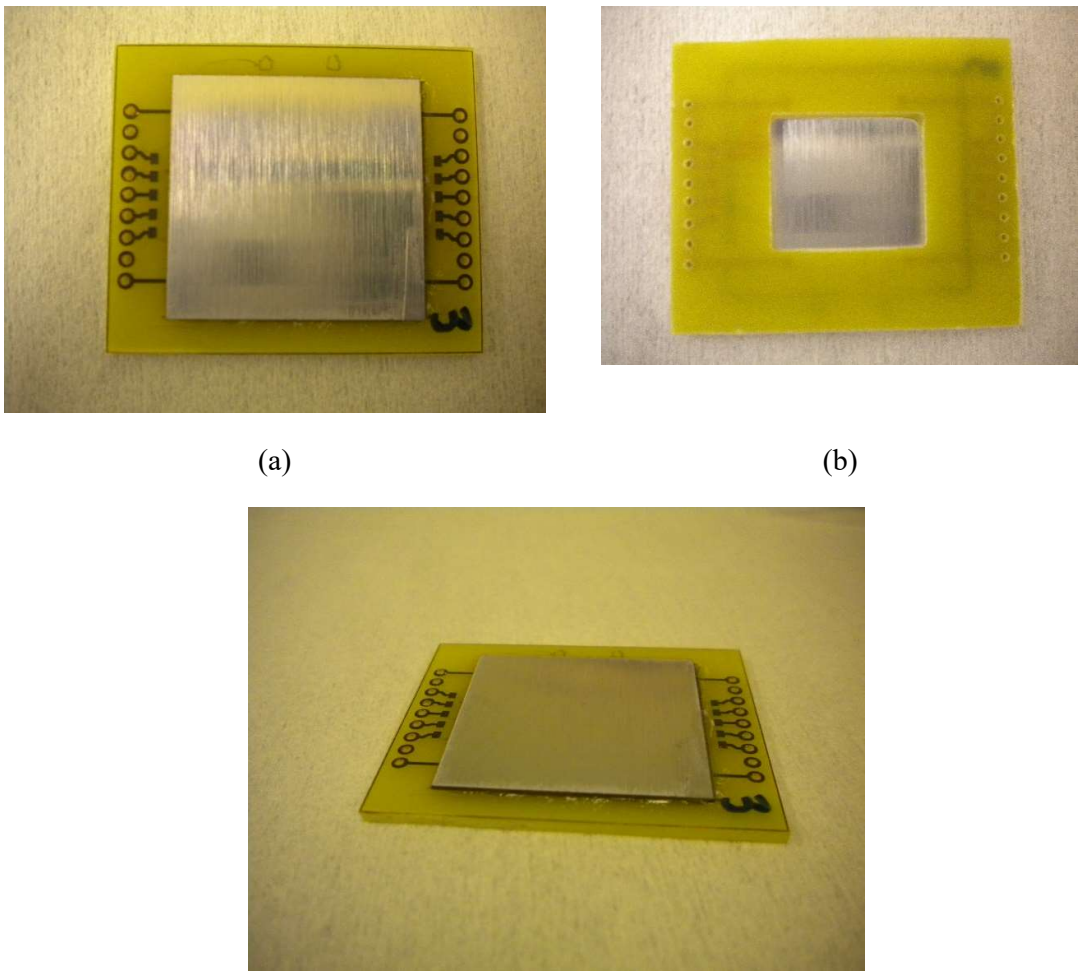

(a) (b)

(c)

Figure 5.1 Sample prototype preparation at the University of Liege through laser ablation method. (a) top view , (b) bottom view, and (c) side view

Figure 5.1 explains a fabrication procedure for the prototype fabricated using laser machining at the University of Liege. Initially, a printed circuit board (PCB) was manufactured with copper tracks to facilitate an electrical connection with the outside measuring equipment. A piece of metal (aluminum with the thickness of 0.5 millimeter) was glued on top of this PCB as can be seen from Figure 5.1 (a). According to our theoretical calculations, an aspect ratio (i.e. *the quotient of workpiece thickness to capacitive gaps*) of about 5 was anticipated post fabrication. This means, we expected to machine a trenches (through the thickness of a metal workpiece) of about 100 micrometers into the aluminum of 500 micrometer thickness. Total size of a prototype is 30 mm^2. Total size of a PCB as a substrate is 45 mm × 37 mm. As Compared with few micrometers capacitive gap size in MEMS devices, we needed to scale-up a cross-sectional capacitive area to keep the same order of capacitance as in MEMS. All related computations and analysis on this is explained in chapter 3.

In Microsys clean room, we attempted to fabricate a kerf width of required size. For this, various parameters of laser machining equipment such as laser wavelength, pulse duration, and power was varied. Figure 5.2 shows optical images of the developed prototype highlighting various features.

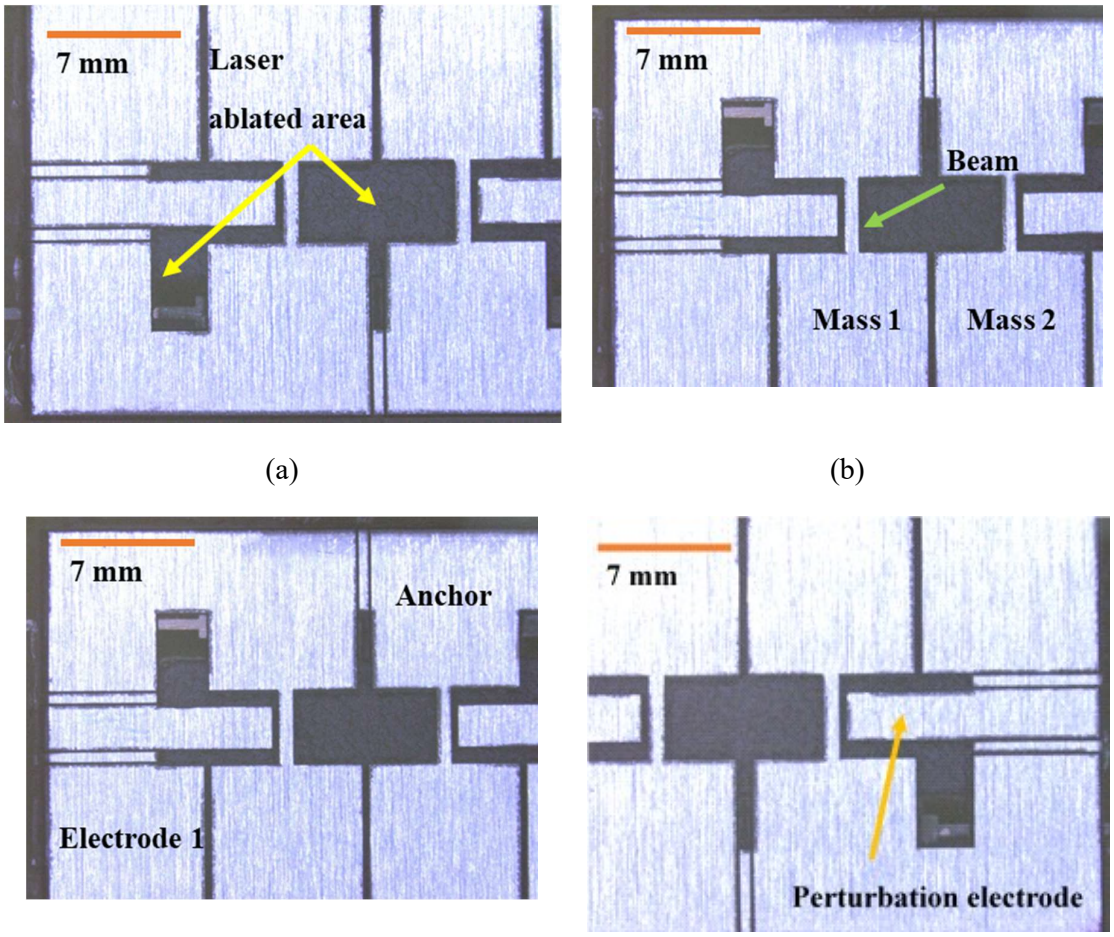

(c) (d)

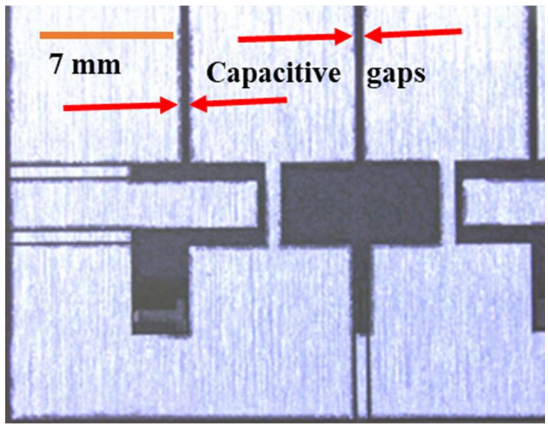

(e)

Figure 5.2 Optical images of a fabricated prototype at the university campus highlighting various device features. (a) metal ablated area, (b) proof masses with beam suspension, (c) electrode to apply electrostatic drive force to proof mass 1, (d) electrode to apply perturbation and (e) kerfs (also called capacitive gaps)

Figure 5.3 shows optical images for the capacitive gap measurements at various location of a developed prototype. A measured gap in this prototype is > 240 μm. In addition, we can notice that there is inconsistency in the size of a gap at several locations on the prototype. This large size of a capacitive gap implies that force of actuation, Fe $\approx F_e \approx \frac{\varepsilon A}{d^2}\left(V^2\right)$ at the resonance

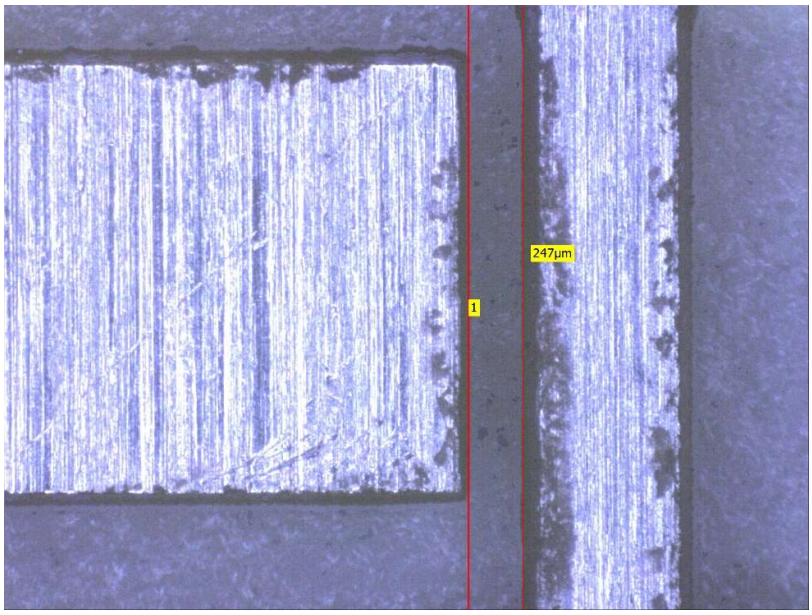

(a)

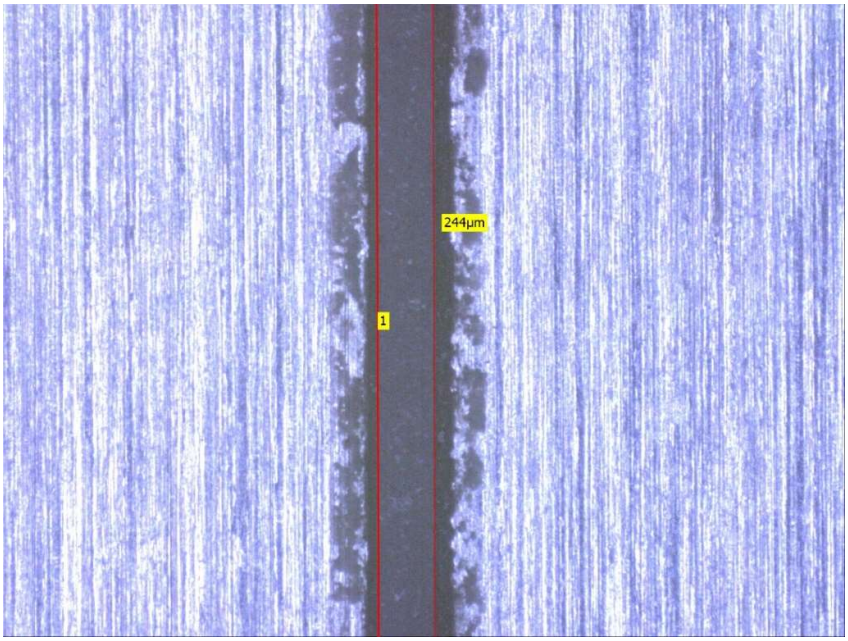

(b)

Figure 5.3 Measurement of a laser cuts (capacitive gaps) in a fabricated prototype

would be low for the designed area, polarization voltages, etc. Further scaling-up in area and/or applied voltages was not possible given the limitation on the minimum size of a gap that we achieved post fabrication.

Figure 5.4 shows a finished part of out prototype highlighting front and backside. Theoretically, it is possible to actuate electrostatically this device for a coupled resonance as intended. However, for similar magnitude of polarization voltages as in MEMS, *i.e.* 50 *V* in [23], net actuation force would be low (in the *nN* range) for a fabricated capacitive air gap of > 240 micrometres and transduction area of about 7 *mm* × 0.5 *mm* (proof mass length × thickness of this prototype). Moreover, computed motional resistance in this fabricated prototype (for a quality factor of about 2500), is approximately $10^{11}\,\Omega$. Based on our computations, even when we intend to scale-up the applied voltages to several hundreds of volts (thus higher net actuation force), a signal detection above the induced effective noise floor in this system would be a challenge in this developed prototype.

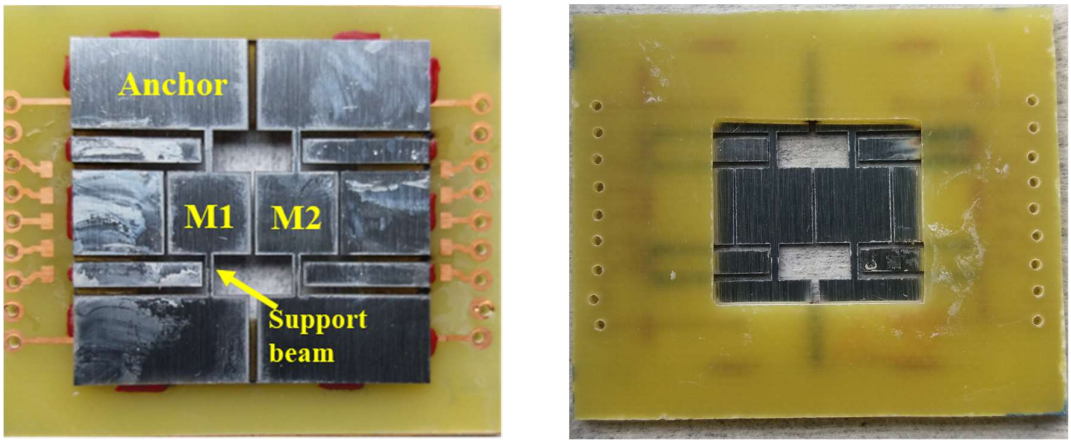

(a) (b)

Figure 5.4 A picture of a finished prototype (a) front view and (b) back view

5.3 Fabrication with the outside company

After studying the outcome of our fabrication at the University of Liege, and, our research on several other micromachining possibilities as explained in 5.1.1 through 5.1.3 above, we approached to a laser micromachining service industry, Synova Inc. [111] and opted to fabricate our prototype with this company. This company offered us to fabricate a relatively smaller and consistent laser cuts thus leading to a capacitive gaps (about 60 micrometers). In addition, it also allowed us to fabricate a structure with high aspect ratio (> 33).

5.3.1 3D AutoCAD file

Post analysis of our design and computations, we discussed the fabrication plan with this company (Synova Inc.) and agreed to submit them an engineering drawing file of our design. Figure 5.5 presents an AutoCAD diagram that was created using a Freecad software [139]. We maintained accuracy and consistency in modelling all the features of our design. Designed kerf-size or capacitive gaps for transduction are ≈ 60 μm. A total size of a drawn pattern is about 80 × 61.3 mm^2. All dimensions are in millimetres (mm). Two metals such as aluminium and stainless steel were used for the fabrication purpose.

Figure 5.6 depicts a 3D finalized pattern that was modelled using a Freecad software [139]. A design consists of a parallel plate capacitors (with about 60 μm gaps) to fabricate a structure for two coupled resonators (referring to Figure 5.6 (a)). Figure 5.6 (b) represents a 3D view of the same design. A design file (with *.dxf, .iges and .stl* format) was sent to the manufacturing company [111]. A choice of fabricating a structure with only two proof masses was made due to the following reasons. A) it was a feasibility test supplied by high development cost of about 800 CHF as supposed by the manufacturing company, and II) adding more resonators in this already scaled-up structure would further have increased the total size of a device which would not fit the vacuum chamber of a fixed size during the test in the laboratory.

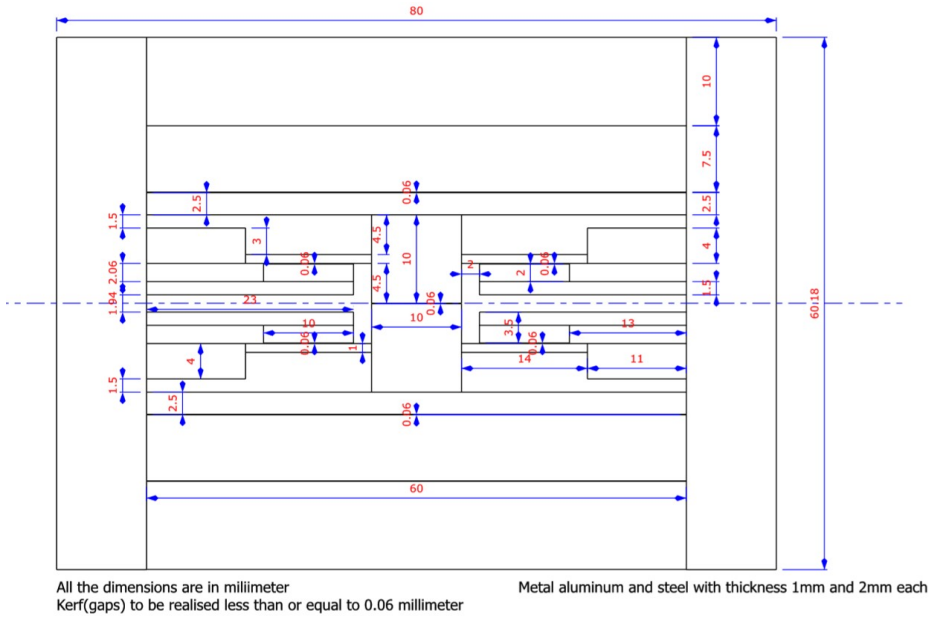

Figure 5.5 An AutoCAD diagram (created using Freecad software [139]) showing all the dimensions for the device features. All dimensions are in *mm*

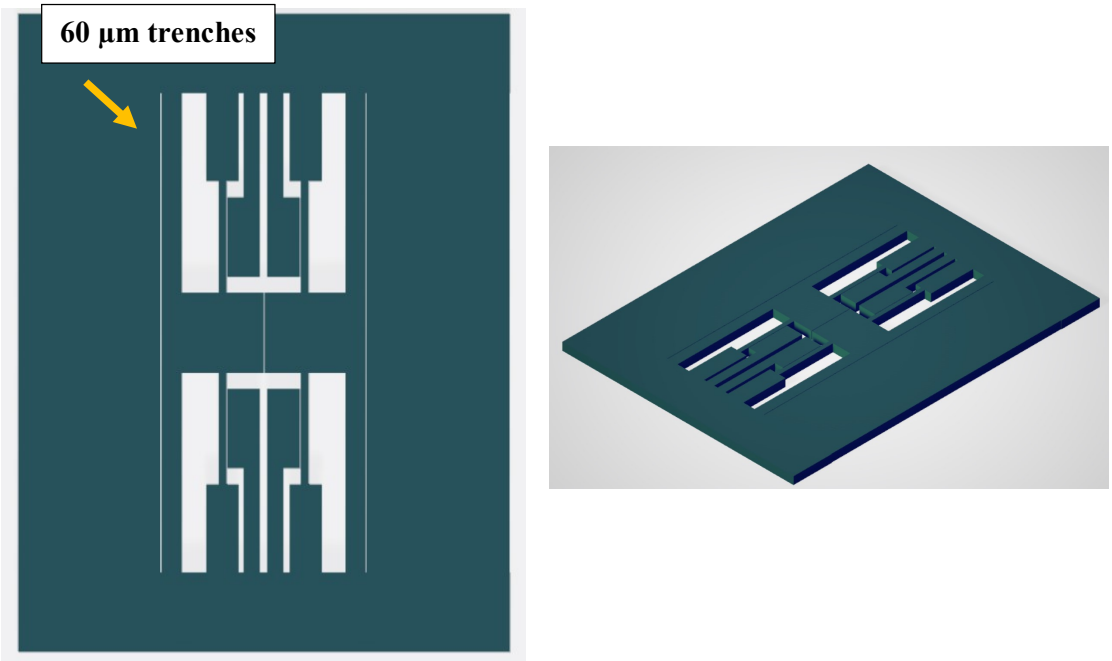

(a) (b)

Figure 5.6 A device prototype pattern drawn using Freecad software [139], (a) A pattern showing the micro-size capacitive gaps to be fabricated, (b) a 3D representation.

5.4 A PCB design for a developed prototype

Figure 5.7 displays a printed circuit board (PCB) development plan for our. All the dimensions are in *mm*. A distance of 10 *mm* were kept from the boundary of our prototype design. Total PCB size is 100 × 80 mm^2.

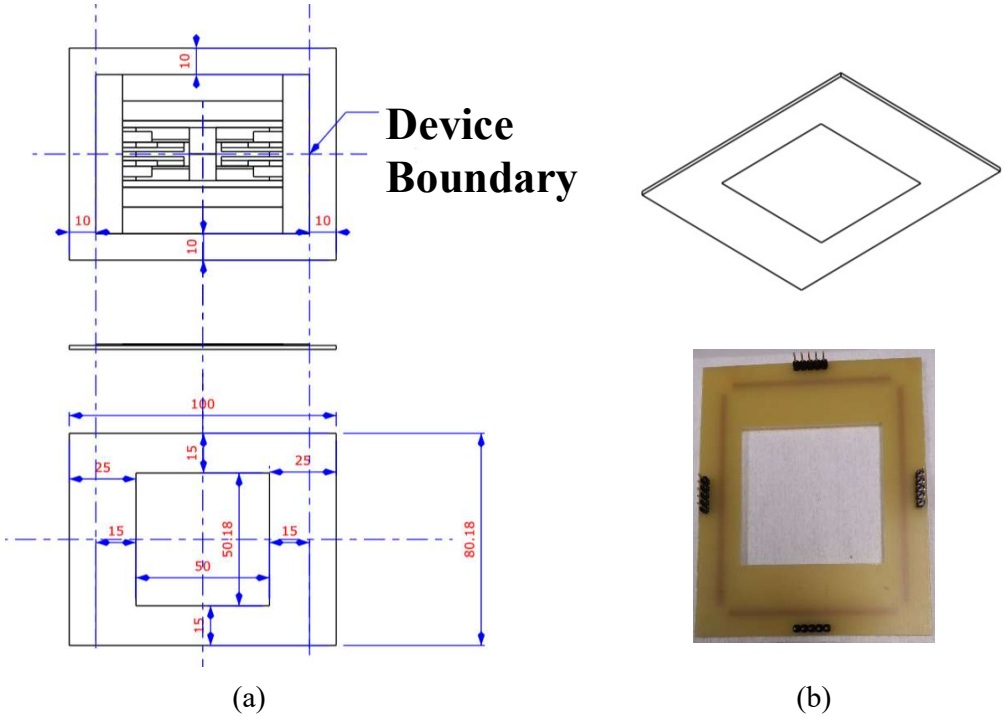

(a) (b)

Figure 5.7 A printed circuit board plan for the developed prototype. (a) drawing pattern and (b) 3D view

5.5 Auxiliary laser cutting for a developed prototype

Post fabrication of our prototype, a supplementary cutting as depicted in Figure 5.8 to electrically isolate sub-parts or components was done using simple dry laser cutting method. This cutting was done using the facility (Optec WS Flex laser machine) [140] in the clean room environment of Microsys laboratory [141] at the University of Liege.

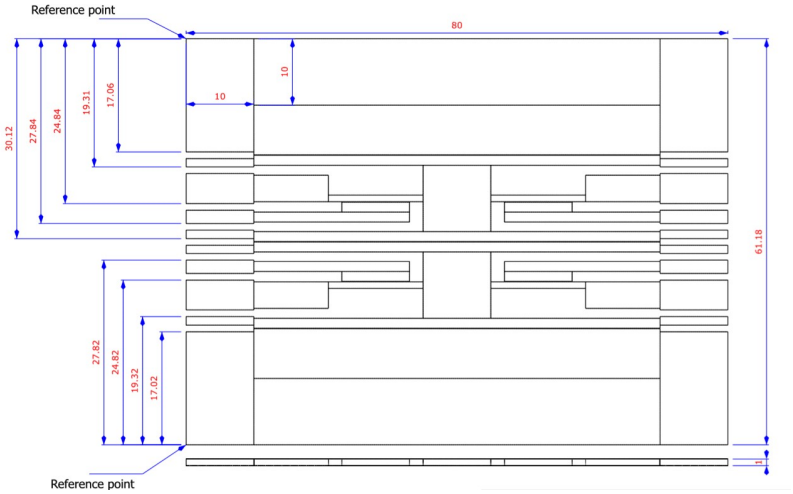

(a)

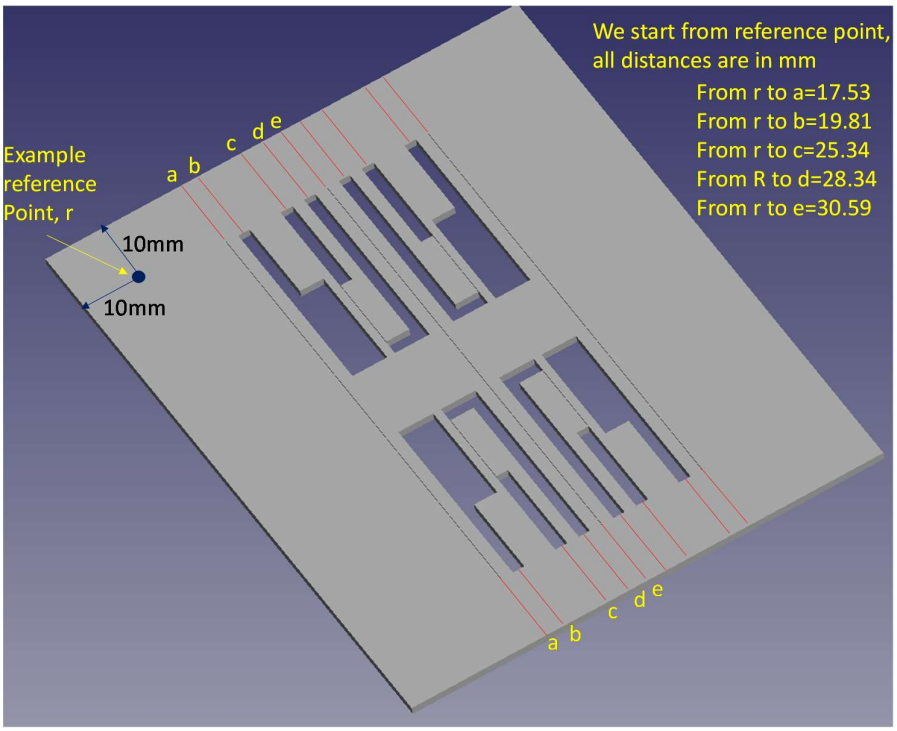

(b)

Figure 5.8 A pattern developed using AutoCAD software to perform a supplementary laser milling at the indicated locations on the finished part

Accuracy and consistency was required during this cutting, as we needed to make sure that after separating the sub-parts (features such as beams, electrodes 1 and 2, anchors, etc.) no two components are electrically short with any other component in the whole part. A basic open circuit test was done using a digital multimeter (DMM) after laser milling of sub-components

of a part. Post laser cutting device was cleaned using ethanol solution in the clean room of Microsys, followed by drying of the part by air gun to remove any debris that may cause the short circuit of the sub-components during the DMM test.

5.6 Assembly plan

Figure 5.9 shows a fabrication flow line for our prototype design. First, a device was machined out of a two metals, i.e. aluminium and steel of 1 *mm* and 2 *mm* thickness each. Parallel kerf-widths of 60 μm were machined. Post machining, the part was immersed in an ultrasonic bath to remove any debris/residues that may get into the kerf-gaps during the material ablation process. A piece of an epoxy laminate (FR4) was utilized to provide a support base for the device. This base was made hollow at the centre to facilitate suspending the moveable part of the device. A prototype device was glued on FR4 base (with Loctite 3609 adhesive[142]) and kept under *150°C* for about 2 minutes in order to form a good adhesion between a device and a laminate. Further laser milling was done on the device to electrically isolate subsections. Aluminum wedge wire-bonding [143] was used to electrically connect subcomponents of the device to copper tracks on the FR4 base. Soldering was used to electrically connect copper tracks to the header connectors.

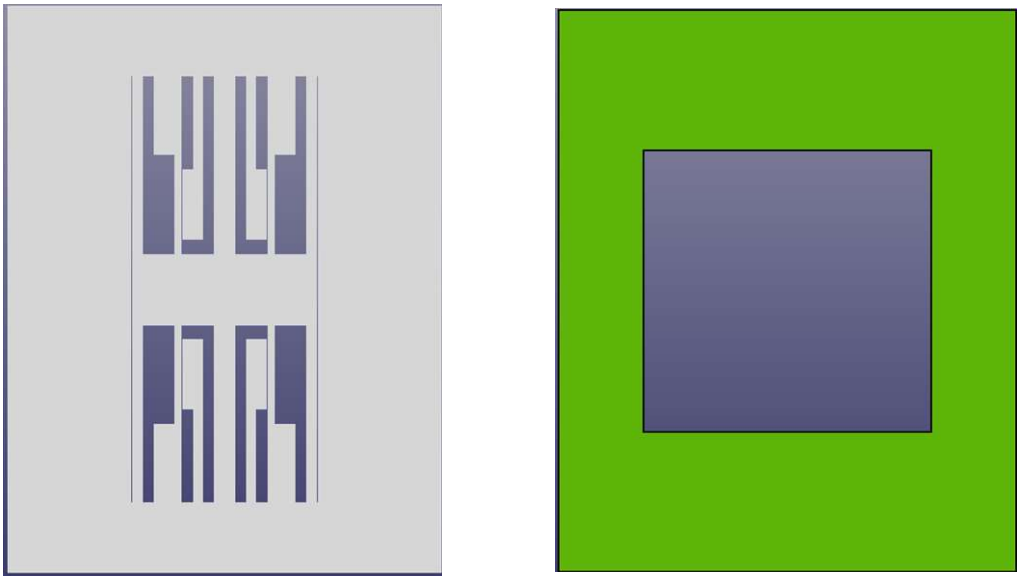

(a) (b)

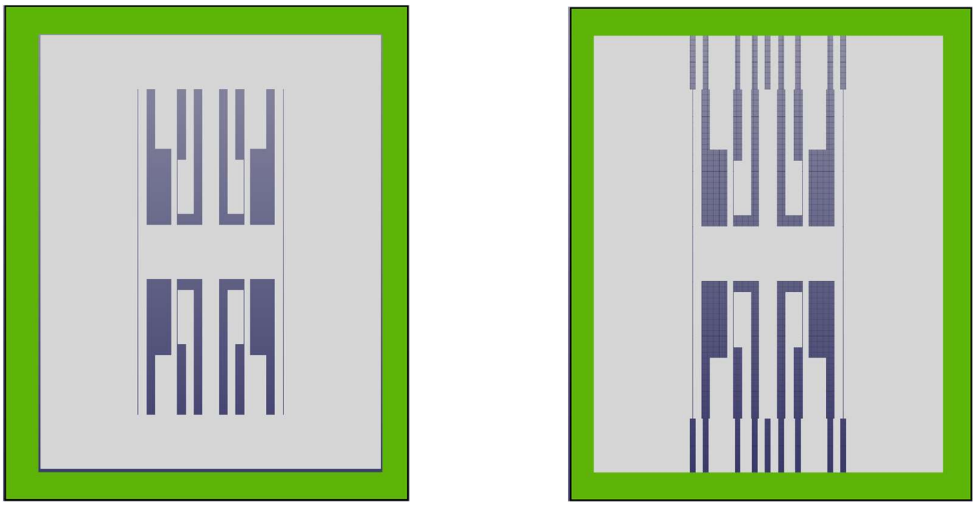

(c) (d)

Figure 5.9 Fabrication flow line of our prototype. (a) Fabricated part as received from the manufacturer, (b) PCB arrangement to support the part as a base, (c) part glued on top of the PCB, and (d) finished part with supplementary laser cutting to electrically isolate sub-parts of a device.

5.7 Finalized part

We utilized a state-of-the-art laser microjet (LMJ) technology provided by Synova Inc. [136,144] and developed our *first-generation* device prototype of two DoF electrostatically coupled resonators. Input parameters (as provided by the manufacturer) for laser cutting of our parts are as follows: - Laser source operating at 532 *nm*, average Power ≈ 10 *W*, and pulse width: between 100 - 400 *ns*. This LMJ technology offered us numerous advantages such as reasonable mechanical precision, parallel kerf walls (i.e. almost no V-shape), unlike in [137,138], relatively smooth cutting surfaces, etc. For our application development, we found laser-assisted machining (for our finished parts) to be alienated from thermal damage, oxidation, and micro-cracks. All these aspects are beneficial and effective for the development of electro-mechanical based transducers and/or devices.

Figure 5.10 shows a photograph of the prototype ready for test and electrical characterization with (a) a top view and (b) bottom view. Another reason to scale-up the device geometry is from manufacturing perspective. It was necessary to make the prototype being machined free from heat-induced structural cracks (residual stress [145]) that may cause a device geometry to bend if the feature sizes in the prototype being machined are thin, i.e. below sub-millimeter size. A bottom side of the prototype illustrates the central open area to facilitate device displacement when subjected to electrostatic actuation force. A boundary is shown to mechanically clamp the device by gluing [142] during laser writing. The total size of a prototype device is 80×60.18 mm^2.

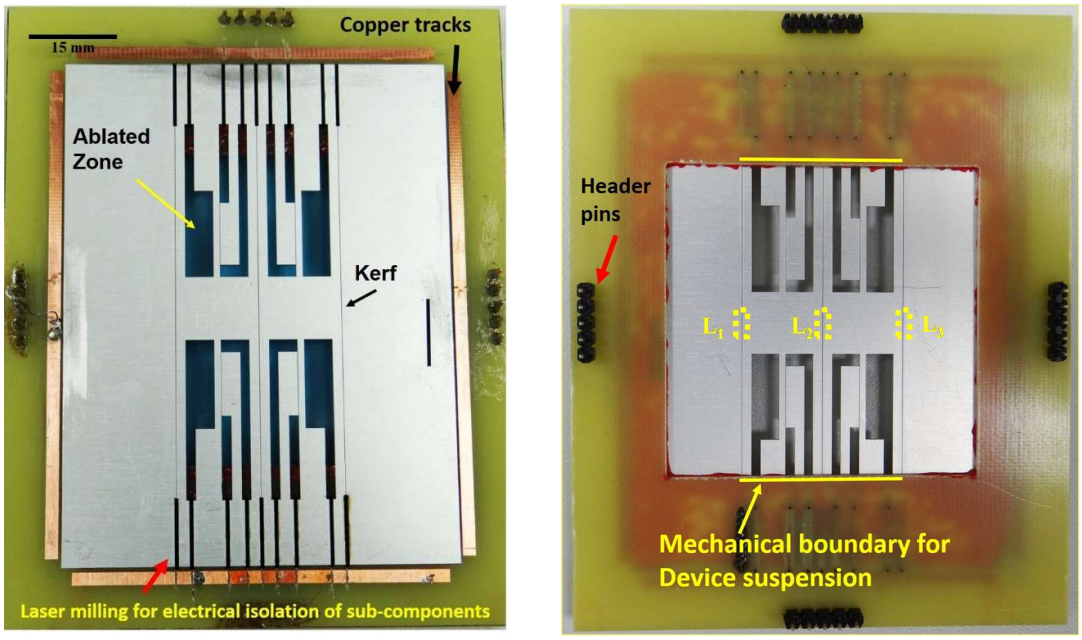

(a) (b)

Figure 5.10 Photograph of a prototype fabricated out of aluminum with thickness, h =1 *mm)*. Ablation zone is an area from where metal has been removed. (a) front view: suspension beams are attached to proof masses at one end and other ends of the beams are fixed on to the base laminate. An electrical connection between device and copper tracks is done through aluminum wedge bonding technique. Copper tracks are subsequently connected to the header connector pins through a wire soldering. (b) back view: a device is fixed onto epoxy laminate (which has a central cut as shown) to allow displacement with the established mechanical boundary conditions. Dashed rectangle shapes indicates the high velocity locations where gap measurements was done.

5.8 Fabricated parts

Figure 5.11 shows photographs of a fabricated prototype (a) side view, (b) top view and (c) bottom view. As seen, a metal thickness of 2 *mm* is shown from which all the components of the part were machined through laser ablation process. A finished part was glued on to the PCB, which offers a base for the part and provides a platform for electrical test and characterization of a device. A capacitive micro size air gaps through the entire thickness of the metal was machined by the laser technology to facilitate electrostatic actuation and capacitive sensing in mechanical resonators. A prototype is of two electrically coupled resonators for stiffness sensing application.

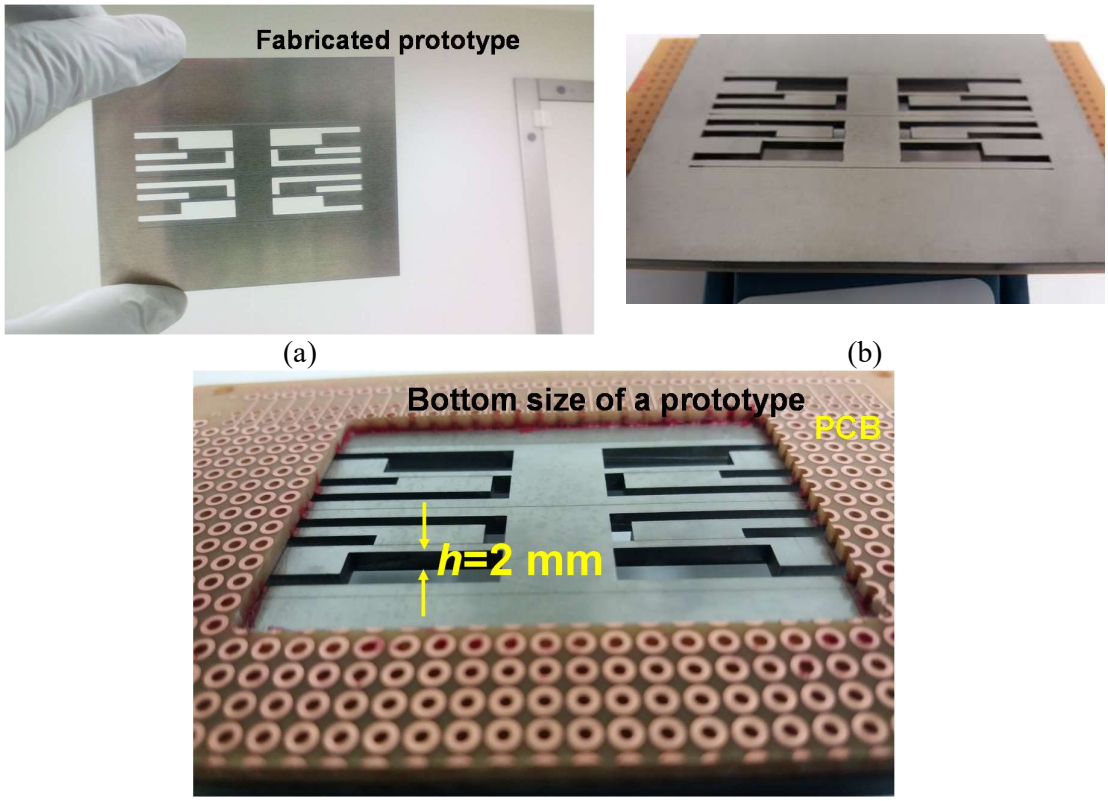

Figure 5.11 photographs of a fabricated prototype (a) side view, (b) top view and (c) bottom view.

5.9 Optical microscopic view and Gap measurements

Figure 5.12 shows the images of the fabricated device acquired through a optical microscope (Leica micro-system digital microscope and imaging system [146]). As seen, we have formed parallel kerfs with no thermal damage resulting in a high-quality cut. This technique also offered us effective removal of debris from the kerf, preventing contamination and burrs and thus leaving clean surfaces. We achieved a cutting ratio of up to 1:33 (kerf width: depth). We observed no deformation of the geometry during and after the machining process.

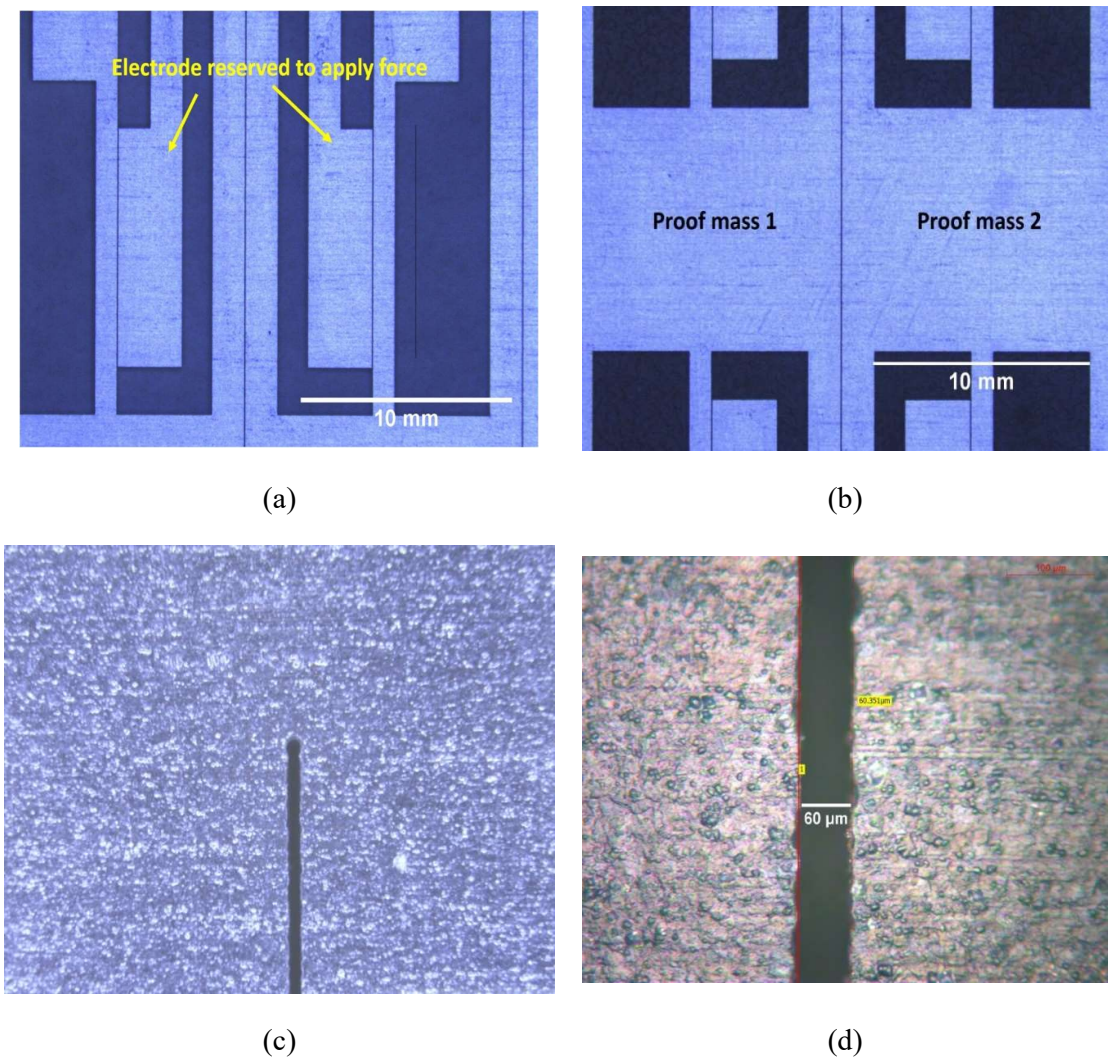

(a) (b)

(c) (d)

Figure 5.12 Images of the prototype (aluminum with 1 *mm* thickness) acquired through Leica microscope. (a) The top portion, showing electrodes reserved to apply external stimulus to alter the stiffness of the beams of the proof masses. (b) Middle portion showing proof masses separated by a micro-size kerf-width. (c) A close-up view of a clean sharp laser-cut thus forming parallel kerf. (d) Close-up view of one of the measured kerf-width. (One between the two proof masses)

Figure 5.13 shows the images of laser cuts (effective kerf widths) acquired through an optical microscope (Leica micro-system digital microscope and imaging system). Nearly parallel kerfs with no thermal damage was observed. This is an acceptable quality cut for our capacitive resonator device. As shown in Figure 5.10 (a), firstly, an effective kerf-width at the arbitrary locations on the red dotted lines (refer 3.1 (a) in chapter 3 for illustration) was measured. A study on width variation for a laser cut at these locations was carried out. A lowest gap size for Al (h =1 *mm*) is ≈ 50.81 μm and for SS (h = 1 *mm*), it is ≈ 54.29 μm. As shown in Figure 5.13 (b), we also measured an effective kerf-width and variations at the locations shown by dashed rectangle shapes L_1-L_3 on Figure 5.10(b). These locations, (with 5× magnification as shown)

are the maximum velocity locations (refer mode shape in Figure 3.8 in chapter 3) of our design subject to applied electric force. A statistical

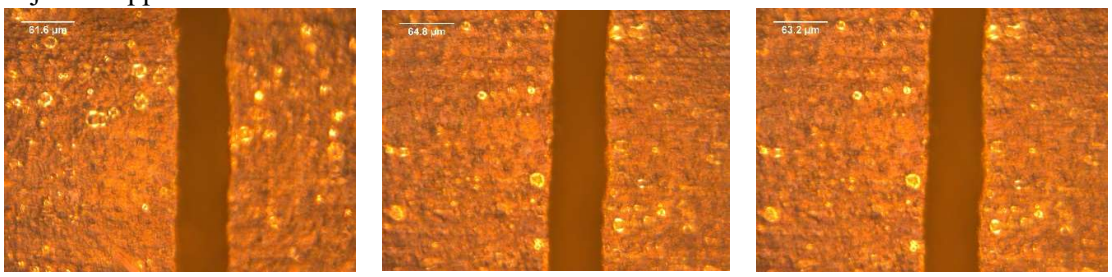

Al *(h=1 mm)*

(i) ***(ii)*** ***(iii)***

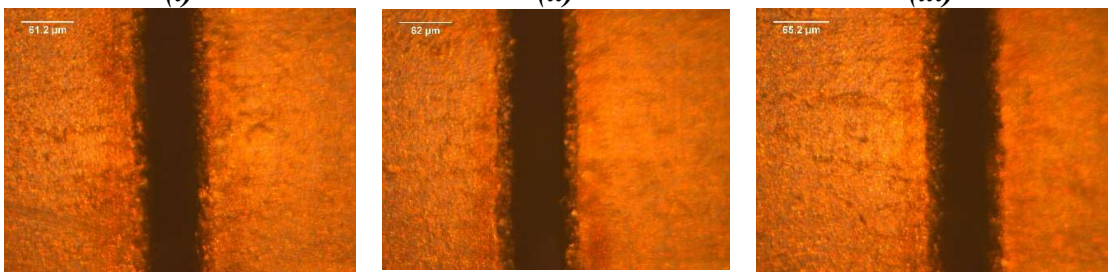

SS *(h=1 mm)*

(iv) ***(v)*** ***(vi)***

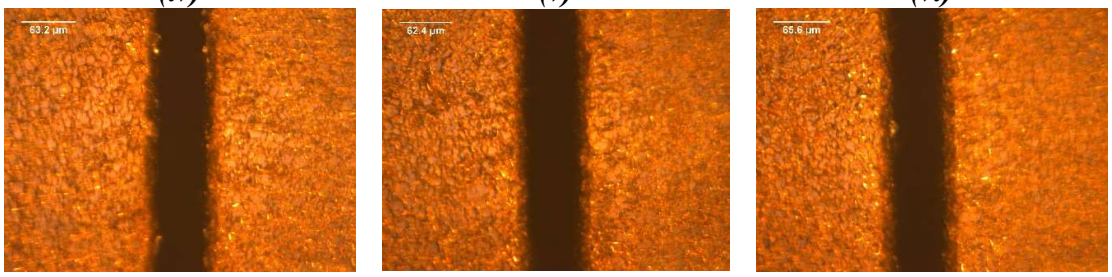

SS *(h=2 mm)*

(vii) ***(viii)*** ***(ix)***

(a)

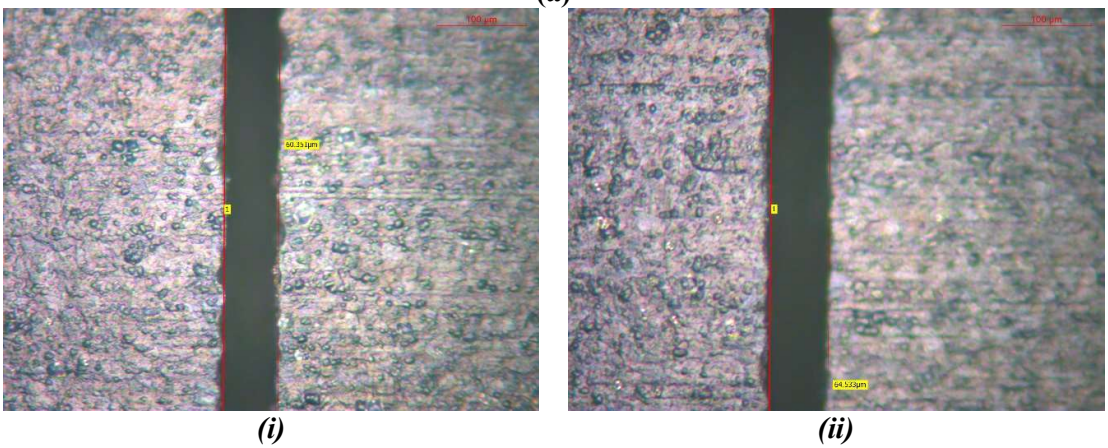

(i) ***(ii)***

Al *(h=1 mm)*

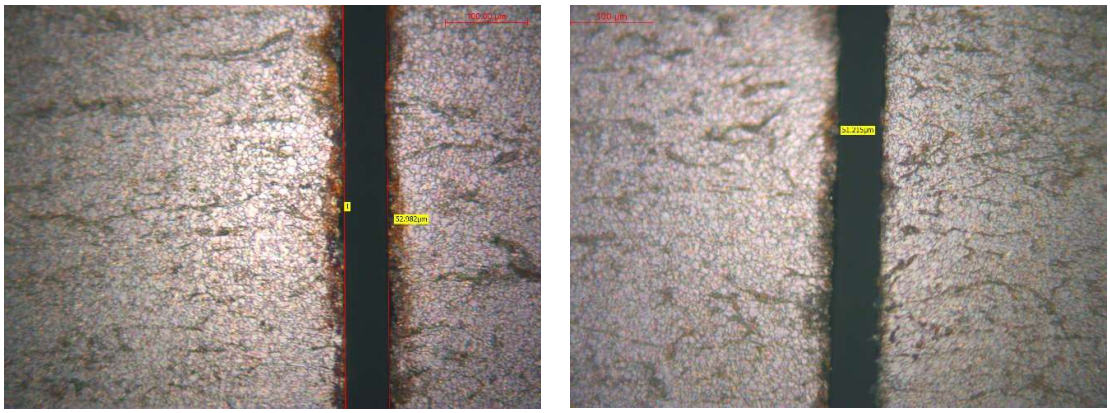

(iii) ***(iv)***

SS *(h=1 mm)*

(b)

Figure 5.13 Microscopic images to present quality of laser cut and width variation

(a) width at the arbitrary locations on the red dotted lines (refer Fig.1 (a) for illustrations and follow red lines from left) - (*i*) on line 2 at bottom, (*ii*) on line 3 at top, (*iii*) on line 2 at top and (*iv*) on line 3 at centre. (b) a kerf width measurement with 5x magnification at the dashed spots (depicted in Fig. 5 (b)) for 3 fabricated parts, (*i-iii*) Al with h = 1 *mm*, (*iv-vi*) SS with h = 1 *mm* and (*vii-ix*) SS with h = 2 *mm*.

analysis providing a measure of variance of a laser cuts for all cases is given in Table 5.1. Values of kerf-width in Table 5.1 are in μm.

Table 5.1 Width variation for a laser cut

Kerf-width variation at arbitrary locations						
Fabricated part	Samples	Kerf-width				
		Mean	Median	Minimum	Maximum	Std. deviation
Al (h=1 *mm*)	10	66.63	69.59	54.29	75.78	7.27
SS (h=1 *mm*)	8	55.88	55.52	50.81	60.99	3.81
Effective kerf-width variation at locations L_1-L_3						
Fabricated part*	Line on Fig. 5.10(b)	Mean	Median	Minimum	Maximum	Std. deviation
Al (h=1 *mm*)	L_1	65.79	66.7	61.8	69.6	2.57
	L_2	64.85	64.45	61.3	69.1	2.54
	L_3	65.49	65.45	63.1	69.4	2.01
SS (h=1 *mm*)	L_1	64.75	64.4	61.6	68.4	2.03
	L_2	64.97	63.55	61.8	68.8	2.66
	L_3	65.08	65	61.4	68.7	3.36
SS (h=2 *mm*)	L_1	66.27	66.8	62.6	69.1	1.99
	L_2	65.5	64.95	63.6	69.9	1.99
	L_3	64.76	64.85	61.8	67.3	2.01
*for a length of a dashed rectangle shapes, 10 samples used						

Summary

A proposition in this chapter attempts to explore the state-of-the-art technological advancements in nonconventional micromachining methods with emphasis on laser micromachining. We demonstrate the potential of laser machining to create micro-size kerf-widths (capacitive gaps) through material ablation. This technique can be used to fabricate devices based on electrostatic actuation and capacitive sensing.

A prototyping fabrication method as proposed here can be particularly useful when there is no cleanroom access and there is a requirement for quick prototyping with materials other than silicon. This can potentially also be extended for small or medium-scale series production.

Chapter 6

6 Electrical test and characterization

In this chapter, we present the electrical test and characterization of our fabricated prototype. A detailed experimental methodology is provided. Initial experiments and measurements are presented for stiffness sensing applications.

6.1 A description of the experimental methodology

Figure 6.1 shows a schematic illustration of an experimental set-up used. We give here a detailed description of the experimental methodology as follows: As shown in Figure 6.1, notations used are,

1) R_1, R_2 are resonators operating in vacuum.

2) V^+ and V^- are the DC voltages applied to the resonators.

4) V_{ac} is the applied AC voltage with the frequency sweep generated by the reference oscillator of the lock-in amplifier.

5) d is the air gap for electrostatic actuation and capacitive transduction.

3) V_{per} is the DC voltage used to apply electrostatic force (across its coupling gap, d) to resonator R_2

6) C is the capacitor of 1 μf, 250V rating used to block DC bias voltages applied to the resonators and let the time-varying motional current output be recorded.

7) C_{f1}, C_{f2} and C_{cf} are the corresponding coupling capacitors and offer path for feedthrough currents in our set-up.

First, a fully assembled coupled resonator device (as shown in Figure 5.10) was placed inside a vacuum chamber (refer appendix C to see vacuum chamber used showing access to all the feedthrough). Electrical connections to and from the device were made as shown in Figure 6.1. A DC power supplies and measuring instrument/s (lock-in amplifier) were initially kept turned OFF. An electrical power to a vacuum chamber was switched ON to lower the operating pressure for the resonator unit placed inside it. A DC Power supply 1 was switched ON and a low DC voltage (in the range of 0 to 10V) was applied to the inputs of the DC-to DC high voltage (HV) converter (with its centre tap option connected to the DC ground) to generate variable DC high voltages (up to +/- 200V) at its output terminals. This DC high voltage of equal magnitude but opposite polarity (+/- 200V) was applied to the two resonators as V^+ and V^-. An AC voltage of 5 V in magnitude was applied to the input port named V_{ac} of the structure and a frequency sweep was performed (from lock-in amplifier) in the frequency range of interests. Post observing the resonance on lock-in screen, a DC voltage (in the range of 0 to 120V) from another power supply 2 was applied to the input port named V_{per} to introduce perturbations into the system. A resonant output signal from the body of resonator 2 was fed to one of the channel of the lock-in amplifier as shown. Figure 6.1 (b) explains through schematic diagram the possible feedthrough path engaged during our experiment methodology.

Capacitors C_{f1}, and C_{f2} provides the feedthrough current for our signal readout. Figure 6.1 (c) maps the representative electrical equivalent condition for the mechanical transducers and/or sensor.

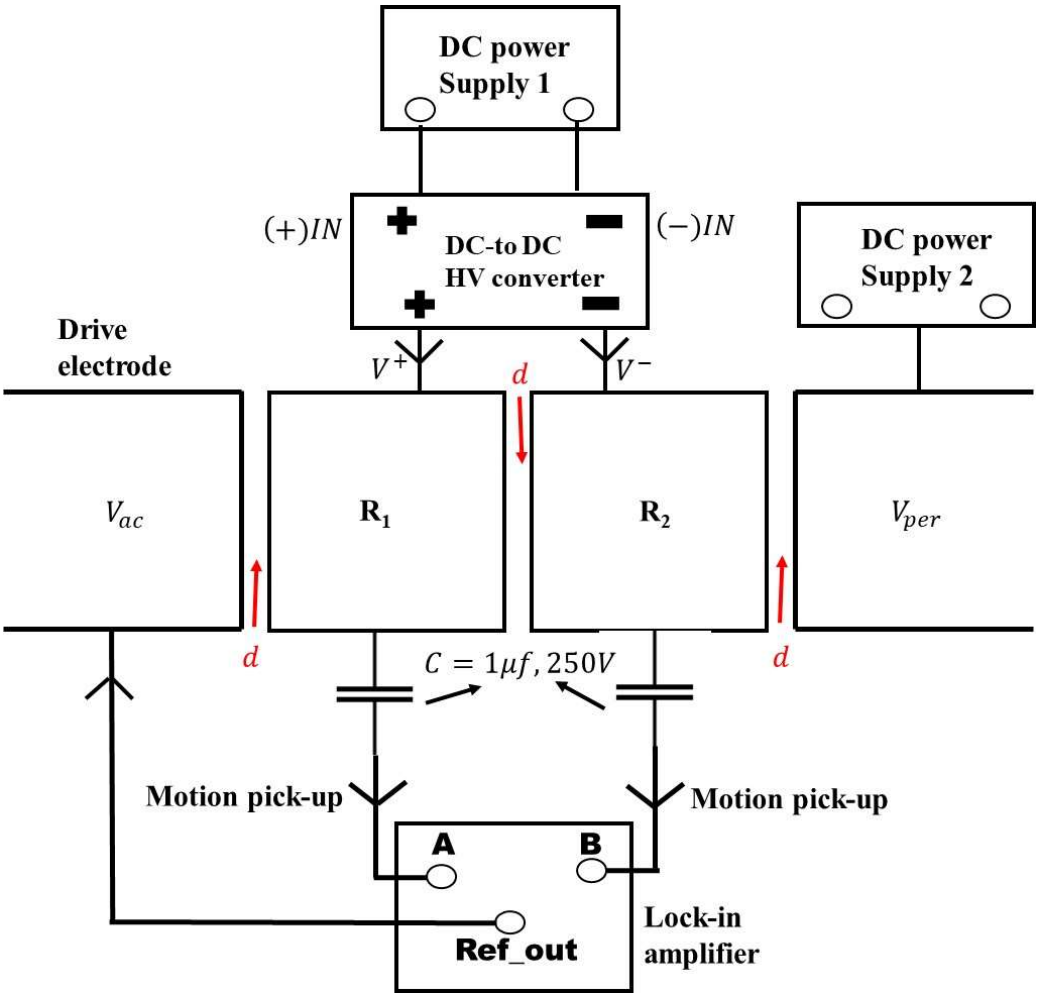

(a)

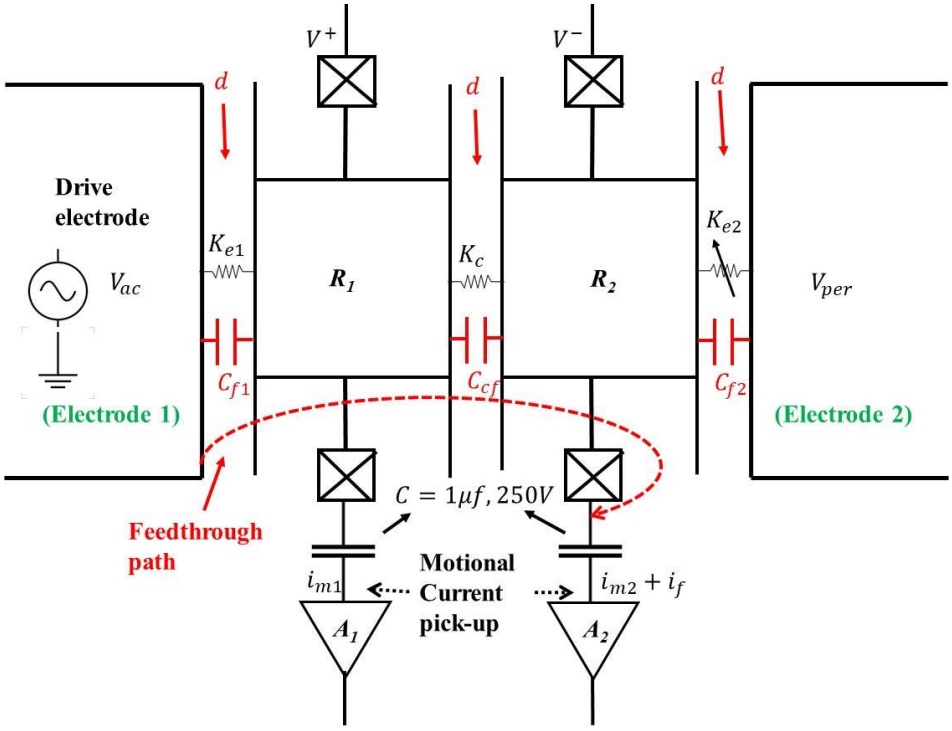

(b)

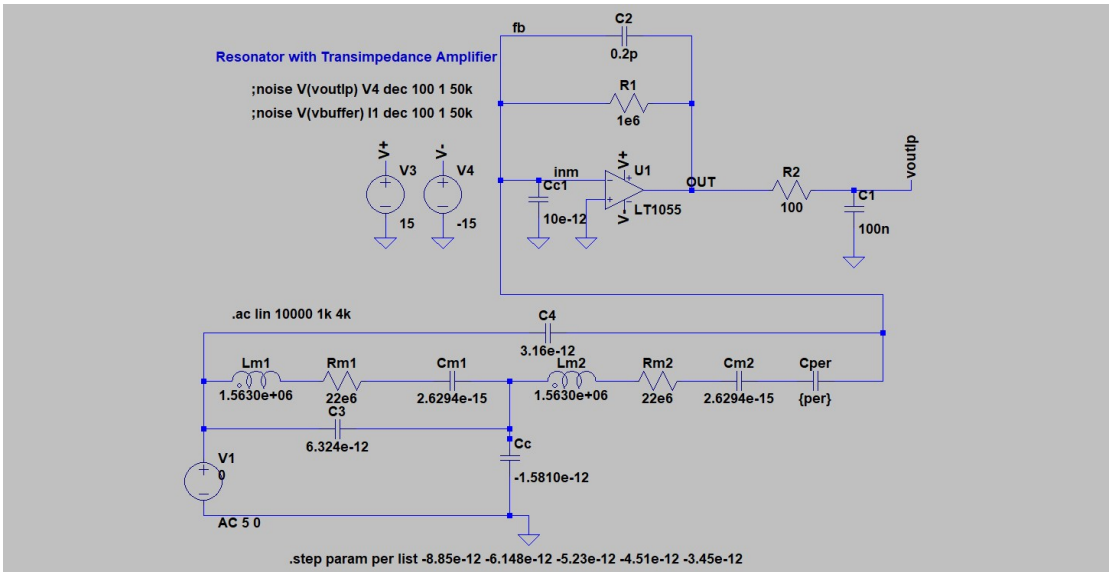

(c)

Figure 6.1 (a) A schematic representation of an experimental set-up, (b) illustrates the schematic representation of our design also highlighting possible feedthrough paths in the circuit, and (c) an equivalent circuit model representing the experimental condition for signal measurement.

An actual device operation and associalted analysis supplied by mathematical calculations for device paramenters is presented as follows: As seen in

Figure 6.2, an electrical characterization of a device was carried out in a vacuum chamber with at a pressure level ≈ 375 $\mu Torr$ (which was the minimum achievable level with the available equipment). A compact DC to high voltage DC converter unit was used to generate high voltages for operation. On the body of a proof mass M_1, a DC voltage $V^+ = 200$V was applied while electrode 1 (as shown in

Figure 6.2) was held at DC ground potential. This created an electrical spring between electrode 1 and a proof mass M_1 owing to the potential difference between them. Similarly, a DC voltage of $V^- = -200$V was applied to the proof mass M_2. An electrode 2 was initially connected to a DC ground. This created another electrical spring between mass M_2 and electrode 2. Here, $k_{e_1} = k_{e_2} = k_e$, where k_{e_1} and k_{e_2} are electrical spring constants of two proof masses M_1 and M_2 respectively, created due to the introduction of DC voltages into the system. This action softened the inherent mechanical springs, $K_{m_1} = K_{m_2} = K_m$ of both the proof masses thus making effective values of the spring constants as $K_{eff_1} = K_{eff_2} = K_{eff}$; $K_{eff} = K_m - K_e$. As proof mass M_1 was DC biased at V^+ and proof mass M_2 at V^- respectively, it established another electrical spring, K_c between the two proof masses thereby electrically coupling the two. On electrode 1, a sinusoidal voltage of 5V in magnitude was applied to exert a net electrostatic force on proof mass M_1 and thus put the coupled device into resonance. An output signal was recorded directly from the body of the resonator 2 by means of a lock-in amplifier (series eLockIn204/2 from Anfatec) which was used as a pick-off circuit for our device. The lock-in amplifier facilitates ultra-low current and voltage input noise measurements. The lock-in amplifier also has a pre-amplification stage before further signal processing; the measured signal is essentially a voltage with an amplification factor of 1 $M\Omega$ to the input current. A DC voltage (in the range of 0V to 120V) was applied as a perturbation on electrode 2 (refer

Figure 6.2) to induce stiffness disorder, Δk on proof mass M_2. The stiffness perturbations were calculated as $\Delta k \approx -\frac{\varepsilon A}{d^3}\left(\Delta v^2\right)$, where, ε, A, and d are the relative permittivity, nominal overlap area and capacitive gap respectively. Δv refers to the difference between the voltages applied on the body of a proof mass, M_2 and electrode 2. A designed device as shown in Figure 5.12 (a) also possess electrodes reserved to which an external electrical force may be applied to alter the stiffness of one of the resonating elements. During the experiments however, we applied an external stimulus on electrode 2 (for enhanced transduction) and recorded corresponding variations in the vibrational amplitudes of the resonator 2.

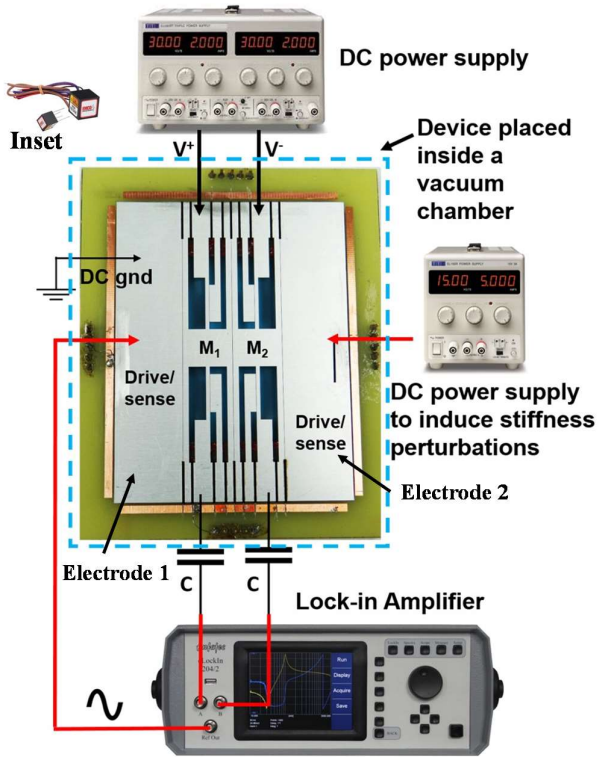

Figure 6.2 A set of DC voltages were applied as illustrated. As shown in the inset, DC to high voltage DC converter was used between a power supply and prototype. An AC drive signal was applied (through the internal reference oscillator of lock-in amplifier) to electrode 1 as shown. A frequency sweep around estimated mode-frequencies was performed and output signal (amplitude-frequency response) was recorded through a lock-in amplifier. In our case, a signal form the body of resonating proof mass, M2 was recorded

6.2 Device measurements

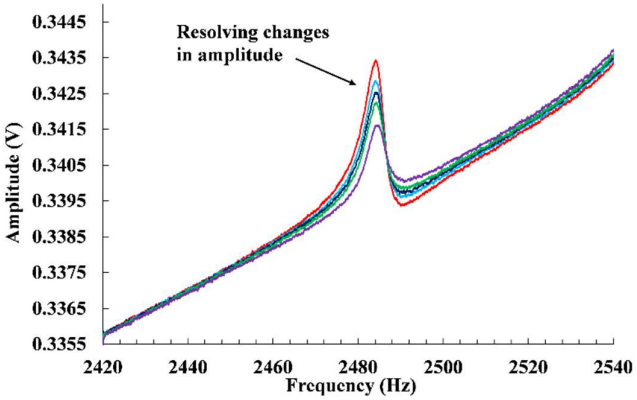

(a)

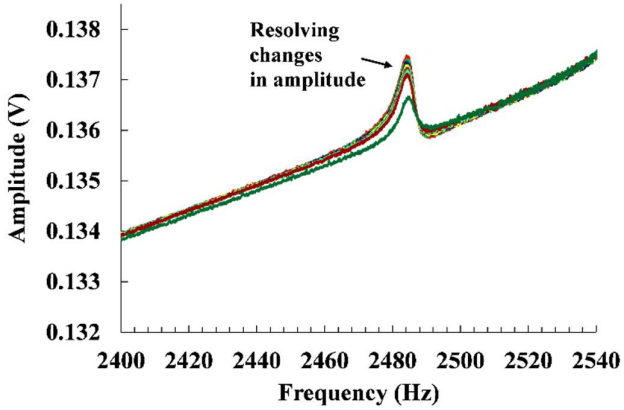

(b)

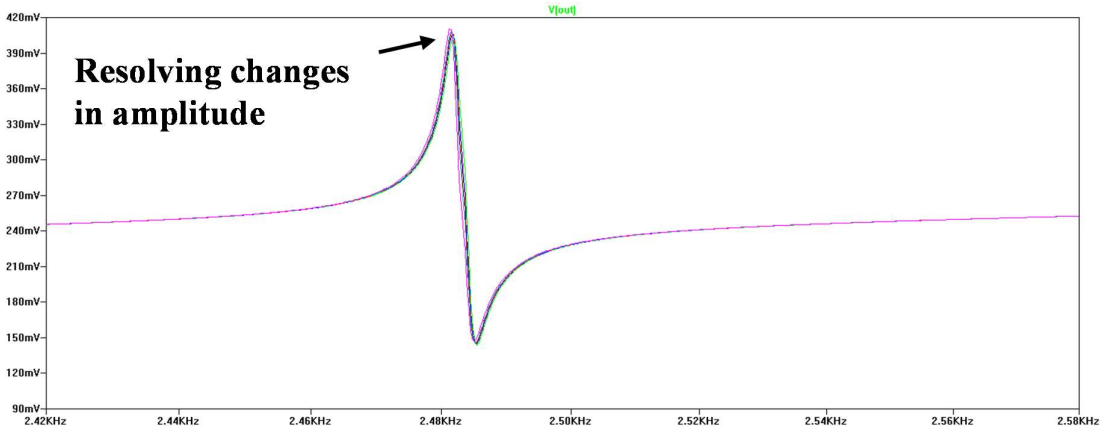

Figure 6.3 (a) With AC = 5V, (b) with AC = 2V. A DC voltages, +200V and -200V were applied to proof mass 1 and 2 respectively. Stiffness perturbation was applied to the resonator 2 and an output was recorded from the resonating proof mass 2. Variations in the vibration amplitudes were prominently observed, and (c) SPICE simulated frequency response from the practical circuit model.

Figure 6.3 shows a measured amplitude-frequency plot of device fabricated out of aluminium with thickness, $h = 1$ *mm*. Two datasets of measurements were generated with i) AC drive voltage set to 5V, Figure 6.3 (a) and ii) 2V, Figure 6.3 (b). As estimated by theoretical calculations, SIMULINK model and COMSOL simulation, first eigenmode (in-phase mode frequency) should appear at 2483 *Hz* whereas the second eigenmode (out-of-phase mode frequency) should occur at 2476 *Hz* (with δ_k=0). However, as discussed in simulation part (section 3), sufficient quality factor is needed, if these two distinct modes separated by about 7 *Hz* are to be resolved. As a result, in the frequency response, only one resonance peak is seen around estimated frequencies. Perturbations were applied to alter the effective stiffness of the resonating proof mass 2 and an output signal from the body of the resonating proof mass 2 was recorded. Corresponding changes in the amplitude of an output signal of the resonating proof

mass 2 were resolved (at the first peak in the response). A simulated response as seen in Figure 6.3 (c) from the equivalent circuit model was found to be matching with the experiment.

6.2.1 Operating point

A weakly coupled resonating sensor is characterized by a veering point/loci from where eigenvalues (mode frequencies) and eigenvectors (vibration amplitudes) of this electrically coupled system rather abruptly change, subject to a perturbation injected into the system [17,18]. In an ideally symmetric system, this reference point should occur when there is no applied stiffness perturbation ($\Delta k = 0$). During our measurement, as shown in Figure 6.4, this veering point/loci occurred at Δk = -98.377 *N/m* or $\delta_k = -7.98\times10^{-4}$ (*normalized*) ($\delta_k = \frac{\Delta k}{K_{eff}}$).

Therefore, this is the operating point of the device; around this point, relative changes into the amplitude and frequency were resolved. In our case, a change in the vibration amplitude was observed as the magnitude of an applied stiffness disorder (*normalized*) was increased (from $\delta_{kmin} = -7.98\times10^{-4}$ to $\delta_{kmax} = -2.017\times10^{-3}$).

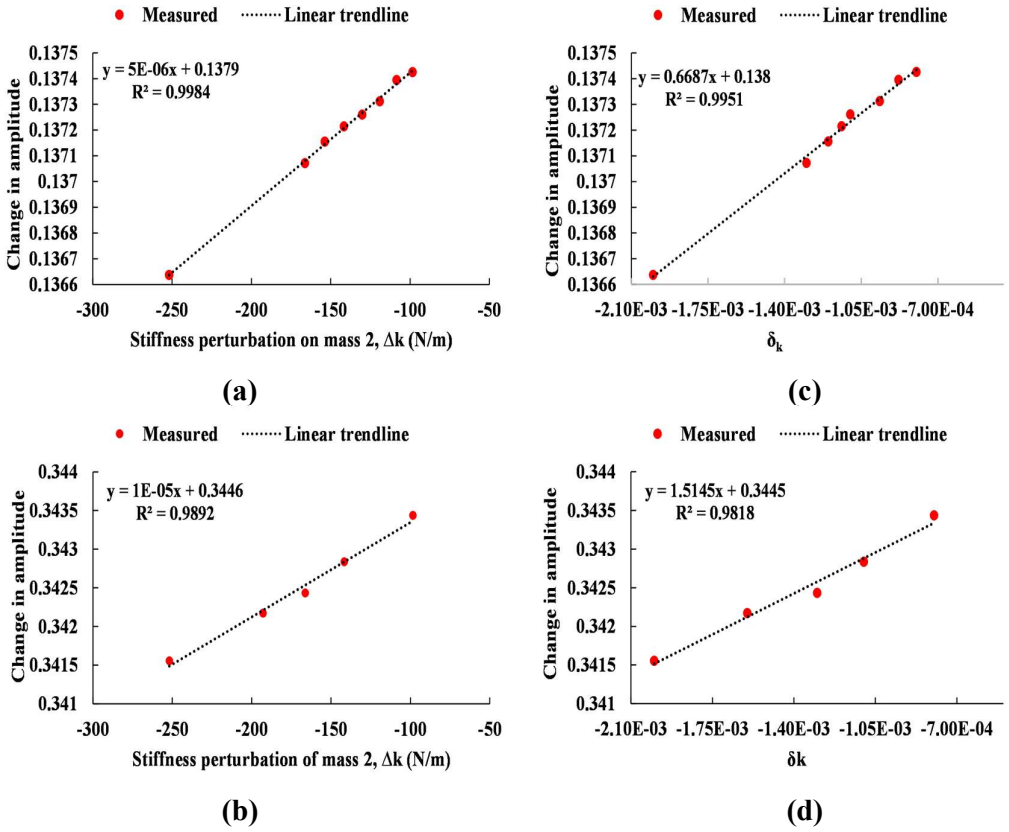

Figure 6.4 Measured vibrational amplitude variations into the output signal of a resonating proof mass 2 for two operational cases, (a) and (c) - when an AC drive signal is set to 2V and, (b) and (d) - when an AC drive signal is set to 5V

Figure 6.5 shows a comparative performance among output metric. A SPICE model as shown in Figure 6.1 (c) was built to model real experimental condition. In the SPICE model, parameters such as nonuniformity of the transduction gaps, d in the fabricated device were altered (increased by about 10 %). This resulted in reduced transduction factor, η (at the drive and sense port), and relatively smaller strength of coupling spring. Kc. Simulations were run in SPICE for varying effective damping loss (quality factor). A corresponding shifts in the output signals were recorded until model was found to be fitting to the experimental curve as shown in the Figure 6.5. An extracted quality factor from the model is about 410.

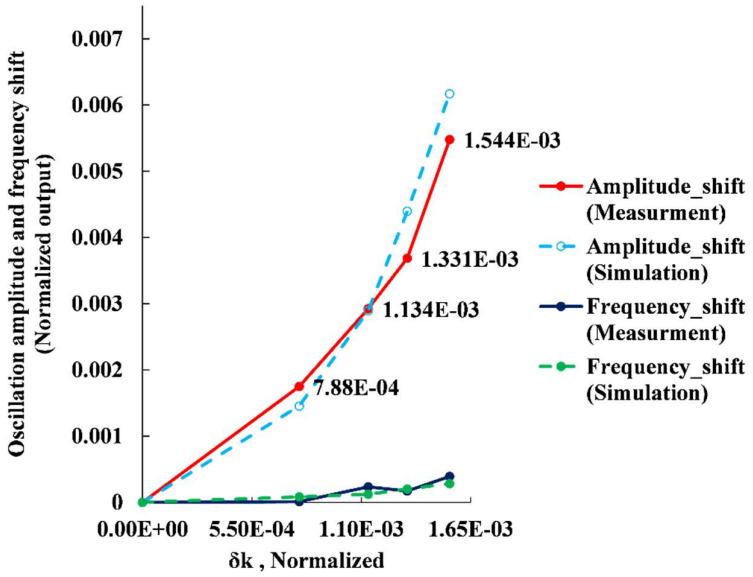

Figure 6.5 Sensitivity to amplitude [0.547% max. shifts in amplitude] was observed to be one order of magnitude higher as compared to sensitivity to frequency [0.038% max. shifts in frequency] (subject to measurement errors)

Summary

In this work, we explore the possibility to apply new manufacturing technique to fabricate devices based on capacitive change. We utilized state-of-the-art laser micro milling to machine micro-size kerf-widths, (referred as a capacitive gap in MEMS) to perform electrostatic actuation and capacitive sensing. The benefit of laser micromachining is the possibility to utilize new materials, which may contribute to enhance device performance. A prototyping fabrication method as proposed here can be particularly useful when there is no cleanroom access and there is a requirement for quick prototyping with materials other than silicon. This can potentially also be extended for small or medium-scale series production.

About device: Based on the design and chosen materials, we demonstrated a two DoF coupled resonators for stiffness sensing application. It is to be noted that due to damping, two distinct modes could not be resolved and device shows the resonance with two modes being merged as the analytical work predicted. A number of studies have demonstrated coupled resonators operating with this situation (i.e. when modes are overlapping each other) [58,59]. A state-of-the-art laser micromachining was used to make μm size trenches with the parallel sidewalls up

to 2 *mm* height (aspect ratio > 33). This fabrication approach has not been reported in the relevant literature, particularly for fabricating an electronic device that performs electromechanical transduction in capacitive gap resonators.

As estimated by theory and simulation models (b)), the sensitivity of amplitude ratio for stiffness perturbation is higher than other forms of the output. Experimentally derived maximum shifts in the amplitude and frequency are 0.547% and 0.038%, respectively (owing to the low output signal level). For a finite value of a quality factor, $Q \approx 2547$, maximum shifts (refer Figure 6.5) into the amplitude ratio, amplitude and frequency are 27%, 4.95% and 0.404% respectively.

Owing to the designed effective value of a mechanical spring (1.248×10^5 N/m) of an individual resonating element of the coupled device, induced frequency shifts are low. Therefore, variations in the frequency could not accurately be resolved during the electrical characterization and are subject to measurement errors. However, a high value of mechanical spring can benefit in increasing the shifts and hence the sensitivity to amplitude and amplitude ratio along with detecting minimum resolvable stiffness. It is worth mentioning that an amplitude ratio can be used as a sensor output for which we have estimated a maximum sensitivity (for a finite value of Q) to change in stiffness of about 135. Similarly, a maximum sensitivity that can be attained for amplitude change based output is 23.73 (refer Table 3.2). A signal amplification to enhance the signal-to-noise ratio is expected to enhance the sensitivity for an amplitude based output and thus minimum detectable stiffness. Importance of the quality factor in coupled resonating sensors is briefly discussed, i) addressing its role in separating individual modes in the measured frequency response, ii) increasing the sensitivity and resolving minimum changes in the measurable quantity. At present, a minimum detectable stiffness perturbation is $\delta_{kmin} = -7.98\times10^{-4}$ (*normalised*) which is expected to improve with the enhanced signal to noise ratio.

Chapter 7

7 Discussion, conclusion and future direction

In this thesis, a transduction principle based on sensing the vibrational pattern of the resonators coupled in 1-dimensional (1-*d*) array is introduced and is discussed in detail in the context of our research. Potential applications of coupled resonators for sensing applications are then addressed. The most fundamental and central aspect of coupled resonators such as sensitivity, resolution (minimum detectable shift in the measurand), noise floor, etc. was determined to be an objective of this research. For the first time, a state-of-the-art laser micro-machining method is introduced. This method is proposed to fabricate a range of devices based on capacitive change with emphasis on fabricating coupled resonator architecture. An importance of this micromachining method is explained over conventional micromachining method in terms of flexibility, quick prototyping, ease with the process, range of available materials, etc.

A theoretical transfer function model for our design is derived based on the governing set of equations of motion. A model developed using COMSOL Multiphysics is also given to determine the mode shape and mode frequencies of our design.

Design and optimization scope through fabrication

A fundamental work on developing a resonant transducer and/or sensor using high-tech laser micromachining is reported. A new fabrication strategy to manufacture devices is presented. Given the transduction gap of about 60 μm that we strategically fabricated for our prototype, we have attained a best trade-off amongst structure size, resonant frequency, cost, and resonant output signal. In general, with MEMS devices, capacitive gap is usually in the range of 2-5 μm. Therefore, in order to exert a same magnitude of net electrostatic drive force as in MEMS, we needed to scale up device transduction area and applied voltages. With the progress in the state of the art in laser micromachining or any other nonconventional micromachining technology for that matter, to machine trenches < 60 μm, with a reasonable aspect ratio in to a piece of metals, semiconductors or conducting ceramics, it is anticipated that device/structure size can further be scaled down. A two coupled resonator structure was patterned for machining. For a larger proof mass (due to scaling-up) and designed resonant frequency of output signal (above kHz region), an effective device spring constant, K_m on the order of 10^5 N/m, resulted for our design. This higher value of spring constant is also attributed to the suspension size, mechanical boundary conditions, and manufacturing feasibility as quoted by the manufacturer.

Given that in capacitive resonators, motional resistance is inversely proposition to the 4^{th} power of a transduction gap, fabricating a smaller gaps (for a given applied drive force), with our proposed direct laser write (DWL) method would further assist in enhancing an output signal and thus device performance for that matter.

Future optimization will account for optimizing on the performance of a transducer and/or sensor. For this several design optimization steps can be taken such as scaling down (to some extent) the effective spring constant of our design, K_m, which at present, is on the order of 10^5

N/m. This would cause higher displacement (output signal) for a given drive force, and thus assist in reducing further overall size of a device. This action however, has a limit that, reducing K_m largely will push the resonant frequency of our design below sub-kHz region, and, therefore, resonant output signal is prone to the low-frequency noise. Moreover, as detailed in chapter 3, device amplitude ratio based sensitivity is directly proportional to effective spring constant of our design. Therefore, a trade-off is required to attain best performance.

In the context of fabrication, optical characterization for device gap measurement is presented.

Model developments

A research on the most fundamental and crucial aspects of the coupled resonators is presented and realistic system level models are developed estimating device sensitivity, resolution and noise floor. Importance of the quality factor in coupled resonating sensors is briefly discussed, i) addressing its role in separating individual modes in the measured frequency response, ii) increasing the sensitivity and resolving minimum changes in the measurable quantity.

Proposed models are exploited to address variety of operating conditions, such as finite quality factor, varying coupled electrostatic spring strength, operation with in-phase/out-of-phase mode, sensitivity in open loop/closed loop mode. A closed-loop configuration of our design showed enhanced amplitude ratio based sensitivity (about 187) and linearity to the applied stiffness perturbations as compared to when operated in open loop for the associated in-phase mode of operation.

Noise floor in our system

Models are exploited to determine an impact of intrinsic and extrinsic noise sources in our design. Theoretical expression for mechanical-thermal noise and electronic noise is obtained. A mechanical-thermal noise source is identified as an ultimate limit of detection. It is observed that lower coupling strength leads to decrease in the mechanical-thermal noise floor. A theoretical estimation of effective noise current for our device (due to intrinsic mechanical-thermal noise) is found to be about $i_{motX_{j1}} \approx 4.29\times10^{-15}\, A_{rms}$ (best case). Furthermore, it is found that a higher quality factor of a system could further improve this detection limit. An effective theoretical noise floor (due to electronic readout) is determined to be $\approx 1.56 \times10^{-13}\, A_{rms}$. It is concluded that though mechanical-thermal noise sets the ultimate noise floor of our design, it is an electronic noise that dominates the overall performance (electronics noise exceeds mechanical noise by two orders of magnitude). An effective noise floor of our design is derived and a good agreement between calculations and the simulations was found. With the derived noise floor, theoretically calculated minimum resolvable shifts (1.21×10^{-7}) in the output metric and thus resolution ($\approx 4.8\times10^{-3}$) of our macro-scale design is determined. These values are comparable to that achieved with MEMS coupled resonators. Influence of coupling strength on effective noise floor is also studied and it is found that smaller coupling strength in our design leads to reduced noise floor (about -12 *dB* gain in noise floor). In terms of noise, it is to be noted that power supply voltages used to polarize the resonators will also induce a noise in to the system. Therefore due to varying power levels, it is likely that it will affect the accuracy of measurements (i.e. ultimate detection limit) amidst varying noise level. Therefore, this issue requires future research.

Possibilities for mode-localized sensor

A mass sensor based on the frequency shift output signal, with a ultra-high resolution (on the order of $\times 10^{-18}$ gram) has been shown [147]. It uses NEMS high-frequency single resonator. Therefore, it remains a subject of continuing research whether and how coupling the resonators in the context of sensing the mass at these or ever-lower scale would eventually be able to surpass resonant sensor with only one resonators. In our design, we have demonstrated through our realistic system-level modelling approach to attain the lowest possible shift approximately $\times 10^{-7}$ for the quantities refereeing the stiffness change. A resolution for the frequency shift output is reported to be better than 1 ppm [19,148]. Therefore, it is worthwhile to investigate how coupled resonators whose output is amplitude shift can provide resolution on the similar or even better scale. At present, this issue is being investigated worldwide. It is anticipated that, coupled resonators with ultra-high sensitivity and resolution go hand in hand.

On prototype fabrication

The state-of-the-art technological advancements in nonconventional micromachining methods with emphasis on laser micromachining is explored. The high-tech laser micromachining is proposed as a novel fabrication platform to develop transducers and/or sensors based on capacitive transduction. A high aspect ratio (> 33) with range of supplied conducting/semiconducting materials to fabricate devices/sensor using laser micro machining is demonstrated for the first time. A fabrication outcome at the University of Liege and the outside manufacturing service is explained in detail. The potential of laser machining to create micro-size kerf-widths (capacitive gaps) through material ablation was demonstrated. A prototyping fabrication method as proposed is put forward to be utilized when there is no cleanroom access and there is a requirement for quick prototyping with materials other than silicon. This can potentially also be extended for small or medium-scale series production.

Owing to the new fabrication platform (state-of-the-art laser micromachining), and in the context of coupled resonators as reported, we have proposed realistic system level models of this new class of sensor. We investigated whether and how this development as proposed in this thesis offers any performance benefits in terms of sensitivity, resolution (detection limit), noise floor, etc.

Electrical test and characterization of fabricated prototype is given. Experiments are performed for stiffness sensing applications. A detailed description of the experimental methodology is given followed by actual measurement results as obtained from the experiments. Role of operating point in the sensor operation is also discussed. A measured amplitude-frequency plot of device fabricated out of aluminium with thickness, $h = 1\ mm$ is given. Two datasets of measurements are generated. A minimum detectable stiffness perturbation, $\delta_{kmin} = -7.98\times10^{-4}$ (*normalised*) is reported.

In conclusion, key contributions from this thesis are highlighted as follows:

a) State-of-the-art laser micromachining as a novel fabrication platform to develop transducers and/or sensors (featuring high aspect ratio) based on electrostatic actuation and capacitive transduction.

b) A theoretically derived sensitivity estimation to stiffness perturbations is of the similar order in magnitude to that attainable using 2-DoF MEMS architecture.

c) Estimation of an effective noise, taking into account all the possible noise sources of errors, in the context of a developed prototype.

d) Reporting of an improved resolution (about four orders high in magnitude) as compared to the resolution attainable using 2-DoF MEMS architecture.

e) This sensor is able to resolve a minimum stiffness perturbation (*normalized*), $\delta_{k_{\min}} = 7.98 \times 10^{-4}$ which is of the same order to that achievable in MEMS based weakly coupled resonators.

Future direction

Given that, this thesis also proposes a novel fabrication technique (laser micro machining) to fabricate electrostatically actuated and capacitively transduced devices, this platform could be utilized to develop any mass-spring-damper physical systems (including coupled resonators as a sensor), on the similar path silicon resonators using conventional MEMS fabrication have been developed in past few decades. Capacitively transduced resonators for that matter can be fabricated exploiting a flexibility high-tech laser micro machining can offer such as choice of materials other than silicon.

Potential applications that can be developed range from 1) single resonators as a device for timing reference and testing its long-term and short-term stability of frequency shift based output signal, 2) single resonators used for sensing applications such as mass sensing, 3) an array of resonators (coupled resonators as proposed in this thesis) in sensing applications.

Given that, resonant frequency of silicon resonators has a reasonable temperature variation and therefore differential architecture (i.e. coupled resonator) has been proposed in sensing applications. It offers an immunity against temperature variation. A resonator with materials other than silicon can be fabricated using DLW method. Its temperature stability can be modelled and characterized and further be compared with the temperature stability of a coupled resonators. This will also reveal what is the real advantage of coupled resonators and whether there is any other merits (other than enhanced parametric sensitivity). Moreover, many researchers across the world are approaching this new transduction principle for a new class of resonant sensing applications. Therefore, it is a need of a time to develop a low power, low-noise interface circuity, preferable with CMOS-MEMS one chip integration platform.

This research initiative can navigate a way in developing a variety of devices/sensors using direct laser writing (with an emphasis on miniaturization) based on capacitive change. Additional benefit is that range of novel materials (metals, conducting ceramics, and semiconductors) can be used to serve the demanding and quick prototyping applications in automobile, biomedical, and Internet-of-things (IoT) applications. This work focussed on a fabrication using a laser micromachining and demonstrated the working prototype. A result with aluminium has been presented.

Peer reviewed publication

Journal

1. Vinayak. Pachkawade, D. Cerica, S. Dricot, S. Stoukatch, M. Kraft, Direct laser writing to fabricate capacitively transduced resonating sensor, Microsyst. Technol. (2019). doi:10.1007/s00542-019-04549-2.

Conference

1. Yuan Wang; Chun Zhao; Chen Wang; Delphine Cerica; Mathieu Baijot; **Vinayak Pachkawade**; Ali Ghorbani; Maxime Boutier; Alain Vanderplasschen and Michael Kraft, "A Reversible Method to Characterize the Mass Sensitivity of a 3-Dof Mode Localized Coupled Resonator under Atmospheric Pressure," Eurosensors 2017 Conference, Paris, France, 3–6 September 2017.

Appendix A

MATLAB SCRIPT TO ESTIMATE POWER SPECTRAL DENSITY AND DETERMINE AVERAGE SIGNAL POWER

```
Fs=50e3 % %Nyquist frequency
x=vout2; % Signal variable
yyaxis left
periodogram(x,hamming(length(x)),[],2*Fs,'centered','psd')
[Pxx, F] = periodogram(x,
hamming(length(x)),[],2*Fs,'centered','psd');
power_freqdomain = bandpower(Pxx,F,'psd')
% power in time-domain
power_timedomain = sum(abs(x).^2)/length(x)
grid on
hold on
```

MATLAB CODE FOR DEVICE PARAMETER COMPUTATIONS

```
clc;
clear all;
close all;

%proof mass design parameters

L = 10e-3 %side length
lp = 60e-3 % Plate length
lw = 1.5e-3 %Plate width

%suspension beam design parameters

lb=14e-3 %Beam length
wb=1e-3 %Beam width
h=1e-3 % Thickness
E=70e9
rho=2700
epsi=8.854e-12;

d=60e-6 %Gap

% effective mass
m1=rho*h*(l^2)
m2=rho*h*lp*lw
m3=rho*h*lb*wb
m=m1+m2+m3

%Cross-sectional area of the parallel plate
A=lp*h % Transduction area at drive/sense as well as coupling
area of two masses
```

```
k=m*(2*3.1415*2483.2)^2 %k1=k2=k % is the frequency determined
by FEM for one device of a pair

C0=epsi*A/d % Nominal capacitance at driving/sensing electrode
or between the two masses

%Natural frequency
w=sqrt(k/m);
f=w/(2*3.1415)

%Force@resonance
Vdc = 200
vdc1= vdc; % A DC voltage difference applied between proof
mass 1 and electrode 1
vdc2=-vdc; % A DC voltage difference applied between proof
mass 2 and electrode 2

ke1=-(epsi*A*(vdc1-0)^2)/(d^3) % electrical spring ke1=ke2=ke
ke2=-(epsi*A*(vdc2-0)^2)/(d^3)
keff1=k+ke1; % effective spring constant keff1=keff2=keff
keff2=k+ke2;
keff=keff1

%Net force@DC
Fdc=(1/2)*epsi*A*vdc^2/(d^2)

% net displacement, x=Fdc/k
xdc=Fdc/keff % displacement at DC

C=epsi*A/(d-xdc);
deltaC=abs(C-C0) % Net change in capacitance

%Force@resonance
vac=5; % AC voltage magnitude
Fer=(epsi*A*vdc*vac)/(d)^2

% net displacement@ resonance, x=Q*Fdc/k
Q=2547; % Assumed value of a quality factor
x=Q*Fer/keff % displacement at resonance
dcdx=(epsi*A)/(d-x)^2; % capacitance gradient at drive
electrode

%Effective coupling stiffness
deltav1=(vdc1-vdc2)
kc=-(epsi*A*deltav1^2)/(60e-6)^3 % electrical spring at drive
electrode
%kc=-100
cfactor=(kc/keff)

%transduction factor
```

```
eta1=epsi*A*vdc/d^2 % at driving/sense electrode

% A motional resisitance in a capacitive transducer
Rx=(d^4*sqrt(keff*m))/(vdc^2*epsi^2*A^2*Q)

%damping coefficient
c=0.0031%
vper=-200
f_per=1;
w_per=2*pi*f_per;

%Area and capacitance of perturbation electrode
perL=2e-3;
Aper=perL*h
Cper=epsi*Aper/d
deltav2=abs((vper-vdc2))
dk=-(epsi*A*deltav2^2)/(d)^3
del=dk/keff

% The variation in the eigenstates owing to an induced
perturbation in the stiffness of one of the resonators
eigenstate=abs(dk/(4*kc))% (u-u0/u0)
% Relative shift in the resonant frequency for the same
induced
%perturbation in stiffness
freq = abs(dk/(2*keff))*100%(f-f0)/f0)
ratio=abs(dk/(2*kc))*100

%In-phase-mode frequency with dk applied
w_ip= sqrt((keff+kc+(1/2)*(dk+sqrt(4*kc^2+dk^2)))/m)
f_ip=w_ip/(2*pi)

%Out-of-mode frequency with dk applied
w_op= sqrt((keff+kc+(1/2)*(dk-sqrt(4*kc^2+dk^2)))/m)
f_op=w_op/(2*pi)

%In-phase-mode  ratio with dk applied
x1_x2_ip=(dk-sqrt(4*kc^2+dk^2))/(2*kc)

%Out-of-mode ratio with dk applied
x1_x2_op=(dk+sqrt(4*kc^2+dk^2))/(2*kc)


%Theory estimate of motional current for case II in thesis
xj_1=0.419e-6; % simulated displacement of jth resonator at
mode 1

xj_2=0.836e-6; % simulated displacement of jth resonator at
mode 2
```

```
ij_1=eta1*2*pi*f_op0*xj_1 % motional current of jth resonator
at mode 1

ij_2=eta2*2*pi*f_ip0*xj_2 % motional current of jth resonator
at mode 2

% mechanical noise force
Fn=8.0635e-22;

%VCO for closed loop
Kvco = 1 % Hz/V
Ts=1e-5; % output sample rate of signal blocks in Simulink -
100e3 Hz
% its not same as the Nyquist sample rate.


%loop to determine performance parameters as given in Table 3
vper=[-120:10:120]
for i=1:length(vper)
deltav2=abs((vper-vdc2))
dk=(-epsi*A*deltav2.^2)/(d).^3
del=abs(dk/keff)
variation_eigenstate=abs(dk/(4*kc))
eigenstate_variation_in_percent=abs(dk/(4*kc))*100
variation_in_freq = abs(dk/(2*keff))
freq_variation_in_percent = abs(dk/(2*keff))*100
variation_in_ratio=abs(dk/(2*kc))
ratio_variation_in_percent=abs(dk/(2*kc))*100
%In-phase-mode frequency with dk applied
w_ip= sqrt((keff+kc+(1/2)*(dk+sqrt(4*kc.^2+dk.^2)))/m)
f_ip=w_ip/(2*pi)
%Out-of-mode frequency with dk applied
w_op= sqrt((keff+kc+(1/2)*(dk-sqrt(4*kc.^2+dk.^2)))/m)
f_op=w_op/(2*pi)
% freq. difference as a function of deltaK
fdiffn=abs(f_ip-f_op)
%In-phase-mode  ratio with dk applied
x1_x2_ip=(dk-sqrt(4*kc.^2+dk.^2))/(2*kc)
%Out-of-mode ratio with dk applied
x1_x2_op=(dk+sqrt(4*kc.^2+dk.^2))/(2*kc)
end
```

MATLAB SCRIPT FOR SPECTRAL ANALYSIS

```
figure(2)
fs = 100e3;  %Nyquist frequency
y = fft(im2); % compute FFT of a output signal
n = length(im2); % number of samples
P2 = abs(y/n);
```

```
P1 = P2(1:n/2+1);
P1(2:end-1) = 2*P1(2:end-1);

f = fs*(0:(n/2))/n;
plot(f,P1)
title('Single-Sided Amplitude Spectrum of X(t)')
xlabel('f (Hz)')
ylabel('|P1(f)|')
grid on
hold on
```

Appendix B

HIGH VOLTAGE DC-DC: Q SERIES

This class of DC to High Voltage DC Converters was used during the experimental methodology provided in 0 above. We required the unit with 0-12V input and 0 to +/-200V output, with current limitation. DC-DC CONVERTER used has feature of +/-200V, 500MW.

Following are the features of the power supply units from EMCO. For details, refer https://www.xppower.com/Product/Q-Series and for datasheet, https://www.xppower.com/Portals/0/pdfs/SF_Q_Series.pdf.

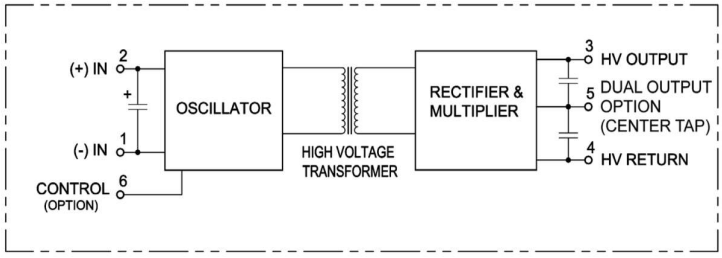

(a)

(b)

Figure: Power supply usage-(a) Pin designators for pin out models up to 5KV, (b) picture representation.

Specifications

DC to High Voltage DC Converters

Isolated Output Voltage is Proportional to Input Voltage

Ultra-Miniature

Low Turn On Voltage: <0.7VDC

100V to 10kV Output Voltage

Positive or Negative

Very Low I/O Leakage Current

Appendix C

A picture of instruments and apparatus used during the experiment setup.

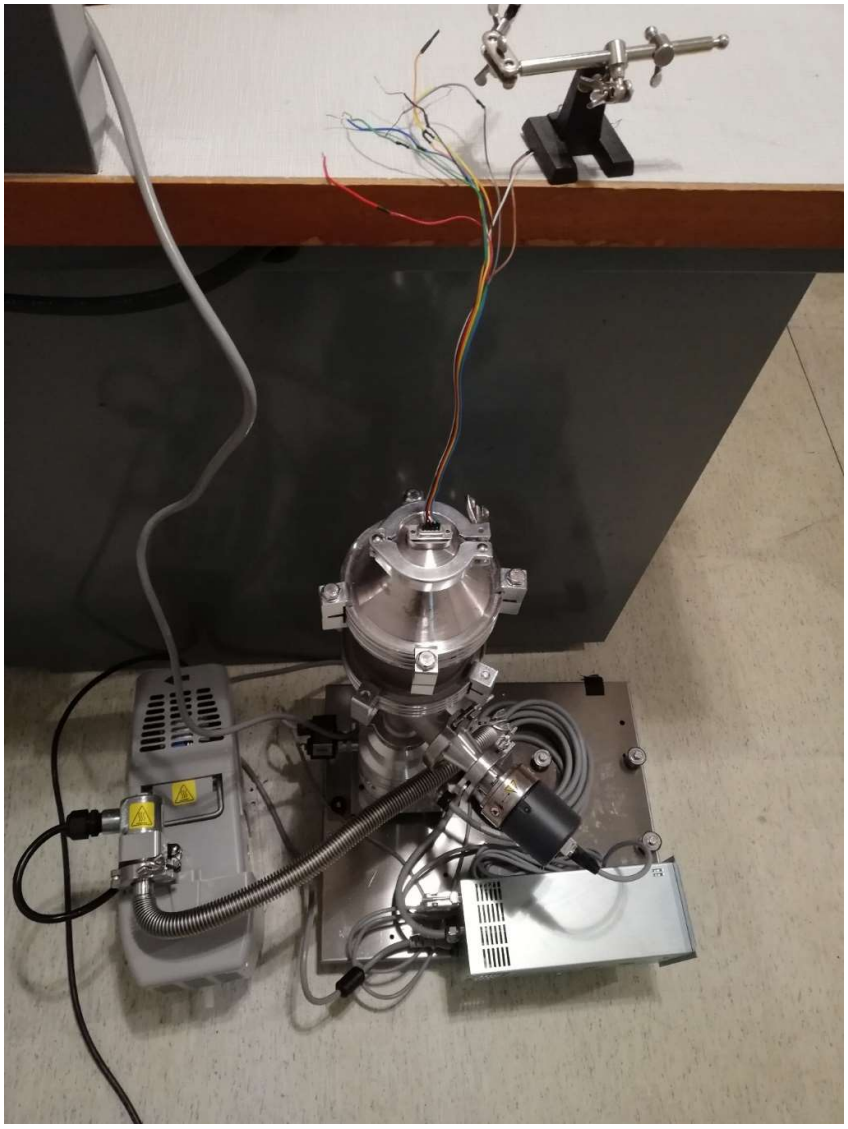

Figure: vacuum chamber

Figure: Power supply used for polarization

Figure: Power supply used for applying perturbations

References

[1] Y. Wang, C. Zhao, C. Wang, D. Cerica, M. Baijot, V. Pachkawade, A. Ghorbani, M. Boutier, A. Vanderplasschen, M. Kraft, A Reversible Method to Characterize the Mass Sensitivity of a 3-Dof Mode Localized Coupled Resonator under Atmospheric Pressure, Proceedings. (2017). doi:10.3390/proceedings1040493.

[2] Jonathan Bernstein, An Overview of MEMS Inertial Sensing Technology | Sensors Magazine, (n.d.). https://www.sensorsmag.com/components/overview-mems-inertial-sensing-technology (accessed March 28, 2019).

[3] S.D. Senturia, Lumped Modeling, in: Microsyst. Des., 2001: pp. 103–124. doi:10.1007/0-306-47601.

[4] G.K. Fedder, Capacitive Resonators, in: Reson. MEMS Princ. Model. Implementation, Appl., 2015: pp. 119–146. doi:10.1002/9783527676330.ch6.

[5] W.T. Hsu, Recent Progress in Silicon MEMS Oscillators, in: 40th Annu. Precise Time Interval Meet., 2008.

[6] R. Abdolvand, B. Bahreyni, J.E.Y. Lee, F. Nabki, Micromachined resonators: A review, Micromachines. (2016). doi:10.3390/mi7090160.

[7] S. Lee, C.T.-C. Nguyen, Mechanically-coupled micromechanical resonator arrays for improved phase noise, in: 2005. doi:10.1109/freq.2004.1418444.

[8] C.T.C. Nguyen, Frequency-selective MEMS for miniaturized low-power communication devices, IEEE Trans. Microw. Theory Tech. (1999). doi:10.1109/22.780400.

[9] J.E.Y. Lee, A.A. Seshia, Direct parameter extraction in feedthrough-embedded capacitive MEMS resonators, Sensors Actuators, A Phys. (2011). doi:10.1016/j.sna.2011.02.016.

[10] J.E.Y. Lee, B. Bahreyni, A.A. Seshia, An axial strain modulated double-ended tuning fork electrometer, Sensors Actuators, A Phys. (2008). doi:10.1016/j.sna.2008.09.010.

[11] P. Enoksson, G. Stemme, E. Stemme, A silicon resonant sensor structure for coriolis mass-flow measurements, J. Microelectromechanical Syst. (1997). doi:10.1109/84.585789.

[12] S. Ren, W. Yuan, D. Qiao, J. Deng, X. Sun, Pressure sensor with integrated resonator operating at atmospheric pressure, Sensors (Switzerland). (2013). doi:10.3390/s131217006.

[13] H.S. Wasisto, S. Merzsch, A. Waag, E. Uhde, T. Salthammer, E. Peiner, Airborne engineered nanoparticle mass sensor based on a silicon resonant cantilever, Sensors Actuators, B Chem. (2013). doi:10.1016/j.snb.2012.04.003.

[14] I.B. Baek, S. Byun, B.K. Lee, J.H. Ryu, Y. Kim, Y.S. Yoon, W.I. Jang, S. Lee, H.Y. Yu, Attogram mass sensing based on silicon microbeam resonators, Sci. Rep. (2017).

doi:10.1038/srep46660.

[15] M. Pandit, C. Zhao, G. Sobreviela, A. Mustafazade, S. Du, X. Zou, A.A. Seshia, Closed-Loop Characterization of Noise and Stability in a Mode-Localized Resonant MEMS Sensor, IEEE Trans. Ultrason. Ferroelectr. Freq. Control. (2019). doi:10.1109/TUFFC.2018.2878241.

[16] M. Spletzer, A. Raman, A.Q. Wu, X. Xu, R. Reifenberger, Ultrasensitive mass sensing using mode localization in coupled microcantilevers, Appl. Phys. Lett. (2006). doi:10.1063/1.2216889.

[17] P. Thiruvenkatanathan, J. Yan, J. Woodhouse, A.A. Seshia, Enhancing parametric sensitivity in electrically coupled MEMS resonators, J. Microelectromechanical Syst. (2009). doi:10.1109/JMEMS.2009.2025999.

[18] C. Zhao, G.S. Wood, J. Xie, H. Chang, S.H. Pu, M. Kraft, A Three Degree-of-Freedom Weakly Coupled Resonator Sensor with Enhanced Stiffness Sensitivity, J. Microelectromechanical Syst. (2016). doi:10.1109/JMEMS.2015.2490204.

[19] C. Zhao, M.H. Montaseri, G.S. Wood, S.H. Pu, A.A. Seshia, M. Kraft, A review on coupled MEMS resonators for sensing applications utilizing mode localization, Sensors Actuators, A Phys. (2016). doi:10.1016/j.sna.2016.07.015.

[20] P. Thiruvenkatanathan, J. Yan, A.A. Seshia, Common mode rejection in electrically coupled MEMS resonators utilizing mode localization for sensor applications, in: 2009 IEEE Int. Freq. Control Symp. Jt. with 22nd Eur. Freq. Time Forum, 2009. doi:10.1109/FREQ.2009.5168201.

[21] P. Thiruvenkatanathan, A.A. Seshia, Mode-localized displacement sensing, J. Microelectromechanical Syst. (2012). doi:10.1109/JMEMS.2012.2198047.

[22] P. Thiruvenkatanathan, J. Yan, A.A. Seshia, Ultrasensitive mode-localized micromechanical electrometer, in: 2010 IEEE Int. Freq. Control Symp. FCS 2010, 2010. doi:10.1109/FREQ.2010.5556368.

[23] C. Zhao, G.S. Wood, J. Xie, H. Chang, S.H. Pu, M. Kraft, A force sensor based on three weakly coupled resonators with ultrahigh sensitivity, Sensors Actuators, A Phys. (2015). doi:10.1016/j.sna.2015.05.011.

[24] H. Zhang, B. Li, W. Yuan, M. Kraft, H. Chang, An Acceleration Sensing Method Based on the Mode Localization of Weakly Coupled Resonators, J. Microelectromechanical Syst. (2016). doi:10.1109/JMEMS.2015.2514092.

[25] G.S. Wood, C. Zhao, S.H. Pu, S.A. Boden, I. Sari, M. Kraft, Mass sensor utilising the mode-localisation effect in an electrostatically-coupled MEMS resonator pair fabricated using an SOI process, Microelectron. Eng. (2016). doi:10.1016/j.mee.2016.03.035.

[26] C. Zhao, G.S. Wood, S. Hui Pu, M. Kraft, A mode-localized MEMS electrical potential sensor based on three electrically coupled resonators, J. Sensors Sens. Syst. (2017). doi:10.5194/jsss-6-1-2017.

[27] X. Zou, P. Thiruvenkatanathan, A.A. Seshia, A high-resolution micro-electro-mechanical resonant tilt sensor, Sensors Actuators, A Phys. (2014).

doi:10.1016/j.sna.2014.10.004.

[28] B. Li, H. Zhang, J. Zhong, H. Chang, A mode localization based resonant MEMS tilt sensor with a linear measurement range of 360??, in: Proc. IEEE Int. Conf. Micro Electro Mech. Syst., 2016. doi:10.1109/MEMSYS.2016.7421786.

[29] X. Zou, P. Thiruvenkatanathan, A.A. Seshia, Micro-electro-mechanical resonant tilt sensor, in: 2012 IEEE Int. Freq. Control Symp. IFCS 2012, Proc., 2012. doi:10.1109/FCS.2012.6243702.

[30] M. Huff, MEMS fabrication, Sens. Rev. (2002). doi:10.1108/02602280210697087.

[31] S. Lee, S. Park, D. Il Cho, Surface/bulk micromachining (SBM) process: A new method for fabricating released MEMS in single crystal silicon, J. Microelectromechanical Syst. (1999). doi:10.1109/84.809055.

[32] M. Aslam, Bulk etching of silicon wafer and development of a polyimide membrane, in: J. Phys. Conf. Ser., 2013. doi:10.1088/1742-6596/439/1/012029.

[33] R. Maeda, M. Takahashi, S. Sasaki, Commercialization of MEMS and nano manufacturing, in: 6th Int. IEEE Conf. Polym. Adhes. Microelectron. Photonics, Polytronic 2007, Proc., 2007. doi:10.1109/POLYTR.2007.4339130.

[34] A.C. Fischer, M. Mäntysalo, F. Niklaus, Inkjet Printing, Laser-Based Micromachining and Micro 3D Printing Technologies for MEMS, in: Handb. Silicon Based MEMS Mater. Technol. Second Ed., 2015: pp. 550–564. doi:10.1016/B978-0-323-29965-7.00026-9.

[35] S. Gao, H. Huang, Recent advances in micro- and nano-machining technologies, Front. Mech. Eng. (2017). doi:10.1007/s11465-017-0410-9.

[36] M.R.H. Knowles, G. Rutterford, D. Karnakis, A. Ferguson, Micro-machining of metals, ceramics and polymers using nanosecond lasers, Int. J. Adv. Manuf. Technol. (2007). doi:10.1007/s00170-007-0967-2.

[37] M.C. Gower, Industrial applications of laser micromachining, Opt. Express. (2000). doi:10.1364/OE.7.000056.

[38] J. Meijer, Laser beam machining (LBM), state of the art and new opportunities, in: J. Mater. Process. Technol., 2004. doi:10.1016/j.jmatprotec.2004.02.003.

[39] F. Dupont, S. Stoukatch, P. Laurent, S. Dricot, M. Kraft, 355 nm UV laser patterning and post-processing of FR4 PCB for fine pitch components integration, Opt. Lasers Eng. (2018). doi:10.1016/j.optlaseng.2017.08.014.

[40] R. Fedosejevs, M. Argument, a. Sardarli, S.E.E. Kirkwood, R. Holenstein, Y.Y.Y. Tsui, Laser micromachining for microfluidic, microelectronic and MEMS applications, Proc. Int. Conf. MEMS, NANO Smart Syst. (2003). doi:10.1109/ICMENS.2003.1221964.

[41] Y. Liao, J. Song, E. Li, Y. Luo, Y. Shen, D. Chen, Y. Cheng, Z. Xu, K. Sugioka, K. Midorikawa, Rapid prototyping of three-dimensional microfluidic mixers in glass by femtosecond laser direct writing, Lab Chip. (2012). doi:10.1039/c2lc21015k.

[42] C.N. LaFratta, O. Simoska, I. Pelse, S. Weng, M. Ingram, A convenient direct laser

writing system for the creation of microfluidic masters, Microfluid. Nanofluidics. (2015). doi:10.1007/s10404-015-1574-4.

[43] N. Tsutsumi, J. Hirota, K. Kinashi, W. Sakai, Direct laser writing for micro-optical devices using a negative photoresist, Opt. Express. (2017). doi:10.1364/OE.25.031539.

[44] M. Hatch, Vibration Simulation Using MATLAB and ANSYS, 2010. doi:10.1201/9781420035759.

[45] M.U. Demirci, M.A. Abdelmoneum, C.T.C. Nguyen, Mechanically corner-coupled square microresonator array for reduced series motional resistance, in: TRANSDUCERS 2003 - 12th Int. Conf. Solid-State Sensors, Actuators Microsystems, Dig. Tech. Pap., 2003. doi:10.1109/SENSOR.2003.1216925.

[46] F.D. Bannon, J.R. Clark, C.T.C. Nguyen, High-Q HF Microelectromechanical Filters, IEEE J. Solid-State Circuits. (2000). doi:10.1109/4.839911.

[47] S. Pourkamali, F. Ayazi, Electrically coupled MEMS bandpass filters: Part I: With coupling element, Sensors Actuators, A Phys. (2005). doi:10.1016/j.sna.2005.03.038.

[48] C.Y. Chen, M.H. Li, C.S. Li, S.S. Li, Design and characterization of mechanically coupled CMOS-MEMS filters for channel-select applications, in: Sensors Actuators, A Phys., 2014. doi:10.1016/j.sna.2014.04.026.

[49] G.S. Wood, C. Zhao, S.H. Pu, I. Sari, M. Kraft, An Investigation of Structural Dimension Variation in Electrostatically Coupled MEMS Resonator Pairs Using Mode Localization, IEEE Sens. J. (2016). doi:10.1109/JSEN.2016.2573850.

[50] H. Zhang, H. Chang, W. Yuan, Characterization of forced localization of disordered weakly coupled micromechanical resonators, Microsystems Nanoeng. (2017). doi:10.1038/micronano.2017.23.

[51] M. Spletzer, A. Raman, H. Sumali, J.P. Sullivan, Highly sensitive mass detection and identification using vibration localization in coupled microcantilever arrays, Appl. Phys. Lett. (2008). doi:10.1063/1.2899634.

[52] B.E. DeMartini, J.F. Rhoads, M.A. Zielke, K.G. Owen, S.W. Shaw, K.L. Turner, A single input-single output coupled microresonator array for the detection and identification of multiple analytes, Appl. Phys. Lett. (2008). doi:10.1063/1.2964192.

[53] C. Zhao, G.S. Wood, J. Xie, H. Chang, S.H. Pu, M. Kraft, A comparative study of output metrics for an MEMS resonant sensor consisting of three weakly coupled resonators, J. Microelectromechanical Syst. (2016). doi:10.1109/JMEMS.2016.2580529.

[54] H. Zhang, J. Huang, W. Yuan, H. Chang, A High-Sensitivity Micromechanical Electrometer Based on Mode Localization of Two Degree-of-Freedom Weakly Coupled Resonators, J. Microelectromechanical Syst. (2016). doi:10.1109/JMEMS.2016.2598780.

[55] J. Yang, H. Kang, H. Chang, A micro resonant electrometer with 9-electron charge resolution in room temperature, in: Proc. IEEE Int. Conf. Micro Electro Mech. Syst., 2018. doi:10.1109/MEMSYS.2018.8346484.

[56] H. Zhang, J. Zhong, J. Yang, W. Yuan, H. Kang, H. Chang, Algebraic summation of

eigenstates as a novel output metric to extend the linear sensing range of mode-localized sensors, in: Proc. IEEE Sensors, 2017. doi:10.1109/ICSENS.2017.8233869.

[57] H. Zhang, W. Yuan, Y. Hao, H. Chang, Influences of the feedthrough capacitance on the frequency synchronization of the weakly coupled resonators, IEEE Sens. J. (2015). doi:10.1109/JSEN.2015.2453401.

[58] M.H. Montaseri, J. Xie, H. Chang, Z. Chao, G. Wood, M. Kraft, Atmospheric pressure mode localization coupled resonators force sensor, in: 2015 Transducers - 2015 18th Int. Conf. Solid-State Sensors, Actuators Microsystems, TRANSDUCERS 2015, 2015. doi:10.1109/TRANSDUCERS.2015.7181140.

[59] Y. Wang, C. Zhao, C. Wang, D. Cerica, M. Baijot, Q. Xiao, S. Stoukatch, M. Kraft, A mass sensor based on 3-DOF mode localized coupled resonator under atmospheric pressure, Sensors Actuators, A Phys. (2018). doi:10.1016/j.sna.2018.06.028.

[60] M.S. Hajhashemi, B. Bahreyni, Characterization of disturbances in systems of coupled micro-resonator arrays, IEEE Sens. J. (2012). doi:10.1109/JSEN.2012.2194279.

[61] D.F. Wang, X. Li, X. Yang, T. Ikehara, R. Maeda, Enhancing amplitude changes by mode localization in trio cantilevers with mass perturbation, J. Micromechanics Microengineering. (2015). doi:10.1088/0960-1317/25/9/095017.

[62] L. Li, In search of optimal mode localization in two coupled mechanical resonators, J. Appl. Phys. (2015). doi:10.1063/1.4926863.

[63] H. Kang, J. Yang, H. Chang, A closed-loop accelerometer based on three degree-of-freedom weakly coupled resonator with self-elimination of feedthrough signal, IEEE Sens. J. (2018). doi:10.1109/JSEN.2018.2817197.

[64] J. Yang, J. Zhong, H. Chang, A Closed-Loop Mode-Localized Accelerometer, J. Microelectromechanical Syst. (2018). doi:10.1109/JMEMS.2017.2787544.

[65] H. Kang, J. Yang, H. Chang, A mode-localized accelerometer based on four degree-of-freedom weakly coupled resonators, in: Proc. IEEE Int. Conf. Micro Electro Mech. Syst., 2018. doi:10.1109/MEMSYS.2018.8346717.

[66] M. Pandit, C. Zhao, G. Sobreviela, A. Mustafazade, X. Zou, A.A. Seshia, A mode-localized MEMS accelerometer with 7μg bias stability, in: Proc. IEEE Int. Conf. Micro Electro Mech. Syst., 2018. doi:10.1109/MEMSYS.2018.8346719.

[67] S. Hafizi-Moori, E. Cretu, Reducing measurement error in capacitive readout circuits based on weakly coupled resonators, IEEE Sens. J. (2017). doi:10.1109/JSEN.2016.2634588.

[68] S. Hafizi-Moori, E. Cretu, Weakly-coupled resonators in capacitive readout circuits, IEEE Trans. Circuits Syst. I Regul. Pap. (2015). doi:10.1109/TCSI.2014.2365331.

[69] M. Manav, A.S. Phani, E. Cretu, Mode localized MEMS transducers with voltage-controlled linear coupling, J. Micromechanics Microengineering. (2017). doi:10.1088/1361-6439/aa6652.

[70] M. Manav, G. Reynen, M. Sharma, E. Cretu, A.S. Phani, Ultrasensitive resonant MEMS transducers with tunable coupling, in: 2013 Transducers Eurosensors XXVII 17th Int. Conf. Solid-State Sensors, Actuators Microsystems, TRANSDUCERS

EUROSENSORS 2013, 2013. doi:10.1109/Transducers.2013.6626937.

[71] H. Zhang, J. Yang, W. Yuan, H. Chang, Linear sensing for mode-localized sensors, Sensors Actuators, A Phys. (2018). doi:10.1016/j.sna.2018.05.006.

[72] P. Thiruvenkatanathan, J. Woodhouse, J. Yan, A.A. Seshia, Limits to mode-localized sensing using micro- and nanomechanical resonator arrays, in: J. Appl. Phys., 2011. doi:10.1063/1.3590143.

[73] G. Tao, H. Zhang, H. Chang, B. Choubey, Inverse Eigenvalue Sensing in Coupled Micro/Nano System, J. Microelectromechanical Syst. (2018). doi:10.1109/JMEMS.2018.2855080.

[74] B. Choubey, C. Anthony, N.H. Saad, M. Ward, R. Turnbull, S. Collins, Characterization of coupled micro/nanoresonators using inverse eigenvalue analysis, Appl. Phys. Lett. (2010). doi:10.1063/1.3491802.

[75] G. Tao, B. Choubey, A simple technique to readout and characterize coupled MEMS resonators, J. Microelectromechanical Syst. (2016). doi:10.1109/JMEMS.2016.2581118.

[76] H. Zhang, J. Zhong, W. Yuan, J. Yang, H. Chang, Ambient pressure drift rejection of mode-localized resonant sensors, in: Proc. IEEE Int. Conf. Micro Electro Mech. Syst., 2017. doi:10.1109/MEMSYS.2017.7863604.

[77] M. Pandit, C. Zhao, G. Sobreviela, A.A. Seshia, Immunity to Temperature Fluctuations in Weakly Coupled MEMS Resonators, in: Proc. IEEE Sensors, 2018. doi:10.1109/ICSENS.2018.8589869.

[78] H. Zhang, H. Kang, H. Chang, Suppression on Nonlinearity of Mode-Localized Sensors Using Algebraic Summation of Amplitude Ratios as the Output Metric, IEEE Sens. J. (2018). doi:10.1109/JSEN.2018.2857923.

[79] M. Pandit, C. Zhao, G. Sobreviela, S. Du, X. Zou, A. Seshia, Utilizing energy localization in weakly coupled nonlinear resonators for sensing applications, J. Microelectromechanical Syst. (2019). doi:10.1109/JMEMS.2019.2894953.

[80] M. Pandit, C. Zhao, G. Sobreviela, A. Mustafazade, A.A. Seshia, Coupled Nonlinear MEMS Resonators for Sensing, in: IFCS 2018 - IEEE Int. Freq. Control Symp., 2018. doi:10.1109/FCS.2018.8597571.

[81] C. Zhao, G. Sobreviela, M. Pandit, S. Du, X. Zou, A. Seshia, Experimental observation of noise reduction in weakly coupled nonlinear MEMS resonators, J. Microelectromechanical Syst. (2017). doi:10.1109/JMEMS.2017.2764138.

[82] M. Pandit, C. Zhao, A. Mustafazade, G. Sobreviela, A.A. Seshia, Nonlinear cancellation in weakly coupled MEMS resonators, in: 2017 Jt. Conf. Eur. Freq. Time Forum IEEE Int. Freq. Control Symp. EFTF/IFC 2017 - Proc., 2017. doi:10.1109/FCS.2017.8088787.

[83] C. Zhao, M. Pandit, G. Sobreviela, A. Mustafazade, S. Du, X. Zou, A. Seshia, On the noise optimization of resonant MEMS sensors utilizing vibration mode localization, Appl. Phys. Lett. (2018). doi:10.1063/1.5025818.

[84] J. Juillard, P. Prache, P.M. Ferreira, N. Barniol, Impact of output metric on the

resolution of mode-localized MEMS resonant sensors, in: 2017 Jt. Conf. Eur. Freq. Time Forum IEEE Int. Freq. Control Symp. EFTF/IFC 2017 - Proc., 2017. doi:10.1109/FCS.2017.8088943.

[85] J. Juillard, P. Prache, P. Maris Ferreira, N. Barniol, Ultimate limits of differential resonant MEMS sensors based on two coupled linear resonators, IEEE Trans. Ultrason. Ferroelectr. Freq. Control. (2018). doi:10.1109/TUFFC.2018.2869415.

[86] C. Zhao, G.S. Wood, S.H. Pu, M. Kraft, A feasibility study for a self-oscillating loop for a three degree-of-freedom coupled MEMS resonator force sensor, in: Procedia Eng., 2015. doi:10.1016/j.proeng.2015.08.766.

[87] J. Yang, J. Huang, J. Zhong, H. Zhang, H. Chang, Self-oscillation for mode localized sensors, in: TRANSDUCERS 2017 - 19th Int. Conf. Solid-State Sensors, Actuators Microsystems, 2017. doi:10.1109/TRANSDUCERS.2017.7994172.

[88] C. Zhao, M. Pandit, B. Sun, G. Sobreviela, X. Zou, A. Seshia, A Closed-Loop Readout Configuration for Mode-Localized Resonant MEMS Sensors, J. Microelectromechanical Syst. (2017). doi:10.1109/JMEMS.2017.2690942.

[89] M. Pandit, C. Zhao, G. Sobreviela, A. Mustafazade, A.A. Seshia, Closed-loop tracking of amplitude and frequency in a mode-localized resonant MEMS sensor, in: 2017 Jt. Conf. Eur. Freq. Time Forum IEEE Int. Freq. Control Symp. EFTF/IFC 2017 - Proc., 2017. doi:10.1109/FCS.2017.8088944.

[90] M. Pandit, C. Zhao, G. Sobreviela, A. Mustafazade, A.A. Seshia, Reduction of amplitude ratio dependence on drive level in mode localized resonant MEMS sensors, in: Proc. IEEE Sensors, 2017. doi:10.1109/ICSENS.2017.8233868.

[91] P. Prache, J. Juillard, P.M. Ferreira, N. Barniol, M. Riverola, Design and characterization of a monolithic CMOS-MEMS mutually injection-locked oscillator for differential resonant sensing, Sensors Actuators, A Phys. (2018). doi:10.1016/j.sna.2017.11.025.

[92] J. Juillard, P. Prache, N. Barniol, Analysis of mutually injection-locked oscillators for differential resonant sensing, IEEE Trans. Circuits Syst. I Regul. Pap. (2016). doi:10.1109/TCSI.2016.2553298.

[93] P. Prache, A. Uranga, N. Barniol, J. Juillard, Temperature-drift rejection and sensitivity to mismatch of synchronized strongly-coupled M/NEMS resonators, in: Proc. IEEE Int. Conf. Micro Electro Mech. Syst., 2016. doi:10.1109/MEMSYS.2016.7421815.

[94] MEMS Software - For Microelectromechanical Systems Simulation, (n.d.). https://www.comsol.com/mems-module (accessed January 31, 2019).

[95] Yu-Wei Lin, Sheng-Shian Li, Yuan Xie, Zeying Ren, C.T.-C. Nguyen, Vibrating micromechanical resonators with solid dielectric capacitive transducer gaps, in: 2006. doi:10.1109/freq.2005.1573914.

[96] L. Hung, C. Nguyen, High-Q Low-Impedance MEMS Resonators, UC Berkeley Electron. Theses Diss. (2012).

[97] H. Zhang, W. Yuan, J. Huang, B. Li, H. Chang, A high-sensitive resonant electrometer

based on mode localization of the weakly coupled resonators, in: Proc. IEEE Int. Conf. Micro Electro Mech. Syst., 2016. doi:10.1109/MEMSYS.2016.7421564.

[98] P. Thiruvenkatanathan, J. Yan, J. Woodhouse, A. Aziz, A.A. Seshia, Ultrasensitive mode-localized mass sensor with electrically tunable parametric sensitivity, 2010. doi:10.1063/1.3315877.

[99] Lecture 22: Finding Natural Frequencies and Mode Shapes of a 2 DOF System | Reducing Problem Vibration and Intro to Multi-DOF Vibration | Engineering Dynamics | Mechanical Engineering | MIT OpenCourseWare, (n.d.). https://ocw.mit.edu/courses/mechanical-engineering/2-003sc-engineering-dynamics-fall-2011/reducing-problem-vibration-and-intro-to-multi-dof-vibration/lecture-22-finding-natural-frequencies-mode-shapes-of-a-2-dof-system/ (accessed June 29, 2019).

[100] T.B. Gabrielson, Mechanical-Thermal Noise in Micromachined Acoustic and Vibration Sensors, IEEE Trans. Electron Devices. (1993). doi:10.1109/16.210197.

[101] Z. Djurić, Mechanisms of noise sources in microelectromechanical systems, Microelectron. Reliab. (2002). doi:10.1016/s0026-2714(00)00004-4.

[102] Precision, Low Power, 18MHz Transimpedance Amplifier, n.d. www.ti.com (accessed June 23, 2019).

[103] TI Precision Labs - Op Amps: Noise 1 | TI.com Video, (n.d.). https://training.ti.com/ti-precision-labs-op-amps-noise-1 (accessed June 23, 2019).

[104] T. Instruments, Noise Analysis in Operational Amplifier Circuits, Texas Instruments. (2007). doi:10.1016/S0026-0576(03)90164-4.

[105] P.R. Gray, R.G. Meyer, Analysis and Design of Analog Integrated Circuits, Eur. J. Eng. Educ. (1993). doi:10.1080/0304379930892171.

[106] Model voltage controlled oscillator - Simulink - MathWorks Benelux, (n.d.). https://nl.mathworks.com/help/msblks/ref/vco.html?searchHighlight=VCO&s_tid=doc_srchtitle (accessed June 24, 2019).

[107] S. Di, X. Chu, D. Wei, Z. Wang, G. Chi, Y. Liu, Analysis of kerf width in micro-WEDM, Int. J. Mach. Tools Manuf. (2009). doi:10.1016/j.ijmachtools.2009.04.006.

[108] Y. Okamoto, T. Ikeda, H. Kurihara, A. Okada, M. Kido, Control of Kerf Width in Multi-wire EDM Slicing of Semiconductors with Circular Section, in: Procedia CIRP, 2018. doi:10.1016/j.procir.2017.12.030.

[109] X. Chen, Y. Wang, Z. Wang, H. Liu, G. Chi, Study on Micro Reciprocated Wire-EDM for Complex Indexing Structure, in: Procedia CIRP, 2018. doi:10.1016/j.procir.2017.12.033.

[110] Sirris | Driving industry by technology, (n.d.). https://sirris.be/fr (accessed June 25, 2019).

[111] Laser MicroJet solutions for high precision and micro-machining, (n.d.). https://www.synova.ch/applications/micro-machining.html (accessed June 10, 2019).

[112] G. Vescio, J. López-Vidrier, R. Leghrib, A. Cornet, A. Cirera, Flexible inkjet printed high-k HfO2-based MIM capacitors, J. Mater. Chem. C. (2016).

doi:10.1039/c5tc03307a.

[113] J. Vaithilingam, E. Saleh, L. Körner, R.D. Wildman, R.J.M. Hague, R.K. Leach, C.J. Tuck, 3-Dimensional inkjet printing of macro structures from silver nanoparticles, Mater. Des. (2018). doi:10.1016/j.matdes.2017.10.070.

[114] M. Saari, B. Cox, E. Richer, P.S. Krueger, A.L. Cohen, Fiber Encapsulation Additive Manufacturing: An Enabling Technology for 3D Printing of Electromechanical Devices and Robotic Components, 3D Print. Addit. Manuf. (2015). doi:10.1089/3dp.2015.0003.

[115] M.A. Skylar-Scott, S. Gunasekaran, J.A. Lewis, Laser-assisted direct ink writing of planar and 3D metal architectures, Proc. Natl. Acad. Sci. (2016). doi:10.1073/pnas.1525131113.

[116] M.T. Rahman, A. Rahimi, S. Gupta, R. Panat, Microscale additive manufacturing and modeling of interdigitated capacitive touch sensors, Sensors Actuators, A Phys. (2016). doi:10.1016/j.sna.2016.07.014.

[117] F. Molina-Lopez, D. Briand, N.F. De Rooij, All additive inkjet printed humidity sensors on plastic substrate, Sensors Actuators, B Chem. (2012). doi:10.1016/j.snb.2012.02.042.

[118] P.M. Harrey, B.J. Ramsey, P.S.A. Evans, D.J. Harrison, Capacitive-type humidity sensors fabricated using the offset lithographic printing process, Sensors Actuators, B Chem. (2002). doi:10.1016/S0925-4005(02)00240-X.

[119] C. Gaspar, J. Olkkonen, S. Passoja, M. Smolander, Paper as active layer in inkjet-printed capacitive humidity sensors, Sensors (Switzerland). (2017). doi:10.3390/s17071464.

[120] T. Sekitani, M. Takamiya, Y. Noguchi, S. Nakano, Y. Kato, K. Hizu, H. Kawaguchi, T. Sakurai, T. Someya, A large-area flexible wireless power transmission sheet using printed plastic MEMS switches and organic field-effect transistors, in: Tech. Dig. - Int. Electron Devices Meet. IEDM, 2006. doi:10.1109/IEDM.2006.346764.

[121] E.S. Park, Y. Chen, T.J.K. Liu, V. Subramanian, A new switching device for printed electronics: Inkjet-printed microelectromechanical relay, Nano Lett. (2013). doi:10.1021/nl4028632.

[122] A. Bessonov, M. Kirikova, S. Haque, I. Gartseev, M.J.A. Bailey, Highly reproducible printable graphite strain gauges for flexible devices, Sensors Actuators, A Phys. (2014). doi:10.1016/j.sna.2013.11.034.

[123] T. Yokota, S. Nakano, T. Sekitani, T. Someya, Plastic complementary microelectromechanical switches, Appl. Phys. Lett. (2008). doi:10.1063/1.2959644.

[124] S. Stoukatch, F. Dupont, L. Seronveaux, D. Vandormael, M. Kraft, Additive low temperature 3D printed electronic as enabling technology for IoT application, in: 2017 IEEE 19th Electron. Packag. Technol. Conf. EPTC 2017, 2018. doi:10.1109/EPTC.2017.8277554.

[125] G.K. Lau, M. Shrestha, Ink-jet printing of micro-elelectro-mechanical systems (MEMS), Micromachines. (2017). doi:10.3390/mi8060194.

[126] H.J. Booth, C.E. Abbott, R.M. Allott, K.L. Boehlen, J. Fieret, J. Greuters, P. Trimble, J. Pedder, Laser micromachining techniques for industrial MEMS applications, in: Phot. Process. Microelectron. Photonics IV, 2005. doi:10.1117/12.599414.

[127] K.A. Ghany, M. Newishy, Cutting of 1.2 mm thick austenitic stainless steel sheet using pulsed and CW Nd:YAG laser, J. Mater. Process. Technol. (2005). doi:10.1016/j.jmatprotec.2005.02.251.

[128] F. Müller, J. Monaghan, Non-conventional machining of particle reinforced metal matrix composite, Int. J. Mach. Tools Manuf. (2000). doi:10.1016/S0890-6955(99)00121-2.

[129] F.A. Al-Sulaiman, B.S. Yilbas, M. Ahsan, CO2 laser cutting of a carbon/carbon multi-lamelled plain-weave structure, J. Mater. Process. Technol. (2006). doi:10.1016/j.jmatprotec.2005.12.004.

[130] D. Herzog, P. Jaeschke, O. Meier, H. Haferkamp, Investigations on the thermal effect caused by laser cutting with respect to static strength of CFRP, Int. J. Mach. Tools Manuf. (2008). doi:10.1016/j.ijmachtools.2008.04.007.

[131] Mechanics of Composite and Multi-functional Materials, Volume 6, 2018. doi:10.1007/978-3-319-63408-1.

[132] R. Pahuja, M. Ramulu, M. Hashish, Abrasive Waterjet Profile Cutting of Thick Titanium/Graphite Fiber Metal Laminate, in: 2017: p. V002T02A013. doi:10.1115/imece2016-67136.

[133] B. Adelmann, C. Ngo, R. Hellmann, High aspect ratio cutting of metals using water jet guided laser, Int. J. Adv. Manuf. Technol. (2015). doi:10.1007/s00170-015-7161-8.

[134] M. Baumeister, K. Dickmann, T. Hoult, Fiber laser micro-cutting of stainless steel sheets, Appl. Phys. A Mater. Sci. Process. (2006). doi:10.1007/s00339-006-3687-9.

[135] D. Perrottet, C. Boillat, S. Amorosi, B. Richerzhagen, PV processing: Improved PV-cell scribing using water jet guided laser., Refocus. (2005). doi:10.1016/S1471-0846(05)70398-X.

[136] J. Battaglia, D. Perrottet, R. Housh, B. Richerzhagen, Synova has re-invented the laser: No heat damage, no beam divergence, no cutting gas, no deposition, in: 2018. doi:10.2351/1.5060916.

[137] J. Wei, Y. Ye, Z. Sun, L. Liu, G. Zou, Control of the kerf size and microstructure in Inconel 738 superalloy by femtosecond laser beam cutting, Appl. Surf. Sci. (2016). doi:10.1016/j.apsusc.2016.02.162.

[138] T. Li, C. Zhou, Z. Liu, W. Wang, Computational and experimental study of nanosecond laser ablation of crystalline silicon, Int. Commun. Heat Mass Transf. (2011). doi:10.1016/j.icheatmasstransfer.2011.05.010.

[139] FreeCAD: Your own 3D parametric modeler, (n.d.). https://www.freecadweb.org/ (accessed June 10, 2019).

[140] WS Flex – Optec, (n.d.). https://optec-laser-systems.com/products/ws-flex/ (accessed June 25, 2019).

[141] Equipement - Microsys: Your partner with microsystems, (n.d.). http://www.microsys.uliege.be/index.php?menu=3&submenu=0&lang=en&eid=26 (accessed June 25, 2019).

[142] LOCTITE ® 5802™, 2009. www.henkel.com/industrial (accessed January 31, 2019).

[143] HB16 - TPT Wire Bonder, (n.d.). https://www.tpt-wirebonder.com/en/wire-bonder/hb16.html (accessed January 31, 2019).

[144] T.A. Mai, B. Richerzhagen, K. Stay, Recent advances in precision machining of various materials with the laser microjet®, in: 2018: p. M704. doi:10.2351/1.5061151.

[145] K.S. Chen, K.S. Ou, MEMS Residual Stress Characterization: Methodology and Perspective, in: Handb. Silicon Based MEMS Mater. Technol. Second Ed., 2015. doi:10.1016/B978-0-323-29965-7.00017-8.

[146] Microscopes and Imaging Systems: Leica Microsystems, (n.d.). https://www.leica-microsystems.com/ (accessed January 31, 2019).

[147] K.L. Ekinci, X.M.H. Huang, M.L. Roukes, Ultrasensitive nanoelectromechanical mass detection, Appl. Phys. Lett. (2004). doi:10.1063/1.1755417.

[148] T.A. Roessig, R.T. Howe, A.P. Pisano, J.H. Smith, Surface-micromachined resonant accelerometer, in: Int. Conf. Solid-State Sensors Actuators, Proc., 1997.